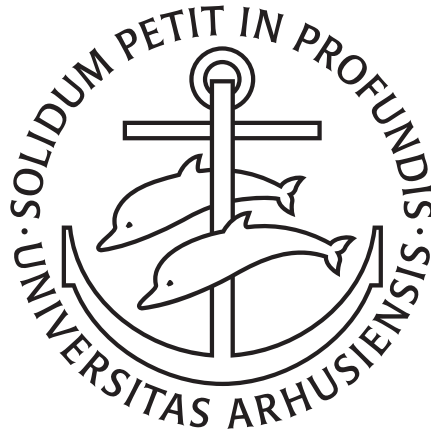


HEAT AT THE MICROSCOPIC LEVEL:
EXPERIMENTAL AND THEORETICAL
PERSPECTIVES



KATÉRINA VERTELETSKY

PHD THESIS
AUGUST 2019

SUPERVISOR: KLAUS MØLMER

DEPARTMENT OF PHYSICS AND ASTRONOMY
AARHUS UNIVERSITY

*“The price an artist pays for doing what he wants
is that he has to do it.”*

— William S. Burroughs

English Summary

Heat. A topic that is so common in everyday life. From the refreshing sorbet to enjoy on a warm summer night to the glow from a crackling fire to bring back to life some fingers still frozen from a well-fought snow battle. It is so common and yet, as common things usually are, not as trivial to describe. It has fascinated physicists for centuries leading to the emergence of its own dedicated field—thermodynamics. It started as an entity to tame and control to transform it into something useful, convert it into work. To be tamed it had to be understood and since its first description, intended to optimize steam engines, it has become an essential question, far beyond its original application. With the emergence of microscopic physics, heat became a reflection of a system’s internal state as the temperature can be described as a function of the system’s degree of excitation. And with the development of experimental tools and techniques that allow a high degree of control at a microscopic level—such as lasers and microscopic traps—it has been nearly suppressed, allowing atoms to be as cold as 500 pK—a trillion times colder than the aforementioned delightful sorbet.

In this PhD thesis, several aspects of microscopic heat are discussed. First, from an ion trapper’s perspective, where heat goes along with motion, rendering it undesirable. We developed a novel experimental technique for ion cooling, by incorporating the heating effects from the micromotion, inherent to Paul traps, into the cooling procedure. It allowed us to form challenging ion crystal structures—pancakes. Then, coming back to its original appreciation, we explored heat from a quantum machinist perspective. By describing the heat dissipated by a two-qubit quantum thermoelectric engine, we suggested a quantum optics description of heat as it could be assimilated to a quantum photodetection process. Going even further, we successfully replicated the effects of heat baths by operating the two-qubit engine solely with projective measurements, offering a new insight into how this fascinating entity can be defined.

Dansk Resumé (Danish Summary)

Varme. Et emne som vi alle kan relatere til i vores hverdag. Fra den forfriskende sorbetis nydt på en varm sommeraften, til skæret fra den knitrende pejls hvor frosne fingre genvinder varmen fra den tidligere sneboldkamp. Men selvom varmen er os så velkendt, så har den, som oftest med velkendte ting, en mere kompliceret beskrivelse end man ville forvente. Varme har i århundreder fascineret fysikere i en sådanne grad, at den har fået sit eget studie—termodynamikken. Termodynamikken tjente først det formål at tæmme og kontrollere varmen for at transformere denne til arbejde, men for at tæmme varmen skal man først forstå denne. Siden den første beskrivelse, formuleret med hensigt på at optimere dampmaskiner, er varmens studie blevet en langt mere essentiel del af fysikken end oprindeligt tiltænkt. I den mikroskopiske fysik bliver varme et mål for et fysiske systems interne tilstand, da systemets temperatur kan relateres til dets excitationsniveau, og i kraft af udviklingen af eksperimentelle værktøjer og teknikker, der fx gennem lasere og mikroskopiske fælder tillader højpræcisionsmanipulation på det mikroskopiske niveau, er det blevet muligt at næsten fuldstændigt undertrykke systemers excitationsniveau, hvilket tillader atomer at køles ned til 500 pK—en billion gange koldere end førnævnte sorbetis.

I denne PhD-afhandling gennemgås og diskuteres flere aspekter af mikroskopisk varme. Først tages udgangspunkt i ionfældefysikerens synspunkt, hvor varme og bevægelse går hånd i hånd og varmen derfor bliver uønsket. Vi udvikler en ny eksperimentel teknik til ionafkøling ved at inkorporere varmeeffekter fra de mikroskopiske bevægelser, som naturligt fremkommer i Paul-fælder—i afkølingsprocessen. Denne teknik tillader os at skabe vanskelige ionkystalstrukturer—pandekager. Herefter betragter vi varme fra en kvantemekanikers synspunkt, hvor vi, ved at undersøge varmedissipationen fra en to-qubit kvantetermoelektrisk maskine, præsenterer en kvanteoptisk beskrivelse af varme i hvilken denne kan identificeres

med en kvantefotodetektionsproces. Yderligere reproducerer vi varmebadets effekt ved udelukkende at drive to-qubit-maskinen med projektive målinger, hvilket tilvejebringer en ny indsigt i varmens natur.

Preface

This dissertation relates the investigations I have conducted during my PhD studies at the Department of Physics and Astronomy, Aarhus University, Denmark, from September 2016 to August 2019. These studies were carried out under the supervision of Professor Michael Drewsen, from September 2016 until February 2018, and Professor Klaus Mølmer, from March 2018 until August 2019.

Notation

$\hbar = 1$ throughout the thesis, unless stated otherwise. In certain locations, where appropriate, explicit indication of dependencies in expressions is omitted, for the sake of brevity.

Acknowledgments

First, I would like to thank Klaus Mølmer for giving me the opportunity of working under his guidance, directing me when needed while giving me the freedom to wander in the wonders of physics. You are without a doubt the best supervisor one could ever wish for and the person I would like to be when I grow up.

I would also like to thank all the amazing people I got the chance to meet and share some time with over my years in Aarhus, in the lab and outside. Thank you Thomas for being a great guide and teammate, I learnt a lot thanks to you and you definitely made those freezing lab sessions warmer. Thank you Jinglei and Itsik for the nice chats, thank you Karen, Julian and Steffan for helping me get through our shared hell, thank you Suzi and Eliska for your friendship and support. And specials thanks to Philip, KD, Felix, Nikolaj and Alexander for dedicating some—non negligible amount—of your time to proof reading this thesis. I

truly appreciate your help.

And then I would like to move on to you, my dearest friends, without whom I would have had some trouble making it through this amazingly interesting yet grueling experience. Pau and M., you are both “my person” and I don’t think I could find the words so I will simply thank you for being in my life. Hugo, thank you for allowing me to take the freedom of being ourselves. Tania and Val, thank you for always finding time for me, no matter how far I am and how little I dare to visit. Pierre, thank you for always reaching out and I promise, I will repay you one day in cafés glacés from Les Deux Magots. David, thank you for simply being my friend through fun and less fun times. And Tib, we did it! To all the others, I did not forget you!

Obviously, I owe infinite thanks to you, Irène and S. For giving me all the tools and freedom of choosing my own path, no matter the sacrifice, and always being by my side. I would like you to know that you have all my love, appreciation and respect. You are wonderful.

Finally, I would like to thank you, Jørgen, for sharing your life with me, always supporting me, helping me tidy my brain without judgement, turkey dancing with me and constantly pushing me to become a better person. Going to Xi’an was most definitely one of the best decisions of my life and I cannot wait for our future adventures!

List of Publications

- [1] K. Verteletsky and K. Mølmer, Work and heat fluctuations reveal the strokes of autonomous quantum heat engines, (2019) arXiv:1907.01039 [quant-ph]. Submitted.

List of Abbreviations

2D	2-Dimensional
3D	3-Dimensional
CCD	Charged Coupled Device
GKLS	Gorini-Kossakowski-Lindblad-Sudarshan
Hz	Hertz
μm	micrometer
MD	Molecular Dynamics
ns	nanosecond
POVM	Positive Operator Valued Measure
QED	Quantum Electro-Dynamics
QRT	Quantum Regression Theorem
RF	Radio-Frequency

Special abbreviations

CH	Cold–Hot. For the measurement only powered thermoelectric engine—where the cold and hot qubits are not coupled to heat baths and measured instead. Refers to an operation cycle where the cold side is measured first.
HC	Hot–Cold. For the measurement only powered thermoelectric engine, refers to an operation cycle where the hot side is measured first.

List of Figures

II.2.1	Radial trapping potential in a quadrupole Paul trap . . .	16
II.2.2	Schematic linear Paul trap	17
II.2.3	Representation of Doppler cooling of a particle by two counter-propagating beams	25
II.2.4	Temperature of a particle cooled by Doppler cooling in a harmonic trap	30
II.2.5	Micromotion direction and amplitude in a linear Paul trap as a function of the ion's position	31
II.2.6	Mean kinetic energy over an RF period for a two level atom in the purely harmonic treatment and including micromotion	34
II.2.7	Shapes of the spheroid as a function of the aspect ratio .	36
II.2.8	Trap frequency ratio as a function of the aspect ratio of a prolate 3D Coulomb crystal	38
II.3.1	Schematic experimental setup for pulsed cooling	42
II.3.2	Energy level structure of $^{40}\text{Ca}^+$	43
II.3.3	Experimental light pulses and RF signal	45
II.3.4	Experimental image of a Coulomb crystal before and after post-processing	50
II.4.1	Definition of the pulse delay with respect to the RF signal	54
II.4.2	Scattering of a Ca^+ ion above the RF nodal line as a function of the pulse delay	56
II.4.3	Experimental pulsed cooled crystals at different pulse lengths	60
II.4.4	Comparison of the best pulse length image to the continuously cooled crystal with the same parameters	61
II.4.5	Experimental pulsed cooled crystals at different intensities and detunings compared to continuously cooled crystals with the same parameters	63

II.4.6	Experimental pulsed cooled crystal with different pulse delays (I)	66
II.4.7	Experimental pulsed cooled crystal with different pulse delays and detunings (II)	67
II.4.8	Experimental continuously cooled crystal with various detunings and intensities	69
II.4.9	Summary of the coldest crystals using optimized pulsed cooling and continuous cooling parameters	70
II.4.10	Pulse cooled Coulomb crystal of ≈ 5350 ions	72
II.4.11	Pulse cooled pancake of ≈ 75 ions	73
II.5.1	Evolution of the temperature during a MD simulation of a Coulomb crystal	81
II.5.2	Evolution of the temperature during the first fifth of an MD simulation of a Coulomb crystal	82
II.5.3	Influence of the ion number and frequency ratio on the aspect of simulated Coulomb crystals	85
II.5.4	Radial profile of the crystal in Fig. II.5.3 (b) plotted with <i>ImageJ</i>	87
II.5.5	Simulated Ca^+ and Mg^+ ions at $T = 1\text{mK}$	89
II.5.6	Simulated crystals of Ca^+ ions at $T = 8\text{ mK}$	90
II.5.7	Simulated temperature catalog for Ca^+ Coulomb crystals	91
II.6.1	Stability regions for a 2D planar crystal calculated for Yb^+ ions	95
II.6.2	Simulated pancakes at $T = 4\text{ mK}$ and $\varphi = 6$	97
II.6.3	Oscillations of the central ion in a pancake after a z -kick compared to the RF trapping signal	98
II.6.4	Oscillations of the central ion in a pancake after a z -kick for different frequency ratios	99
II.6.5	Central ion oscillation frequency after a z -kick as a function of the trap frequency ratio	100
III.A.2.1	Schematic representation of a two-qubit engine powered by heat baths	114
III.A.2.2	Steady state output power of the engine as a function of $t\kappa$ and λ	118
III.A.2.3	Engine efficiency as a function of the hot and cold qubit frequency ratio ω_h/ω_c	121

III.A.2.4	Engine output power as a function of cold, n_c^B , and hot, n_h^B , bath occupation numbers	122
III.A.3.1	Steady state expectation values for the current and cold qubit occupation number	133
III.A.3.2	Mean value and fluctuations of the number of quanta $\mathcal{N}_c(\mathcal{T})$, transferred to the cold bath	134
III.A.4.1	Two-time correlations calculated for different values of the coupling λ to the Josephson junction	139
III.A.4.2	Two-time correlations calculated for different values of the coupling κ to the baths	140
III.A.4.3	Two-time correlations for the emission into the cold bath calculated for two values of E_J	141
III.A.4.4	Normalized three-time correlations and corresponding pure three-body contributions	146
III.B.2.1	Schematic representation of a two-qubit engine powered by measurements	156
III.B.2.2	Operation protocol of a two-qubit engine powered by measurements	158
III.B.3.1	Work generated by the engine measured on the hot side for various projector orientations	167
III.B.3.2	Current generated by the engine measured on the hot side for various operation regimes	168
III.B.3.3	Work generated by the engine measured on the cold side for various projector orientations	170
III.B.3.4	Current generated by the engine measured on the cold side for various measurement frequencies	172
III.B.4.1	Generated work and integrated qubit occupation number difference for the engine measured on both the hot and the cold sides for various projector orientations	179
III.B.4.2	Current generated by the engine measured on both sides at various frequencies and angles	182
III.B.4.3	Selective measurement trajectories	184
III.B.4.4	Selective measurement trajectories—work distribution	186
III.B.4.5	Work produced by the engine adaptively measured on both sides and heat provided by the measurements	189

List of Tables

II.3.1	Trap parameters	47
II.4.1	Experimental parameters—pulse length optimization . .	59
II.4.2	Experimental parameters—pulse intensity and detuning optimization	61
II.4.3	Experimental parameters—pulse delay optimization . . .	64
II.4.4	Experimental parameters—second pulse delay optimization	65
II.4.5	Experimental parameters—continuous cooling optimization	68
II.4.6	Experimental parameters—trapping of a large crystal . .	71
II.4.7	Simulation parameters—large crystal	71
II.4.8	Experimental parameters—trapping of a pancake	72
II.4.9	Simulation parameters—pancake	72
II.6.1	MD Simulated phase transition frequency ratios \mathcal{F}_{MD} .	101
III.A.2.1	Optimized engine parameters	119

Contents

Preface	v
Notation	v
Acknowledgments	v
List of Publications	vii
List of Abbreviations	vii
List of Figures	viii
List of Tables	xi
I Introduction	1
I.1 Thesis Outline	5
II Experimental Perspective – Pulsed Cooling of Trapped Ca^+ Coulomb Crystals	9
II.1 Introduction	11
II.2 Theory of ion trapping and cooling	15
II.2.1 Ion trapping & cooling and micromotion	15
II.2.1.a Ion trapping	15
II.2.1.a.i Trapping potentials	15
II.2.1.a.ii Secular motion	18
II.2.1.b Doppler cooling of trapped ions	19
II.2.1.b.i Atom-light interaction	19
II.2.1.b.ii Doppler cooling	25
II.2.1.c Micromotion	30

	II.2.1.c.i	Origins of the micromotion . . .	30
	II.2.1.c.ii	Micromotion and cooling	32
II.2.2		Trapping of Coulomb crystals	35
II.3		Experimental system and setup	41
II.3.1		System overview	41
	II.3.1.a	Ca ⁺ level structure	41
	II.3.1.b	Experimental setup overview and pulsed cooling	43
	II.3.1.b.i	Overview—45° cooling	43
	II.3.1.b.ii	Pulsed doppler cooling	44
II.3.2		Experimental setup—details	47
	II.3.2.a	Trap	47
	II.3.2.b	Lasers	48
	II.3.2.c	Imaging system	49
	II.3.2.d	Ion trapping procedure	50
II.4		Pulsed cooling of Coulomb crystals	53
II.4.1		Definition and determination of the parameters . .	54
	II.4.1.a	Rising, Falling, Both	54
	II.4.1.b	Pulse delay	55
	II.4.1.c	Intensity	57
II.4.2		Optimization of the pulsed cooling	57
	II.4.2.a	Length	58
	II.4.2.b	Intensity and detuning	61
	II.4.2.c	Delay	64
II.4.3		Pulsed cooling <i>vs.</i> continuous cooling	68
II.4.4		Summary	69
	II.4.4.a	Coldest Coulomb crystals	69
	II.4.4.b	Formation of challenging structures . . .	70
II.4.5		Insight into some of the observed features	73
II.5		Temperature catalog—Molecular Dynamics sim- ulations	77
II.5.1		Newton propagator	78
II.5.2		Thermalizer	79
II.5.3		Input/Output	83
II.5.4		Reproducing experimental data	85
	II.5.4.a	Influence of the number of ions and trap frequencies on the aspect of a crystal . .	85

II.5.4.b	Parameter determination	86
II.5.5	Temperature catalog	88
II.6	Applications—pancakes	93
II.6.1	Experimental formation of pancakes	93
II.6.2	3D–2D phase transition investigation	94
II.6.2.a	Simulation procedure	94
II.6.2.b	Phase transition frequency	99
II.6.2.b.i	Characteristic motion of the central ion	99
II.6.2.b.ii	Determination of the phase transition frequency ratio	100
II.6.2.c	Stability region	101
II.7	Conclusion	103
III	Theoretical Perspective – Powering a Quantum Thermoelectric Engine	105
III.A	Powering a Quantum Thermoelectric Engine by Heat Baths	109
III.A.1	Introduction	109
III.A.2	System overview and optimization	113
III.A.2.1	System Hamiltonian and Master equation	113
III.A.2.1.a	Hamiltonian in the rotating wave approximation	113
III.A.2.1.b	GKLS master equation	115
III.A.2.2	System characterization and optimization	116
III.A.2.2.a	Engine output power	116
III.A.2.2.a.i	Current operator	116
III.A.2.2.a.ii	Power optimization	117
III.A.2.2.a.iii	Engine efficiency	119
III.A.2.2.b	Engine directionality	121
III.A.3	Work and heat—mean values and fluctuations	125
III.A.3.1	Steady state average values	126
III.A.3.1.a	Average work produced by the engine	126

III.A.3.1.b	Average heat transferred to the cold bath	126
III.A.3.2	Fluctuations	127
III.A.3.2.a	Work fluctuations	127
III.A.3.2.b	Heat fluctuations	128
III.A.3.2.b.i	Derivation procedure	128
III.A.3.2.b.ii	Heat variance	128
III.A.3.2.c	Calculation of two-time correlation functions	129
III.A.3.2.c.i	Quantum Regression Theorem	129
III.A.3.2.c.ii	Two-time correlations of the emission into the cold bath	130
III.A.3.2.c.iii	Two-time correlations of the current	131
III.A.3.3	Work and Heat—comparisons	132
III.A.3.3.a	Work vs. Heat	132
III.A.3.3.b	Heat vs. Heat	133
III.A.4	Dynamics of the energy transfer	137
III.A.4.1	Strokes of the engine from two-time correlations	138
III.A.4.1.a	Derivation of the relevant correlations	138
III.A.4.1.b	Damped oscillations in the energy transfer	138
III.A.4.1.c	Frequency of the oscillations	141
III.A.4.2	Three-time correlations	142
III.A.4.2.a	Derivation of the relevant correlations	142
III.A.4.2.a.i	Three-time correlations	142
III.A.4.2.a.ii	Pure three-body contributions	144
III.A.4.2.b	Interesting features	145
III.A.5	Conclusion	149
III.B	Powering a Quantum Thermoelectric Engine by Projective Measurements	153
III.B.1	Introduction	153
III.B.2	Procedure overview and relevant Master Equations	155
III.B.2.1	System and operation protocol	155

III.B.2.1.a	Measurement powered systems	155
III.B.2.1.b	Operation protocol	156
III.B.2.2	Measuring the qubits	157
III.B.2.2.a	Theory of projective measurements on the density matrix	158
III.B.2.2.b	Choice of measurement operators	161
III.B.2.3	Master equation evolution of the system	162
III.B.3	Measurement on the cold or hot side	165
III.B.3.1	Choice of operation parameters	165
III.B.3.1.a	Initial density matrix	165
III.B.3.1.b	Measurement frequency	166
III.B.3.2	Measurement on the hot side	166
III.B.3.2.a	Optimal projectors	167
III.B.3.2.b	Operation regimes	168
III.B.3.3	Measurement on the cold side	169
III.B.3.3.a	Optimal projectors	170
III.B.3.3.b	Operation regimes	171
III.B.4	Measurement on both sides	175
III.B.4.1	Derivation of the periodic steady state	175
III.B.4.2	Heat provided by the measurements	177
III.B.4.3	Unselective measurements	178
III.B.4.3.a	Optimal projectors	178
III.B.4.3.b	Long-time-limit work	180
III.B.4.3.b.i	Measurement at engine charac- teristic frequency	180
III.B.4.3.b.ii	Measurement not at engine fre- quency	181
III.B.4.3.b.iii	Measurement with small angles	181
III.B.4.3.c	Trajectories and work distribution	183
III.B.4.4	Adaptive measurements	187
III.B.4.4.a	Measurement protocol	187
III.B.4.4.b	Maximum obtainable work	188
III.B.5	Conclusion	191

IV	Summary and Outlook	195
	Appendix	203
A	Quantum thermoelectric engine	
	—rotating wave Hamiltonian derivation	203
A.1	Pauli spin matrices	203
A.2	Derivation of the rotating wave hamiltonian . . .	205
B	Quantum thermoelectric engine	
	—derivation of the steady state expectation value of the current	207
C	Quantum thermoelectric engine	
	—derivation of the work fluctuations	209
D	Quantum thermoelectric engine	
	—derivation of the heat fluctuations	213
E	Quantum thermoelectric engine	
	—note on Glauber’s photodetection theory	221
F	Quantum thermoelectric engine	
	—derivation of the two-time correlations	225
F.1	Hot bath–current correlations	225
F.2	Current–cold bath correlations	226
F.3	Hot bath–cold bath correlations	227
G	Quantum thermoelectric engine	
	—derivation of the three-time correlations	229
G.1	Hot bath three-time correlations	229
	G.1.a Derivation	229
	G.1.b Pure three-body contributions	231
G.2	Hot bath–current–cold bath three-time correlations	232
	G.2.a Derivation	232
	G.2.b Pure three-body contributions	233

H	Quantum thermoelectric engine	
	—derivation of the time evolution of the measured engine	235
H.1	Derivation of the time evolution	235
H.2	Derivation of the periodic steady state	238
H.3	Inverse of a matrix of orthogonal eigenvectors . . .	240
I	Quantum thermoelectric engine	
	—Measurement matrices for the no-bath system	243
	Bibliography	256



PART I:
INTRODUCTION

Introduction

What is heat? A very hot topic, that has been the center of lively debates for centuries. Going back to 400 B.C. and the atomic theory formulated by Democritus, who stated that matter was composed of atoms, constantly moving, colliding and rearranging in structures that can induce the feeling of hot or cold. Heat was merely the consequence this special arrangement had on the measuring body. Fascinatingly, from our extremely knowledge biased perspective from which it is so easy to judge the past, the scientific community preferred to wallow in the Aristotelian aether. Since the void was unacceptable, so was a lack of material definition and the phlogiston theory kept rising from its own ashes over the course of the 18th century. Until Lavoisier finally put it out in the late 1700's with the oxygen theory of combustion. Notwithstanding, the fluid description of heat would not dissipate as Lavoisier himself defined in 1789 the concept of the caloric—a subtile fluid, penetrating between the molecules of matter causing its expansion, and which accumulation leads to the sensation of heat [2]. The caloric spread into Carnot's description of classical heat engines in 1824 [3], considered to be the birth of thermodynamics, *i.e.* the description of heat in terms the work that can be drawn from it. At the same time, starting with Bernoulli's revival of the millennium old *clinamen* [4] in 1738, the kinetic theory of heat was gaining supporters. This description of heat as a consequence of microscopic collisions of gas particles sparked the genesis of statistical mechanics by Maxwell [5] and Boltzmann [6, 7]. These two speculated origins of heat were reconciled by Clausius in 1851 [8], who stated that what heat actually was was not of significant importance, as what mattered was its effects on the system it affects. However, with the increasing interest in the microscopic regime and the development of experimental tools which allow us to access it, this blinkered position on the question is unsatisfactory. In order to gain control over a microscopic system, one must understand the microscopic processes it is subject to, and the successful realization of Bose-Einstein

condensation [9], would not have been possible without the description of the system made by Bose [10] and Einstein [11]. However, by using this example, we make the common abusive assimilation of heat and temperature. While the temperature is a state function, *i.e.* a characteristic property of a given system, heat is a process quantity, depending on the path the system took between two moments in time and describing its evolution. Heat gives an integrated picture of the interaction between a system and its environment. Moreover, contrary to work, it does not have palpable effects. These properties of heat render it challenging to grasp.

For a microscopic system in contact with an environment, heat has been defined as the dissipative part of the system evolution, the Hamiltonian part of the evolution giving the work [12, 13]. These definitions however leave room for debate. In fact, they do not address situations where the equation describing the evolution of the system cannot easily be separated into a dissipative and a hamiltonian term. This gives rise to a question: can heat only be defined as the consequence of a dissipative process?

In the course of the PhD related in this thesis, I embraced my national heritage and joined the exciting task of attempting to understand and define heat. With the conviction that knowledge at the microscopic level can be extended to macroscopic manifestations of the same phenomenon, and thus allow a full understanding, I focused my interest to the microscopic scale.

First, I took an ion trapper's perspective. In this setting, heat is assimilated with temperature. Following the statistical description of thermodynamics, hotter systems present a larger energy distribution and are consequently not located in a well-defined state. Therefore, this statistical spread does not allow for precision experiments and is undesirable. For trapped ions, several levels of state definition exist, which each can be associated with a temperature. They can be divided into two categories: the ions' motion and their internal state. In the investigations I took part in in the course of this PhD, the goal was to reduce the temperature associated with the ions' motion. Even though the Doppler cooling technique has been widely used and optimized, this proves to be challenging in Paul trapped three-dimensional ion crystals, as this specific type of trap gives rise to a driven motion of the ions: the micromotion. I participated in developing a new cooling technique, based on Doppler cooling, that takes into account the presence of this additional motion of the ions—pulsed cooling. This allowed me to see that heat could be tamed.

Then, I came back to the original perception of heat, *i.e.* as a source of work. My system became a quantum thermoelectric engine made of two qubits connected *via* a Josephson junction and each coupled to a heat bath. Analytically studying this simple engine, and thus precisely deriving the equations describing its operation, allowed me to get a glimpse into the heat generating processes and to how it can be described. The heat exchanged between the qubit and its respective bath could be expressed in terms of the qubit occupation number and evaluated by a photodetection process. Moreover, I was able to observe the heat traveling through the system which revealed strokes in the operation of the engine, similar to the chuffing of a steam engine.

Finally, in the goal of getting a deeper understanding of heat by gaining even more control over the heat generating processes, I considered a modified design of the two-qubit thermoelectric engine, where one or both baths were replaced by measurements applied to the respective qubits. The engine being operational under these conditions suggested that the measurements can successfully replicate heat baths. This allowed me to describe the heat as the excitation added to the system by the measurement operation, which both gives a definition of heat at the quantum level and provides the cost of the measurement itself.

The three directions of heat investigation I was able to take part in allowed me to form a definition of *heat* as *the additional excitation trapped in a system after the action of an external source.*

I.1 Thesis Outline

In Part II, the experimental insight into heat from the perspective of ion trapping is given. It was conducted on Paul trapped and Doppler cooled Ca^+ ions and more specifically three-dimensional Coulomb crystals formed by a collection of ions. After an introduction to the field in Chapter II.1, the theoretical description of ion trapping and cooling is given—Chapter II.2. Then, in Chapter II.3, the experimental system and setup is described. In particular, Section II.3.1 describes the pulsed cooling procedure that was developed in the course of the study. In Chapter II.4 the optimization of the pulsed cooling applied to calcium Coulomb crystals is presented. The pulse cooled crystals are compared to the customarily continuously cooled structures. The application of this cooling technique to the formation of challenging structures—large Coulomb crystals and two-dimensional structures in the radial plane (pancakes) are also shown. The tempera-

ture of the crystals was assessed by comparison with Molecular Dynamics simulations of ion trapping, which is presented in Chapter II.5. Finally, in Chapter II.6 we focus on investigating the phase transition from the three-dimensional crystal to the pancake structure. Finally, we conclude on our investigations and give a quick outlook in Chapter II.7.

In Part III, the theoretical insight into heat is described.

In Part III.A, the operation of a quantum thermoelectric engine—made of two qubits each coupled to a heat bath, and connected by a Josephson junction—is presented. In Chapter III.A.1 the investigation is contextualized in the field of quantum thermodynamics. Then, in Chapter III.A.2, the system is presented and characterized in terms of power and efficiency in steady state. The electric work produced by the engine at the junction and the heat it exchanges with the baths are defined in Chapter III.A.3. Where both the mean values and fluctuations of these quantities are derived. In Chapter III.A.4, we go beyond the steady state properties of the engine and investigate the dynamics of the energy transfer by-way of multi-time correlation functions. Finally, a conclusion as well as further application of our study are given in Chapter III.A.5.

In Part III.B, we describe the operation of an engine based on the model used in Part III.A, where one or both heat baths were replaced by a measurement protocol. Chapter III.B.1 introduces the topic and Chapter III.B.2 gives a description of the new system and operation protocol of the measured engine. In Chapter III.B.3, we describe the situation where only one of the baths is substituted by measurements. Sec. III.B.3.2 focuses on the case where the hot bath is replaced, while the cold bath is kept, and Sec. III.B.3.3, on the opposite situation (cold bath replaced, hot bath conserved). Both baths are removed and replaced by measurements in Chapter III.B.4. The periodic steady state for the bath-less measured system is derived in Sec. III.B.4.1. It is used in the analysis of the engine's performance when it is unselectively measured (Sec. III.B.4.3). Based on our observation of selective measurement trajectories, a more optimal measurement scheme—adaptive measurements—is described and assessed in Sec. III.B.4.4. Finally, a conclusion and outlook are given in Chapter III.B.5.

In Part IV the main conclusions of the thesis are presented, along with possible directions for further research.

In accordance with GSST rules, Part II contains material that was also used in the progress report for the qualifying examination.



PART II:

EXPERIMENTAL PERSPECTIVE
– PULSED COOLING OF TRAPPED
 Ca^+ COULOMB CRYSTALS

Introduction

The understanding of energy transport at a microscopic level has many applications, ranging from optimizing miniature devices [14] to having a basis for describing more complex systems [15]. Trapped cold ions are ideal candidates for such a study as they are spaced enough to allow for single-site address (the average distance being approximately $10\mu\text{m}$ —see [16] and Fig. **II.5.4**) and can be pinned [17] and brought to a well-defined quantum state [18]. They have already been used to study microscopic friction [19] and phonon dynamics [20]. In order to achieve the desired pinned initial state, the ions have to be trapped—in our case, in a linear Paul trap—and placed in an optical cavity generating the pinning lattice, which renders the customary cooling along the trap axis impossible [21].

Another option for the cooling has to be adopted: a cooling laser at 45° with respect to the axis (see Fig. **II.3.1** for a schematic representation of such a setup). This cooling configuration is challenging, as it excites the radial micromotion of the ions inherent to this type of traps [22], thus reducing the cooling efficiency, which can be dramatic for structures with a large extension in the radial plane, such as large Coulomb crystals [23] or pancakes [24]. We adopted a novel cooling strategy: by pulsing the cooling beam at the frequency of the RF trapping signal responsible for the micromotion, the cooling efficiency was increased and challenging structures could be formed. This technique was developed and optimized on calcium ion Coulomb crystals in the Ion Trap Group and constitutes my experimental insight into heat at the microscopic level.

First, a theoretical introduction to ion trapping and cooling is given (Chap. II.2). Then, after a description of the experimental setup (Chap. II.3), the pulsed cooling optimization is described (Chap. II.4), followed by an outline of the Molecular Dynamics simulation procedure used to assess the efficiency of the cooling scheme (Chap. II.5). Finally, an application of this technique to the formation of challenging structures—two-dimensional radial crystals referred to as pancakes—is presented (Chap. II.6). I single-handedly performed the simulations and theoretical analysis, and conducted the experimental investigations jointly with Thomas Lauprêtre (post-doctoral fellow in the Ion Trap Group).

The laboratory frame axes are denoted by capital letters (X, Y, Z), and the trap axes by (x, y, x).

The character ゃ used to describe the trap frequency ratio in Chap. II.6 is a Japanese hiragana pronounced “ya”.

In accordance with GSST rules, parts of this section was also used in the progress report for the qualifying examination.

Theory of ion trapping and cooling

The experiments were performed using $^{40}\text{Ca}^+$ ions in a linear Paul trap [25, 26]. This design allows a three-dimensional (3D) confinement of the ions but also gives rise to micromotion induced by the oscillating RF field. The confined ions were further cooled by Doppler cooling. We focused our investigations on 3D structures: Coulomb crystals formed by approximately 550 ions. This chapter gives an introduction to the theory of ion trapping and Doppler cooling, the effects of the micromotion on these methods of heat reduction, as well as presents the properties of Coulomb crystals.

II.2.1 Ion trapping & cooling and micromotion

II.2.1.a Ion trapping

II.2.1.a.i Trapping potentials

For an electrostatic field taken in a region with no charge, Gauss's law reduces to Laplace's equation [27]:

$$\Delta_x\phi(x, y, z) + \Delta_y\phi(x, y, z) + \Delta_z\phi(x, y, z) = 0 \quad (\text{II.2.1})$$

where $\Delta_i = \partial^2/\partial i^2$ is the Laplacian and $\phi(x, y, z)$ the potential from which the field is derived. It was shown by Earnshaw that the consequence of this equation is the impossibility to achieve a 3D confinement using static fields

only—no global minimum achievable in the three directions [28]. Thus, the ion trapping in a Paul trap is performed using a static field along one direction (axial direction z) and a fast-oscillating radio-frequency (RF) field along the two other directions (radial plane (x, y)). This creates a time-averaged harmonic trapping potential $\phi(x, y, z)$ [29] (see Fig. **II.2.1**).

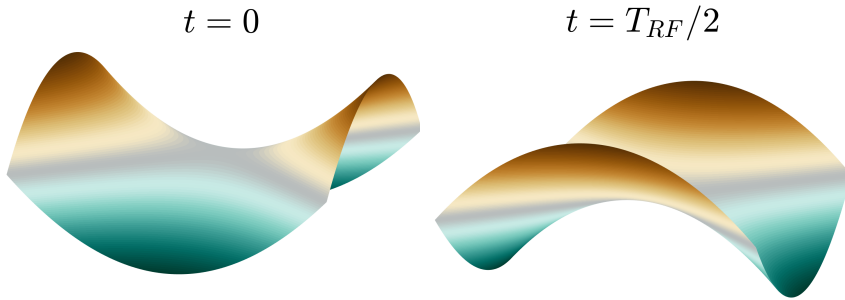


Figure II.2.1: Sketch of the two-dimensional potential in the radial plane in a quadrupole Paul trap at $t = 0$ and at half of the RF oscillation period $t = T_{RF}/2$. The ions always remain confined in one direction while the other direction is unstable. The RF potential being switched relatively fast compared to the ion's motion, they remain effectively trapped.

The trap itself consists of four metallic rods each split into three electrodes (see Fig. **II.2.2**).

The axial confinement is obtained by applying a constant voltage V_{DC} to the eight end electrodes (1, 3, 4, 6, 7, 9, 10, 12). Thus, the electric potential along the z -axis can be described as:

$$\phi_{ax}(z) = \eta V_{DC} \frac{z^2}{z_0^2} \quad (\text{II.2.2})$$

with η the trap geometry constant and z_0 the half-length of the center electrodes.

The radial confinement is obtained by applying time-varying voltages U_{RF} and $-U_{RF}$ (with $U_{RF} = -\frac{1}{2}V_{RF} \cos(\Omega_{RF}t)$) to the diagonally opposite sets of electrodes. At $t = 0$, the set (1, 2, 3, 10, 11, 12) from Fig. **II.2.2** is

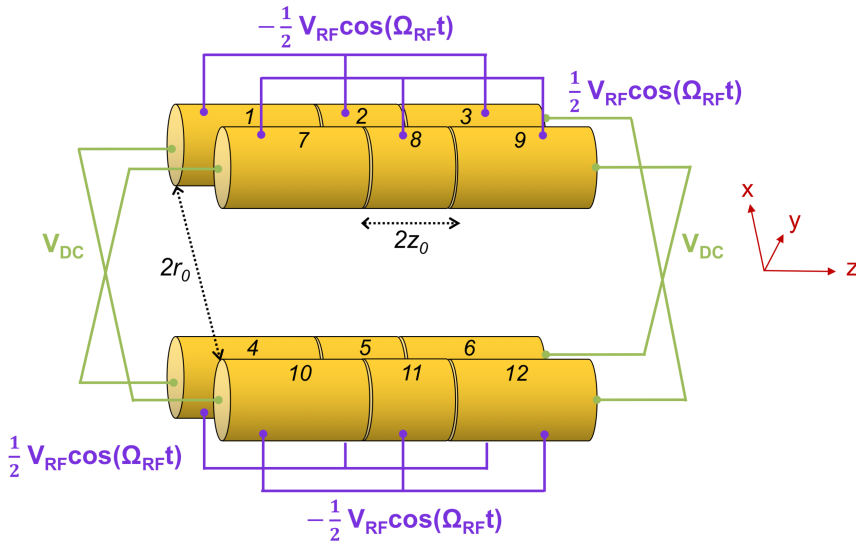


Figure II.2.2: Schematic linear Paul trap. The electrodes of the quadrupole trap are numbered 1–12. r_0 and z_0 are characteristic properties of the trap geometry—respectively the inter-electrode inscribed radius and the half-length of the center electrodes. In red, the trap axes. In green, the DC potential responsible for the static trapping field in the z direction; in purple, the oscillating RF potential trapping the ions in the radial (x, y) plane.

at the voltage $-\frac{1}{2}V_{RF}$ and the set $(4, 5, 6, 7, 8, 9)$ at $\frac{1}{2}V_{RF}$. The resulting potential can be described by:

$$\phi_{RF}(x, y, t) = -\frac{1}{2}V_{RF} \cos(\Omega_{RF}t) \frac{x^2 - y^2}{r_0^2}, \quad (\text{II.2.3})$$

with V_{RF} the peak-to-peak amplitude of the RF signal, Ω_{RF} its angular frequency and r_0 the inter-electrode inscribed radius.

The total radial confinement is a superposition of the effect of the static and RF potentials and can be described by:

$$\phi_{rad}(x, y, t) = -\frac{1}{2}V_{RF} \cos(\Omega_{RF}t) \frac{x^2 - y^2}{r_0^2} - \frac{1}{2}\eta V_{DC} \frac{x^2 + y^2}{z_0^2}. \quad (\text{II.2.4})$$

II.2.1.a.ii Secular motion

The equations of motions in the z direction and (x, y) radial plane can be derived in order to describe the motion of one ion in the trap [22].

In the axial direction, the motion is described by a harmonic oscillator equation:

$$\frac{d^2z}{dt^2} = -\frac{2Q\eta V_{DC}}{mz_0^2}z \quad (\text{II.2.5})$$

with Q the charge of the ion in *Coulomb* and m its mass in kg.

The frequency of this harmonic oscillation is thus given by:

$$\omega_z = \sqrt{\frac{2Q\eta V_{DC}}{mz_0^2}}, \quad (\text{II.2.6})$$

and the axial potential can be rewritten as:

$$\Phi_{ax}(z) = \frac{1}{2}\omega_z^2 z^2. \quad (\text{II.2.7})$$

The motion in the radial plane is more challenging to derive. The equations of motion are given by:

$$\begin{cases} \frac{d^2x}{dt^2} = -\frac{Q}{m} \left(\frac{\eta V_{DC}}{z_0^2} + \frac{V_{RF} \cos(\Omega_{RF}t)}{r_0^2} \right) x, \\ \frac{d^2y}{dt^2} = -\frac{Q}{m} \left(\frac{\eta V_{DC}}{z_0^2} - \frac{V_{RF} \cos(\Omega_{RF}t)}{r_0^2} \right) y. \end{cases} \quad (\text{II.2.8})$$

They can be rewritten and described in terms of the Mathieu equations [30]:

$$\frac{d^2u}{d\tau^2} + [a - 2q_u \cos(2\tau)]u = 0, \quad u = x, y \quad (\text{II.2.9})$$

with:

$$\tau = \frac{\Omega_{RF}t}{2}, \quad a = -4 \frac{\eta Q V_{DC}}{mz_0^2 \Omega_{RF}^2}, \quad q_x = -q_y = 2 \frac{\eta Q V_{RF}}{mr_0^2 \Omega_{RF}^2}. \quad (\text{II.2.10})$$

The a and q parameters determine the limits where the solutions to the Mathieu equations represent a bound motion of the ion. They can be used to draw up regions of stability for the trapping of ions. In the case where $|a|, |q| \ll 1$ (usual trap operation conditions), Eq. (II.2.9) can be

expanded into a power series in q_u , and its first order solutions are given by [22, 29]:

$$u(t) = u_0 \left[1 - \frac{q_u}{2} \cos(\Omega_{RF}t) \right] \cos(\omega_r t) \quad (\text{II.2.11})$$

where ω_r describes the secular radial motion and is given by:

$$\begin{aligned} \omega_r &= \frac{\Omega_{RF}}{2} \sqrt{\frac{q^2}{2} + a} \\ &= \sqrt{\frac{Q^2 V_{RF}^2}{2m^2 r_0^4 \Omega_{RF}^2} - \frac{\eta Q V_{DC}}{M z_0^2}}. \end{aligned} \quad (\text{II.2.12})$$

This motion is of low frequency and high amplitude relative to the motion in $\cos(\Omega_{RF}t)$ —called micromotion—as $\omega_r \ll \Omega_{RF}$ and $|q| \ll 1$. The micromotion can therefore be averaged out and a radial harmonic pseudo-potential of frequency ω_r can be constructed:

$$\Phi_{rad}(r) = \frac{1}{2} \omega_r^2 r^2. \quad (\text{II.2.13})$$

II.2.1.b Doppler cooling of trapped ions

Doppler cooling is a widely used technique for cooling atoms and ions to mK-temperatures [31]. In order to describe the cooling of $^{40}\text{Ca}^+$ ions, we derive the atom-light interaction using a two-level system (based on Ref. [32–34] where a more detailed approach can be found). It draws an appropriate picture of the process as Doppler cooling is performed using preferably a closed transition between two levels, as it relies on many absorption-emission cycles. In the case of the cooling of a single ion, the derivation is similar to that of a neutral particle.

II.2.1.b.i Atom-light interaction

A two level one-electron particle (atom or ion) is considered. Its ground state $|g\rangle$ and its excited state $|e\rangle$ are eigenstates of the atomic Hamiltonian \hat{H}_{at} with E_g and E_e the respective eigenvalues. The transition from $|e\rangle$ to $|g\rangle$ is of frequency $\omega_{eg} = \frac{E_e - E_g}{\hbar}$ and Γ is its natural decay rate. \hat{H}_{at} can be written as:

$$\hat{H}_{at} = \hbar \frac{\omega_{eg}}{2} (|e\rangle \langle e| + |g\rangle \langle g|), \quad (\text{II.2.14})$$

and the atomic state is described by the wavefunction:

$$\Psi(\mathbf{r}, t) = c_g(t) |g\rangle + c_e(t) |e\rangle. \quad (\text{II.2.15})$$

Free particle

At first, any spontaneous emission is neglected. The two-level atom interacts with a monochromatic travelling-wave light-field described by:

$$\mathbf{E}(\mathbf{r}, t) = E_0 \hat{\mathbf{e}} \cos(\mathbf{k} \cdot \mathbf{r} - \omega_L t + \phi), \quad (\text{II.2.16})$$

with E_0 the amplitude of the field, \mathbf{k} its wave vector, ϕ its phase, $\omega_L \approx \omega_{eg}$ its frequency and $\hat{\mathbf{e}}$ a unit vector describing its polarization.¹

In the dipole approximation, the interaction Hamiltonian is given by [35]:

$$H'(\mathbf{r}, t) = \mathbf{E}(\mathbf{r}, t) \cdot \mathbf{D}, \quad (\text{II.2.17})$$

with $\mathbf{D} = -e\mathbf{r}$ the electric dipole moment operator (e being the elementary charge).

The time-evolution of the system can be obtained solving the time-dependent Schrödinger equation:

$$i\hbar \frac{\partial \Psi}{\partial t} = (\hat{H}_{at} + \hat{H}') \Psi. \quad (\text{II.2.18})$$

Using the description of the wavefunction given in Eq. (II.2.15), and passing to the interaction picture [36], Eq. (II.2.18) translates into the coupled differential equations for the coefficients c_g and c_e given by:

$$\begin{cases} i\hbar \dot{c}_g &= H'_{ge} \tilde{c}_e e^{-i\omega_{eg}t}, \\ i\hbar \dot{\tilde{c}}_e &= H'_{eg} c_g e^{i\omega_{eg}t}, \end{cases} \quad (\text{II.2.19})$$

with $\tilde{c}_e = c_e e^{i\omega_{eg}t}$. $H'_{ge} = \langle g | \hat{H}' | e \rangle = (H'_{eg})^*$ and can be derived using Eq. (II.2.17) to (II.2.19):

$$H'_{ge} = \frac{\hbar\Omega}{2} (e^{i(\mathbf{k} \cdot \mathbf{r} - \omega_L t + \phi)} + e^{-i(\mathbf{k} \cdot \mathbf{r} - \omega_L t + \phi)}). \quad (\text{II.2.20})$$

¹The atom-light interaction is derived using a semi-classical description with a quantum treatment of the atom interacting with a classical field. The light field in this process can be treated as classical due to the properties of the laser light creating a field of many photons.

Ω is the Rabi frequency given by:

$$\Omega = -\frac{eE_0 \langle e|r|g \rangle}{\hbar}, \quad (\text{II.2.21})$$

with $r = \hat{\mathbf{e}} \cdot \mathbf{r}$.

Introducing the detuning $\delta = \omega_L - \omega_{eg}$ and assuming $|\delta| \ll \omega_{eg}$ (laser frequency close to the transition frequency), Eq. (II.2.19) can be rewritten:

$$\begin{cases} i\hbar\dot{c}_g &= \frac{\hbar\Omega^*}{2}\tilde{c}_e[e^{i(\mathbf{k}\cdot\mathbf{r}-\delta t-2\omega_{eg}t+\phi)} + e^{-i(\mathbf{k}\cdot\mathbf{r}-\delta t+\phi)}], \\ i\hbar\dot{\tilde{c}}_e &= \frac{\hbar\Omega}{2}c_g[e^{-i(\mathbf{k}\cdot\mathbf{r}-\delta t-2\omega_{eg}t+\phi)} + e^{i(\mathbf{k}\cdot\mathbf{r}-\delta t+\phi)}]. \end{cases} \quad (\text{II.2.22})$$

Under the Rotating Wave Approximation (RWA), *i.e.* neglecting the fast oscillating terms, it becomes:

$$\begin{cases} i\hbar\dot{c}_g &\approx \frac{\hbar\Omega^*}{2}\tilde{c}_e e^{-i(\mathbf{k}\cdot\mathbf{r}-\delta t+\phi)}, \\ i\hbar\dot{\tilde{c}}_e &\approx \frac{\hbar\Omega}{2}c_g e^{i(\mathbf{k}\cdot\mathbf{r}-\delta t+\phi)}. \end{cases} \quad (\text{II.2.23})$$

Setting the initial populations to: $c_g(t=0) = 1$ and $\tilde{c}_e(t=0) = 0$, and the position $\mathbf{r} = \mathbf{0}$, the solutions to Eq. (II.2.23) can be expressed as:

$$\begin{cases} i\hbar\dot{c}_g(t) &= \left[\cos\left(\frac{\chi t}{2}\right) - \frac{i\delta}{2} \sin\left(\frac{\chi t}{2}\right) \right] e^{i\delta t/2}, \\ i\hbar\dot{\tilde{c}}_e &= -\frac{i\Omega}{\chi} \sin\left(\frac{\chi t}{2}\right) e^{-i(\delta t/2-\phi)} \end{cases} \quad (\text{II.2.24})$$

with $\chi = \sqrt{|\Omega|^2 + \delta^2}$ the off-resonant Rabi frequency. The evolution of the population in the ground and excited states can be monitored by calculating $|c_g(t)|^2$ and $|c_e(t)|^2 = 1 - |c_g(t)|^2$.

Free particle with spontaneous emission

Introducing spontaneous emission in the interaction process calls for a density matrix treatment. The density matrix for the two-level system is

given by [34]:

$$\hat{\rho} = \begin{array}{c} \langle g| \\ |g\rangle \\ \langle e| \\ |e\rangle \end{array} \begin{array}{cc} \langle g| & \langle e| \\ \rho_{gg} & \rho_{ge} \\ \rho_{eg} & \rho_{ee} \end{array} = \begin{pmatrix} |c_g|^2 & c_g c_e^* \\ c_e c_g^* & |c_e|^2 \end{pmatrix}. \quad (\text{II.2.25})$$

The time evolution of the density matrix elements is given by the Optical Bloch Equations (OBE) [37]:

$$\left\{ \begin{array}{l} \frac{\partial \rho_{gg}}{\partial t} = \Gamma \rho_{ee} + \frac{i}{2} (\Omega^* e^{-i\delta t} \rho_{eg} - \Omega e^{i\delta t} \rho_{ge}), \\ \frac{\partial \rho_{ee}}{\partial t} = -\Gamma \rho_{ee} - \frac{i}{2} (\Omega^* e^{-i\delta t} \rho_{eg} - \Omega e^{i\delta t} \rho_{ge}), \\ \frac{\partial \rho_{ge}}{\partial t} = -\left(\frac{\Gamma}{2} + i\delta\right) \rho_{ge} + \frac{i}{2} \Omega^* e^{-i\delta t} (\rho_{ee} - \rho_{gg}), \\ \frac{\partial \rho_{eg}}{\partial t} = -\left(\frac{\Gamma}{2} - i\delta\right) \rho_{eg} - \frac{i}{2} \Omega e^{i\delta t} (\rho_{ee} - \rho_{gg}). \end{array} \right. \quad (\text{II.2.26})$$

In the steady state limit, reached for $t \gg 1/\Gamma$, the coefficients do not vary and Eq. (II.2.26) can be solved analytically. The population of the excited state is thus given by:

$$\rho_{ee} = \frac{|\Omega|^2/4}{\delta^2 + |\Omega|^2/2 + \Gamma^2/4} = \frac{1}{2} \frac{s}{1+s}, \quad (\text{II.2.27})$$

where s is the saturation parameter defined by:

$$s = \frac{|\Omega|^2/2}{\delta^2 + \Gamma^2/4}. \quad (\text{II.2.28})$$

For $s \gg 1$, the excited state population approaches its limit value of $1/2$. In addition, the excitation rate, γ , is then equal to the decay rate from the excited state ($\gamma = \Gamma \rho_{ee}$) and can be expressed as:

$$\gamma = \Gamma \frac{|\Omega|^2/4}{\delta^2 + |\Omega|^2/2 + \Gamma^2/4}, \quad (\text{II.2.29})$$

and the natural linewidth Γ can be described as a function of various parameters of this derivation [35]:

$$\Gamma = \frac{\omega_{eg}^3 e^2 |\langle e | r | g \rangle|^2}{3\pi\epsilon_0 \hbar c^3}, \quad (\text{II.2.30})$$

where ϵ_0 is the vacuum permittivity and c the vacuum velocity of light.

It is useful to introduce some parameters, such as the saturation intensity I_{sat} and the on-resonance saturation parameter s_0 , that we will refer to in the following sections:

$$I_{sat} = \frac{\hbar\Gamma\omega_{eg}^3}{12\pi c^2}, \quad (\text{II.2.31})$$

$$s_0 = s(\delta = 0) = 2 \frac{|\Omega|^2}{\Gamma^2} = \frac{I}{I_{sat}}, \quad (\text{II.2.32})$$

where $I = \epsilon_0 E_0^2/2$ is the intensity of the light field.

Particle in a harmonic trap

As discussed in Sec. II.2.1.a.ii, the trapping potential can be approximated by a harmonic potential in each of the three directions (the micromotion being neglected). The atomic Hamiltonian \hat{H}_0 is therefore described by [33, 38, 39]:

$$\hat{H}_0 = \hat{H}_{at} + \hat{H}_{trap}. \quad (\text{II.2.33})$$

Assuming that there is no anharmonicity, \hat{H}_{trap} reads:

$$\hat{H}_{trap} = \hbar\omega_z \left(a_z^\dagger a_z + \frac{1}{2} \right) + \hbar\omega_x \left(a_x^\dagger a_x + \frac{1}{2} \right) + \hbar\omega_y \left(a_y^\dagger a_y + \frac{1}{2} \right) \quad (\text{II.2.34})$$

with a_i^\dagger and a_i ($i = x, y, z$) respectively the harmonic oscillator creation and annihilation operators. The atomic eigenstates can therefore be described by the combination $|g\rangle \otimes |n\rangle \equiv |g, n\rangle$ and $|e\rangle \otimes |n\rangle \equiv |e, n\rangle$ (with $|n\rangle$ denoting the motional eigenstate of the atom arising from the trapping potential).

The interaction Hamiltonian with the above-mentioned light field couples the electronic and motion states of the ion [38]:

$$\hat{H}' = \frac{\hbar\Omega}{2} (|g\rangle \langle e| + |e\rangle \langle g|) (e^{i(\mathbf{k}\cdot\mathbf{r}) - \omega_L t + \phi} + e^{-i(\mathbf{k}\cdot\mathbf{r}) - \omega_L t + \phi}). \quad (\text{II.2.35})$$

Expressing \hat{H}' in the interaction picture (following Ref. [40] with \hat{H}_0 the free Hamiltonian and \hat{H}' the interaction) allows us to see the possible transitions more easily. The resulting expression, applying the RWA, is given by:

$$\hat{H}'_I = \frac{\hbar\Omega}{2} |e\rangle \langle g| e^{i(\phi - \delta t)} e^{i(\mathbf{k}\cdot\hat{\mathbf{x}})} e^{i(\mathbf{k}\cdot\hat{\mathbf{y}})} e^{i(\mathbf{k}\cdot\hat{\mathbf{z}})} + H.c. \quad (\text{II.2.36})$$

where $H.c.$ stands for Hermitian conjugate. $\mathbf{x}(t) = \mathbf{x}_0 (e^{i\omega_x t} \hat{a}_x + e^{-i\omega_x t} \hat{a}_x^\dagger)$ is the Heisenberg picture expression of the position operator (the ion's position oscillating due to the harmonic trap) and $\mathbf{x}_0 = x_0 \hat{\mathbf{x}}$, $x_0 = \sqrt{\hbar/(2m\omega_x)}$, is the one-dimensional extension of the ion's ground state wavefunction in the harmonic trapping potential.

Thus, the one-dimensional interaction operator $\hat{H}'_{I,x}$ can be written as (a similar expansion can be used for the other dimensions in order to obtain the three dimensional description):

$$\hat{H}'_{I,x} = \frac{\hbar\Omega}{2} |e\rangle \langle g| e^{i(\phi - \delta t)} e^{i\eta_{x,eg} (e^{-i\omega_x t} \hat{a}_x + e^{i\omega_x t} \hat{a}_x^\dagger)} + H.c. \quad (\text{II.2.37})$$

In this expression, $\eta_{x,eg} = \mathbf{k}\cdot\mathbf{x}_0$ is the Lamb-Dicke parameter that determines the transition probability between the harmonic oscillator eigenstates. In the limit where $\eta_{x,eg} \sqrt{\langle (\hat{a}_x + \hat{a}_x^\dagger)^2 \rangle} \ll 1$, it can be expanded to:

$$\hat{H}'_{I,x} = \frac{\hbar\Omega}{2} |e\rangle \langle g| (e^{i(\phi - \delta t)} + i\eta_{x,eg} (e^{-i(\omega_x + \delta)t} \hat{a}_x + e^{i(\omega_x - \delta)t} \hat{a}_x^\dagger)) + H.c. \quad (\text{II.2.38})$$

If we consider the transition between two motional states of the atom, *i.e.* the states $|g, n_x\rangle$ and $|e, n'_x\rangle$, the effective Rabi frequency is given by:

$$\Omega_{n'_x n_x} = \Omega \langle n'_x | e^{i\eta_{x,eg} (\hat{a}_x + \hat{a}_x^\dagger)} | n_x \rangle. \quad (\text{II.2.39})$$

We can see from Eqs. (II.2.38) and (II.2.39) that if the laser detuning is $\delta = 0$, the transition will not affect the motional states. However, if $\delta = \omega_x$ [$\delta = -\omega_x$], the motional state of the ion will be changed to $n'_x = n_x + 1$ [resp. $n'_x = n_x - 1$]. The blue sideband (resp. red sideband) transition is thus driven [18].

In order for the sideband transitions to be resolved, both the natural linewidth Γ and the linewidth of the laser have to be much smaller than ω_x . This is not the regime in which this work has been performed ($\Gamma \sim 20$ MHz and $\omega_x \sim 100$ kHz). Therefore, the ion-light interaction that describes the system accurately is of a free particle (i.e. where the effects of the trapping potential, described by \hat{H}_{trap} , can be ignored).

II.2.1.b.ii Doppler cooling

Cooling of a two-level particle

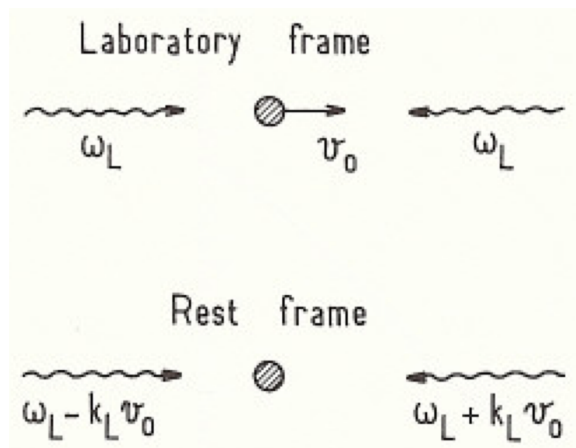


Figure II.2.3: Representation of Doppler cooling of a particle by two counter-propagating beams, from Ref. [41]. ω_L is the frequency of the laser with wave vector \mathbf{k}_L ; v_0 is the velocity of the atom. The top sketch represents the situation in the laboratory frame, the bottom one in the atom frame.

Doppler cooling relies on the Doppler effect affecting the frequency of a laser irradiating a moving particle [42]. When the particle moves

towards the light source with a velocity \mathbf{v}_0 (counter-propagating scheme), the frequency of the laser—set to ω_L —appears higher in the particle frame and equal to $\omega_{eff} = \omega_L + \mathbf{k}_L \cdot \mathbf{v}_0$ (with \mathbf{k}_L the wave vector of the laser light). In the co-propagating scheme, the light frequency is shifted towards lower frequencies and $\omega_{eff} = \omega_L - \mathbf{k}_L \cdot \mathbf{v}_0$.

In addition to this effect, the absorption of a photon leads to the modification of the momentum \mathbf{p} of the particle: $\mathbf{p}_{final} = \mathbf{p}_{initial} + \hbar \mathbf{k}_L$. Given those two effects and the fact that the absorption cross-section is at its maximum when the light is on resonance with an atomic transition (of frequency ω_{eg}) [43], the Doppler cooling strategy was developed: the laser light is red-detuned with respect to the transition ($\omega_L < \omega_{eg}$). Then, the absorption is privileged when the particle and laser counter-propagate, leading to a reduction in the momentum of the particle [31]. In the case of a free particle, three sets of counter-propagating laser beams are necessary in order to efficiently cool all three dimensions of the motion.

Cooling force

In order to better understand the cooling process, the cooling force can be derived (see Ref. [41]). Starting from the Heisenberg equations of motion of the two-level particle interacting with a traveling light field and assuming a semi-classical regime where the particle wave-packet is sufficiently localized in space and momentum, the optical Bloch equations for the steady state internal particle density matrix can be solved (see Sec. II.2.1.b.i). The mean dissipative force (or radiation pressure force) can then be expressed in terms of the parameters defined in the previous section by:

$$\mathbf{F} = \hbar \mathbf{k}_L \frac{\Gamma}{2} \frac{\Omega^2/2}{\delta^2 + (\Gamma^2/4) + (\Omega^2/2)} \quad (\text{II.2.40})$$

This force is a consequence of the absorption-emission cycles in steady state².

In the case of a moving particle, the force can be rewritten by taking into account the Doppler shift: δ is replaced by $\delta - \mathbf{k}_L \cdot \mathbf{v}_0$. Projecting \mathbf{F} onto the propagation axis \mathbf{z} ($\mathbf{v}_0 = v_0 \mathbf{z}$) leads to two expressions: one

²The influence on the particle's momentum due to spontaneous emission has been neglected in the derivation and is a good approximation since the emission process is isotropic and therefore the change in momentum is zero on average.

for the counter-propagating regime (F^-) and one for the co-propagating regime (F^+):

$$\begin{cases} F^+ &= \hbar k_L \frac{\Gamma}{2} \frac{\Omega^2/2}{(\delta+k_L v_0)^2+(\Gamma^2/4)+(\Omega^2/2)}, \\ F^- &= -\hbar k_L \frac{\Gamma}{2} \frac{\Omega^2/2}{(\delta-k_L v_0)^2+(\Gamma^2/4)+(\Omega^2/2)} \end{cases} \quad (\text{II.2.41})$$

For small velocities ($v_0 \approx 0$) F can be expanded around 0:

$$\begin{aligned} F(v_0) &\approx F(v_0 = 0) + \left. \frac{dF}{dv_0} \right|_{v_0=0} F v_0 \\ &= F_0 - \alpha v_0 \end{aligned} \quad (\text{II.2.42})$$

where α is the friction parameter and the expansion is truncated at the first order. Thus, the expression for F^+ and F^- to the first order is given by:

$$\begin{cases} F^+(v_0) &= \hbar k_L \frac{\Gamma}{2} \frac{\Omega^2/2}{(\delta)^2+(\Gamma^2/4)+(\Omega^2/2)} - \underbrace{\left(-\hbar k_L^2 \frac{s}{(1+s)^2} \frac{\delta\Gamma}{\delta^2+(\Gamma^2/4)} \right)}_{\alpha} v_0, \\ F^-(v_0) &= -\hbar k_L \frac{\Gamma}{2} \frac{\Omega^2/2}{(\delta)^2+(\Gamma^2/4)+(\Omega^2/2)} - \left(-\hbar k_L^2 \frac{s}{(1+s)^2} \frac{\delta\Gamma}{\delta^2+(\Gamma^2/4)} \right) v_0. \end{cases} \quad (\text{II.2.43})$$

We can see from this expression that the friction parameter α is the same for both propagation regimes and $\alpha > 0$ for $\delta < 0$. In addition, for a fixed value of the saturation parameter s , α is maximal for $\delta = -\Gamma/2$, leading to a better cooling. For a fixed detuning $\delta = -\Gamma/2$, the optimal value for s is $s = 1$ which corresponds to $\Omega = \Gamma$.

Taking the detuning equal to half the natural linewidth of the transition, $\delta = -\Gamma/2$, and the saturation $s = 1$, the maximum value of α can be reached:

$$\alpha_{max} = \frac{\hbar k_L^2}{4}. \quad (\text{II.2.44})$$

The radiation pressure constant force F_0 has to be compensated for in order to ensure an optimal cooling. The compensation can be done by

performing the cooling by two counter-propagating beams. In this case, the resulting cooling force $F_{cp} = F^+ + F^- = -2\alpha v_0$ is purely a friction force.

Momentum diffusion and Doppler cooling limit

The derivation presented above gave an expression for the mean force \mathbf{F} . However the full force due to the interaction of the particle with the light field \mathbf{F}_{tot} is given by [41]:

$$\mathbf{F}_{\text{tot}} = \mathbf{F} + \delta\mathbf{F}, \quad (\text{II.2.45})$$

where $\delta\mathbf{F}$ is the Langevin force arising from the randomness of the absorption and emission processes. The presence of this fluctuation in the force is responsible for heating of the particle as it gives rise to momentum diffusion D . The momentum p of the particle absorbing and spontaneously reemitting n photons can be expressed in terms of photon statistics [44]:

$$p = p_0 + n\hbar k_L + \sum_{i=1}^n \hbar k_L \cos(\theta_i), \quad (\text{II.2.46})$$

where p_0 is the initial momentum of the particle and θ_i the angle at which the photon is emitted by spontaneous emission. Therefore, the average momentum $\bar{p} = p_0 + \hbar k_L \bar{n}$ and the emission process is isotropic. The dispersion of momentum, which gives rise to the heating, is given by its variance $\sigma_p^2 = \overline{p^2} - \bar{p}^2$, which can be expressed by:

$$\sigma_p^2 = \sigma_{p_0}^2 + \hbar^2 k_L^2 (\sigma_n^2 + \xi \bar{n}), \quad (\text{II.2.47})$$

with ξ a geometry factor for the emission process ($\xi = 2/5$ for an $S-P$ transition—see Ref [44] for the derivation). The term $\xi \bar{n}$ represents the random walk in momentum space due to the process of spontaneous emission, whereas the term σ_n^2 represents the variation in the number of absorbed photons.

The momentum diffusion is defined as the rate of increase of the momentum variance: $2D = \frac{d\sigma_p^2}{dt}$ [41] and can be calculated following Refs.

[41, 45, 46]. In the limit of low intensity $s_0 \ll 1$ and for $\delta = -\Gamma/2$ it is given by:

$$D = \hbar^2 k_L^2 \Gamma s_0. \quad (\text{II.2.48})$$

The friction force induces a decrease in the kinetic energy of the particle with the rate $R_{cool} = \frac{\alpha}{m} \overline{p^2}$. The heating rate is $R_{heat} = 2D = 2\hbar^2 k_L^2 \Gamma s_0$ [37, 38]. If a steady state has been reached, $R_{cool} = R_{heat}$ and the equilibrium temperature T_D (recalling $\frac{1}{2} k_B T_D = \frac{\overline{p^2}}{2m}$ with k_B the Boltzmann constant) is given by:

$$T_D = \frac{\hbar \Gamma}{2k_B}. \quad (\text{II.2.49})$$

T_D is called the Doppler cooling limit and is the minimum temperature reachable by Doppler cooling.

More generally, the temperature limit of a Doppler cooled ion in a harmonic potential due to the secular motion can be expressed as a function of Γ , s and δ [38, 47] (see Fig. **II.2.4**):

$$T = \frac{\hbar \Gamma}{8k_B} (1 + \xi) \left((1 + s_0) \frac{\Gamma}{2|\delta|} + \frac{2|\delta|}{\Gamma} \right). \quad (\text{II.2.50})$$

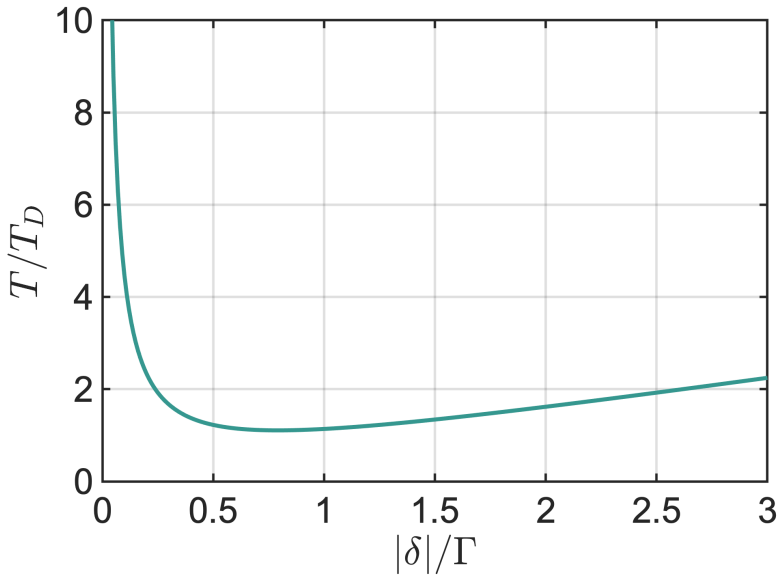


Figure II.2.4: Temperature of a particle cooled by Doppler cooling in a harmonic trap normalized by the Doppler cooling limit. It was calculated using Eq. (II.2.50) with $\xi = 2/5$ and $s_0 = 1.5$.

II.2.1.c Micromotion

II.2.1.c.i Origins of the micromotion

The micromotion (the term $\cos(\Omega_{RF}t)$ in Eq. (II.2.11)) is driven by the RF field. Therefore, there is no micromotion excitation at the RF nodal line—along the z axis. For a single ion, which equilibrium position is on the axis, reducing the amplitude of the secular radial motion, of frequency ω_r , by Doppler cooling the ion for instance, also reduces the micromotion (as can be seen from Eq. (II.2.11)). However in the case of a two-dimensional (2D) (zigzag), or three-dimensional (3D) (crystal) structures, some ions will necessarily have their equilibrium positions outside of the RF nodal zone. Its effect on the motion of the ions can be described by the case of an ion displaced from the z -axis by a uniform static electric field E_{DC} [22].

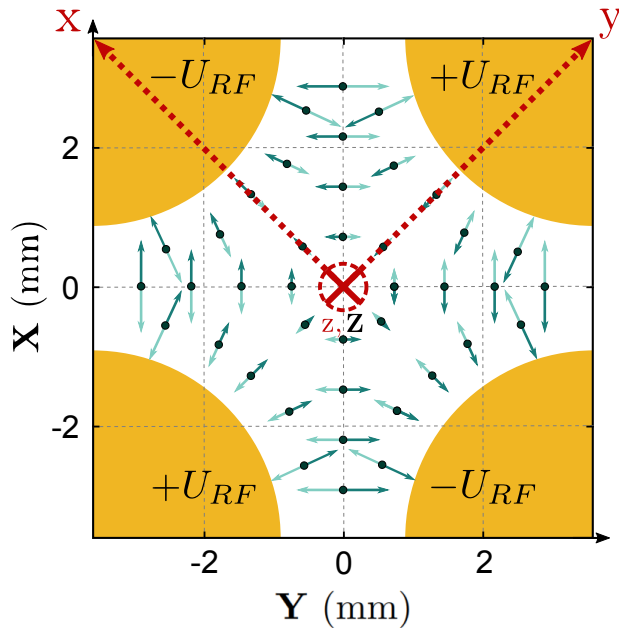


Figure II.2.5: Micromotion direction and amplitude in a linear Paul trap as a function of the ion's position (blue arrows) taken at the points in the RF period T_{RF} corresponding to the minimum and maximum of micromotion. The same shade of blue corresponds to the same time in T_{RF} . The electrodes are sketched in brown. In red, the trap axes as defined above; in black, the lab frame axes. At the same point in the RF period, the micromotion on opposite sides of the nodal line (center of figure) has the same amplitude but opposite directions.

If such a field is added to the existing trapping fields, Eq. (II.2.9) becomes:

$$\frac{d^2 u}{d\tau^2} + [a - 2q_u \cos(2\tau)]u = \frac{Q\mathbf{E}_{DC}\cdot\mathbf{u}}{m}, \quad u = x, y \quad (\text{II.2.51})$$

with \mathbf{E}_{DC} the static field vector and \mathbf{u} the unit vector associated with the x or y axis.

The solution to this equation to the lowest order in a and q_u is given

by:

$$u(t) = \left[1 - \frac{q_u}{2} \cos(\Omega_{RF}t) \right] [u_0 \cos(\omega_r t) + u_1], \quad (\text{II.2.52})$$

where $u_1 \approx \frac{Q\mathbf{E}_{DC} \cdot \mathbf{u}}{m\omega_r^2}$ is the average displacement of the ion along the direction u due to \mathbf{E}_{DC} .

At the position (x_1, y_1, z_1) , the RF field causes a micromotion of amplitude $\frac{1}{2}u_1q_u$ ($u = x, y$, there is no effect on z). This excess micromotion driven by the RF field cannot be reduced by reducing the secular radial motion via cooling as it depends on the offset in position of the ion with respect to the z -axis of the trap. The amplitude and direction of this micromotion as a function of the ion's position in the trap is shown in Fig. **II.2.5**. That is, at a given time in T_{RF} , two ions at the same distance from the RF nodal line but on opposite sides are subject to a micromotion of identical amplitude but opposite directions.

II.2.1.c.ii Micromotion and cooling

In order to efficiently cool down Coulomb crystals, the effects of the micromotion (neglected thus far) have to be accounted for as some ions are necessarily outside of the nodal RF axis. Therefore, it is preferable to apply axial cooling in order to avoid driving the micromotion. In the case of 2D (zigzag structures) and 3D crystals, the radial and axial motions being coupled, axial cooling is sufficient and is usually done by two counter propagating beams. However, this is not always a possible experimental realization and the design of the setup only allows for cooling with an angle with respect to the Z axis, which unavoidably excites the micromotion modes.

The effects of the micromotion on the cooling are described in Refs. [38, 48, 49]. Some key-points of the derivation are presented below.

As in Sec. II.2.1.b.i, we restrict our derivations to one dimension (along the direction x). The three-dimensional description can be recovered by applying the same procedure to the other directions.

The time-dependent motion Hamiltonian including micromotion $\hat{H}_{trap,m}$ is given by:

$$\hat{H}_{trap,m} = \frac{\hat{p}^2}{2m} + \frac{m}{2}W(t)\hat{x}, \quad (\text{II.2.53})$$

where $W(t) = \frac{\Omega_{RF}^2}{4}[a_x + 2q_x \cos(\Omega_{RF}t)]$ can be seen as a time-varying spring constant similar to ω_x in the harmonic regime.

In order to solve the Heisenberg equations of motion, $\mathbf{x}(t)$ has to be replaced by a function $u(t)$. The solution is then given by:

$$u(t) = e^{\beta_x \Omega_{RF} t / 2} \sum_{n=-\infty}^{+\infty} C_{2n} e^{in\Omega_{RF} t}, \quad (\text{II.2.54})$$

with β_x a real function of a_x and q_x independent of the initial conditions. The boundary conditions on $u(t)$ are given by:

$$\begin{cases} u(0) &= \sum_{n=-\infty}^{\infty} C_{2n} = 1, \\ -i\dot{u}(0) &= \omega_x = \Omega_{RF} \sum_{n=-\infty}^{\infty} C_{2n} (\beta_x / 2 + n). \end{cases} \quad (\text{II.2.55})$$

The time-dependent ion position $\mathbf{x}(t)$ can then be re-expressed as:

$$\mathbf{x}(t) = \sqrt{\frac{\hbar}{2m\omega_x}} (\hat{a}_x u^*(t) + \hat{a}_x^\dagger u(t)). \quad (\text{II.2.56})$$

Assuming the Lamb-Dicke regime— $\eta_{x,eg,m} (= \sqrt{\frac{\hbar}{2m\omega_x}}) \ll 1$ —the interaction Hamiltonian $\hat{H}'_{I,x}$ in Eq. (II.2.38) can be expanded to the first order in $\eta_{x,eg,m}$ to:

$$\begin{aligned} \hat{H}'_{I,x,m}(t) &= \frac{\hbar\Omega}{2} [|e\rangle \langle g| e^{i(\phi-\delta)t} + H.c.] \\ &+ \frac{\hbar\Omega}{2} \left[\sum_{n=-\infty}^{\infty} i\eta_{x,eg,m} C_{2n} |e\rangle \langle g| e^{i(\phi-\delta)t} \right. \\ &\quad \times \left(\hat{a}_x e^{-i(\omega_x+n\Omega_{RF}t)} + \hat{a}_x^\dagger e^{i(\omega_x+n\Omega_{RF}t)} \right) \\ &\quad \left. + H.c. \right] \end{aligned} \quad (\text{II.2.57})$$

The first term represents the carrier excitation with Rabi frequency Ω . The second term represents pairs of combined secular and micromotion sideband excitations at detunings $\pm(\omega_x + n\Omega_{RF})$ with Rabi frequency $\eta_{x,eg,m}\Omega|C_{2n}| < \Omega$. This last term shows that the motional modes of the

ion are modified due to micromotion and thus the conditions the laser detuning needs to satisfy in order to achieve cooling. For $\delta = -\omega_r - n\Omega_{RF}$, cooling is achieved, and for $\delta = \omega_r \pm n\Omega_{RF}$, heating is induced.

In the case where $\Gamma \gg (\omega_r, \Omega_{RF})$ that is relevant in this study, the sidebands are not resolved and all those in $(\omega_r \pm n\Omega_{RF})$ will lead to heating even with a red-detuned laser. The heating due to micromotion is therefore hard to compensate in situations where the micromotion is inevitable.

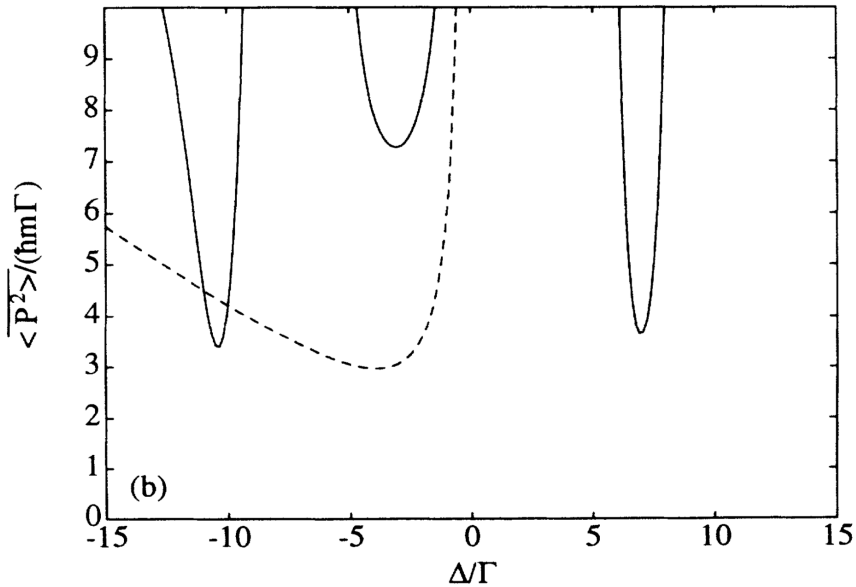


Figure II.2.6: Mean kinetic energy over an RF period for a two level atom in the purely harmonic treatment (dashed line) and including micromotion (solid line). Taken from Ref. [48].

The mean kinetic energy of the ion averaged over an RF-period can be derived and expressed as a function of the detuning. It has been plotted by J. I. Cirac *et al.* in Ref. [48] for $\Omega = 2\Gamma$, $a_x = 0$, $\omega_x = 1.5\Gamma$, $\Omega_{RF} = 10\Gamma$ and $m = 0.01$ and compared to the kinetic energy in a harmonic trap situation (see Eq. (II.2.50) and Fig. II.2.4). It is shown in Fig. II.2.6. The kinetic energy, a smooth function of the detuning for a harmonic trap, presents several sharp dips in the negative and positive detuning

regions, which correspond to the optimal detunings. This corroborates the unavoidable excitation of the ions in our setup, which does not allow for this sharp resolution.

II.2.2 Trapping of Coulomb crystals

If several ions are trapped and cooled, they form Coulomb crystals due to the repulsion from the Coulomb potential. A few parameters can be derived in order to describe the properties of 3D crystals.

The Coulomb crystallization effect was first presented by Wigner [50] in the case of a gas of free electrons in a metal. Ionic Coulomb crystals can be described by the classical Strongly Correlated One-Component Plasmas (SCOCP) ³ [23, 53]. SCOCPs are characterized by a coupling constant Γ_{cr} —defined as the ratio of the mean Coulomb energy ($\overline{E_{Coulomb}}$) to the mean kinetic energy ($\overline{E_{kin}}$)—greater than one.

The kinetic energy per particle for an ensemble of particles obeying classical statistics at temperature T is given by $E_{kin} = k_B T$. The Coulomb energy per particle in an OCP can be estimated by $E_{Coulomb} = \frac{Q^2}{4\pi\epsilon_0 a_{ws}}$, where Q is the total charge of the ion species and a_{ws} the Wigner-Seitz radius defined by [54]:

$$a_{ws} = \sqrt[3]{\frac{3V}{4\pi N}}, \quad (\text{II.2.58})$$

with V the volume of the ensemble and N the number of particles it contains. Thus, Γ_{cr} can be expressed for a plasma obeying classical statistics as:

$$\Gamma_{cr} = \frac{Q^2}{4\pi\epsilon_0 a_{ws} k_B T}. \quad (\text{II.2.59})$$

The transition from a liquid phase to a solid crystal phase in trapped ion systems has been shown to happen at $\Gamma_{cr} \approx 170$ [55–57], the stable crystal structure being Basic Cubic Centered (BCC) [52].

³In order for those structures to be formed, a neutralizing potential must be present. In the case of ion crystals in traps, the neutralization is done by the trapping potentials [51, 52].

Some of the structural properties of 3D ion Coulomb crystals, as their shape and density have been shown to be well described by a zero temperature Charged Liquid Model (CLM) [58, 59]. They are derived following Refs. [51, 60].

A zero temperature charged liquid in a 3D trapping potential will be shaped as a spheroid at equilibrium with length L and radius R (see Fig. II.2.7). Its aspect ratio α is then defined by:

$$\alpha = 2R/L, \quad (\text{II.2.60})$$

and its volume is given by:

$$V = \frac{4}{3}\pi R^2 L. \quad (\text{II.2.61})$$

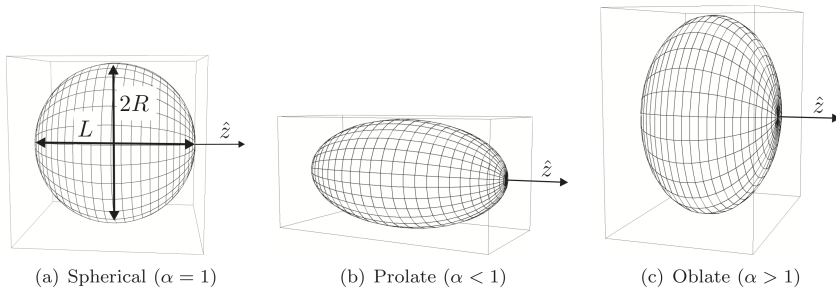


Figure II.2.7: Shapes of the spheroid as a function of the aspect ratio, from Ref. [29].

The aspect ratio α can be expressed as a function of the trapping frequencies ω_z and ω_r (frequencies as defined in Sec. II.2.1.a.ii) by the following procedure.

The potential inside the spheroid is the sum of the trap potential (Φ_{trap}) and the charge potential from the ion plasma (Φ_{charge}). The trap potential is defined by: $\Phi_{trap} = \Phi_{ax} + \Phi_{rad}$ (see Eqs. II.2.7 and II.2.13), and the charge potential from the ion plasma Φ_{charge} can be expressed as:

$$\begin{aligned}
 \Phi_{charge} &= \frac{\rho Q^2}{4\epsilon_0} R^2 L \left[\frac{2}{\sqrt{R^2 - L^2}} \sin^{-1} \left(\sqrt{1 - \frac{L^2}{R^2}} \right) \right] \\
 &= -\frac{\rho Q}{4\epsilon_0} R^2 L r^2 f(R, L) - \frac{\rho Q}{4\epsilon_0} R^2 L z^2 g(R, L)
 \end{aligned} \tag{II.2.62}$$

with ρ the constant charge density and $f(R, L)$ and $g(R, L)$ given by:

$$\left\{ \begin{array}{l}
 f^{\alpha < 1}(R, L) = - \left[\frac{1}{(R^2 - L^2)^{3/2}} \sinh^{-1} \left(\sqrt{\frac{L^2}{R^2} - 1} \right) - \frac{L}{(L^2 - R^2)R^2} \right], \\
 g^{\alpha < 1}(R, L) = \left[\frac{2}{(R^2 - L^2)^{3/2}} \sinh^{-1} \left(\sqrt{\frac{L^2}{R^2} - 1} \right) - \frac{2}{(L^2 - R^2)L} \right], \\
 f^{\alpha > 1}(R, L) = \left[\frac{1}{(R^2 - L^2)^{3/2}} \sin^{-1} \left(\sqrt{1 - \frac{L^2}{R^2}} \right) - \frac{L}{(L^2 - R^2)R^2} \right], \\
 g^{\alpha > 1}(R, L) = - \left[\frac{2}{(R^2 - L^2)^{3/2}} \sin^{-1} \left(\sqrt{1 - \frac{L^2}{R^2}} \right) - \frac{2}{(L^2 - R^2)L} \right].
 \end{array} \right. \tag{II.2.63}$$

Since the potential inside the spheroid is constant, and neither Φ_{charge} or Φ_{trap} contain any cross-terms in z and r , the following relation can be obtained for the frequency ratio⁴ by inserting Eqs. II.2.7 and II.2.13:

$$\frac{\omega_z^2}{\omega_r^2} = \frac{g(R, L)}{f(L, R)} = \left\{ \begin{array}{l}
 -2 \left[\frac{\sinh^{-1}(\sqrt{\alpha^2 - 1}) - \alpha \sqrt{\alpha^2 - 1}}{\sinh^{-1}(\sqrt{\alpha^2 - 1}) - \alpha^{-1} \sqrt{\alpha^2 - 1}} \right], \quad \text{for } \alpha < 1, \\
 -2 \left[\frac{\sin^{-1}(\sqrt{1 - \alpha^2}) - \alpha \sqrt{1 - \alpha^2}}{\sin^{-1}(\sqrt{1 - \alpha^2}) - \alpha^{-1} \sqrt{1 - \alpha^2}} \right], \quad \text{for } \alpha > 1.
 \end{array} \right. \tag{II.2.64}$$

The trap frequency ratio as a function of the aspect ratio is depicted in Fig. **II.2.8**. It is a useful tool for experimental realization as it indicates how to choose the trapping frequencies in order to obtain a specific crystal shape. It can also be used to determine one of the trapping frequencies from the crystal image, given that the second is known—which is a commonly encountered situation, as ω_z is usually easier to measure.

⁴In the case of weakly interacting particle plasmas, $\alpha = \omega_z/\omega_r$.

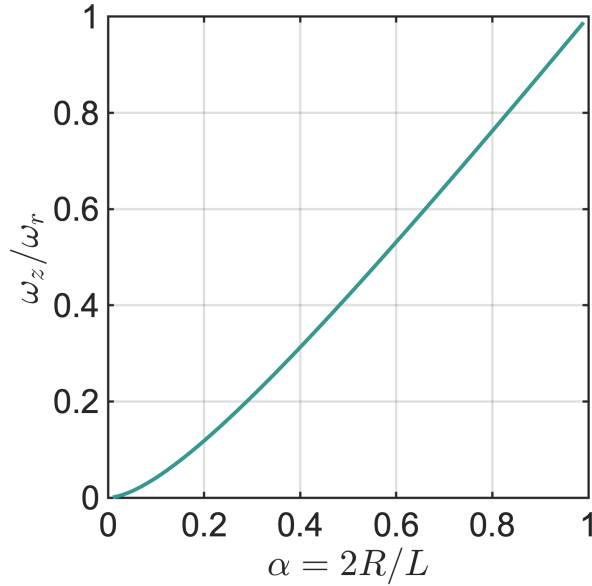


Figure II.2.8: Trap frequency ratio as a function of the aspect ratio of a prolate 3D Coulomb crystal ($\alpha < 1$).

Another useful characteristic of the crystal, its density ρ , can be derived. Taking the Laplacian of the equation $\Phi_{trap} + \Phi_{charge} = \text{constant}$:

$$\Delta\Phi_{trap} = \frac{Q\rho}{\varepsilon_0}, \quad (\text{II.2.65})$$

and, recalling the expressions of ω_z and ω_r (Eqs. (II.2.6) and (II.2.12)), ρ can be expressed by the relation:

$$\rho = \frac{\varepsilon_0 V_{RF}^2}{mr_0^4 \Omega_{RF}^2}. \quad (\text{II.2.66})$$

Experimental system and setup

In the scope of the study of energy transport along strings of calcium ions, the presence of cavity mirrors on both ends of the trap necessary to generate the pinning lattice, prevents any axial cooling. Thus, the direction of the cooling laser forms an angle with the axis of the trap—set to 45° for optimally cooling both the radial and axial motions. This property of the cooling requires taking into account the effects of the micromotion, of which the modes are being excited. In order to reduce its impact on the cooling, we developed a cooling technique that follows the oscillations of the RF field and thus of the micromotion: pulsed cooling. This chapter gives a description of the system and experimental setup that were used in the context of pulsed cooling optimization. The setup is sketched in Fig. II.3.1.

II.3.1 System overview

II.3.1.a Ca^+ level structure

The calcium ion possesses one active electron and, as discussed in Sec. II.2.1.b.i, its interaction with the cooling laser field can be treated as that of a free-particle and the results presented in Sec. II.2.1.b.ii apply. However, it does not present a closed two-level transition. Therefore, in order to ensure an optimal cooling, additional lasers have to be used to repump the population

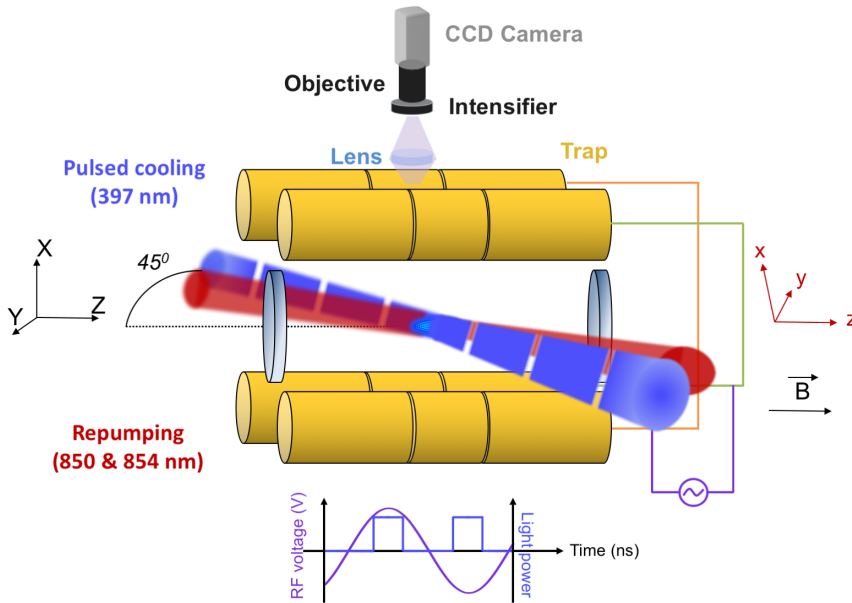


Figure II.3.1: Schematic experimental setup for pulsed cooling. In red: trap axes, in black: lab frame.

and reproduce a closed two-level system. The energy level structure of the $^{40}\text{Ca}^+$ ion with the relevant transitions for Doppler cooling, including the transition widths and state lifetimes, is shown in Fig. **II.3.2**.

The transition that is used for Doppler cooling is $^2S_{1/2} - ^2P_{1/2}$ as it is ideal due to its broadness (although $^2S_{1/2} - ^2P_{3/2}$ can also be used). The $^2P_{1/2} - ^2D_{3/2}$ transition being dipole-allowed, the $^2D_{3/2}$ has to be repumped which is achieved by driving the $^2D_{3/2} - ^2P_{3/2}$ and $^2P_{3/2} - ^2D_{5/2}$ dipole-allowed transitions. The $^2D_{3/2}$ and $^2D_{5/2}$ states are quadrupole-coupled to $^2S_{1/2}$ and are metastable. This cooling scheme allows for future efficient detection of ion localization in an optical lattice based on the electron shelving method (in the $^2D_{5/2}$ state) [70–74].

In the case of Doppler cooling of trapped ions, the presence of trapping potentials compensates the effects of F_0 , introduced in Sec. II.2.1.b.ii, since the ions reverse their motion following the harmonic oscillation described previously. It is therefore not necessary to have sets of counter-propagating beams—a single beam is enough if \mathbf{k}_L has a component in each of the

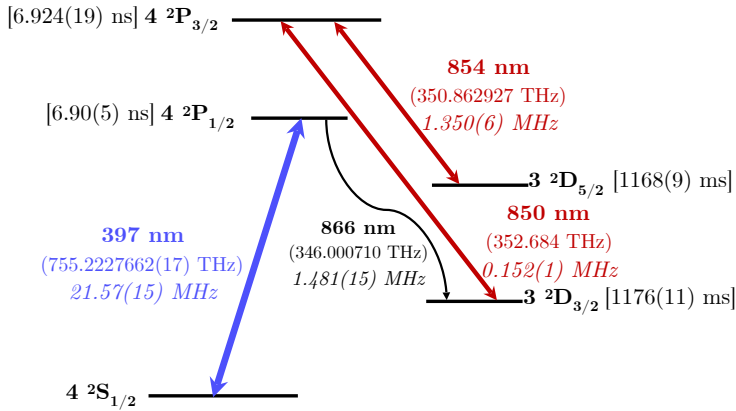


Figure II.3.2: Energy level structure of $^{40}\text{Ca}^+$ [61–66], not to scale. In blue, the cooling transition and in red, the repumping transitions. In black, the natural de-excitation transition. In brackets, the lifetime of the corresponding state [61–63]. In bold, the wavelength of the transition in nm and underneath in parentheses the corresponding frequency in THz [65, 67–69]. In italic, the natural linewidth of the transition $\Gamma/2\pi$ in MHz [61, 64].

three directions.

II.3.1.b Experimental setup overview and pulsed cooling

II.3.1.b.i Overview— 45° cooling

The cooling beam coming with an angle of 45° with respect to the \mathbf{z} axis leads to $\mathbf{k}_L = k_{L,x}\mathbf{x} + k_{L,y}\mathbf{y} + k_{L,z}\mathbf{z}$ (trap axes, different from the lab axes and defined in Figs. II.2.5 and II.3.1). As mentioned in the previous section, this single beam should suffice to cool down Coulomb crystals. However, it is also exciting the micromotion modes in the radial

plane (x, y) . A cooling strategy has been developed in order to reduce the micromotion excitation: pulsed cooling.

II.3.1.b.ii Pulsed doppler cooling

The pulsed cooling strategy consists in pulsing the cooling beam at Ω_{RF} so that the ions can be addressed at specific moments of the RF period only. A classical picture of the RF-induced motion can be drawn to understand its concept.

From Eq. (II.2.8), we can see that the velocity of the ion due to micromotion is described by:

$$\mathbf{v}_{\mathbf{RF}}(x, y, t) \propto \begin{pmatrix} -x\Omega_{RF} \sin(\Omega_{RF}t) \\ y\Omega_{RF} \sin(\Omega_{RF}t) \end{pmatrix}. \quad (\text{II.3.1})$$

The component of the ion's velocity due to micromotion oscillates at the same frequency as the RF field with a phase of $\frac{\pi}{2}$. If the ion is addressed by an infinitely short pulse at the moments when $\mathbf{v}_{\mathbf{RF}}(x, y, t) = \mathbf{0}$ (noted t_0), then it interacts with the laser field only when it is virtually free from micromotion effects and the cooling force can be described by the free-particle situation described in Sec. II.2.1.b.ii. The micromotion should therefore not be excited.

In the real setup, the pulse has a time extension τ (of minimum $\tau = 9.1$ ns, to compare with the RF-period $T_{RF} = 252.15$ ns see Fig. **II.3.3**) and the situation is more complex¹.

For a single ion displaced from the RF nodal line (introduced in Sec. II.2.1.c.i), if the light pulse is centered around t_0 , the cooling should be similar to the effect of an ideal infinitely short pulse, since $\langle v_{RF}(x, y, t) \rangle_{\tau} = 0$. Indeed, if there is a heating effect due to the micromotion component to the velocity for $t < t_0$, it will be compensated by a similar cooling effect for $t > t_0$ (given that the pulse intensity and frequency are symmetric with respect to t_0).

In the case where a crystal is to be cooled, the best pulsed cooling scheme is not as straightforward and a few parameters, described in the

¹The experiments were performed using either one light pulse or two light pulses separated by $T_{RF}/2$ —see Fig. **II.4.1** in Sec. II.4.1.

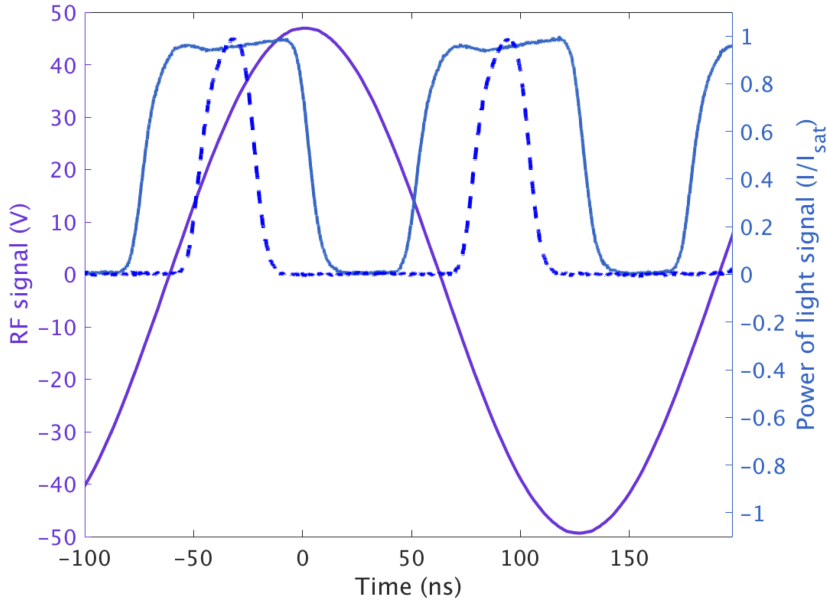


Figure II.3.3: Experimental light pulses (blue) and RF signal (purple). Solid blue line: $\tau = 80$ ns, dashed blue line: $\tau = 30$ ns.

following paragraphs, should be optimized. They are at the center of our experimental investigation.

Pulse duration τ

The optimal choice of the pulse duration is not obvious. Indeed, a longer pulse maximizes the Doppler cooling time but also increases the impact of the micromotion on the cooling. However, since the crystal structure allows for sympathetic cooling, a duration offering an optimal tradeoff between these two effects could be found.

Pulse intensity I

A higher laser intensity allows for a larger number of photons to be scattered

and therefore maximizes the micromotion-free Doppler cooling. However, due to the fact that the pulse has a temporal extension, the optimal intensity is not necessarily I_{sat} (maximum intensity that saturates the transition) because of residual micromotion effects that could lead to a dramatic heating if excited to an extent that the cooling phase cannot compensate. From these arguments, the ideal pulse seems to be the one that balances out duration and intensity.

Detuning δ

In free Doppler cooling, negative (red) detunings were shown to be favorable and the optimal detuning for the cooling laser was found to be $\delta = -\Gamma/2$ (in Sec. II.2.1.b.ii). For a system presenting a range of velocities to be cooled at once, a far-red detuned beam would ensure that all the particles would be cooled. However, we showed in Sec. II.2.1.c.ii that in the case of the presence of micromotion, a far red-detuned cooling beam does not necessarily imply cooling only as the total kinetic energy of the system is not a smooth function of the detuning (see Fig. II.2.6). This incited us to test the performance of our cooling scheme for a range of detunings.

Pulse delay t_d

Finally, the pulse delay ($t_d = t_{pulse} - t_0$ where t_{pulse} is the center of the pulse) has to be considered. Since $v_{RF}(x, y, t)$ is proportional to the ion's position, the cooling/heating effects due to this oscillation will be more pronounced for ions far from the \mathbf{z} axis. If the crystal is not centered around the RF nodal line, it is possible to imagine that the cooling will be more efficient at $t \neq t_0$ where the majority of the ions animated by the micromotion counter-propagate with the cooling beam (and the heated portion of the crystal being smaller and sympathetically cooled [51, 75])².

The optimization of those parameters was explored experimentally and is presented in Chap. II.4. The study of the underlying theoretical

²This effect should not be observed if two pulses symmetrical in time with respect to the RF maximum are used. In this situation, the first pulse would be cooling the ions on one side of the (X,Z) plane and heating the other, and the second, heating the side previously cooled and cooling the other.

processes that can explain the results was engaged but is not advanced enough to reach full understanding and will only be outlined. It would be a good candidate for the next stages of investigation of this topic.

II.3.2 Experimental setup—details

II.3.2.a Trap

The ions are trapped in a linear Paul trap as described in Sec. II.2.1.a. The trap parameters are given by Table **II.3.1**.

Parameter	Value
r_0 (mm)	2.35
z_0 (mm)	2.5
η	0.342
Ω_{RF} (Mrad s ⁻¹)	$2\pi \times 3.996$
ω_z (krad s ⁻¹)	$\approx 2\pi \times 82.5$
ω_r (krad s ⁻¹)	$\approx 2\pi \times 164.5$

Table II.3.1: Trap parameters.

The trapping frequencies, ω_z and ω_r , were usually set to the values in Table **II.3.1** (frequencies for Coulomb crystal trapping). However, the values of the frequencies calculated from the voltages applied to the trap (using Eqs. II.2.6 and II.2.12) do not give their real experimental values as the presence of electronic noise in the system leads to a difference between the voltage applied to the trap and the voltage at the trap. Since their values highly influence the properties of the crystal, as described in Sec. II.2.2, they are measured for each experiment.

The measurement procedure of the axial [respectively radial] frequency is done as follows: first, an ion is trapped with axial and radial cooling. Then, the cooling in the axial [resp. radial] direction is highly reduced and a sinusoidal modulation is applied to the endcap electrodes—(1-4-7-10) and (3-6-9-12) [resp. (1-2-3-10-11-12) and (4-5-6-7-8-9)] on Fig. **II.2.2**—while cooling in the radial [resp. axial] direction is maintained. As the frequency of the modulation approaches the axial [resp. radial] frequency, the ion displays an oscillatory motion in the trap of increasing amplitude axially [resp. radially], its motional mode being excited in this direction. At the

point of maximal motion amplitude, the trap axial [resp. radial] frequency is reached. This allows a determination of the trapping frequency with a reading precision of approximately 0.5%

A magnetic field is produced by a set of coils and determines the quantization axis (along the trap axis), taking into account the corrections for the Earth's magnetic field.

II.3.2.b Lasers

Several lasers are used in order to achieve the cooling scheme described in Sec. II.3.1.a.

First, an ionizing UV laser at 272 nm which consists of a fiber laser successively doubled in frequency to 544 nm then 272 nm is used to produce Ca^+ ions by ionizing the atomic beam of Ca from the oven.

When the cooling is done continuously and along the axial and radial directions, it relies on the 397 nm light of a doubled Ti:Sapphire ring oscillator pumped by a **Verdi** laser. The 794 nm light from the Ti:Sapphire is frequency-stabilized by a cavity and doubled to 397 nm.

When the pulsed cooling scheme is chosen, the 397 nm light is produced by the doubling of the 794 nm light of a **Toptica** TA Pro laser similarly frequency stabilized. The production of the pulsed light is done by a pigtailed Acousto-Optic Modulator (AOM) driven by a pulse generator triggered on the RF signal at Ω_{RF} .

Two diode lasers at 850 nm and 854 nm are used for the repumping of the metastable $^2D_{3/2}$ and $^2D_{3/2}$ states.

Prior to taking data, the laser frequencies are scanned: the scattering profile as a function of the laser detuning is recorded and fit to a Lorentzian (397 nm light) or Gaussian profile (850 nm diode). The resonance is then defined and the frequency of the lasers set to either the transition frequency (for the 850 nm) or to a detuned frequency (in the case of the 397 nm cooling lasers—which maximizes the cooling). The 854 nm diode is voluntarily detuned by 30 MHz with respect to resonance in order to avoid any dark resonances by interaction with the 850 nm laser [76].

II.3.2.c Imaging system

The imaging apparatus consists of an achromatic lens³ of focal length $f = 70$ mm at the bottom of which a cardboard diaphragm with a 15 mm wide opening is placed (in order to minimize possible optical aberrations [77]). It is connected to the couple imaging intensifier—CCD camera detecting the 397 nm cooling light scattered by the ions⁴.

We measure the magnification of the apparatus following the study of equilibrium positions of ions in a trapped string conducted by James in Ref. [16]. James shows that the equilibrium positions of the ions are well defined in this configuration and the minimum distance between two ions can be expressed analytically as a function of the axial trap frequency ω_z . The distance between two ions in a two-ion string is thus given by:

$$d = \left(\frac{Z^2 e^2}{2\pi\epsilon_0 M \omega_z^2} \right)^{1/3}, \quad (\text{II.3.2})$$

where Z is the degree of ionization of the ions, e the elementary charge, ϵ_0 the vacuum permittivity, M the mass of the ions, and ω_z the axial frequency of the trap (in Hz).

In order to determine the magnification, two ions are trapped and the distance between them is measured using an image processing software (*ImageJ*). Since the size of a pixel on the camera (9.9 μm in this case) is known, by measuring the axial frequency ω_z , we are able to calculate the magnification: 10.70 ± 0.03 .

The object–image size correspondence is then calculated to be $\zeta = 0.925 \pm 0.003 \mu\text{m}/\text{pixel}$. This parameter is used in the Molecular Dynamics simulator in order to produce an image-like output from the real positions of the ions (see Sec. II.5.3).

³An achromatic lens is designed in a specific way to reduce chromatic and spherical aberrations [77].

⁴The role of the intensifier is to transform the low intensity radiation from the ions into fluorescence on a phosphor screen that can be detected by the CCD camera. The incident light induces the release of electrons from a photocathode by photoelectric effect. Those electrons are then accelerated until they hit a micro-channel plate, at which point they cause the release of a large number of electrons, thus amplifying the signal that will be responsible for the emission of fluorescence when absorbed by phosphor screen [78].

This imaging system is responsible for the presence of a diffraction pattern on the images. This was experimentally investigated but could not be suppressed as it seemed to originate between the chamber window and the intensifier. The images are therefore post-processed in order to minimize this effect that can make the crystals look colder than they are—the diffraction rings possibly overlapping with ion layers (see Fig. **II.3.4**). For that purpose, each experiment is preceded by taking a background image (no ions or light in chamber, intensifier off) giving the minimum level of CCD counts and a reference image (continuous cooling of a crystal at the maximum power) which are then used to correct the experimental data taken with a crystal of the same size as the reference.

The axial and radial resolutions, $\sigma_{res,z}$ and $\sigma_{res,r}$ of the system were determined prior to this work by trapping two ions and measuring their spot size for increasing values of the axial and radial frequencies respectively. They were found to be: $\sigma_{res,z} = 2.23 \pm 0.02 \mu\text{m}$ and $\sigma_{res,r} = 2.09 \pm 0.02 \mu\text{m}$. They are used in the construction of the Gaussian blur of the *Matlab* post-processing of MD simulation outputs. The detection efficiency was previously measured as well ($1.663 \pm 0.01 \cdot 10^{-4}$) [79].

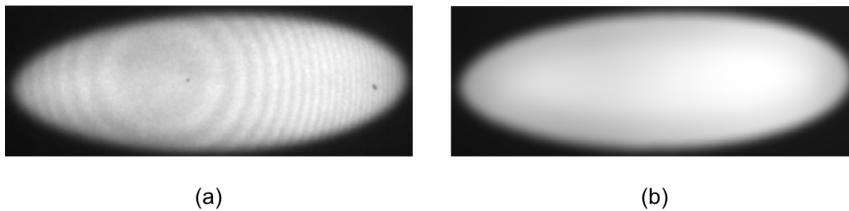


Figure II.3.4: Experimental image of Coulomb crystal before (a) and after (b) post-processing. The presence of the diffraction rings can lead to a misdetermination of the crystal’s temperature as they may induce the ion layers to appear more defined (and thus, colder).

II.3.2.d Ion trapping procedure

Our experiments are performed as follows.

The cooling and repumping lasers are sent to the trap and the axial and radial frequencies are set to the usual crystal trapping values (see

Table **II.3.1**), as they offered a good compromise in terms of trapping power (a too tight trap hindering the loading). Then, the UV laser is sent in the trap which allows us to form the Ca^+ to trap (assuming that the oven is open thus releasing calcium in the trap). It is left on until the desired number of ions is loaded. After the formation of this initial crystal, if another structure is desired, the axial and radial frequencies are slowly changed, deforming it into the shape of interest ($\omega_r \gg \omega_z$ for strings, $\omega_z \gg \omega_r$ for pancakes).

If all cooling and trapping conditions remain stable, the ions can be durably kept in the trap. Typically, in our experiments, the Coulomb crystals were kept over the course of a day.

Pulsed cooling of Coulomb crystals

As discussed in Sec. II.3.1.b.ii, the key parameters for the best pulsed cooling scheme are the pulse length τ , the pulse delay with respect to the zero-micromotion reference t_d , the intensity I and the detuning δ of the pulsed light. They were sequentially optimized for a Coulomb crystal of approximately 550 ions. The performance of the cooling scheme was assessed by comparing the resulting structures to a molecular dynamics generated temperature catalog for crystals with the same size and using the same trapping parameters (the simulation procedure is described in Chap. II.5). The resulting coldest possible crystal was compared to the optimally continuously cooled ensemble.

In the following sections, the frequencies ($\omega_z, \omega_r, \Omega_{RF}$) are given either in rad/s or Hz. In the former case, the general notation is: $\omega_i = 2\pi \times f_i$ with f_i the frequency in Hz to which the unit is attached ($[\omega_i] = \text{rad/s} = 2\pi \times [f_i] = 2\pi \times \text{Hz}$). In the latter case, even though they are not technically angular frequencies, the same notation was kept and thus $\omega_i \equiv f_i$. This choice is made to avoid any confusion arising from an increasing number of variables, as the numerical values can easily be converted.

II.4.1 Definition and determination of the parameters

II.4.1.a Rising, Falling, Both

The pulsed cooling is performed with one or two pulses per RF period. In the case of one pulse, two options are considered depending on the phase of the RF on which the pulse is triggered. In the case of the Rising [respectively Falling] pulse, the triggering is done on the rising [falling] part of the RF signal. The two pulses case, referred to as Both, corresponds to the combination of Rising and Falling taken for the same absolute value of the delay—Fig. II.4.1 illustrates this description.

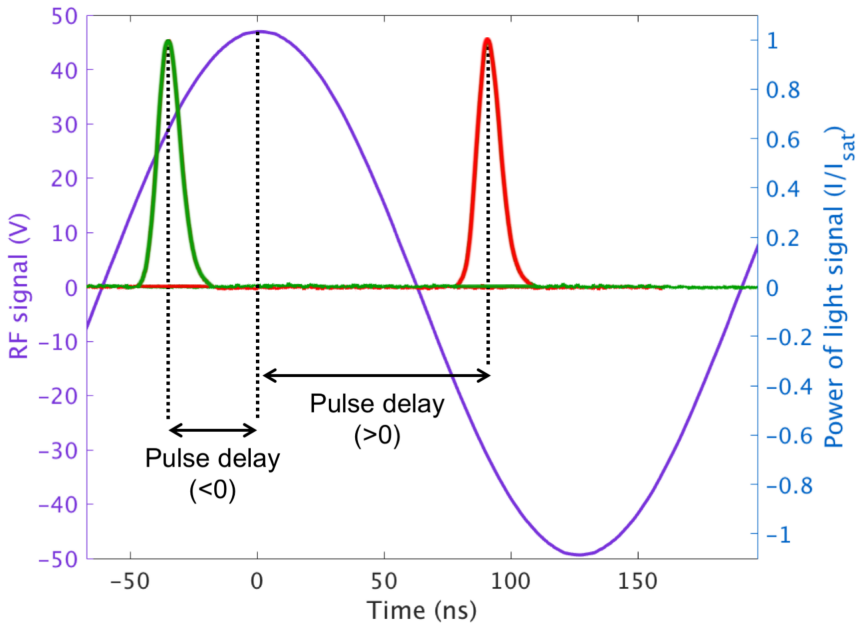


Figure II.4.1: Definition of the pulse delay with respect to the RF signal. In lilac: RF signal—the zero of time (0 ns) is set to the zero of micromotion (where $\mathbf{v}_{\mathbf{RF}} = \mathbf{0}$). In red: Falling light pulse; in green: Rising light pulse.

When set to the same absolute value of delay $|t_d^R| = |t_d^F|$, the Rising

and Falling pulses address the same class of RF phase and thus the same class of ion velocities—motions of same amplitude but opposite direction on the two sides of the RF reference (see Fig. **II.2.5**).

Since the ions are detected by recording the scattering from the pulsed cooling laser, the images are shots of the ions' positions integrated over the length of the pulse. In the situation of one trapped ion displaced from the RF nodal line and cooled by either a Rising or Falling pulse, as the delay is increased, its position is centered increasingly further from its initial position (in one direction for Rising and the other for Falling), as it moves away from its equilibrium position under the influence of the micromotion (see Fig. **II.2.5** and Eq. (II.2.52) in Sec. II.2.1.c.i). It is illustrated in the simulated experiment in Fig. **II.5.5**.

II.4.1.b Pulse delay

The pulse delay is defined as the time difference between the center of the pulse and the time of zero-micromotion reference t_0 —*i.e.* the point in the RF signal at which the ions' velocities due to micromotion is zero, which corresponds to an extremum of RF—(see Fig. **II.4.1** where the time reference (0 ns) is set at the point of zero-micromotion).

Even though the pulse generator is triggered on the RF, the light pulse is delayed with respect to the RF signal due to its generation time. Therefore the actual value of the pulse delay on the generator that corresponds to a zero delay for the light pulse has to be determined.

The t_0 determination procedure consists of trapping one ion ($\omega_r = 2\pi \times 240$ kHz, $\omega_z = 2\pi \times 75$ kHz) and displacing it out of the RF nodal line (by ≈ 44 μm), therefore adding excess micromotion (the amplitude of the micromotion is estimated to 5.5 μm). Then, pulses (of length $\tau = 9.1$ ns, detuning $\delta = \Gamma$ and intensity $I = 1.5I_{sat}$) with different delays are sent and the scattering of the ion recorded. Since the micromotion induces a shift in the ion's velocity as described in Sec. II.2.1.c and Sec. II.3.1.b.ii, the effective detuning varies with it, which influences the scattering intensity. This procedure is performed with Rising pulses followed by Falling pulses which allows us to address the ion on both sides of the RF reference of zero-micromotion. The scattering of the ion as a function of the pulse delay is shown in Fig. **II.4.2**. The zero-micromotion reference is given by the point where the two curves cross (where the micromotion does not

influence the cooling).

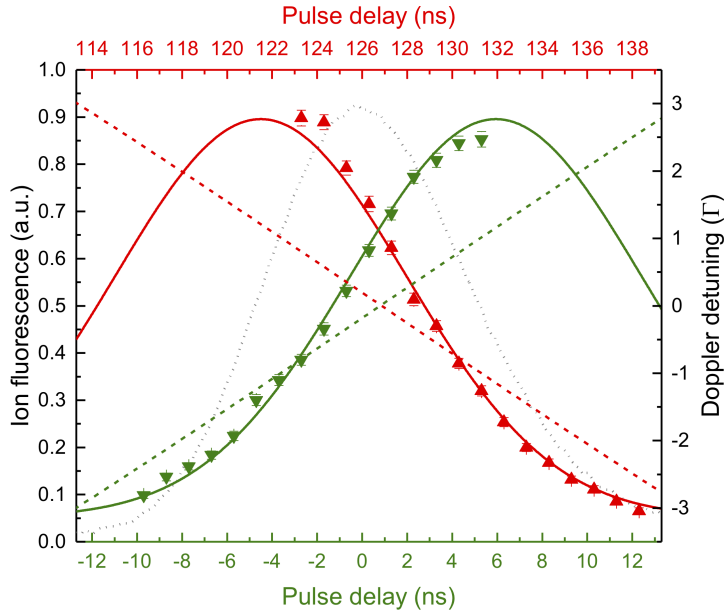


Figure II.4.2: Scattering of a Ca^+ ion above the RF nodal line as a function of the pulse delay. In red: scattering from the Falling pulse; in green: Rising pulse. Triangle: experimental data; full line: Lorentzian fit to the experimental data; dashed line: Doppler detuning due to micromotion; grey dotted line: shape of a light pulse.

It can be noted that the amplitude of the scattering signal is different for the two cases. This can be due to several effects.

First, if the pulse shape is not symmetrical around its maximum, the Rising and Falling cases would be addressing the same classes of RF phase (and thus velocity) with different intensities which would explain the scattering difference (as the detected scattered light is the one from the pulsed laser¹). However, the pulse is shown to be symmetrical.

¹The scattering is actually a convolution of the pulse shape and the linewidth of the

Another possible source of asymmetry can be the difference in cooling dynamics in the two cases—since the effective detuning increases in one case and decreases in the other. If there is presence of dynamic cooling effects, the cooling and consequently the scattering would be different for Rising *vs.* Falling. However, the cooling dynamics is much slower than any effects of the micromotion ($\Gamma \ll 1/\tau$), and therefore the cooling should be well described by a steady state. This argument is open to discussion and can be verified by monitoring the cooling process under pulsed cooling by explicitly implementing it the MD simulations (solving the optical Bloch equations at each time step and calculating the scattering).

Finally, a non-uniform response from the imaging system due to the position could also lead to a difference in the recorded scattering amplitude (since the ion is above its central position in one case and below in the other—see Fig. II.2.5 and Eq. (II.2.52) in Sec. II.2.1.c.i). This can be resolved in future experiments by calibrating the response of the imaging system as a function of the ion position by cooling it continuously and displacing it in the imaging field.

The micromotion reference is verified and adjusted by loading a crystal and pulse cooling it with a delay $t_{d,-} = t - t_0$ and $t_{d,+} = t + t_0$ for several phases in the RF period t . If t_0 is correctly defined, $t_{d,+}$ and $t_{d,-}$ give similarly cold crystals. If that is not the case, t_0 is adjusted and verified in the same way.

II.4.1.c Intensity

The pulse intensity is expressed in terms of the saturation parameter at zero detuning, $s_0 = I/I_{sat}$ (see Eqs. (II.2.31) and (II.2.32)). It represents the maximum intensity of the pulse.

II.4.2 Optimization of the pulsed cooling

The above-mentioned parameters are optimized in order to find the best pulsed cooling scheme. The optimization is done using the Rising, Falling and Both schemes for one or two parameters at a time, even though they are not independent, because scanning the full parameter space is not

laser. The latter was shown to be symmetrical.

experimentally feasible. Even though this does not allow to present with certainty the best pulsed cooling scheme, it allows us to show that the temperatures observed with pulsed cooling are lower than their continuous counterpart.

All the experiments are performed at $\omega_z \approx 2\pi \times 82.2$ kHz, $\omega_r \approx 2\pi \times 164.65$ kHz, $\Omega_{RF} = 2\pi \times 3.966$ MHz (set on the generator) which corresponds to $T_{RF} = 252.15$ ns (measured). The crystals are loaded to be of the same size for each experiment with an estimated number of ions (determined by MD simulation) $N_{ion} \approx 555$ ions. A crystal is loaded and centered around the RF nodal line (although not perfectly for some of the experiments as can be seen in Fig. II.4.6) and the beam alignment is optimized on the crystal at each experiment. The dark species (molecular ions that can form over time) are regularly flushed by sending the ionizing UV beam on the crystal. In the case of a loss of the ions for an unexpected reason, a crystal of the same size using the same trapping parameters is reloaded. All images are recorded using the same imaging settings and images of each crystal in a given set of optimization are recorded for the same time, ensuring that the difference in aspect of the crystals can be related to a difference in temperature².

In the experimental data figures that follow, the coldest crystals are circled in red. The symbol “ \sim ” indicates that the parameter is varied and optimized.

II.4.2.a Length

We start our investigation from the usual continuous cooling parameters and by verifying whether reducing the length of the pulse from quasi-continuous to almost Dirac would lead to a better cooling in our given configuration. The pulse is centered around the zero of micromotion per our hypothesis on the optimal delay. The trapping and cooling parameters are given in Table II.4.1

The results are combined in Fig. II.4.3. The numbers in red represent the order in which the data is taken. This randomized order is done to

²The image recording consists of integrating the photon count on the CCD over a given time. Thus, the bigger the amplitude of the ion’s motion, the larger it will appear on the image. Since mean velocity and average temperature are related, a larger spot size indicates a higher temperature for the ion. The consequence of this effect on crystals is a higher definition in the shells for lower temperatures.

Parameter	Value
ω_z [kHz]	82.2
ω_r [kHz]	154.5
$\Gamma/2$ [MHz]	16.3

Parameter	Value
δ [MHz]	-34
τ [ns]	\sim
t_d [ns]	0
s_0	0.1

(a) Trap frequencies and cooling linewidth. (b) Pulsed cooling optimization parameters.

Table II.4.1: Experimental parameters—pulse length optimization.

avoid being biased by a possible loss of ions during the experiment³. The optimal pulse length appears to be $\tau_{opt} = 80$ ns for a 2-pulse scheme (Both). The comparison to the continuously cooled crystal with the same parameters is shown in Fig. II.4.4.

The pulsed scheme produces a colder crystal than the continuous one. Indeed, using the MD simulated temperature scale (see Fig. II.5.7), the temperature of the pulse cooled crystal can be estimated to 9 mK *vs.* 15 mK. However, an optimal pulse length of 80 ns, which results in the crystal being cooled during 160 ns (almost 2/3 of T_{RF}) goes against our original hypothesis on the optimal length (better cooling for the shortest pulse) and lead us to think that our detuning and/or intensity might not be optimal for pulsed cooling.

³Following the reflexion on Fig. II.5.3, a difference in the number of ions can make the crystal appear warmer or colder. Several crystals at the same temperature but with ion numbers ranging from 575 to 525 by steps of 15 ions were simulated and it was observed while the ion number is being reduced, the crystal appears alternatively colder then warmer.

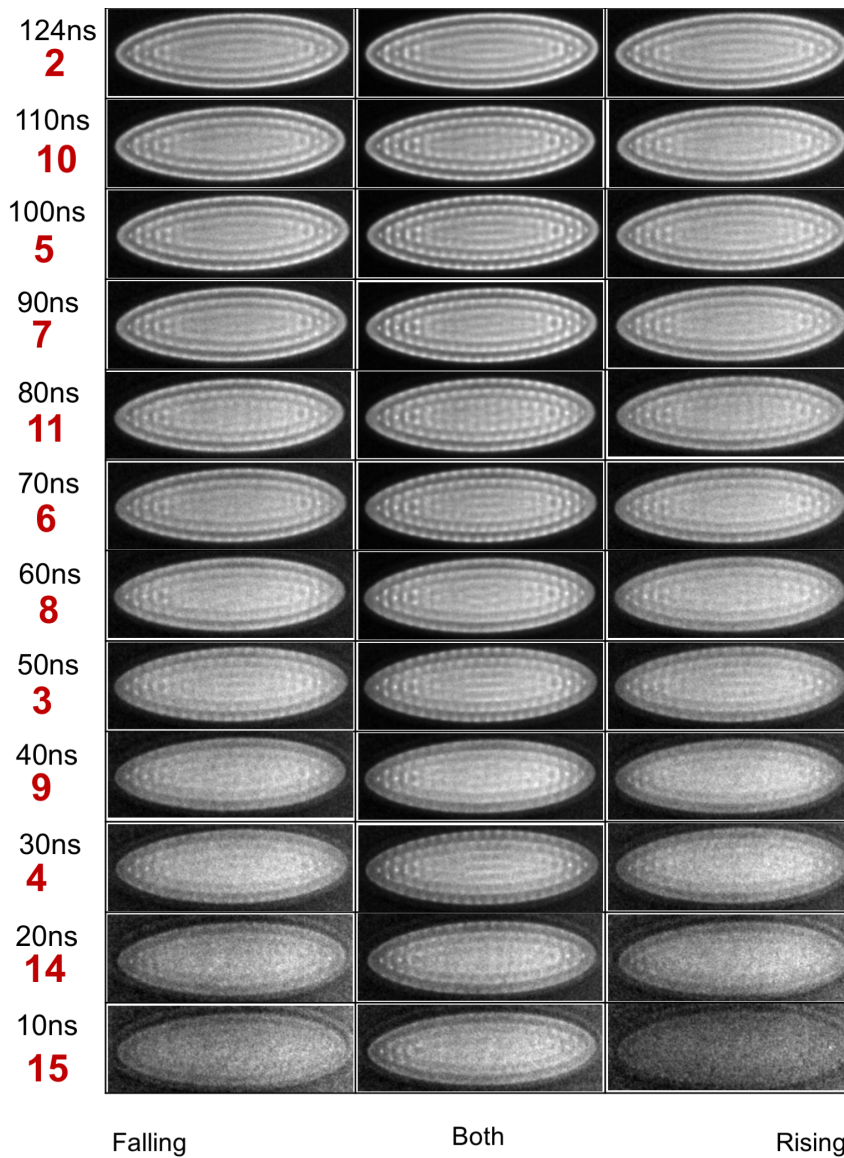
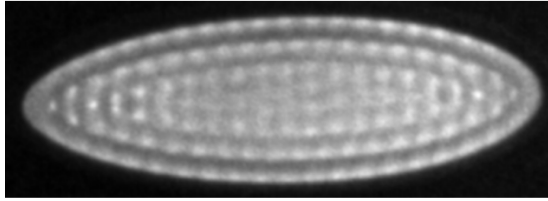
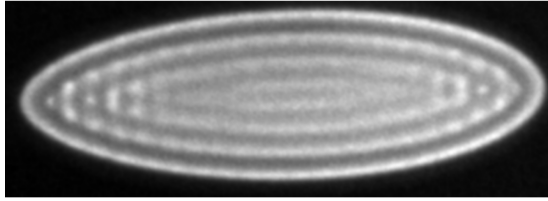


Figure II.4.3: Experimental pulsed cooled crystals at different pulse lengths. The other parameters are given in Table II.4.1.

1 Continuous



80ns Both

Figure II.4.4: Comparison of the best pulse length image to the continuously cooled crystal with the same parameters. The other parameters are given in Table II.4.1.

II.4.2.b Intensity and detuning

Based on our previous observations and our original hypothesis, we consider the shortest possible pulse centered around the RF reference and attempt the optimization of its intensity and detuning. The experimental parameters are summarized in Table II.4.2.

Parameter	Value
ω_z [kHz]	82.5
ω_r [kHz]	164.05
$\Gamma/2$ [MHz]	17

Parameter	Value
δ [MHz]	\sim
τ [ns]	9.1
t_d [ns]	0
s_0	\sim

(a) Trap frequencies and cooling linewidth. (b) Pulsed cooling optimization parameters.

Table II.4.2: Experimental parameters—pulse intensity and detuning optimization.

The results are combined in Fig. **II.4.5**. The optimal cooling parameters appear to be $s_{0,opt} = 1.5$, $\delta_{opt} = -20$ MHz with a 2-pulse scheme (Both). The coldest crystal in this case had a temperature of approximately 8 mK which allows us to conclude that our original parameters were indeed not adapted for an efficient cooling with a short pulse—the temperature of the crystal cooled with a 10 ns pulse with the parameters from Table **II.4.1** is approximately 15 mK.

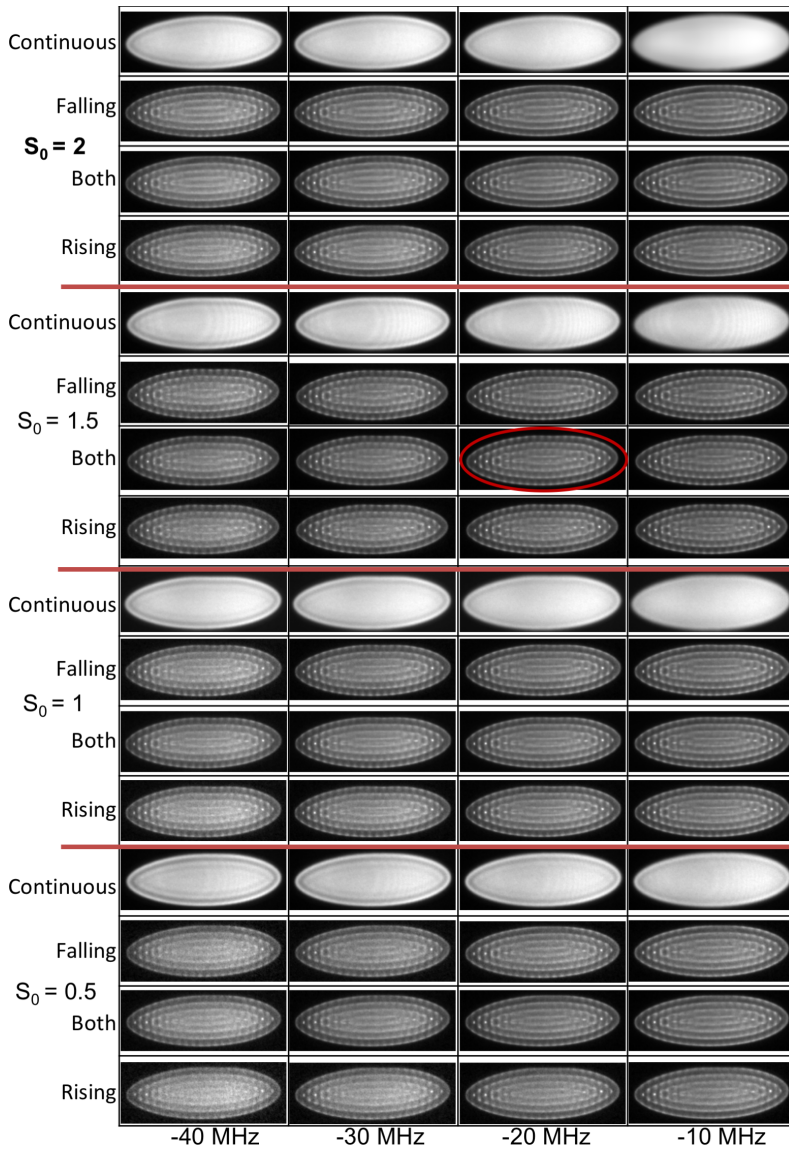


Figure II.4.5: Experimental pulsed cooled crystals at different intensities and detunings compared to continuously cooled crystals with the same parameters. The coldest crystal is circled in red. The other parameters are given in Table II.4.2.

II.4.2.c Delay

Using the short-pulse optimized detuning and intensity, we conduct the investigation on the pulse delay, while keeping the length of the pulse to its shortest value⁴. The parameters are given in Table **II.4.3** and the results in Fig. **II.4.6**.

Parameter	Value	Parameter	Value
ω_z [kHz]	82.2	δ [MHz]	-15
ω_r [kHz]	155.65	τ [ns]	9.1
$\Gamma/2$ [MHz]	17	t_d [ns]	~
		s_0	1.5

(a) Trap frequencies and cooling linewidth. (b) Pulsed cooling optimization parameters.

Table II.4.3: Experimental parameters—pulse delay optimization.

If the reference delay is properly defined and if the crystal is positioned at the center of the trap (same number of ions above and below the RF nodal line), the crystals are expected to be cooled similarly for $t_d = \pm t$ in the case of the Both scheme. At $t_d = +t$, half of the crystal would be cooled down and the other heated up, then, when $t_d = -t$, the effect on both sides would be symmetrically reversed. Similarly, the cooling with a Falling [respectively Rising] pulse at $t_d - t$ [$t_d + t$] should be similar to the Rising [Falling] case at $t_d + t$ [$t_d - t$]. The experimental images diverge from these predictions. It is attributed to both an imprecise reference determination and a poor crystal centering. These imprecisions are corrected in the experiments that lead to the results presented in Fig. **II.4.7**.

The optimal cooling appears to be obtained with the Both scheme and for $t_{d,opt,1} = 0$ ns and $t_{d,opt,2} = \pm 10$ ns—all three leading to a crystal temperature $T_{opt} = 8$ mK.

An optimal delay at ± 10 ns is rather unexpected as it does not correspond to a moment when the ions' velocities are unaffected by the micromotion (*cf.* discussion in Sec. II.3.1.b.ii). To verify this observation, another set

⁴As mentioned previously, the parameter investigation had to be done on the different parameters independently. In this case, the choice of setting the pulse length to the shortest was made based on the desire to minimize heating effects and having a more precise investigation of the effect of the position of the pulse in T_{RF} as the velocity distribution of the ions was therefore more resolved

of data is taken using two pulses and varying the detuning as well. The parameters are summarized in Table II.4.4 and the results in Fig. II.4.7

Parameter	Value
ω_z [kHz]	82.6
ω_r [kHz]	155.28
$\Gamma/2$ [MHz]	17

Parameter	Value
δ [MHz]	\sim
τ [ns]	9.1
t_d [ns]	\sim
s_0	1.5

(a) Trap frequencies and cooling linewidth. (b) Pulsed cooling optimization parameters

Table II.4.4: Experimental parameters—second pulse delay optimization.

This second investigation shows that indeed, the best pulse delay is $t_{d,opt} = \pm 10$ ns with $\delta_{opt} = -24$ MHz. The temperature of the crystal is then around $T_{opt} = 7$ mK. This observation is briefly discussed in Sec. II.4.5 and asks for a deeper theoretical investigation of the processes at play for a better understanding.

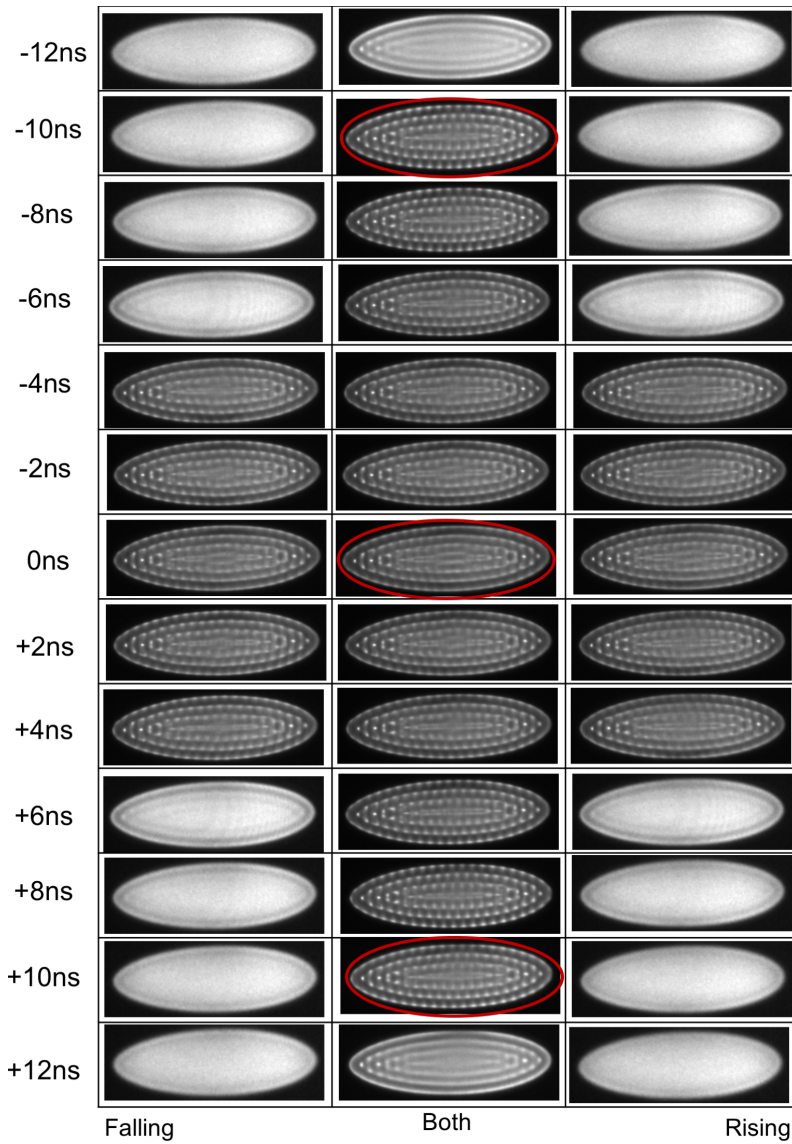


Figure II.4.6: Experimental pulsed cooled crystal with different pulse delays (I). The other parameters are given in Table II.4.3.

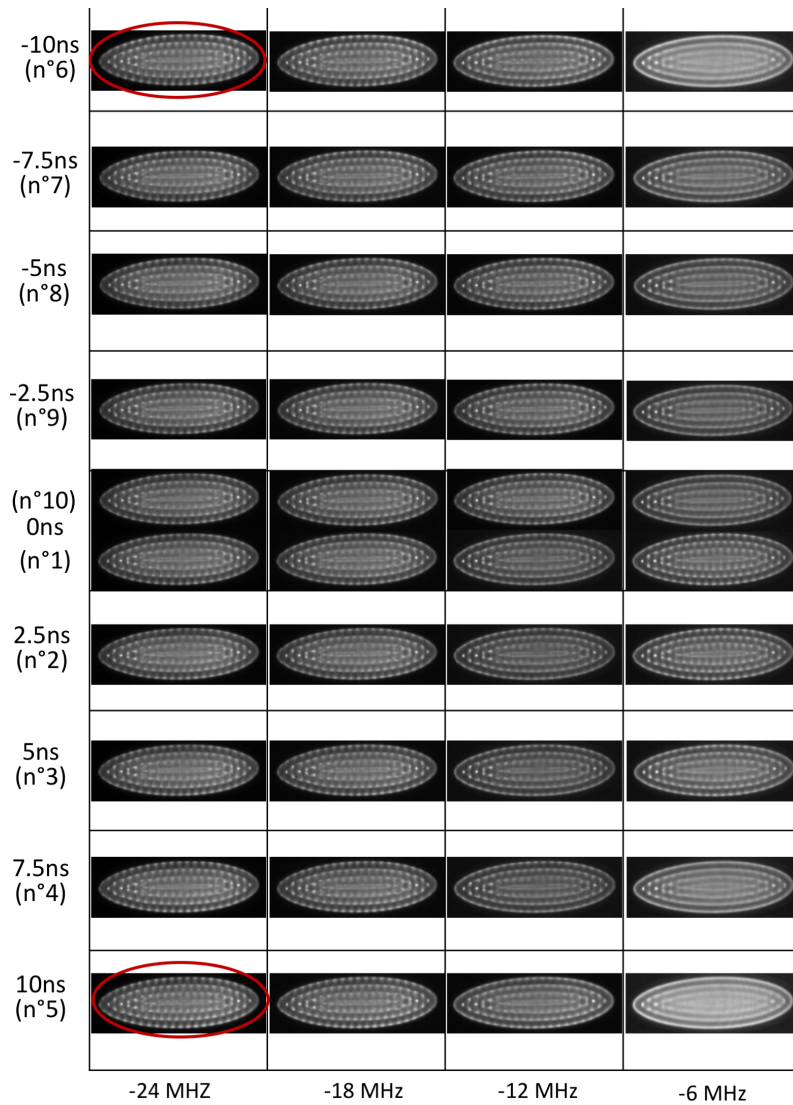


Figure II.4.7: Experimental pulsed cooled crystal with different pulse delays and detunings (II). The other parameters are given in Table II.4.4.

II.4.3 Pulsed cooling vs. continuous cooling

In order to verify that in our setup with 45° cooling, a pulsed cooling scheme is indeed more efficient than a continuous one, the continuous cooling parameters are re-optimized. The experimental parameters are given in Table II.4.5.

Parameter	Value
ω_z [kHz]	82.2
ω_r [kHz]	164.65
$\Gamma/2$ [MHz]	16

Parameter	Value
δ [MHz]	\sim
s_0	\sim

- (a) Trap frequencies and cooling linewidth. (b) Continuous cooling optimization parameters

Table II.4.5: Experimental parameters—continuous cooling optimization.

The coldest crystals are shown in Fig. II.4.8. The best (detuning, intensity) couples appear to be $(-28 \text{ MHz}, 0.11)$, $(-32 \text{ MHz}, 0.11)$, and $(-36 \text{ MHz}, 0.11)$. These newly optimized parameters are similar to our original $(\delta, s_0) = (-34 \text{ MHz}, 0.1)$ and lead to crystals of comparable temperature. Using the temperature catalog (Fig. II.5.7), the lowest temperature (obtained for these optimal parameters) is estimated to 15 mK which is around twice as high as the lowest temperature obtained by pulsing the cooling laser, thus indicating that, as we originally suspected, in this trap configuration constraining the cooling angle to 45° with respect to the trap axis, a pulsed cooling is indeed more efficient.

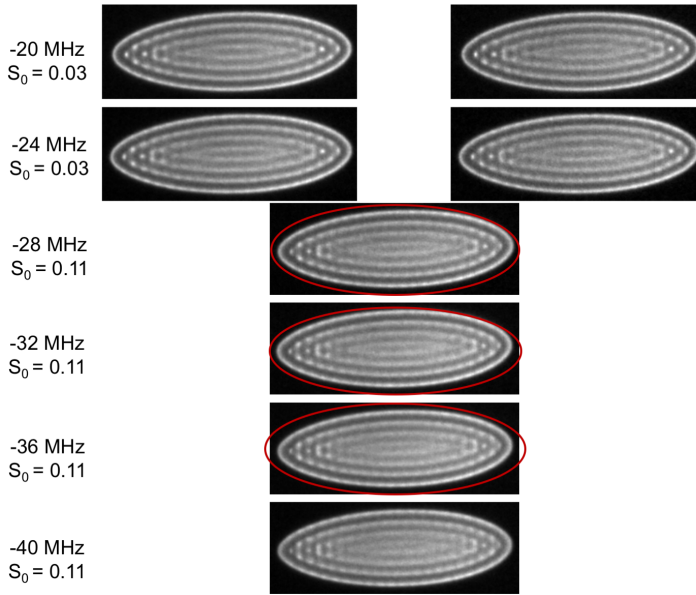


Figure II.4.8: Experimental continuously cooled crystal with various detunings and intensities. The other parameters are given in Table II.4.5.

II.4.4 Summary

II.4.4.a Coldest Coulomb crystals

A summarized version of the experimental investigations is shown in Fig. II.4.9. These results confirm that, for an ion trapping setup presenting a single cooling beam at an angle of 45° with respect to the radial plane, a pulsed cooling scheme is a more efficient cooling option than a continuous one as it allows us to reach lower temperatures for trapped calcium Coulomb crystals. Using two symmetrically delayed pulses per RF period, *i.e.* the Both scheme, seems to always be more efficient than only using one (Rising/Falling)⁵. However, a more thorough investigation of the different parameters has to be done if the absolute best pulsed cooling scheme needs to be found.

⁵This effect is understandable as the ions are cooled for twice as long with the Both scheme—if compared to Rising/Falling—at low-micromotion effect phases

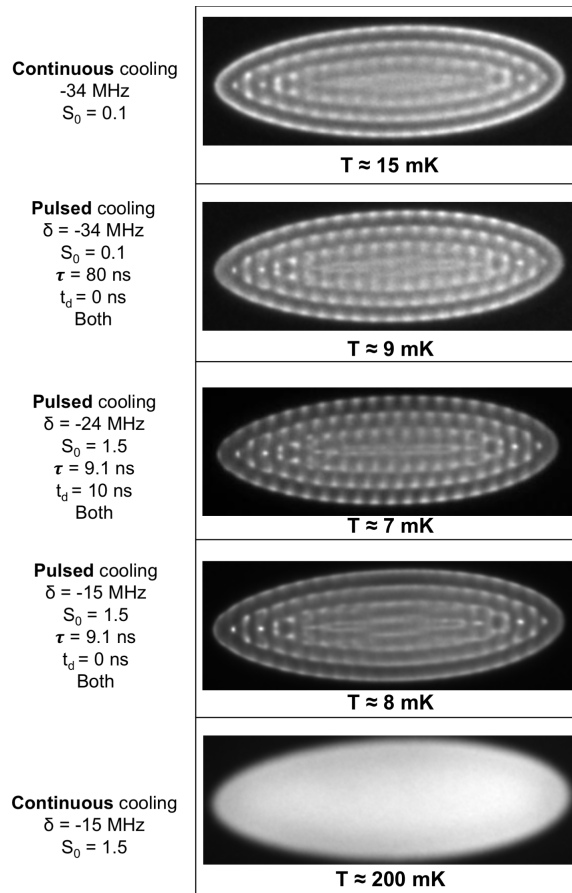


Figure II.4.9: Summary of the coldest crystals using optimized pulsed cooling and continuous cooling parameters.

II.4.4.b Formation of challenging structures

To further test the efficiency of the pulsed cooling, we attempt the formation of challenging structures which are impossible to obtain using a continuous 45° cooling: large Coulomb crystals (formed by thousands of ions) and pancakes. What we refer to as pancakes, are 2D crystals formed in the radial (x, y) plane, rendering them highly subject to micromotion.

Using our optimized pulsed cooling parameters, we are able to effi-

ciently trap and cool both a large crystal of approximately 5350 ions and a pancake of around 75 ions. These structures are reproduced by Molecular Dynamics simulations (following the parameter determination procedure described in Sec. II.5.4) which allows us to determine their temperature. Table II.4.6 gives the experimental parameters used to form the large Coulomb crystal in Fig. II.4.10(a) and Table II.4.7 those used to simulate the structure in Fig. II.4.10(b).

Similarly, Fig. II.4.11(a) shows the experimental image of a pancake trapped using the parameters in Table II.4.8—view in the (X, Z) plane, and Fig. II.4.11(b) and Fig. II.4.11(c) show respectively the views in the (X, Z) and (X, Y) planes of the simulated pancake using the parameters in Table II.4.9⁶.

Parameter	Value	Parameter	Value
ω_z [kHz]	236	δ [MHz]	-15
ω_r [kHz]	482	τ [ns]	9.1
$\Gamma/2$ [MHz]	16	t_d [ns]	0
		s_0	1.5

(a) Trap frequencies and cooling linewidth. (b) Pulsed cooling parameters.

Table II.4.6: Experimental parameters—trapping of a large crystal [Fig. II.4.10(a)].

Parameter	Value
ω_z [kHz]	240.72
ω_r [kHz]	472.549
N_{ion}	5349
T [mK]	100

Table II.4.7: Simulation parameters—large crystal [Fig. II.4.10(b)].

⁶The size of the simulated pancake is not exactly similar to the experimental one, further frequency adjustment could correct that effect.

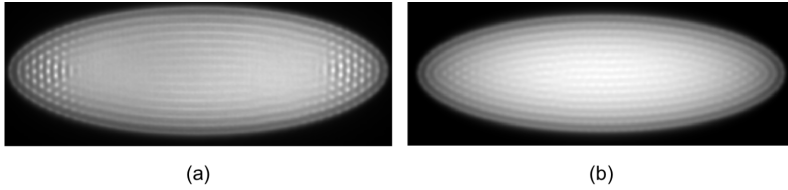


Figure II.4.10: Pulse cooled Coulomb crystal of ≈ 5350 ions. (a) Experimental crystal obtained using the parameters given in Table II.4.6. (b) Molecular Dynamics simulated crystal of 5349 ions using the parameters from Table II.4.7.

Parameter	Value	Parameter	Value
ω_z [kHz]	280	δ [MHz]	-15
ω_r [kHz]	80	τ [ns]	9.1
$\Gamma/2$ [MHz]	16	t_d [ns]	0
		s_0	1.5

(a) Trap frequencies and cooling linewidth. (b) Pulsed cooling parameters.

Table II.4.8: Experimental parameters—trapping of a pancake [Fig. II.4.11(a)].

Parameter	Value
ω_z [kHz]	310
ω_r [kHz]	90
N_{ion}	75
T [mK]	4

Table II.4.9: Simulation parameters—pancake [Fig. II.4.11 (b) and (c)].

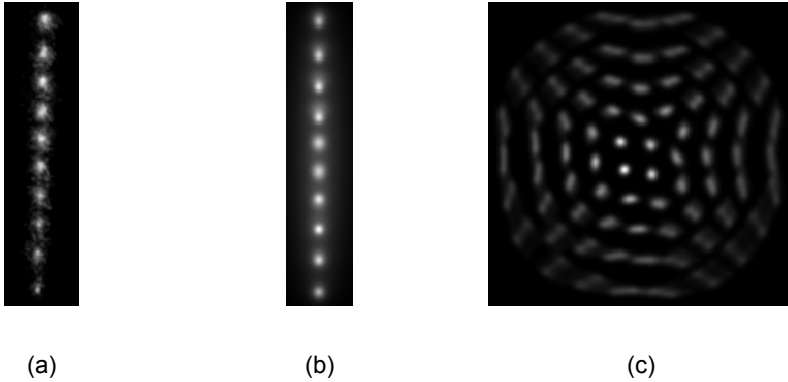


Figure II.4.11: Pulse cooled pancake of ≈ 75 ions. **(a)** Experimental structure obtained using the parameters given in Table II.4.8—the image is taken in the usual (X, Z) plane. **(b)** and **(c)** Molecular Dynamics simulated pancake of 75 ions using the parameters from Table II.4.9, viewed in the (X, Z) plane **(b)** and (X, Y) plane **(c)**.

II.4.5 Insight into some of the observed features

A few things can be noted from our optimization procedure. First, the intensities of the cooling light are much higher in the best pulsed scheme *vs.* the best continuous scheme. This can be explained by the fact that in the case of the pulsed cooling, the micromotion being less excited, the intensity (and thus the number of scattering events) can be higher before it poses a problem whereas in the continuous case, the micromotion heating becomes dramatic quite quickly.

Secondly, the optimal pulse delay apparently being $t_{d,opt} = \pm 10$ ns is an unexpected result since it does not address the phase of zero-micromotion. A first investigation of the cooling was performed by calculating the friction force (as defined in Sec. II.2.1.b.ii) due to the 45° cooling beam. However it was inconclusive and should be lead further by expanding the force to higher orders, for instance.

This effect is found to be even more pronounced with a pulse length of $\tau = 30$ ns, suggesting that the cooling dynamics during the pulse might

be responsible. A more complete investigation of the phenomenon would be to solve the optical Bloch equations with the pulsed cooling scheme introducing a detuning that varies following the RF oscillation.

Finally, for $t_d = \pm 10$ ns, the optimal detuning is different from the usual $|\delta_{opt}| = \Gamma/2$ as here: $|\delta_{opt}| = 24$ MHz $> \Gamma/2$. This could be explained by the fact that, the ions being addressed at a moment of non-zero micromotion, this value of the detuning could be more optimal as it would limit the heating by allowing for the majority of the ions to remain on the less steep side of the temperature–detuning curve. In addition, due to the three-dimensional extension of the crystals, if they are addressed at a point of non-zero micromotion with a pulse of well chosen detuning, half of the crystal would be cooled down while the other half is heated up, and vice-versa for a pulse with opposite delay. Since the Coulomb crystals are subject to sympathetic cooling effects [75], the total cooling over one RF period with a Both scheme could overall be efficient. This effect is also present in the case of a continuous cooling, however, if addressed over the entire RF period, the range of velocities that need to be compensated by the detuning might be too high for efficiency. Solving the optical Bloch equations for the pulsed cooling could give some insight to these observations as well.

Although the theory behind pulsed cooling was not fully understood, classical Molecular Dynamics (MD) simulations of the trapped ions gave us an insight to the phenomena observed experimentally. The next section outlines how the simulations were constructed and performed.

Temperature catalog—Molecular Dynamics simulations

The efficiency of pulsed cooling and its comparison to the continuous cooling scheme is determined by the final temperature of the crystals. For that purpose, a temperature catalog to be used as a scale was simulated by Molecular Dynamics¹. The simulations were conducted using the same trapping parameters, size and ion number as that of the experimental results—the aspect of the crystal, especially the size of the ions, being directly related to its temperature. The cooling process was not simulated in itself and the resulting simulated structure mimics an equilibrium crystal once the cooling process has reached a steady state.

The MD simulator was developed by previous members of the Ion Trap Group [80, 81]. It was adjusted in the course of this work to fit the requirements of the pulsed cooling experiments.

In this chapter, sections II.5.1, II.5.2 and II.5.3 give a quick outline of the main features of the simulator. A more detailed theoretical description can be found in Ref. [81] and details on the operation of the simulator can

¹The catalog was used as a quick estimation tool of the crystals' temperature during our optimization procedure. For the final optimal crystals in Fig. II.4.9, the given temperatures were simulated for more precision.

be found in Refs. [82, 83]. Sections II.5.4 and II.5.5 describe the procedure followed to generate the temperature catalog. Even though we focus our discussion on the simulation of Coulomb crystals, the program can be used for a wide range of one- or two-species structures.

II.5.1 Newton propagator

The crystals are simulated by solving the classical equations of motion for the ions with the force F_{Tot} . The forces at play are the trapping force F_{Trap} and the Coulomb force F_{Coul} . For a given ion i they are given by:

$$F_{Trap,i} = \begin{cases} -\frac{Q}{m} \left(\frac{\eta V_{DC}}{z_0^2} + \frac{V_{RF} \cos(\Omega_{RF} t)}{r_0^2} \right) x_i \\ -\frac{Q}{m} \left(\frac{\eta V_{DC}}{z_0^2} - \frac{V_{RF} \cos(\Omega_{RF} t)}{r_0^2} \right) y_i \\ -\frac{2Q\eta V_{DC}}{mz_0^2} z_i \end{cases}, \quad (\text{II.5.1})$$

and

$$F_{Coul,i} = \frac{q^2}{4\pi\epsilon_0} \sum_{n \neq i}^N \frac{\mathbf{r}_i - \mathbf{r}_n}{|\mathbf{r}_i - \mathbf{r}_n|^2}. \quad (\text{II.5.2})$$

$F_{Tot,i}$ for the ion i can thus be expressed as:

$$F_{Tot,i} = \frac{q^2}{4\pi\epsilon_0} \sum_{n \neq i}^N \frac{\mathbf{r}_i - \mathbf{r}_n}{|\mathbf{r}_i - \mathbf{r}_n|^2} + \begin{cases} -\frac{Q}{m} \left(\frac{\eta V_{DC}}{z_0^2} + \frac{V_{RF} \cos(\Omega_{RF} t)}{r_0^2} \right) x_i \\ -\frac{Q}{m} \left(\frac{\eta V_{DC}}{z_0^2} - \frac{V_{RF} \cos(\Omega_{RF} t)}{r_0^2} \right) y_i \\ -\frac{2Q\eta V_{DC}}{mz_0^2} z_i \end{cases} \quad (\text{II.5.3})$$

with $\mathbf{r}_i = (x_i, y_i, z_i)$ the position vector of the ion i of charge q , and N the total number of ions.

At each time step t , $F_{Coul,i}$ is calculated for each ion interacting with all the other ions on GPU cores and $F_{Trap,i}$ on CPU cores. The position and velocity of the ion i at the next time step $t + dt$ are thus given by:

$$\begin{cases} u_i(t + dt) &= u_i(t) + dt^2 \frac{F_{Tot,u,i}}{2m} + dt v_{u,i}(t) \\ v_{u,i}(t + dt) &= v_{u,i}(t) + dt \frac{F_{Tot,u,i}}{m} \end{cases}, \quad u = x, y, z \quad (\text{II.5.4})$$

where dt is the time step size given by $dt = 2\pi/(\Omega_{RF}\tau_{RF})$ with τ_{RF} the number of time steps per period².

It should be noted that given the definition of F_{tot} and the simulation process, the effects of the micromotion on the ions' velocities and crystal temperature are visible in the simulation.

II.5.2 Thermalizer

In order to generate images at a given temperature T_{target} , the simulation is started at a chosen starting temperature T_{start} , higher than the desired final temperature³. The ions are then cooled following the procedure outlined below—it was previously shown that choosing $T_{start} \gg T_{target}$ and thus cooling down the ions was a more robust simulation procedure [81].

The temperature of the ion ensemble at each time step is calculated using $T = \frac{\overline{p^2}}{2mk_B} = m \frac{\overline{v^2}}{k_B}$ with $\overline{v^2}$ the averaged velocity of the system given by:

$$\overline{v^2} = \frac{1}{3N} \sum_{i=1}^N \sum_{u=x,y,z} v_{u,i}^2. \quad (\text{II.5.5})$$

The temperature of the system can thus be expressed as:

$$T = \frac{m}{3Nk_B} \sum_{i=1}^N \sum_{u=x,y,z} v_{u,i}^2. \quad (\text{II.5.6})$$

In order to direct the simulation towards cooling, the calculated next-time-step velocity $v_{u,i}(t + dt)$ is rescaled by the factor $a_{T,u}$ to $v_{rescaled,u}(t + dt) = a_{T,u}v_u(t + dt)$. The scaling factor is given by:

² τ_{RF} was optimized for optimal convergence prior to this study and set to 105 [81]

³For a target temperature of a few mK, the simulation is usually started at $T_{start} = 100\text{mK}$.

$$a_{T,u} = \sqrt{\frac{T_{target}}{T_u}}, \quad (\text{II.5.7})$$

where T_u is the average temperature along the direction u :

$$T_u = \frac{m}{Nk_B} \sum_{i=1}^N v_{u,i}^2. \quad (\text{II.5.8})$$

To prevent any brutal cooling, $a_{T,u}$ is limited to values between 0.98 and 1.02. If the calculated $a_{T,u}$ is lower than the lower bound, it is set to $a_{T,u} = 0.996$ and for values higher than the upper bound, to $a_{T,u} = 1.00002$ (those were previously found to be optimal [81]).

Taking the rescaling procedure into account, the actual positions and velocities at the next time step are calculated from:

$$\begin{cases} u_i(t + dt) &= u_i(t) + dt^2 \frac{F_{Tot,u,i}}{2m} + dt v_{rescaled,u,i}(t) \\ v_{u,i}(t + dt) &= v_{rescaled,u,i}(t) + dt \frac{F_{Tot,u,i}}{m} \end{cases}, \quad u = x, y, z. \quad (\text{II.5.9})$$

The length of a time step (dt) is determined by the RF period as the number of time steps per period is set to its previously optimized value. Our simulations are all run using the experimental RF frequency ($T_{RF} = 252.15$ ns) resulting in time steps of approximately 2.4 ns.

The temperature evolution during a simulation is monitored and can be seen in Fig. **II.5.1** and a magnified view of the first fifth of the simulation is shown in Fig. **II.5.2**.

The average temperature along the z direction, T_z , has stabilized at the target value after $t_{th} = 857 \times T_{RF}$ ($\approx 90,000$ time steps). The simulation phase for times before t_{th} is referred to as the thermalization phase. During this phase the equations of motion are solved, but the ions' positions and velocities are not recorded as the crystal has not yet reached a stable configuration at the target temperature. It is followed by the recording phase, in which the crystal has reached a stable configuration at the

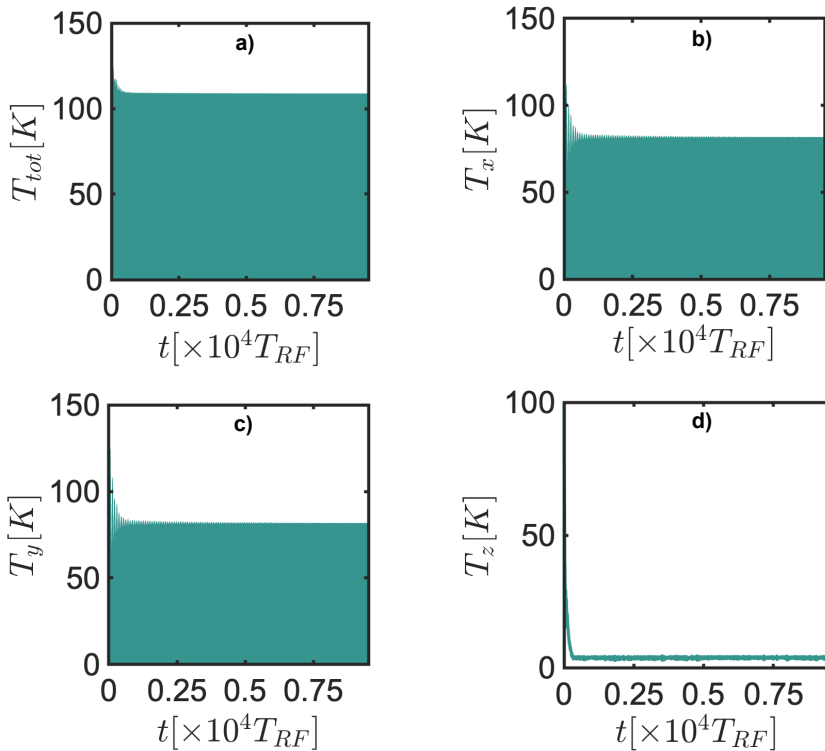


Figure II.5.1: Evolution of the temperature (given in K) as a function of the simulation time (in timesteps) during a MD simulation of a Coulomb crystal. This simulation was performed over $t_{sim} = 9524 \times T_{RF}$ with an ensemble of 40 ions, with $T_{target} = 4$ mK and trap frequencies $\omega_z = 2\pi \times 248.0760$ kHz, $\omega_r = 2\pi \times 41.346$ kHz. (a) Total average temperature calculated from Eq. (II.5.6); (b), (c) and (d) Average temperature along the x , y and z direction respectively, calculated from Eq. (II.5.8).

desired average temperature. During this phase, the equations of motions are solved and the ions' positions and velocities are recorded in order to generate an image resembling those obtained from the experimental imaging system. The duration of the thermalization phase depends on the chosen T_{target} , number of ions and trap parameters. In our simulations, we customarily set the start of the recording phase to $t_{th} = 858 \times T_{RF}$ and the

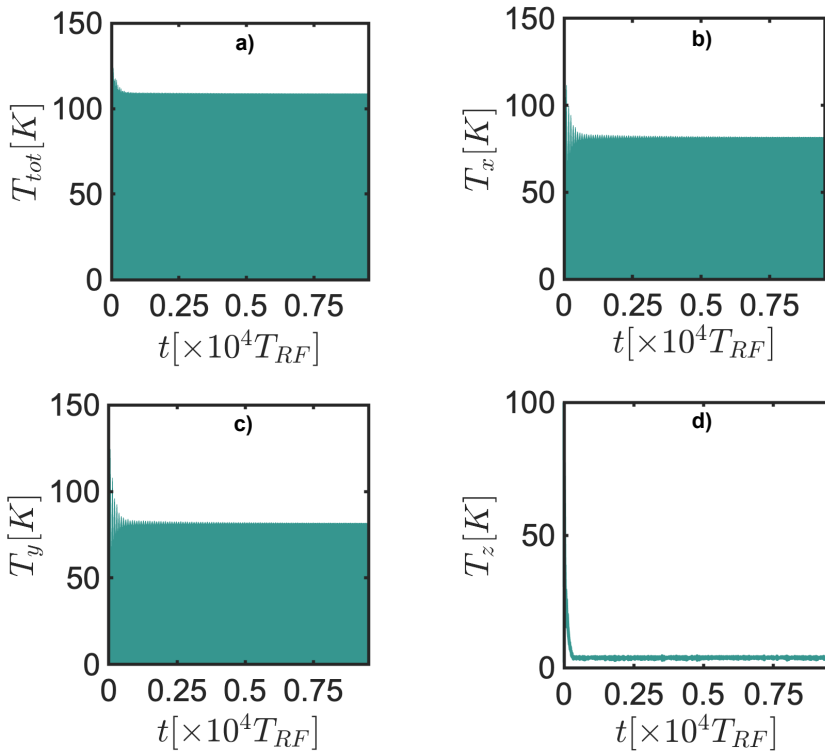


Figure II.5.2: Evolution of the temperature (given in K) as a function of the simulation time (in timesteps) during the first $1428 \times T_{RF}$ ($= 150,000$ time steps) of an MD simulation of a Coulomb crystal. This simulation was performed with an ensemble of 40 ions, with $T_{target} = 4$ mK and trap frequencies $\omega_z = 2\pi \times 248.0760$ kHz, $\omega_r = 2\pi \times 41.346$ kHz. **(a)** Total average temperature calculated from Eq. (II.5.6); **(b)**, **(c)** and **(d)** Average temperature along the x , y and z direction respectively, calculated from Eq. (II.5.8).

total simulation duration to $t_{sim} = 9524 \times T_{RF}$ ($= 1,000,020$ time steps). T_x and T_y , although stabilized, do not converge at the target value of the temperature. This is due to the presence of micromotion in those directions.

II.5.3 Input/Output

The simulation allows for several parameters to be chosen in an input file⁴. A few notable ones are the number of ions, the start and target temperatures, the trapping secular axial and radial frequencies, the RF frequency, the number of thermalization time steps and the total number of time steps. The trap geometry (r_0 , z_0 and η as defined in Fig. II.2.2) is also set in the input file.

The simulation starts at the given starting temperature. The initial ion positions can either be read from an input file or set to a BCC structure centered around the center of the trap (default), as it was shown to be the equilibrium crystal structure (see Sec. II.2.2). An offset on the initial position of the ions can be set from the input file as well, which reproduces the situation where the single ion or crystal are displaced from the trap axis by a static electric field (described in Sec. II.2.1.c).

After the thermalization phase, when the target temperature has been reached, the ions' positions are recorded in a file which mimics the pixel histogram file obtained experimentally from the CCD camera images. Its size (H_X, H_Y, H_Z) is given in the input file⁵. An ion positioned at (X_i, Y_i, Z_i) , will be recorded in a given bin N_U of the histogram given by:

$$N_U = \frac{U_i}{\zeta} + \frac{H_U}{2} \quad , \quad U = (X, Y, Z) \quad (\text{II.5.10})$$

where U_i is the position of the ion in terms of lab frame axes and ζ the experimental pixel size.

The final histogram gives the number of occurrences of ions in each bin N_U over the recording phase. This allows for the construction of an accurate image of the Coulomb crystal at a given temperature as it takes into account the variations of ion positions due to temperature effects. The position distribution due to the thermal and micromotion effects is therefore described and as in the experimental images, a better definition of the ions indicates a lower temperature.

⁴The detail of program functions and the input/output files and parameter list can be found in Refs. [82, 83].

⁵The size of the histogram is given in terms of the lab frame (X, Y, Z) as it is most relevant for a comparison to experimental images.

In order to mimic the pulsed cooling scheme, the simulator was modified to record the ion positions in the histogram file for a given time window only (centered around the chosen pulse delay and of size equal to the size of the pulse).

The histogram file is then analyzed by a *Matlab* routine that produces a grayscale image. The resolution of the imaging system is taken into account in this simulation post-processing in forms of a blur function.

We use this simulation tool to build a temperature catalog for the pulsed Coulomb crystals. The procedure is described in the next sections.

II.5.4 Reproducing experimental data

II.5.4.a Influence of the number of ions and trap frequencies on the aspect of a crystal

In order to obtain the most accurate reproduction of experimental data, the simulations have to be performed with the same trapping parameters. The experimental values for the trap geometry and RF frequency can be directly used in the simulations as their experimental determination is accurate.

The other key parameters are the trap secular frequencies and ion number as they strongly influence the final aspect of the crystal (see Fig. II.5.3). Indeed, as described in Sec. II.2.2, the frequency ratio influences the aspect ratio of the crystal, and the radial frequency the ion density (see Eqs. (II.2.64) and (II.2.66), respectively).

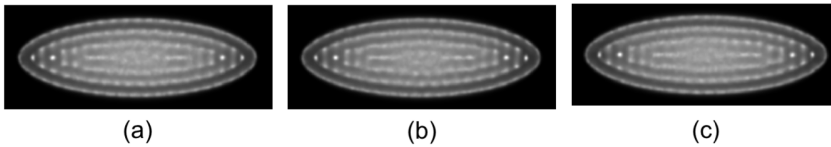


Figure II.5.3: Influence of the ion number and frequency ratio on the aspect of simulated Coulomb crystals. All three simulations were run at $T = 10$ mK and $\omega_r = 2\pi \times 162.72$ kHz. **(a)** $N_{ion} = 555$, $\omega_z = 2\pi \times 83.16$ kHz; **(b)** $N_{ion} = 560$, $\omega_z = 2\pi \times 83.16$ kHz; **(c)** $N_{ion} = 560$, $\omega_z = 2\pi \times 82.5$ kHz. **(a)–(b)** The ion number is changed, **(b)–(c)** the axial frequency is changed.

From the ion spread and shell definition for the three crystals on Fig. II.5.3, it could be inferred that $T_{(a)} < T_{(b)} < T_{(c)}$. However, all three crystals were simulated at the same target temperature. Indeed, even a relatively small variation in ion number or frequency ratio ($< 1\%$) impacts the aspect of the crystal enough to lead to an erroneous determination of the temperature. Thus, the determination of these experimental parameters is crucial if a precise evaluation of the temperature is desired.

If an estimation of the trap frequencies can be determined experi-

mentally⁶, the resulting values cannot be considered accurate, due to the discrepancy between the frequency of the modulating signal (sent) and the frequency of this signal at the trap (seen by the ions)—which is the actual trap frequency to be used in the simulations⁷. Therefore, for the simulation, the experimentally measured values require to be adjusted to match their values at the trap.

II.5.4.b Parameter determination

The adjustment of the ion number and secular frequencies is conducted as follows.

Experimental aspect ratio and volume determination

In order to calculate the aspect ratio and experimental volume of the crystal (given by Eq. (II.2.60) and Eq. (II.2.61) respectively) needed for the parameter adjustment, the charged liquid model length L and radius R of the crystal need to be estimated.

For that purpose, the shell structure of the crystals is obtained by plotting the radial and axial profiles of the images using *ImageJ*. Then, following the procedure described in [29] (p. 169), from the length L' and radius R' of the experimental crystal—defined as the distance between the centers of the external shell on both sides—the charged liquid model parameters are calculated: $L = L' + \delta R$, $R = R' + \delta R$ —where δR is the inter-shell spacing, known to be the same radially and axially (see Fig. II.5.4).

The adjustment of the trap frequencies, crystal ion number and temperature is then performed.

⁶We recall: the measurement of the axial and radial frequencies can be done by trapping an ion and adding a sinusoidal modulation to the trap electrodes axially (or radially) while cooling it in the other direction. When the frequency of the modulation is equal to the trap frequency, the oscillation mode is excited and the ion starts oscillating axially (resp. radially). This allows a determination of the trapping frequency with a reading precision of $\approx 0.5\%$.

⁷This difference between the sent signal frequency and seen signal frequency can be attributed to electronic noise.

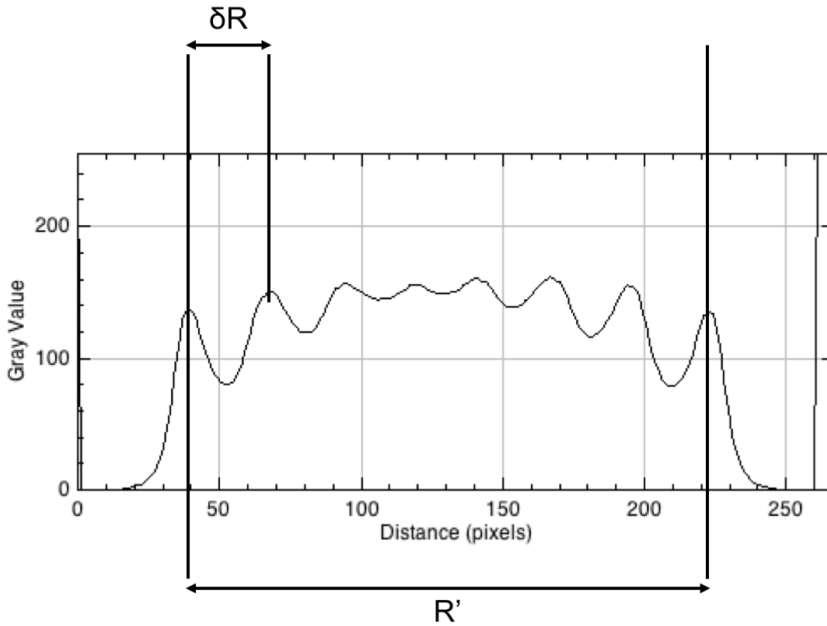


Figure II.5.4: Radial profile of the crystal in Fig. II.5.3 (b) plotted with *ImageJ*.

Temperature optimization

First, the ion number is estimated from the expression of the density ρ (Eq. (II.2.66)) using the experimental volume V_{exp} given by Eq. (II.2.61) and the experimental frequencies $\omega_{z,exp}$ and $\omega_{r,exp}$. Then, simulations at different target temperatures are run using these parameters until the simulated crystals appear similar to the experimental ones⁸.

Trap frequency optimization

Using the previously determined target temperature and ion number, the trapping secular frequencies are adjusted until the simulations reproduce

⁸The comparison between simulated and experimental images is done based on their visual aspect at first and then, if the differences are not discernible, by analyzing the axial and radial shell profiles with *ImageJ*.

the same aspect ratio as the one experimentally observed (the relation between these ratios is given in Eq. (II.2.64)).

Ion number determination

Then, a corrected number of ions (N_{corr}) is calculated from the simulation density ρ_S (which is determined from the simulated crystal's volume and number of ions): $N_{corr} = \rho_S V_{exp}$.

Further simulations

Finally, the simulations are restarted with the corrected frequencies and number of ions (which at this point are considered to be similar to the experimental parameters). In the case of a temperature catalog generation, they are run for various values of target temperature as described in the next section. If an estimate of the experimental crystal's temperature is desired, the target simulation temperature is further optimized to obtain maximum similarity with the experimental images.

II.5.5 Temperature catalog

In order to be able to estimate the temperature of the experimental crystals, a temperature catalog is simulated and used as a scale. Although a time-gated simulation mimicking the pulsed cooling would be the most accurate replica of the experimental crystals, as it would give a picture of the crystal with the ions being at the position they occupy at this specific moment of the RF period (see Fig II.5.5), it is found to be similar to a simulation integrated over the entire RF period for the crystals and range of temperatures we consider (see Fig. II.5.6).

Indeed, we can see in Fig II.5.5 the influence of excess micromotion on the positions of a calcium ion and a magnesium ion as they are artificially displaced by approximately 30 μm from the RF nodal line (see Sec. II.2.1.c.i). For each RF period, the images are either recorded at the moment of zero displacement and maximum micromotion induced velocity ($t = T_{RF}/4$)—(a), at the moment of maximum displacement and zero micromotion induced velocity ($t = T_{RF}/2$)—(b), or over the entire RF

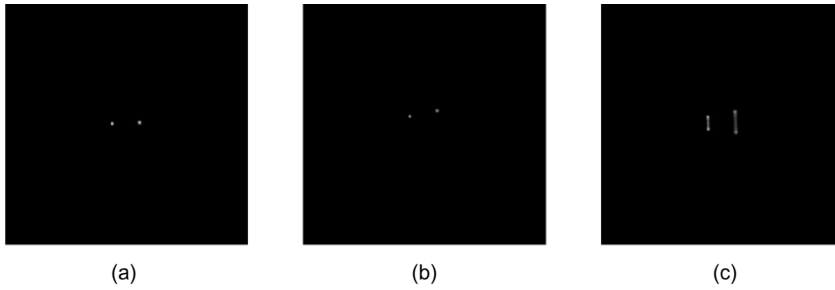


Figure II.5.5: Simulated Ca^+ (left) and Mg^+ (right) ions at $T = 1$ mK, $\omega_z = 2\pi \times 115.644$ kHz, $\omega_r = 2\pi \times 381.525$ kHz, initially displaced $30 \mu\text{m}$ from the trap axis along X . (a) Positions recorded over 4.8 ns around $t = T_{RF}/4$ —ions at their central positions, point of maximum micromotion induced velocity, no blur applied; (b) Positions recorded over 4.8 ns around $t = T_{RF}/2$ —ions at their position extremum, point of zero micromotion induced velocity, no blur applied; (c) Positions recorded over the entire T_{RF} , no blur applied.

period—(c). Since the simulations are performed at a very low temperature ($T = 1$ mK), the ion’s spread is very small and the effects of the micromotion are clearly visible: the ions oscillate around their equilibrium position at the RF frequency.

For a crystal simulated at $T = 8$ mK reproducing our experimental conditions, even when considered with perfect resolution (as not applying the blur function produces images rendering exactly the ions’ positions), the effects of the micromotion are hardly visible (one can notice the presence of additional shadow between the ions when integrated over the entire RF period, Fig. II.5.6 (c), compared to the situation reproducing a Both pulsed cooling scheme around the zero of micromotion, Fig. II.5.6 (d)). Thus we can deduce that the contribution of the micromotion is not the dominant effect on the temperature-induced dispersion of the position of the ions in our crystals. When the blur is applied, taking into account the resolution of our imaging system, the differences between a pulsed simulation, Fig. II.5.6 (a), and a continuous simulation Fig. II.5.6 (b), vanish.

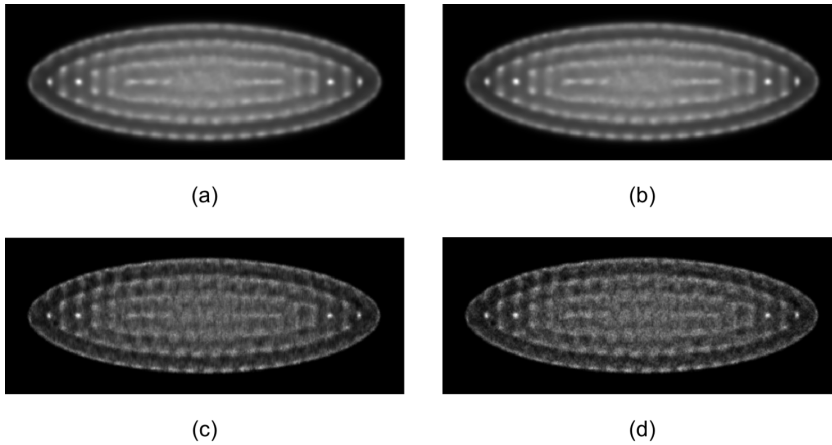


Figure II.5.6: Simulated crystals of Ca^+ ions at $T = 8$ mK, $\omega_z = 2\pi \times 83.16$ kHz, $\omega_r = 2\pi \times 162.72$ kHz, $N_{ion} = 555$. (a) Positions recorded over the entire T_{RF} , image blurred in post-processing; (b) Positions recorded during 9.6 ns (shortest experimental pulse) around $t = T_{RF}/4$ and $t = 3T_{RF}/4$ —ions at their central positions, point of maximum micromotion induced velocity, image blurred in post-processing; (c) Positions recorded over the entire T_{RF} , no blur applied; (d) Positions recorded during 9.6 ns around $t = T_{RF}/4$ and $t = 3T_{RF}/4$, no blur applied.

The temperature catalog is therefore generated by integrating the ions' positions over the entire RF period.

The experiments being performed by always setting the trapping frequencies to a similar value with a crystal of the same length (and therefore number of ions), the temperature catalog can be used throughout the presented experimental work. It is obtained for parameters determined following the procedure described in the previous section: $N_{ion} = 555$, $\omega_z = 2\pi \times 83.16$ kHz (compared to $\omega_{z,exp} = 2\pi \times 82.2$ kHz) and $\omega_r = 2\pi \times 162.72$ kHz (compared to $\omega_{r,exp} = 2\pi \times 164.65$ kHz) and $\Omega_{RF} = \Omega_{RF,exp} = 2\pi \times 3.966$ MHz. It is shown in Fig. II.5.7.

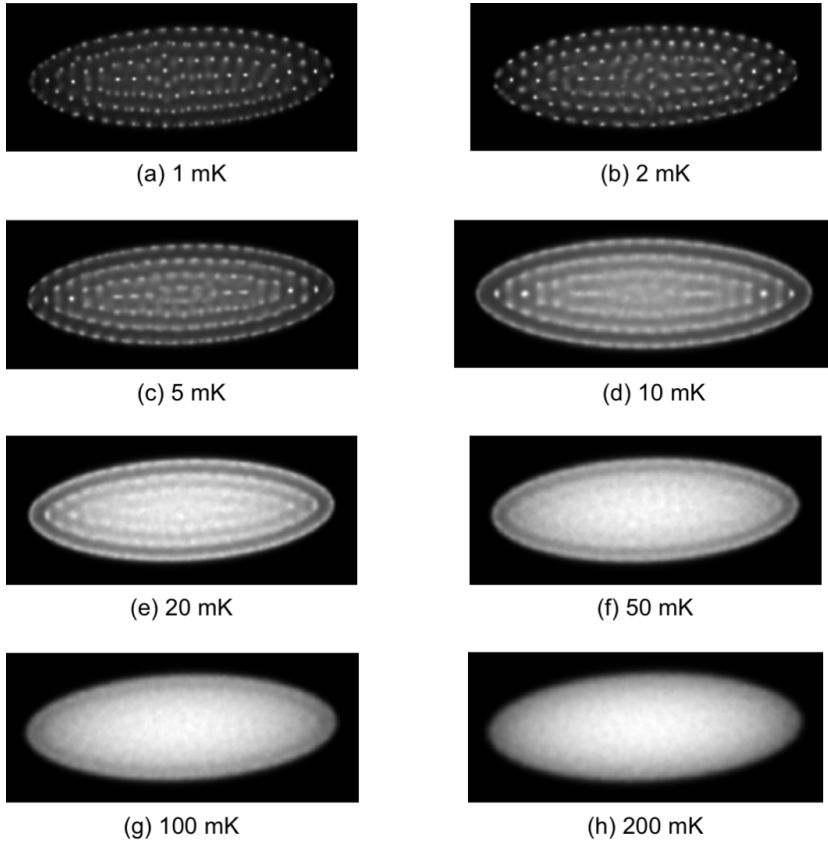


Figure II.5.7: Simulated temperature catalog for Ca^+ Coulomb crystals. It was obtained using parameters determined as described in Sec. II.5.4.b: $N_{ion} = 555$, $\omega_z = 2\pi \times 83.16$ kHz, $\omega_r = 2\pi \times 162.72$ kHz, and $\Omega_{RF} = \Omega_{RF,exp} = 2\pi \times 3.966$ MHz. The ion positions were recorded over the entire T_{RF} and the images were blurred in post-processing.

Applications—pancakes

In addition to the more efficient cooling of three-dimensional crystals, pulsed cooling allows the formation of structures highly sensitive to micromotion such as two-dimensional discs in the radial plane—pancakes—with a unique 45° cooling beam (see Sec. II.4.4.b). Pancakes are especially interesting candidates for two-dimensional quantum simulators [84]. Indeed, they allow for a larger number of gates than one-dimensional string structures (as the number of ions in string ion trapping is limited) and present more scalable simulator options [24]. They can be used for instance, to study lattice spin models beyond the restrictions of one-dimensional systems and shed light on areas of quantum many-body physics that cannot be solved analytically [85]. Those structures have been formed, for instance, in Penning traps [86], but the large ion separation and fast rotation inherent to these setups limit the ability to obtain fast quantum gates and an efficient individual addressing of ions. Thus, Paul trapped pancakes seem to be good candidates despite the presence of micromotion.

II.6.1 Experimental formation of pancakes

Pancakes are 2D structures in the (x, y) plane that can be formed when the trapping frequency ratio $\wp = \omega_z/\omega_r$ ¹ becomes larger than 1 [85]. Because of their radial extension, they are subject to the RF driven micromotion (see Sec. II.2.1.c) which makes their cooling challenging, especially with a

¹We recall: \wp is a Japanese hiragana pronounced “ya”.

single laser beam.

As described in Sec. II.4.4.b, we are able to form and keep in the trap pancakes of approximatively 75 ions (shown in Fig. II.4.11) using a two-pulse scheme (Both). The formation procedure consists of first loading a small crystal into the trap using usual frequencies (given in Table II.3.1 for instance) and the pulsed cooling scheme. Then, slowly compressing it axially while releasing it radially by increasing the axial frequency and decreasing the radial frequency until it forms the desired pancake structure (which appears as a vertical string on the CCD image).

II.6.2 3D–2D phase transition investigation

The phase transition from a 3D crystal to a 2D pancake has previously been investigated by Dubin [87], who derived a general analytical expression for this phase transition frequency ratio excluding micromotion effects, and by Richerme [85], who took into account the effects of the micromotion in his analysis of the phase transition applied to Yb^+ ions. For a crystal of 75 ions—the N_{ion} of our experimentally formed pancakes—Dubin predicts the transition to happen for $\varphi > (2.264N_{ion})^{1/4} \approx 3.6$, which is in agreement with Richerme’s assessment of the phase transition without micromotion (red curve in Fig. II.6.1). However, as we stated previously, pancakes are highly subject to micromotion and in order to conduct a complete study of the phase transition, its effects should be included. In this case, the phase transition frequency ratio predicted in [85] for Yb^+ is $\varphi \approx 5$. Nonetheless, we were able to form stable pancakes at a frequency ratio $\varphi_{exp} = 3.5$. This apparently contradictory observation motivated our study of the 3D crystal–2D pancake phase transition using the MD simulator presented in Chap. II.5, as it includes the effects of micromotion².

II.6.2.a Simulation procedure

The simulations are performed using Ca^+ ions. The initial Mathieu parameters q and a (see Eq. (II.2.10)) are set to be equal to $q = 0.125$ and $a = -0.0073$ (parameters used in Ref. [85]) in order to obtain comparable results (since we are not studying the same ion species). With $\Omega_{RF} = 2\pi \times 3.996$ MHz, the corresponding trapping frequencies are equal

²The simulator was further modified to fit the requirements of those calculations.

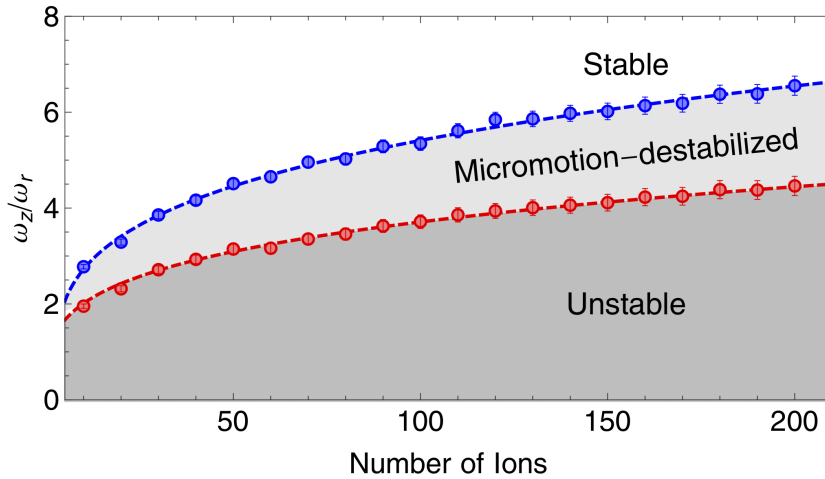


Figure II.6.1: Stability regions for a 2D planar crystal—pancake—calculated for Yb^+ ions. The data points represent the frequency ratios ω_z/ω_r at which the phase transition is predicted to happen for a given number of ions. The red curve represents the resulting stability limit for a model excluding the effects of micromotion; the blue curve shows the limit of stability for a model including micromotion. In each model, frequency ratios higher than the stability limit allow for a stable pancake formation. The micromotion is a destabilizing effect as it requires a tighter relative radial confinement for the formation of pancakes. The plot is taken from Ref. [85].

to: $\omega_r = 2\pi \times 41.346$ kHz, $\omega_z = 2\pi \times 242.27$ kHz and $\wp = 5.8596^3$.

Starting from these frequencies, several values of the frequency ratio \wp are considered by changing the axial frequency ω_z ⁴.

The determination of the phase transition is based on the fact that for "magic number" Coulomb crystals, *i.e.* those with a single ion in the

³The geometry of the trap is kept similar to the one of the experimental setup used in this study, see Table II.3.1.

⁴This way of adjusting the value of \wp was chosen because it mimics the experimental realization of the pancake formation. From a 3D crystal, the DC voltage is increased, creating an axial compression, then the RF voltage is decreased allowing a radial relaxation.

center [52], the lowest frequency mode is the mode of oscillation of the central ion in opposition to the rest of the crystal. This mode is a soft mode and collapses to zero frequency at a given limit⁵. This limit for pancake phase transitions was described in [87] in terms of the trap frequency ratio \wp as a consequence of the limit on the spacing between charges (below a certain spacing, the structure is not stable anymore due to the Coulomb repulsion). Therefore, if a kick is given to the central ion—thus exciting this soft mode—it should exhibit an oscillatory motion in the case where the pancake structure is stable and a ballistic motion in the case where the mode is of zero frequency.

Our procedure of construction of the stability limit of pancake structures is as follows:

1. First, a few magic configurations are identified. The ones for $N_{ion} = 33, 80, 150$ were selected as they offer a satisfying range for a first investigation⁶.
2. Then, those structures are cooled down from 100 mK to 4 mK starting from the default BCC structure at $\wp = 6$ (where the pancake structure is stable for all the considered N_{ion} according to Ref. [85])—see Fig. **II.6.2**.
3. Then a new simulation is run—the next steps are then taken for each N_{ion} and each $\wp \in [2, 6]$:
 - Setting the frequency ratio to the value to investigate ($\wp \in [2, 6]$) and starting from the configuration obtained in the previous step, the pancakes are further cooled down to $T_{target} = 0.01$ mK (mimicking a 0 K regime⁷) by freezing the z dimension ($z_i = 0, v_{z,i} = 0$ for all ions i)—which ensures that the crystal remains in its 2D radial planar shape.

⁵See Refs. [16, 88] for the definition of the soft modes in the case of ion strings and zigzag-string phase transitions.

⁶Other magic configurations can be found at, *e.g.* $N_{ion} = 7, 17, 57, 114$.

⁷The same simulations at a higher temperature show a destabilization of the pancake phase at higher frequency ratios, which is expected as the thermal energy would help relax the structure.

- Once the pancake has reached the target temperature⁸, a kick is given to the central ion in the z direction by changing its velocity $v_{z,c}$ to the value corresponding to the kick temperature $T_{kick} = 0.1$ mK.
- After the kick, the z direction is released and the evolution of the pancake, especially the motion of the central ion, is monitored for $80 \times T_{RF}$. This monitoring time is chosen based on the fact that the period of the soft mode is of the order of $1 \mu\text{s} = 4 \times T_{RF}$ in the region of stability for the pancakes [87] and a slower motion is expected closer to the transition ratio φ_{tr} (see Fig. II.6.3).

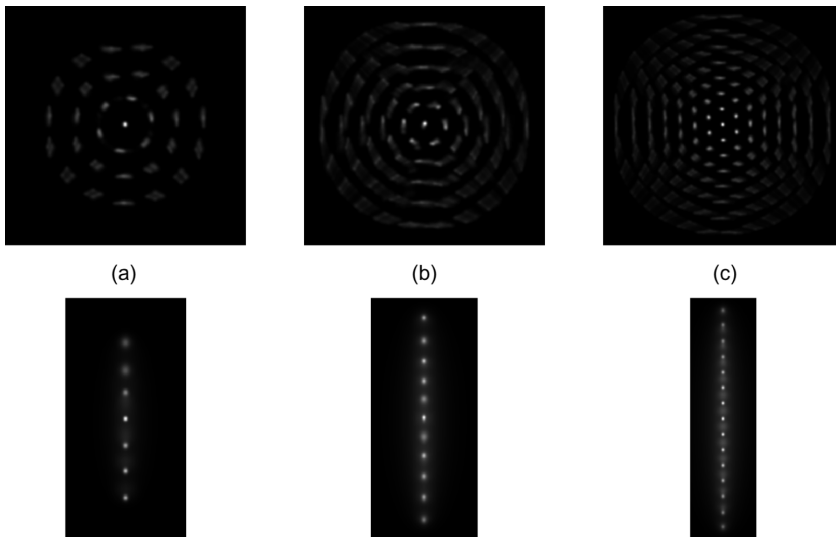


Figure II.6.2: Simulated pancakes at $T = 4$ mK and $\varphi = 6$ for (a) 33 ions, (b) 80 ions and (c) 150 ions. Upper line: (X, Y) view, lower line: (X, Z) view. The selected frequency ratio allows for a stable formation of a pancake structure for the three considered ion numbers. The pancakes all present an ion at the center of the structure: the ion numbers considered here are “magic numbers”.

⁸The length of the thermalization phase was reoptimized for each frequency ratio as the one used previously for \sim mK temperatures was too short.

The amplitude of the z -kick is chosen to be small enough to allow for the ion to be dragged back by the oscillatory force but large enough to disrupt the system and induce the oscillation ($T_{kick} > T_{target}$ is a necessary condition for the kick not to be thermalized, the cooling still being present after the disruption).

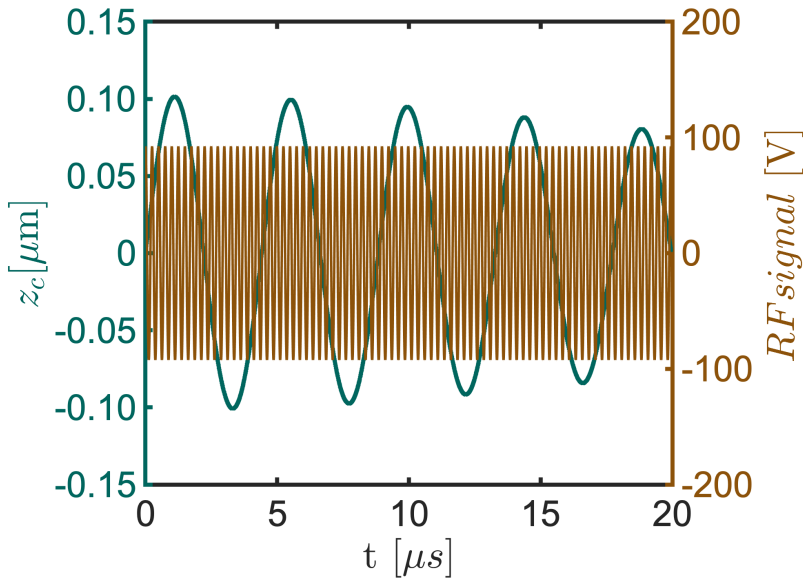


Figure II.6.3: Oscillations of the central ion in a pancake after a z -kick (green) and trapping RF signal (brown). The position of the ion along the z -axis (z_c) is given relative to the position of the pancake (set to $0 \mu\text{m}$). It was simulated for a pancake of $N_{ion} = 33$, formed at the frequency ratio $\wp = 6$, cooled down to $T_{target} = 0.01$ mK, and kicked with $T_{kick} = 0.1$ mK. The amplitude of the RF signal is $V_{RF} = 92.3771\text{V}$ and the total record time corresponds to $80 \times T_{RF}$.

II.6.2.b Phase transition frequency

II.6.2.b.i Characteristic motion of the central ion

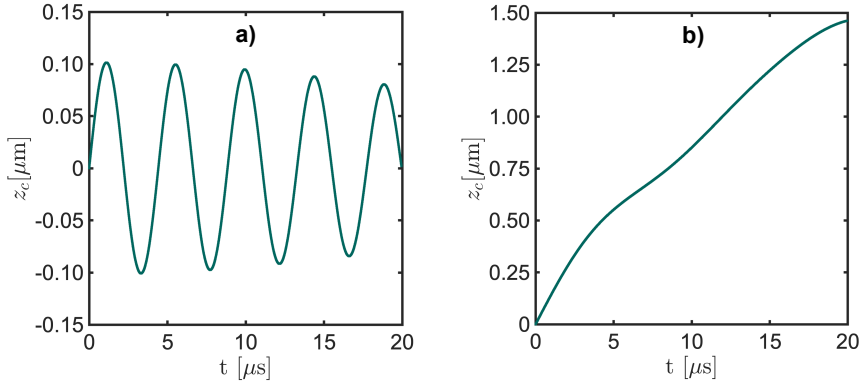


Figure II.6.4: Oscillations of the central ion along the z direction in a pancake after a z -kick for different frequency ratios. The position of the ion along the z -axis (z_c) is given relative to the position of the pancake (set to 0 μm). The simulations were conducted for a pancake of $N_{ion} = 33$, cooled down to $T_{target} = 0.01$ mK, and kicked with $T_{kick} = 0.1$ mK. **a)** Pancake trapped at the moment of the kick with a frequency ratio $\varphi = 6$ ($\varphi > \varphi_{tr}$); **b)** $\varphi = 2.7$ ($\varphi \approx \varphi_{tr}$). The total record time corresponds to $80 \times T_{RF}$.

As suspected, the oscillations of the central ion after the z -kick display a characteristic behavior depending on whether the frequency ratio is higher, equal or lower than the phase transition ratio φ_{tr} .

Indeed, for ratios higher than the phase transition ratio, the central ion starts oscillating along z around its initial position after the kick (the higher the ratio, the faster the oscillations) until it eventually gets back to its original coordinates (see Fig. II.6.4 (a)). This is a consequence of the excitation of the soft mode.

At $\varphi = \varphi_{tr}$, the kicked central ion freely moves away from the pancake along the z -axis (see Fig. II.6.4 (b)). The motion is ballistic as there is no dragging force bringing the ion back to its initial position. This corresponds to the soft mode going to zero frequency.

When the frequency ratio is lower than \wp_{tr} , the pancake structure being unstable, a 3D crystal is formed after the kick and the central ion moves in the three directions to a new equilibrium position.

II.6.2.b.ii Determination of the phase transition frequency ratio

In order to determine precisely the phase transition ratio for each N_{ion} , the oscillation frequency of the central ion is recorded for each value of $\wp > \wp_{tr}$ and extrapolated to zero frequency (at which point $\wp = \wp_{tr}$)—see Fig. II.6.5. For the three sizes of pancake we considered, simulations at \wp_{tr} support its determination as, for each of the cases, the central ion's motion is ballistic after the kick.

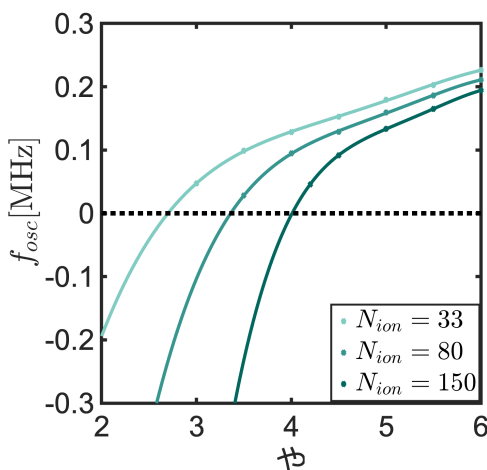


Figure II.6.5: Central ion oscillation frequency f_{osc} after a z -kick as a function of the trap frequency ratio \wp . The simulations were conducted for pancakes cooled down to $T_{target} = 0.01$ mK, and kicked with $T_{kick} = 0.1$ mK. In light green: 33 ion pancake; in green: 80 ion pancake; in dark green: 150 ion pancake. Circles: simulation points; solid lines: polynomial fits. The $f_{osc} = f(\wp)$ curves were fitted to a fourth order polynomial function as it provided the best precision without showing signs of overfitting. The point at which the curves each cross the x axis (dashed black line) corresponds to the extrapolated phase transition frequency ratio.

II.6.2.c Stability region

Our investigation of the phase transition from 3D crystal to pancake seems to contradict the predictions made in Ref. [85] as the trap frequencies at which the transition takes place are closer to the micromotion-free model from Ref. [87] (see Table **II.6.1**) instead⁹. These observations suggest that the possibly destabilizing effect of the micromotion has very little influence on the phase transition in our case.

However additional points of comparison would be necessary in order to confirm this trend—by theoretically determining the phase transition for a broader ion number range of magic configuration pancakes, for instance.

N_{ion}	\wp_{MD}	\wp_{F}	\wp_{D}
33	2.7	2.9	3.9
80	3.4	3.7	5.0
150	4.0	4.3	6.0

Table II.6.1: MD Simulated phase transition frequency ratios \wp_{MD} compared to the micromotion-free ratios \wp_F calculated with the model described in Ref. [87], and micromotion-destabilized ratios \wp_D obtained in Ref. [85].

These results could not be tested experimentally in the course of this work, which would be the next natural investigation step.

⁹The transition frequency ratios are found to be well described by the micromotion-free model in Ref. [85] as well.

Conclusion

A novel cooling technique for trapped ions minimizing the effects of micromotion, inherent to the design of linear Paul traps, was developed and optimized using Coulomb crystals formed by $^{40}\text{Ca}^+$ ions. Micromotion is a driven motion of the ions in the radial plane due to the oscillating radio-frequency field essential for trapping, and if excited it reduces the efficiency of the cooling. For that reason, an axial cooling along the trap axis is often preferred. In the case where the experimental design only allows for one cooling beam at 45° with respect to the axis, micromotion excitation is unavoidable. Such a setup was considered. Pulsed cooling was shown to cool down three dimensional Coulomb crystals to lower temperatures (≈ 7 mK for 555 ions) than the continuous cooling scheme (≈ 15 mK). It was also shown to allow the efficient cooling of structures highly susceptible to micromotion such as large 3D crystals (several thousands of ions) or 2D discs in the radial plane—pancakes, which could not be formed with a continuous 45° cooling beam.

However, the properties of the pulsed cooling were not fully understood and this calls for a theoretical description of the process, *e.g.* by studying the cooling dynamics through the solutions to the optical Bloch equations. Pulsed cooling will be a valuable tool for the experimental study of the 3D–2D pancake phase transition that was investigated theoretically in the course of this work. Its range of application goes well beyond the scope of investigations conducted in this study, as it can be used for cooling any system presenting an oscillatory driven motion.



PART III:
THEORETICAL PERSPECTIVE
– POWERING A QUANTUM
THERMOELECTRIC ENGINE



III.A POWERING A QUANTUM THERMOELECTRIC ENGINE BY HEAT BATHS

Introduction

Quantum thermodynamics is a hotbed of eager investigation as it both addresses the issues arising from the constant miniaturization of industrial devices, the development of the quantum computer—where heat conduction is of great interest [89–91], and provides understanding to the quantum contributions involved in thermodynamic processes [92–95] aiming to reconcile the microscopic and the macroscopic realms [91, 96–100]. These investigations have been supported by various theoretical realizations of quantum thermal machines such as the three-level heat pump [101], the noise-driven quantum absorption refrigerator [102], or thermal valves [103]. In the case of quantum engines, the information on the generated work has been obtained through several designs of the working body, *e.g.* as a harmonic oscillator [104] or an infinite ladder [105]. Experimental realizations of quantum thermal machines have been achieved using, for instance, trapped ions [106, 107]. However, the possibilities for the design of such machines are not limited to the listed options [108] and one exciting proposal is the thermoelectric engine where heat is converted into an electric current. In such a setup, the work is directly measurable in terms of current which allows for experimental verification of theoretical predictions. Thermoelectric engines have been previously investigated on the nanoscale [109, 110] as well as on the microscale [111] where in a circuit QED thermoelectric engine an electric current is being driven by excitation transfer between superconducting resonators in contact with separate heat baths.

As in classical thermodynamics, work and heat are not state functions but process quantities, defined by the exchange of energy between the engine and its environment. For transient processes of finite duration, this has led to definitions of work and heat that refer explicitly to the Hamiltonian and dissipative parts of the system evolution [12, 13], while generalizations to the quantum regime of classical fluctuation theorems [96, 112–117] have employed measurement statistics [118, 119] and quantum trajectory dynamics [120–122].

We constructed a simple autonomous thermoelectric engine operated out of thermal equilibrium—due to its constant coupling to baths with different temperatures—based on the models proposed in Refs. [105, 111]: two qubits, each coupled to a thermal bath are connected *via* a Josephson junction [123] (see Fig. **III.A.2.1** for a schematic representation of the system). In ideal conditions, the heat is transferred from the hot qubit (acting as a heat source) to the cold qubit (heat sink), and work is produced at the junction in the form of an electrical current. We study the dynamics of the machine by solving the Gorini-Kossakowski-Lindblad-Sudarshan (GKLS) master equation [124–126]. The bareness of the system allowed us to derive analytical expressions for the Hamiltonian and steady-state solution of the master equation. For this system, work and heat are exchanged with the environment with mean rates that we can express by steady state expectation values of suitable system observables. Fluctuations in the integrated work and heat over finite time intervals are not simply the variances of the same observables but employ more complex quantum correlation functions. In particular, we showed that the transfer of heat into the cold bath is equivalent to the process of spontaneous emission from a quantum light source, and its temporal correlations thus follow from Glauber’s photodetection theory [127] in quantum optics. Finally, we went beyond the steady state properties of the engine and studied the conditional dynamics of the excitation propagating through the system by way of two-time correlation functions [128, 129] and using the Quantum Regression Theorem (QRT) [130]. They reveal a cyclical, dynamical transfer of energy mimicking the chuffing of a classical steam engine.

This part is organized as follows. In Chapter III.A.2, the system is presented and optimized in steady state. Specifically, in Sec. III.A.2.1, the Hamiltonian of the system and the master equation are derived; in Sec. III.A.2.2, it is characterized and optimized in steady state. In Chapter III.A.3, the work and heat of the engine are derived: Sec. III.A.3.1 describe their average values in steady state, Sec. III.A.3.2 investigates their fluctuations and Sec. III.A.3.3 concludes with a comparison between

work and heat. Chapter III.A.4 focuses on the dynamics of the energy transfer. In Sec. III.A.4.1 the strokes of the engine are revealed by selected two-time correlation functions and Sec. III.A.4.2 shows the more complex dynamics features arising from higher-order correlations. Finally, a conclusion to the heat bath powered quantum thermoelectric engine is offered in Chapter III.A.5.

Unless stated otherwise, $\hbar = 1$ throughout. The relevant frequencies are either expressed in Hz or in rad/s and in the latter they are denoted $2\pi \times [\text{Hz}]$. The notation α is used to indicate the unspecified $\{c \equiv \text{cold}, h \equiv \text{hot}\}$ case for the relevant properties. The subscript ss is used to denote that the density matrix is taken in its steady state. In the case of correlation functions, it indicates that the system is in steady state at the earliest time.

Some of the material and discussions in this section were adapted from Ref. [1].

System overview and optimization

The system we conduct our investigations on is based on the minimal quantum heat engine proposed by Popescu [105] where the work obtained by excitation transfer between two qubits in contact with separate heat baths is used to excite an ancillary ladder system. In our system (see Fig. III.A.2.1 for a schematic representation), the ladder is replaced by a voltage biased Josephson junction following the oscillator based experimental proposal for a quantum thermoelectric engine presented in [111]. The presence of the junction allows for the production of electrical work that can be measured or used to charge a battery providing the voltage bias V , for instance, and offers an interesting implementation option. Although our work was based on this specific architecture for concreteness, the analysis we conducted can be applied to other engine designs.

III.A.2.1 System Hamiltonian and Master equation

III.A.2.1.a Hamiltonian in the rotating wave approximation

Following the same procedure as Hofer *et al.* in Ref. [111], we obtain the two qubit Hamiltonian [123, 131]:

$$\begin{aligned} \hat{H} = & \hbar\omega_h\hat{\sigma}_h^+\hat{\sigma}_h^- + \hbar\omega_c\hat{\sigma}_c^+\hat{\sigma}_c^- & \text{(III.A.2.1)} \\ & -E_J\cos(2eVt + 2\lambda_h(\hat{\sigma}_h^+ + \hat{\sigma}_h^-) + 2\lambda_c(\hat{\sigma}_c^+ + \hat{\sigma}_c^-)) \end{aligned}$$

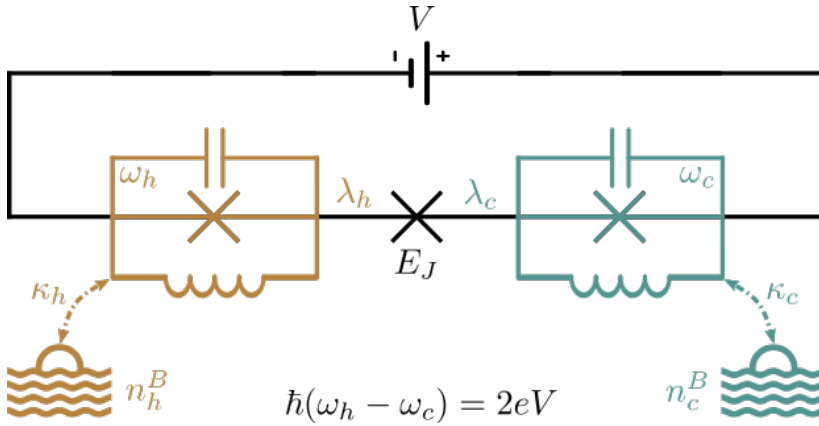


Figure III.A.2.1: Schematic representation of a two-qubit engine powered by heat baths and performing work by resonant tunneling of Cooper pairs against a bias voltage V . Excitation transfer between the qubits is mediated by a tunneling current with Josephson oscillations tuned to the difference $2eV = \hbar(\omega_h - \omega_c)$ between the qubit excitation energies. The qubits are coupled to the Josephson junction with constants $\lambda_{h,c}$ and to bosonic heat baths with average excitation numbers $n_{h,c}^B$, with rates $\kappa_{h,c}$.

where $\hat{\sigma}_h^+$ [$\hat{\sigma}_c^+$] and $\hat{\sigma}_h^-$ [$\hat{\sigma}_c^-$] are the Pauli spin operators exciting and de-exciting the hot [cold] qubit with oscillation frequency ω_h [resp. ω_c], E_J is the energy of the junction, V is the bias voltage across the junction, and λ_h [λ_c] is the coupling constant of the hot [cold] qubit to the junction. Changing to a rotating frame at the Josephson oscillation frequency and using the Baker-Campbell-Hausdorff formula, we employed the rotating wave approximation and retained only terms representing resonant excitation transfer between the two qubits (see Appendix A for details of the derivation):

$$\hat{H}_{RWA} = \frac{E_J}{2} \sin(2\lambda_h) \sin(2\lambda_c) (\hat{\sigma}_h^- \hat{\sigma}_c^+ + \hat{\sigma}_h^+ \hat{\sigma}_c^-). \quad (\text{III.A.2.2})$$

The resonance condition, $\hbar(\omega_h - \omega_c) = 2eV$, ensures that for each quantum of excitation being transferred from the hot to the cold qubits a Cooper pair of charge $2e$ passes across the junction, *i.e.* against the voltage difference V [132]. Due to the coupling of the qubits to their respective heat baths, the hot qubit is excited and energy from the cold qubit is

dissipated sustainably. Thus, the qubit cycle is autonomous and the system is described by a density matrix with a time independent master equation.

III.A.2.1.b GKLS master equation

The density operator for the two qubit system can be expressed in the joint basis $|i_h\rangle \otimes |k_c\rangle \in \mathbb{H} \otimes \mathbb{C}$ —where \mathbb{H} [resp. \mathbb{C}] represents the ensemble of hot [cold] qubit eigenvectors. It can be written as [133]:

$$\begin{aligned}\hat{\rho}_{hc} &= \sum_{i,j,k,,l} \rho_{ijkl} (|i_h\rangle \otimes |k_c\rangle) (\langle j_h| \otimes \langle l_c|) \\ &= \sum_{i,j,k,l} \rho_{ijkl} |i_h\rangle \langle j_h| \otimes |k_c\rangle \langle l_c|\end{aligned}\quad (\text{III.A.2.3})$$

with $\rho_{ijkl} = \langle i_h k_c | \rho_{hc} | j_h l_c \rangle$. In matrix form, it can be written as:

$$\rho_{hc} = \begin{array}{c} |00\rangle \\ |01\rangle \\ |10\rangle \\ |11\rangle \end{array} \begin{pmatrix} \langle 00| & \langle 01| & \langle 10| & \langle 11| \\ \rho_{0000} & \rho_{0001} & \rho_{0100} & \rho_{0101} \\ \rho_{0010} & \rho_{0011} & \rho_{0110} & \rho_{0111} \\ \rho_{1000} & \rho_{1001} & \rho_{1100} & \rho_{1101} \\ \rho_{1010} & \rho_{1011} & \rho_{1110} & \rho_{1111} \end{pmatrix}. \quad (\text{III.A.2.4})$$

The density operator possesses a few notable properties [133]:

1. $\hat{\rho}$ is Hermitian: $\hat{\rho}^\dagger = \hat{\rho}$ and $\rho_{ijkl}^* = \rho_{jilk}$.
2. $\hat{\rho}$ is positive semidefinite: for any state $|O\rangle$, $\langle O | \hat{\rho} | O \rangle \geq 0$ —all eigenvalues of $\hat{\rho}$ are positive or zero.
3. $\text{Tr}[\hat{\rho}] = 1$.
4. $\text{Tr}[\hat{\rho}^2] \leq 1$ with equality for a pure state.

Expressing the spin operators in the joint basis: $\hat{\sigma}_h^\pm \equiv \hat{\sigma}_h^\pm \otimes \mathbb{1}_C$ and $\hat{\sigma}_c^\pm \equiv \mathbb{1}_H \otimes \hat{\sigma}_c^\pm$, we make the Born-Markov approximation—assuming the baths to be memoryless, with timescales much shorter than system's, and for bath and system states to be initially separable [134]—and obtain the conventional Gorini-Kossakowski-Lindblad-Sudarshan (GKLS) master

equation with coupling to the thermal baths [124–126] (a detailed derivation can be found in Refs. [135, 136]):

$$\frac{d\hat{\rho}(t)}{dt} = -i[\hat{H}_{RWA}, \hat{\rho}(t)] + \mathcal{L}_B\hat{\rho}(t), \quad (\text{III.A.2.5})$$

where the dissipative interaction with the heat baths is given by:

$$\begin{aligned} \mathcal{L}_B\hat{\rho}(t) = & \sum_{\alpha=c,h} \kappa_\alpha (n_\alpha^B + 1) \\ & \times \left(\hat{\sigma}_\alpha^- \hat{\rho}(t) \hat{\sigma}_\alpha^+ - \frac{1}{2} (\hat{\sigma}_\alpha^+ \hat{\sigma}_\alpha^- \hat{\rho}(t) + \hat{\rho}(t) \hat{\sigma}_\alpha^+ \hat{\sigma}_\alpha^-) \right) \\ & + \kappa_\alpha n_\alpha^B \\ & \times \left(\hat{\sigma}_\alpha^+ \hat{\rho}(t) \hat{\sigma}_\alpha^- - \frac{1}{2} (\hat{\sigma}_\alpha^- \hat{\sigma}_\alpha^+ \hat{\rho}(t) + \hat{\rho}(t) \hat{\sigma}_\alpha^- \hat{\sigma}_\alpha^+) \right). \end{aligned} \quad (\text{III.A.2.6})$$

with κ_α (with $\alpha = \{h, c\}$) denoting the energy damping rate associated with the bath α and n_α^B the bath occupation number. The baths are assumed to be thermal bosonic heat baths, thus the occupation number of bath α is given by: $n_\alpha^B = 1/(e^{\frac{\omega_\alpha}{k_B T_\alpha}} - 1)$ (with k_B the Boltzmann constant) [137]. The second term accounts for the existence of quanta that the qubit can absorb from its respective bath and become excited and the first term for the possibility for the qubit to, once excited, decay by a spontaneous emission process stimulated by the bath.

In steady state Eq. (III.A.2.5) reduces to $\frac{d\hat{\rho}(t)}{dt} = 0$ and we derive the analytical solution.

III.A.2.2 System characterization and optimization

III.A.2.2.a Engine output power

III.A.2.2.a.i Current operator

In order to analyze the performance of the engine, the electrical work produced at the junction needs to be derived. The work generated during a time \mathcal{T} can be naturally defined as the product of the voltage and the accumulated electrical charge transferred through the Josephson junction $Q(\mathcal{T})$, given by the integral of the electrical current going through the

junction over the given time. The production of current being due to the deexcitation of the hot qubit inducing a charge transfer of $2e$ at the junction and the concomitant excitation of the cold qubit, the current through the junction is given by $2e$ multiplied with the rate of change of the cold qubit excited state population due to the commutator with the Hamiltonian (Eq. (III.A.2.2)). Thus, we define the current operator as:

$$\begin{aligned}\hat{I} &= \frac{2e}{i\hbar}[\hat{\sigma}_c^+\hat{\sigma}_c^-, \hat{H}_{RWA}] \\ &= -ieE_J \sin(2\lambda_h) \sin(2\lambda_c)(\hat{\sigma}_h^-\hat{\sigma}_c^+ - \hat{\sigma}_h^+\hat{\sigma}_c^-).\end{aligned}\tag{III.A.2.7}$$

In the case $\kappa_h = \kappa_c = \kappa$, we derive an analytical expression for the steady state expectation value of the current (see Appendix B for details of the derivation):

$$\begin{aligned}\langle \hat{I} \rangle_{ss} &= \frac{e}{(n_h^B + n_c^B + 1)} \\ &\quad \times \frac{n_h^B - n_c^B}{\left[\frac{1}{\kappa} + \frac{\kappa}{(E'_J)^2} (2n_c^B + 1)(2n_h^B + 1) \right]}\end{aligned}\tag{III.A.2.8}$$

with $E'_J = E_J \sin(2\lambda_h) \sin(2\lambda_c)$.

III.A.2.2.a.ii Power optimization

In the following, we restrict ourselves to the case $\kappa_h = \kappa_c = \kappa$ for consistency¹.

The average output power of the engine can be readily evaluated from Eq. (III.A.2.8):

$$P = \langle \hat{I} \rangle_{ss} V.\tag{III.A.2.9}$$

In watts, it reads:

$$P[\text{Watt}] = \frac{\langle \hat{I} \rangle_{ss}}{2\pi} \frac{\hbar(\omega_h - \omega_c)}{2e}\tag{III.A.2.10}$$

where we divide the current by 2π in order to express it in amperes.

¹If the couplings to the baths are different on both sides, the simulated current cannot be compared to the analytically derived steady state value. Nonetheless this asymmetric situation can be implemented.

Using the operation parameters from Ref. [111] as a starting point, we optimize the engine's properties for maximal output power: Table **III.A.2.1** shows the optimized parameters.

Optimal couplings to baths and to the Josephson junction

From Eq. (III.A.2.8) we can see that $\langle \hat{I} \rangle_{ss} \propto [\sin(2\lambda_h) \sin(2\lambda_c)]^2$. Therefore the optimal values for the coupling parameters to the Josephson junction would be $\lambda_h = \lambda_c = \pi/4$. This reflects the fact that the more efficient the energy transfer from the qubits is, the more power can be produced at the junction. However, the dependence on κ is not as straightforward, as the current is a function of the $\kappa/\sin(2\lambda)$ ratio.

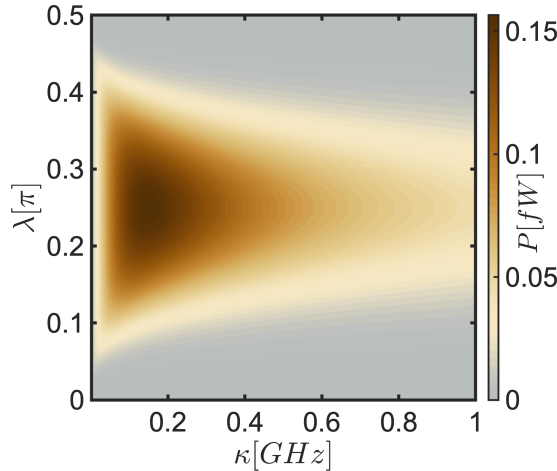


Figure III.A.2.2: Steady state output power of the engine as a function of the bath coupling constant κ and qubit coupling to the Josephson junction λ . The system parameters are based on Ref. [111]: $E_J = 2\pi \times 0.3$ GHz, $\omega_h = 2\pi \times 13.5$ GHz, $\omega_c = 2\pi \times 3.0$ GHz, $n_h^B = 1.5$, $n_c^B = 0$. The maximum power, $P_{max}^{\kappa, \lambda} = 0.16$ fW, is reached for $\lambda = \pi/4$ and $\kappa = 2\pi \times 0.151$ GHz.

The steady state power of the engine calculated for a range of κ and λ ($= \lambda_h = \lambda_c$) is shown in Fig. **III.A.2.2**. As a function of the coupling strength κ , the output power reaches a maximum value and decreases for

stronger couplings to the baths. This is due to the fact that a stronger coupling to the baths suppresses the qubit coherence responsible for the excitation transfer. The maximum power, $P_{max}^{\kappa,\lambda} = 0.16$ fW, is reached for $\kappa = 2\pi \times 0.151$ GHz and, as previously shown, $\lambda = \pi/4$.

Optimal bath properties

In the case of a classical thermal engine, the critical factor is the temperature difference between the heat source and sink, resulting in a continuous transfer of energy. In our situation, the temperatures of the baths have to be normalized by the oscillation frequency of the corresponding qubits as the excitation transfer is quantized. Therefore, the key factor for our engine is the bath occupation number that encompasses those properties, as it can be seen in Eqs. (III.A.2.8). We recall:

$$n_{\alpha}^B = 1/(e^{\frac{\omega_{\alpha}}{\kappa_B T_{\alpha}}} - 1) \quad (\text{III.A.2.11})$$

Setting κ and λ to their previously optimized values, the optimal bath occupation numbers are found to be $n_h^B = 1.5$ and $n_c^B = 0$. The situation where $n_c^B = 0$ corresponds to $T_c = 0$ K, hence the cold bath is an ideal heat sink.

Engine operation parameters

The optimal operation parameters are summarized in Table **III.A.2.1**. They are used throughout our investigations, unless stated otherwise.

κ [GHz]	λ	E_J [GHz]	n_h^B	T_h [K]	ω_h [GHz]	n_c^B	T_c [K]	ω_c [GHz]
0.151	$\pi/4$	0.3	1.5	1.26835	13.5	0	0	3.0

Table III.A.2.1: Optimized engine parameters.

III.A.2.2.a.iii Engine efficiency

The evolution of the qubit occupation number is given by:

$$\frac{d\langle \hat{n}_{\alpha}(t) \rangle}{dt} = -i\langle [\hat{n}_{\alpha}, \hat{H}_{RWA}] \rangle + \kappa_{\alpha}(n_{\alpha}^B - (2n_{\alpha}^B + 1)\langle n_{\alpha} \rangle) \quad (\text{III.A.2.12})$$

The first term in Eq. (III.A.2.12) corresponds to the coupling to the rest of the quantum system and the second term, to the excitation flux from the heat bath. The qubit and respective bath can in our case exchange one quantum of energy ω_α . Therefore, the mean heat current provided by the bath α is given by:

$$J_\alpha = \omega_\alpha \kappa_\alpha \left(n_\alpha^B - (2n_\alpha^B + 1) \langle n_\alpha \rangle \right), \quad (\text{III.A.2.13})$$

and in steady state:

$$\begin{aligned} \frac{J_\alpha}{\omega_\alpha} &= i \langle [\hat{n}_\alpha, \hat{H}_{RWA}] \rangle \\ &= \epsilon_\alpha \frac{\langle \hat{I} \rangle_{ss}}{2e} \end{aligned} \quad (\text{III.A.2.14})$$

with: $\epsilon_\alpha = \begin{cases} +1 & \text{if } \alpha \equiv h \\ -1 & \text{if } \alpha \equiv c \end{cases}$.

In order to be expressed in watts, the heat current should be calculated from:

$$J_\alpha [\text{Watt}] = \epsilon_\alpha \frac{\hbar \omega_\alpha}{2\pi} \frac{\langle \hat{I} \rangle_{ss}}{2e} \quad (\text{III.A.2.15})$$

The efficiency *eta* of the engine converting heat from the hot qubit into electrical work at the junction is given by:

$$\eta = \frac{P}{J_h} = 1 - \frac{\omega_c}{\omega_h}$$

In order to probe the performance of our engine, we calculate its efficiency η for a range of frequency ratios ω_h/ω_c and compare it to the classical Carnot efficiency limit $\eta_c = 1 - \frac{T_h}{T_c}$ [138]. The qubit engine works at the Carnot maximal efficiency when $\omega_h/\omega_c = T_h/T_c$ (see Fig. **III.A.2.3**).

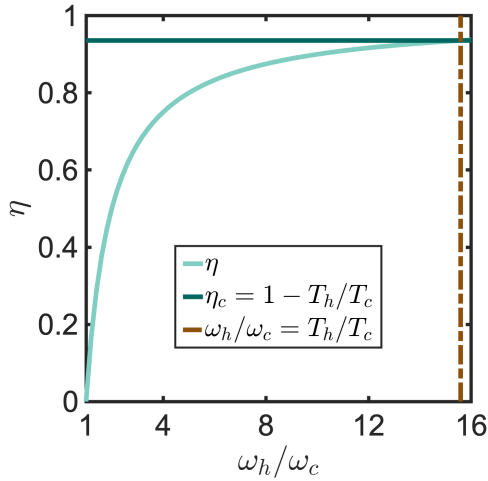


Figure III.A.2.3: Engine efficiency as a function of the hot and cold qubit frequency ratio ω_h/ω_c , in light green. In dark green, the Carnot limit $\eta_c = 1 - \frac{T_h}{T_c}$. In dashed brown, the case $\omega_h/\omega_c = T_h/T_c$. The efficiency η was calculated from the analytical solution to the steady state master equation with usual system parameters (see Table III.A.2.1). The numerical integration converges to the same values.

III.A.2.2.b Engine directionality

As mentioned in Sec. III.A.2.2.a.ii, the key factor for our engine's performance is the bath occupation number. Indeed, the presence of the term $(n_h^B - n_c^B)$ in the expression of the steady state current given in Eq. (III.A.2.8) indicates that the directionality of the engine is governed by the bath occupation number difference. This property can be seen in Fig. III.A.2.4 where the power output is symmetric with respect to $n_c^B = n_h^B$. Our engine is therefore capable of producing negative current in the case $n_h^B < n_c^B$.

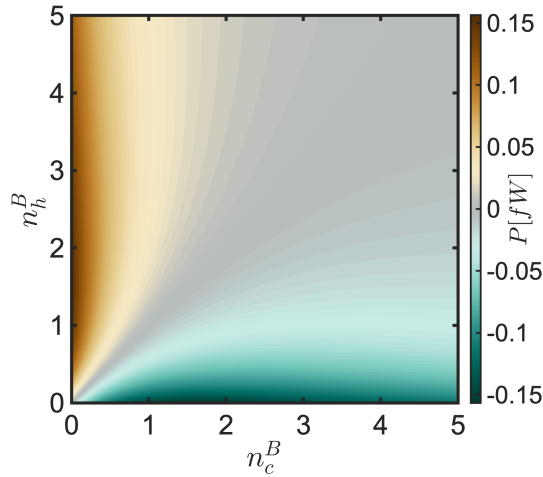


Figure III.A.2.4: Engine output power as a function of cold, n_c^B , and hot, n_h^B , bath occupation numbers. It was calculated from the analytical solution to the steady state master equation with $\lambda = \pi/4$, $\kappa = 2\pi \times 0.151$ GHz, and the other system parameters as in Fig. III.A.2.2. The numerical integration converges to the same values. The maximum power, $P_{max}^{n_h^B, n_c^B} = 0.16$ fW, is obtained for $n_h^B = 1.5$ and $n_c^B = 0$.

Work and heat—mean values and fluctuations

A well suited parameter to analyze the performance of a thermal machine is the work it can produce, compared to the heat it was provided. In the case of a classical engine, from the definition of the work as the difference in free energy for a quasistatic process [139], numerous developments have been made in order to quantify its fluctuations in the case of a transformation out of equilibrium [96, 112, 140–142]. In the case of a quantum mechanical system, the derivation of these fluctuations is more cumbersome, as the definition of work in this setting is in itself not straightforward. A few options are available: to define a work operator and treat it as an observable of the system [143] or to define work as the difference between two outcomes of energy difference measurements [92, 144] and derive a work distribution function [145] (see Ref. [13] for a comparison of these methods).

We focus our analysis on the mean values and fluctuations of the integrated electrical work and heat exchanged with a cold bath of vanishing temperature $n_c^B = 0$. Work and heat are defined by the accumulated effects of coherent and incoherent processes involving the engine quantum system and its environment, respectively. While their average rates can be expressed by steady state expectation values of chosen system observables, the derivations of their fluctuations is more complex as it involves quantum correlation functions. In addition, we show that the transfer of heat into the cold bath was equivalent to the process of spontaneous emission from a quantum light source and thus follows Glauber’s photodetection theory [127].

III.A.3.1 Steady state average values

The populations of the qubit states being constant in steady state, their rate of change due to dissipation is the exact opposite of their rate of change due to the Hamiltonian term in Eq. (III.A.2.12). The rate at which the cold qubit loses excitation is therefore equal to both the rate of transfer of Cooper pairs across the junction and the net rate of excitation of the hot qubit made available to the rest of the system (*i.e.* excluding the excitation–deexcitation processes through the coupling to the hot bath). Thus, the total energy is conserved and the total heat transfer from the hot bath equals the sum of the work and the heat delivered to the cold bath.

III.A.3.1.a Average work produced by the engine

For a system operating in steady state, the average work produced by the engine during an operation time \mathcal{T} can be directly derived from the output power (Eq. (III.A.2.9)):

$$W(\mathcal{T}) = \langle \hat{I} \rangle_{ss} V \mathcal{T}. \quad (\text{III.A.3.1})$$

III.A.3.1.b Average heat transferred to the cold bath

The heat transfer between the qubits and their respective baths is determined by the rate of change of the excited state populations due to the dissipative terms in the master equation (III.A.2.5, III.A.2.6). In the case of the cold bath of vanishing temperature considered here—where the cold qubit cannot be re-excited by its bath—the mean rate of quanta dissipated by the cold qubit equals $\kappa \langle \hat{\sigma}_c^+ \hat{\sigma}_c^- \rangle$ and the corresponding power dissipated as heat is given by $\hbar \omega_c \kappa \langle \hat{\sigma}_c^+ \hat{\sigma}_c^- \rangle$. Therefore, the average heat transferred into the cold bath during a time \mathcal{T} is given by:

$$Q_c(\mathcal{T}) = \hbar \omega_c \langle \hat{\sigma}_c^+ \hat{\sigma}_c^- \rangle \kappa \mathcal{T}. \quad (\text{III.A.3.2})$$

III.A.3.2 Fluctuations

III.A.3.2.a Work fluctuations

In order to derive the fluctuations of the work done by the engine, we introduce an operator expression for the work generated over a time interval \mathcal{T} :

$$\hat{W}(\mathcal{T}) = V \int_0^{\mathcal{T}} \hat{I}(t) dt. \quad (\text{III.A.3.3})$$

The mean value in Eq. (III.A.3.1) can be recovered from this expression by assuming the system to be in steady state throughout the integration time \mathcal{T} and evaluating it in the Schrödinger picture by transferring the time dependence of the Heisenberg picture current operator to the constant steady state density matrix.

We can then derive the variance of the work using the customary definition:

$$\text{Var}[W(\mathcal{T})] = \langle \hat{W}(\mathcal{T})^2 \rangle - \langle \hat{W}(\mathcal{T}) \rangle^2. \quad (\text{III.A.3.4})$$

The first term in this equation can be written explicitly as:

$$\begin{aligned} \langle \hat{W}(\mathcal{T})^2 \rangle &= V^2 \left\langle \left(\int_0^{\mathcal{T}} \hat{I}(t) dt \right) \left(\int_0^{\mathcal{T}} \hat{I}(t') dt' \right) \right\rangle \\ &= V^2 \int_0^{\mathcal{T}} \int_0^{\mathcal{T}} \langle \hat{I}(t) \hat{I}(t') \rangle dt dt'. \end{aligned} \quad (\text{III.A.3.5})$$

For t, t' , and $|t - t'|$ larger than a few κ^{-1} , the correlations reach their infinite time limit and, according to the Quantum Regression Theorem (QRT) [130], the correlation function $\langle \hat{I}(t) \hat{I}(t') \rangle$ factorizes as $\langle \hat{I} \rangle_{ss}^2$. Assuming $\mathcal{T} \gg \kappa^{-1}$, we can rewrite the double integral as \mathcal{T} multiplied with the integral of the steady state correlation function over the time difference $\tau = t' - t$, for which the upper limit can be taken to infinity (see Appendix C for the detail of the derivation). The work variance is then given by:

$$\text{Var}[W(\mathcal{T})]_{\infty} = 2\mathcal{T}V^2 \int_0^{\mathcal{T}} \left[\mathcal{R}e \left(\langle \hat{I}(t) \hat{I}(t + \tau) \rangle_{ss} \right) - \langle \hat{I} \rangle_{ss}^2 \right] d\tau. \quad (\text{III.A.3.6})$$

The two-time correlation function is evaluated with the quantum regression theorem (see Sec. III.A.3.2.c) [130].

III.A.3.2.b Heat fluctuations

III.A.3.2.b.i Derivation procedure

Since the emission of quanta into the cold bath is an incoherent process governed by a rate, the number of quanta emitted into the cold bath during a time \mathcal{T} is a stochastic variable. We can simulate the continuous detection of the arrival of quanta in the cold bath and assess the counting statistics of such a hypothetical experiment by a quantum jump stochastic master equation [146, 147]. The cold bath is thus acting as a photodetector for the quanta emitted by deexcitation of the cold qubit. Therefore, the statistics of the heat emission are subject to Glauber's photodetection theory [127] (see Appendix E for a brief introduction) and the heat fluctuations are intimately related to the way that detection disturbs the steady state and induces conditional transient dynamics (see Sec. III.A.3.2.c).

III.A.3.2.b.ii Heat variance

In order to calculate the fluctuations of the heat dissipated into the cold bath, based on our previously described assumption on the heat detection process, we define $\mathcal{N}_c(\mathcal{T})$, the integrated number of quanta arriving in the cold bath during \mathcal{T} :

$$\mathcal{N}_c(\mathcal{T}) = \int_0^{\mathcal{T}} \hat{N}_c(t) dt \quad (\text{III.A.3.7})$$

where $\hat{N}_c(t) = (\hat{a}_c^\dagger \hat{a}_c)(t)$ is the field operator for the cold bath counting the arriving quanta from the cold qubit. In the Heisenberg picture the field annihilation operator can be expressed by the emitter lowering operator, and the probability of detecting one quantum is proportional to [127, 148, 149]:

$$\langle \hat{N}_c \rangle = \kappa_c \langle \hat{n}_c \rangle \quad (\text{III.A.3.8})$$

For a two-click detection event at times t and t' (with $t' \geq t$), the probability is given by the normal- and time-ordered expression [127]:

$$G^2(t, t') = \langle \hat{a}_c^\dagger(t) \hat{a}_c^\dagger(t') \hat{a}_c^-(t') \hat{a}_c^-(t) \rangle \quad (\text{III.A.3.9})$$

and is proportional to the two-event emission probability:

$$G^2(t, t') = \kappa^2 \langle \hat{\sigma}_c^+(t) \hat{\sigma}_c^+(t') \hat{\sigma}_c^-(t') \hat{\sigma}_c^-(t) \rangle. \quad (\text{III.A.3.10})$$

The fluctuations of such a detection process are given by:

$$\text{Var}[\mathcal{N}_c(\mathcal{T})] = \langle \mathcal{N}_c(\mathcal{T})^2 \rangle - \langle \mathcal{N}_c(\mathcal{T}) \rangle^2. \quad (\text{III.A.3.11})$$

They were derived following Refs. [150, 151] (see Appendix D).

The variance of the heat dissipated into the cold bath during a time \mathcal{T} is proportional to the detection fluctuations, with the energy carried by each quantum of heat $\hbar\omega_c$ constant, hence, for long time intervals \mathcal{T} , the variance is given by:

$$\begin{aligned} \text{Var}[Q_c(\mathcal{T})]_\infty = (\hbar\omega_c)^2 \left(2\kappa^2 \mathcal{T} \int_0^{\mathcal{T}} \left[\langle \hat{\sigma}_c^+(t) \hat{\sigma}_c^+(t+\tau) \hat{\sigma}_c^-(t+\tau) \hat{\sigma}_c^-(t) \rangle_{ss} \right. \right. \\ \left. \left. - \langle \hat{\sigma}_c^+(t) \hat{\sigma}_c^-(t) \rangle_{ss}^2 \right] d\tau \right. \\ \left. + \kappa \mathcal{T} \langle \hat{\sigma}_c^+(t) \hat{\sigma}_c^-(t) \rangle_{ss} \right). \end{aligned} \quad (\text{III.A.3.12})$$

where the system is taken in steady state at the earlier time t .

Similarly to the work variance, the steady state fluctuations of the heat dissipated into the cold bath involve the two-time correlation function for the detection of quanta arriving into the cold bath, which we evaluate using the QRT [130], as described in the next section.

III.A.3.2.c Calculation of two-time correlation functions

III.A.3.2.c.i Quantum Regression Theorem

In order to calculate the work and heat variances, the two-time correlation functions of the current and number of quanta emitted from the cold qubit need to be evaluated. This is done using the QRT [129, 130] which states that, for a system described by a density matrix and subject to the Born-Markov approximation, the two-time correlation function of an operator in the Heisenberg picture can be evaluated by applying the operator at an initial time t to the density matrix, then letting the system evolve using the master equation, and finally applying the same operator at the later time $t + \tau$. The correlation function is then the expectation value of the final operator obtained by this procedure. This procedure can be applied to any number of operators and times, as long as $t + \tau \geq t$.

In our derivation of the fluctuations and thus the two-time correlations we assume the system to be in steady state at the earliest time t and described by the steady state density matrix $\hat{\rho}_{ss}$.

III.A.3.2.c.ii Two-time correlations of the emission into the cold bath

In the case of heat fluctuations (Eq. (III.A.3.12)), the correlation function to be evaluated is:

$$F_{cc}^{(2)}(t, t + \tau) = \langle \hat{\sigma}_c^+(t) \hat{\sigma}_c^+(t + \tau) \hat{\sigma}_c^-(t + \tau) \hat{\sigma}_c^-(t) \rangle. \quad (\text{III.A.3.13})$$

Assuming that the system has reached steady state at the moment of first detection, it can be expressed as:

$$\begin{aligned} F_{cc}^{(2)}(t_{ss}, t_{ss} + \tau) &= \langle \hat{\sigma}_c^+(t) \hat{\sigma}_c^+(t + \tau) \hat{\sigma}_c^-(t + \tau) \hat{\sigma}_c^-(t) \rangle_{ss} \\ &= \langle \hat{\sigma}_c^+(t_{ss}) \hat{\sigma}_c^+(t_{ss} + \tau) \hat{\sigma}_c^-(t_{ss} + \tau) \hat{\sigma}_c^-(t_{ss}) \rangle \\ &= \text{Tr}[\rho_{ss} \hat{\sigma}_c^+(t_{ss}) \hat{\sigma}_c^+(t_{ss} + \tau) \hat{\sigma}_c^-(t_{ss} + \tau) \hat{\sigma}_c^-(t_{ss})] \\ &= \text{Tr}[\hat{\sigma}_c^-(t_{ss} + \tau) \hat{\sigma}_c^- \rho_{ss} \hat{\sigma}_c^+ \hat{\sigma}_c^+(t_{ss} + \tau)] \\ &= \text{Tr}[\hat{\sigma}_c^- \tilde{\rho}^c(t_{ss} + \tau) \hat{\sigma}_c^+] \\ &= \tilde{\rho}_{0011}^c(t_{ss} + \tau) + \tilde{\rho}_{1111}^c(t_{ss} + \tau) \end{aligned} \quad (\text{III.A.3.14})$$

where $\tilde{\rho}^c(t_{ss} + \tau)$ satisfies the master equation Eq. (III.A.2.5) and has the initial condition:

$$\tilde{\rho}^c(t_{ss}) = \hat{\sigma}_c^- \rho_{ss} \hat{\sigma}_c^+. \quad (\text{III.A.3.15})$$

The infinite time limit for the density matrix is given by the steady state density matrix multiplied by the expectation value of the cold qubit occupation number at the earliest time, which in our case is the steady state:

$$\lim_{\tau \rightarrow \infty} \tilde{\rho}^c(t_{ss} + \tau) = \langle \hat{\sigma}_c^+ \hat{\sigma}_c^- \rangle_{ss} \rho_{ss}, \quad (\text{III.A.3.16})$$

and, since the system is initially in steady state, the limit for the correlations is given by the steady state expectation value of the cold qubit occupation number multiplied by itself:

$$\lim_{\tau \rightarrow \infty} F_{cc}^{(2)}(t_{ss}, t_{ss} + \tau) = \langle \hat{\sigma}_c^+ \hat{\sigma}_c^- \rangle_{ss} \langle \hat{\sigma}_c^+ \hat{\sigma}_c^- \rangle_{ss}. \quad (\text{III.A.3.17})$$

It can be noted from this derivation that the fluctuations of the heat dissipated into the cold bath depend on the modification of the steady state by the detection process and the detection-induced conditional dynamics.

III.A.3.2.c.iii Two-time correlations of the current

The variance of the electrical work (Eq. (III.A.3.6)) requires the evaluation of

$$F_{II}^{(2)}(t, t + \tau) = \langle \hat{I}(t) \hat{I}(t + \tau) \rangle. \quad (\text{III.A.3.18})$$

Assuming that the system has reached steady state at the earliest time, it can be expressed as:

$$\begin{aligned} F_{II}^{(2)}(t_{ss}, t_{ss} + \tau) &= \langle \hat{I}(t + \tau) \hat{I}(t) \rangle_{ss} \\ &= -ieE_J \sin(2\lambda_h) \sin(2\lambda_c) \\ &\quad \times (\tilde{\rho}_{1001}^I(t_{ss} + \tau) - \tilde{\rho}_{0110}^I(t_{ss} + \tau)) \end{aligned} \quad (\text{III.A.3.19})$$

where $\tilde{\rho}^I(t_{ss} + \tau)$ satisfies the master equation Eq. (III.A.2.5) and has the initial condition:

$$\tilde{\rho}^I(t_{ss}) = \hat{I} \rho_{ss}. \quad (\text{III.A.3.20})$$

The corresponding infinite time limits are given by:

$$\lim_{\tau \rightarrow \infty} \tilde{\rho}^I(t_{ss} + \tau) = \langle \hat{I} \rangle_{ss} \rho_{ss} \quad (\text{III.A.3.21})$$

and:

$$\lim_{\tau \rightarrow \infty} F_{II}^{(2)}(t_{ss}, t_{ss} + \tau) = \langle \hat{I} \rangle_{ss}^2. \quad (\text{III.A.3.22})$$

III.A.3.3 Work and Heat—comparisons

III.A.3.3.a Work vs. Heat

For a cold bath of vanishing temperature, *i.e.* with $n_c^B = 0$, it is straightforward to see by combining Eqs. (III.A.2.12) and (III.A.2.8)—which lead to the relation $\langle \hat{\sigma}_c^+ \hat{\sigma}_c^-(t) \rangle_{ss} = \langle \hat{I}(t) \rangle_{ss} / (2e\kappa)^1$ —that the steady state mean values of the work produced by the engine $W(\mathcal{T})$ (Eq. (III.A.3.1)) and heat released into the cold bath $Q_c(\mathcal{T})$ (Eq. (III.A.3.2)) are equivalent up to the ratio of the microscopic energies (see Fig. **III.A.3.1a**):

$$Q_c(\mathcal{T}) = (\hbar\omega_c/2eV) W(\mathcal{T}). \quad (\text{III.A.3.23})$$

Although not as straightforward to infer, their variances for infinitely long time intervals ($\mathcal{T} \gg \kappa^{-1}$) are also proportional, with constant $(\hbar\omega_c/2eV)^2$.

Thus, we can conclude that in the case of an engine with a cold bath of vanishing temperature, the work produced by the machine and the heat transferred to the cold bath have equivalent mean values and variances for long operation times, despite their different origin in coherent and dissipative processes, and their quantitative properties being associated with direct operator integrals and measurement processes, respectively.

If the cold bath has a non-zero occupation number, the work and heat mean values and fluctuations diverge. This effect is due to the excitation-deexcitation processes between the cold qubit and its bath leading to cold quantum detection not stemming from the current generation process only. If we were to subtract the rates associated with these processes from the heat received by the cold bath, we would recover the long time limit convergence.

¹For the relation given for a cold bath of non-vanishing temperature, see Eq. (B.6) in Appendix B.

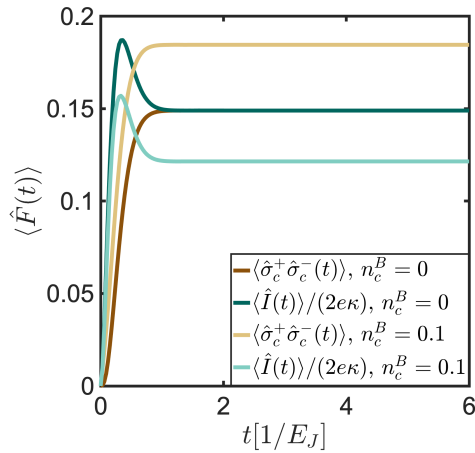


Figure III.A.3.1: Expectation values for the current, $\langle \hat{I}(t) \rangle$ (light and dark green lines), and cold qubit occupation number, $\langle \hat{\sigma}_c^+ \hat{\sigma}_c^- \rangle$ (yellow and brown lines), as functions of engine operation time t expressed in units of Josephson junction frequency $[1/E_J]$. $\hat{F}(t)$ is a generic notation for $\{\hat{I}(t), \hat{\sigma}_c^+ \hat{\sigma}_c^-(t)\}$. The solid lines are obtained by numerical integration of the master equation (Eq. (III.A.2.5)), for long operation times they reach their analytical steady state expectation values. The darker colored curves were obtained for $n_c^B = 0.1$, the lighter ones for $n_c^B = 0$. The other parameters are the usual working parameters from Table III.A.2.1. For $n_c^B = 0$ the steady state mean values of the current produced at the junction and of the cold qubit occupation number (dark green and brown curves, respectively) are proportional with constant $(2e\kappa)$, and consequently the mean values of the work produced by the engine and heat transferred to the cold bath are proportional up to the ratio of the microscopic excitation energies. For $n_c^B > 0$, the steady state mean values (light green and yellow curves) diverge due to excitation-deexcitation processes between the cold qubit and its bath.

III.A.3.3.b Heat vs. Heat

We compare the mean value and variance of the integrated number of quanta emitted into the cold bath, $\mathcal{N}_c(\mathcal{T}) = Q_c(\mathcal{T})/(\hbar\omega_c)$, in the situation where the cold bath occupation number is zero—see Fig. III.A.3.2.

It is interesting to note that $\mathcal{N}_c(\mathcal{T})$ exhibits the sub-Poissonian behavior characteristic of photon counting from a two-level emitter [152].

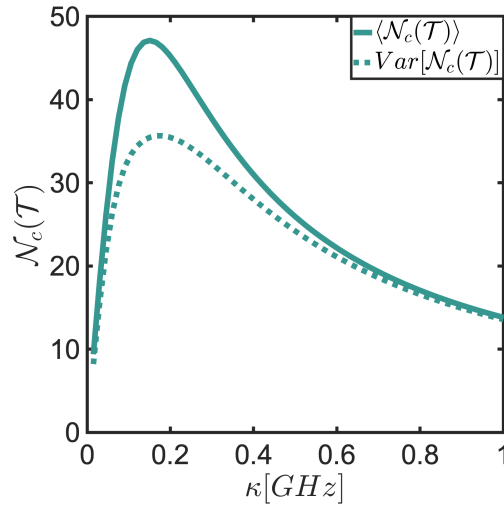


Figure III.A.3.2: Mean value and fluctuations of the number of quanta $\mathcal{N}_c(\mathcal{T}) = Q_c(\mathcal{T})/(\hbar\omega_c)$, transferred to the cold bath during a time interval, $\mathcal{T} = 100 \times (1/E_J)$, as function of κ with the usual system parameters from Table III.A.2.1. The excitation transfer count exhibits a sub-Poissonian behavior.

Dynamics of the energy transfer

In addition to being convenient tools for the derivation of work and heat fluctuations, multi-time correlation functions allow us to get an insight into the dynamics of the energy transfer in our thermoelectric engine and hence its properties beyond the steady state. Indeed, the multi-time correlation function can be seen as a function of the conditional evolution of our system, showing us how it evolves after we initiate its dynamics (see Ref. [153] for another example of the use of correlation functions as conditioned dynamics investigative tools). The two-time correlations of the current through the junction in combination with the heat absorption and emission events allow us to see the strokes of the machine, mimicking the chuffing of a classical steam engine, hiding underneath the steady state. Moreover, by investigating three-time correlations, we are able to peer even closer into the dynamics of the engine and show that they go beyond pure two-time contributions.

In the next sections we use a generic notation for the correlation functions $F_{ijk}^{(n)}(t_0, \tau_1, \tau_2)$, where n indicates the correlation order (2-time correlations for $n = 2$, 3-time correlations for $n = 3$). The indices ijk and t_0, τ_1, τ_2 indicate the functions between which the correlations are considered and the corresponding times of evaluation: for $n = 2$, the correlations are considered between i at t_0 and j at $t_0 + \tau_1$ (k and τ_2 being void) and for $n = 3$, the correlations are considered between i at t_0 , j at $t_0 + \tau_1$ and k at $t_0 + \tau_1 + \tau_2$. The indices i, j , and k can each represent

c , I , or h where c stands for emission into the cold bath, I the current generation, and h the emission from the hot bath.

III.A.4.1 Strokes of the engine from two-time correlations

III.A.4.1.a Derivation of the relevant correlations

In addition to the emission into the cold bath and current two-time correlations presented in Sec. III.A.3.2.c, we derive the two-time correlations between the heat extraction from the hot bath and the current through the junction ($F_{hI}^{(2)}(t, \tau) = \langle \hat{\sigma}_h^-(t) \hat{I}(t + \tau) \hat{\sigma}_h^+(t) \rangle_{ss}$), between the current through the junction and the heat emission into the cold bath ($F_{Ic}^{(2)}(t, \tau) = \langle \hat{I}(t) \hat{\sigma}_c^+(t + \tau) \hat{\sigma}_c^-(t + \tau) \rangle_{ss}$), and between the heat extraction from the hot bath and the heat emission into the cold bath ($F_{hc}^{(2)}(t, \tau) = \langle \hat{\sigma}_h^-(t) \hat{\sigma}_c^+(t + \tau) \hat{\sigma}_c^-(t + \tau) \hat{\sigma}_h^+(t) \rangle_{ss}$). This allows us to assess the properties of the excitation going through the system. The explicit derivations can be found in Appendix F.

III.A.4.1.b Damped oscillations in the energy transfer

We calculate the previously described correlation functions for a range of bath coupling κ and junction coupling λ parameters.

We first focus our analysis on the two-time correlations of the emission into the cold bath. The λ dependence shown in Fig. III.A.4.1 indicates an increasing correlation with $\sin(2\lambda)$. This is in agreement with Eqs. (III.A.2.2) and (III.A.2.8) as the detection of a quantum in the cold bath entails that a current was produced and therefore directly relies on the coupling of the qubit to the junction. It can be noted that the other correlation functions show the same trend in λ -dependence.

The two-time correlations of the emission into the cold bath taken for a range of κ shown in Fig. III.A.4.2a reveal interesting features. First, we note that each discrete detection of a quantum of energy released or absorbed by the baths causes a measurement back action, *i.e.*, a quench of the state of the engine. After the detection of a quantum emitted from the cold qubit the remaining excitation left in the hot qubit starts to oscillate, with stronger oscillations for smaller couplings to the baths. The oscillation

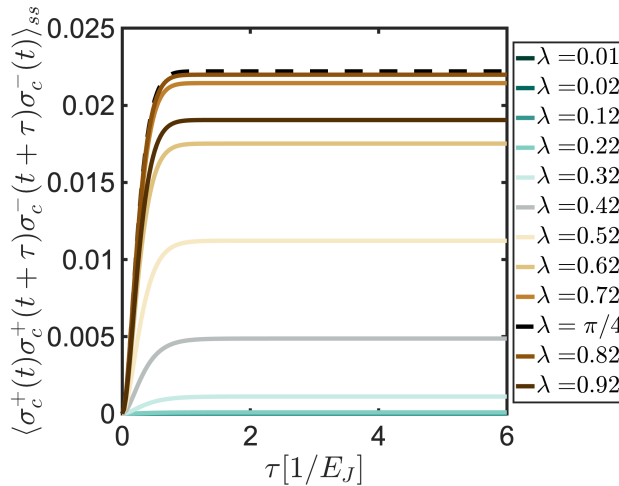


Figure III.A.4.1: Two-time correlations of the emission into the cold bath calculated for different values of the coupling λ to the Josephson junction. The system is taken in steady state at the early time t , and τ is given in units of the junction oscillation frequency inverse $1/E_J$. The other parameters are the given in Table III.A.2.1. The maximum is obtained for $\lambda = \pi/4$ (dashed black line). At long times, the correlations reach their steady state expectation values.

eventually dissipates after a few κ^{-1} , thus allowing another emission into the cold bath. The back action from monitoring the engine breaks time symmetry and induces the appearance of strokes in the excitation transfer, similar to the characteristic chuffing stemming from the periodic motion of the piston in the classical steam engine.

The emission from the hot bath–current $F_{hI}^{(2)}$ (Fig. III.A.4.2b), current–emission into the cold bath $F_{Ic}^{(2)}$ (Fig. III.A.4.2c) and emission from the hot bath–emission into the cold bath $F_{ch}^{(2)}$ (Fig. III.A.4.2d) two-time correlations allow us to follow the excitation throughout the different parts of the engine: the incoherent excitation of the hot qubit by absorption from the hot bath is followed by a transient transfer of energy towards the cold qubit and thus a positive work production. However, the oscillations in the correlation functions indicate a return of the excitation and thus a negative work production, and as κ decreases, the excitation remains trapped in

the system longer, traveling back and forth between the two qubits and alternately producing positive and negative work. This oscillatory process nonetheless leads to a positive work on average in the long time limit.

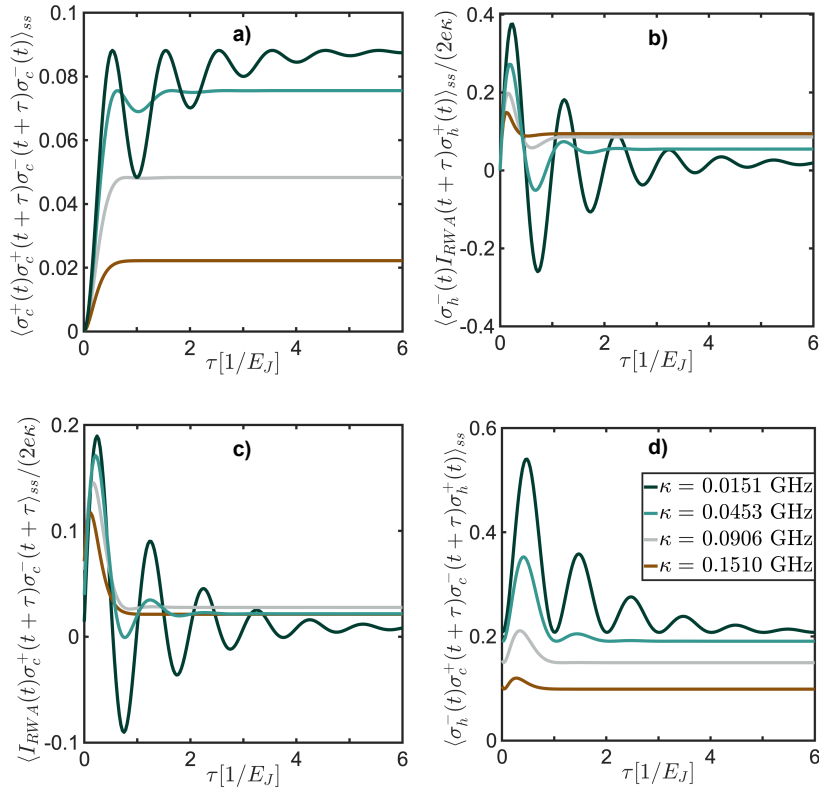


Figure III.A.4.2: Two-time correlations calculated for different values of the coupling κ to the baths—see legend in panel d). The system is taken to be in its steady state at the early time t , and τ is given in units of the junction oscillation frequency inverse $1/E_J$. The other parameters are the same as in Table III.A.2.1. **a)** Correlations for the heat emission into the cold bath; **b)** Correlations between the heat extraction from the hot bath and the current through the junction; **c)** Correlations between the current through the junction and the heat emission into the cold bath; **d)** Correlations between the heat extraction from the hot bath and the heat emission into the cold bath.

III.A.4.1.c Frequency of the oscillations

We showed in the previous section that the frequency at which the engine can perform its operation cycles is governed by κ : the larger the coupling to the baths is, the faster the engine is ready for a new cycle. As far as the dynamics of the excitation transfer between the engine parts is concerned, the frequency of its oscillations is equal to the Josephson junction frequency E_J (see Fig. III.A.4.3).

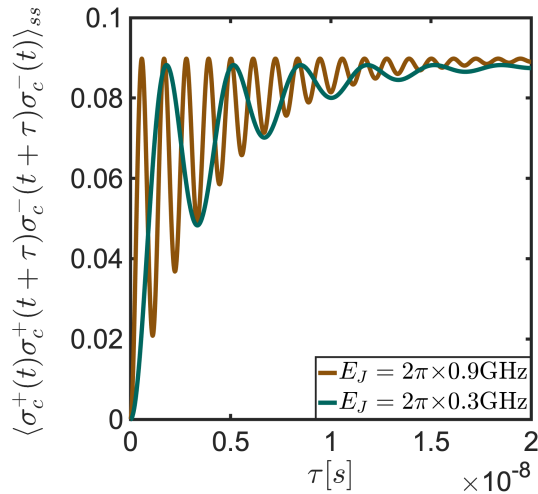


Figure III.A.4.3: Two-time correlations for the emission into the cold bath calculated with $\kappa = 2\pi \times 0.0151$ GHz for $E_J = 2\pi \times 0.9$ GHz (brown) and $E_J = 2\pi \times 0.3$ GHz (green). At long times, the correlations converge to their respective analytical steady state values. The system is taken in steady state at the starting time t . The other operation parameters are set to the values in Table III.A.2.1. The oscillations follow the junction frequency and are three times faster for $E_J = 2\pi \times 0.9$ GHz compared to $E_J = 2\pi \times 0.3$ GHz.

Then:

$$\hat{\sigma}_c^-(t_{ss} + \tau_1) \tilde{\rho}_1^{ccc}(t_{ss} + \tau) \hat{\sigma}_c^+(t_{ss} + \tau_1) = \hat{\sigma}_c^- \tilde{\rho}_1^{ccc}(t_{ss} + \tau_1) \hat{\sigma}_c^+ \quad (\text{III.A.4.4})$$

and $\tilde{\rho}_2^{ccc}(t_{ss} + \tau_1 + \tau_2)$ satisfies the master equation Eq. (III.A.2.5) and has the initial condition:

$$\tilde{\rho}_2^{ccc}(t_{ss} + \tau_1) = \hat{\sigma}_c^- \rho_1(t_{ss} + \tau_1) \hat{\sigma}_c^+ \quad (\text{III.A.4.5})$$

Then:

$$\begin{aligned} \hat{\sigma}_c^-(t_{ss} + \tau_1 + \tau_2) \tilde{\rho}_2^{ccc}(t_{ss} + \tau_1 + \tau_2) \hat{\sigma}_c^+(t_{ss} + \tau_1 + \tau_2) \\ = \hat{\sigma}_c^- \tilde{\rho}_2^{ccc}(t_{ss} + \tau_1 + \tau_2) \hat{\sigma}_c^+ \end{aligned} \quad (\text{III.A.4.6})$$

The infinite time limits are thus given by:

$$\begin{aligned} \lim_{\tau_1, \tau_2 \rightarrow \infty} \tilde{\rho}_2^{ccc}(t_{ss} + \tau_1 + \tau_2) &= \langle \hat{\sigma}_c^+ \hat{\sigma}_c^- \rangle_{ss} \rho_{ss} \\ &= (\rho_{0011,ss} + \rho_{1111,ss})^2 \rho_{ss} \end{aligned} \quad (\text{III.A.4.7})$$

and:

$$\begin{aligned} \lim_{\tau_1 \rightarrow \infty} F_{ccc}^{(3)}(t_{ss}, \tau_1, \tau_2) &= \langle \hat{\sigma}_c^+(t) \hat{\sigma}_c^+(t + \tau_2) \hat{\sigma}_c^-(t + \tau_2) \hat{\sigma}_c^-(t) \rangle_{ss} \langle \hat{\sigma}_c^+ \hat{\sigma}_c^- \rangle_{ss} \\ \lim_{\tau_2 \rightarrow \infty} F_{ccc}^{(3)}(t_{ss}, \tau_1, \tau_2) &= \langle \hat{\sigma}_c^+(t) \hat{\sigma}_c^+(t + \tau_1) \hat{\sigma}_c^-(t + \tau_1) \hat{\sigma}_c^-(t) \rangle_{ss} \langle \hat{\sigma}_c^+ \hat{\sigma}_c^- \rangle_{ss} \\ \lim_{\tau_1, \tau_2 \rightarrow \infty} F_{ccc}^{(3)}(t_{ss}, \tau_1, \tau_2) &= \langle \hat{\sigma}_c^+ \hat{\sigma}_c^- \rangle_{ss}^3 \\ &= (\rho_{0011,ss} + \rho_{1111,ss})^3 \end{aligned} \quad (\text{III.A.4.8})$$

The three time correlations for the emission into the hot bath— $F_{hhh}^{(3)}(t, \tau_1, \tau_2) = \langle \hat{\sigma}_h^-(t) \hat{\sigma}_h^-(t + \tau_1) \hat{\sigma}_h^-(t + \tau_1 + \tau_2) \hat{\sigma}_h^+(t + \tau_1 + \tau_2) \hat{\sigma}_h^+(t + \tau_1) \hat{\sigma}_h^+(t) \rangle$, and for detection of emission from the hot bath then current and finally the detection of emission into the cold bath— $F_{hIc}^{(3)}(t, \tau_1, \tau_2) = \langle \hat{\sigma}_h^-(t) \hat{\sigma}_c^+(t + \tau_1 + \tau_2) \hat{\sigma}_c^-(t + \tau_1 + \tau_2) \hat{I}(t + \tau_1) \hat{\sigma}_h^+(t) \rangle$ can be derived in a similar way.

III.A.4.2.a.ii Pure three-body contributions

Following the procedure described in Ref. [154] based on the theory of cumulants, a purely three-body contribution to the three-time correlations, $g_{c,p}^{(3)}$, can be derived.

$$g_{c,p}^{(3)} = 2 + g_c^{(3)}(t, t + \tau_1, t + \tau_1 + \tau_2) - g_c^{(2)}(t, t + \tau_1) - g_c^{(2)}(t, t + \tau_1 + \tau_2) - g_c^{(2)}(t + \tau_1, t + \tau_1 + \tau_2) \quad (\text{III.A.4.9})$$

where $g_c^{(3)}(t, t + \tau_1, t + \tau_1 + \tau_2)$ is the normalized three-time correlation function for the emission into the cold bath given by ([154, 155]):

$$g_c^{(3)}(t, t + \tau_1, t + \tau_1 + \tau_2) = \frac{F_{ccc}^{(3)}(t, \tau_1, \tau_2)}{\langle \hat{\sigma}_c^+(t) \hat{\sigma}_c^-(t) \rangle \langle \hat{\sigma}_c^+(t + \tau_1) \hat{\sigma}_c^-(t + \tau_1) \rangle} \times \frac{1}{\langle \hat{\sigma}_c^+(t + \tau_1 + \tau_2) \hat{\sigma}_c^-(t + \tau_1 + \tau_2) \rangle} \quad (\text{III.A.4.10})$$

For $t = t_{ss}$, it becomes:

$$g_c^{(3)}(t_{ss}, t_{ss} + \tau_1, t_{ss} + \tau_1 + \tau_2) = \frac{F_{ccc}^{(3)}(t_{ss}, \tau_1, \tau_2)}{\langle \hat{\sigma}_c^+ \hat{\sigma}_c^- \rangle_{ss}^3} \quad (\text{III.A.4.11})$$

Similarly, $g_c^{(2)}(t_i, t_i + \tau_j)$ is the normalized two-time correlation function given by:

$$g_c^{(2)}(t_i, t_i + \tau_j) = \frac{F_{cc}^{(2)}(t_i, \tau_j)}{\langle \hat{\sigma}_c^+(t_i) \hat{\sigma}_c^-(t_i) \rangle \langle \hat{\sigma}_c^+(t_i + \tau_j) \hat{\sigma}_c^-(t_i + \tau_j) \rangle} \quad (\text{III.A.4.12})$$

For $t_i \geq t_{ss}$, it becomes:

$$g_c^{(2)}(t_i, t_i + \tau_j) = \frac{F_{cc}^{(2)}(t_i, \tau_j)}{\langle \hat{\sigma}_c^+ \hat{\sigma}_c^- \rangle_{ss}^2} \quad (\text{III.A.4.13})$$

It should be noted that $g_p^{(3)}$ reflects the purely three-body contributions only in the case where the three functions are taken at different times. Otherwise, it cannot be obtained from a trivial cumulant expansion (non commutation of the creation and annihilation operators).

The pure three-body contributions to the correlations for the emission from the hot bath— $g_{h,p}^{(3)}$, and hot bath–current–cold bath— $g_{hIc,p}^{(3)}$ can be derived similarly.

III.A.4.2.b Interesting features

The three-time correlations for the emission into the cold bath $g_c^{(3)}$ (Fig. **III.A.4.4 a**) contain the same periodicity as the respective two-time correlations. They are symmetric with respect to the $(\tau_1 = \tau_2)$ line. This is due to the commutation of the spin operators at two different times, $[\hat{\sigma}_c^\pm(t + \tau_1), \hat{\sigma}_c^\pm(t + \tau_1 + \tau_2)] = 0$. At long τ_1 and τ_2 , the three-body contributions to the correlations, $g_{c,p}^{(3)}$, vanish as per Eq. (III.A.4.8). The three-time correlations for the hot bath give a similar profile.

The hot-current-cold correlations $g_{hIc}^{(3)}$ (Fig. **III.A.4.4 b**) allow us to get a closer look into the dynamics of the excitation transfer. Indeed, the positive nodes (brown) indicate the times (τ_1, τ_2) at which our engine is operating favorably: heat is emitted from the hot bath at the initial time, then current is generated at τ_1 , followed by de-excitation of the cold qubit into its bath at τ_2 . The excitation, after inducing a current generation, is detected by the cold bath after a delay $\tau_2 = 1/4E_J$, which is in accordance with the two-time correlations shown in Fig. **III.A.4.2**. Another detection can then occur after a delay equal to $1/E_J$, accounting for the excitation going back into the system. The negative nodes (green), indicate that the engine had generated negative current at τ_1 . These effects are clearly described by the three-body contributions $g_{hIc,p}^{(3)}$, both suggesting their usefulness in the investigation of the dynamics of the excitation transfer, and indicating that two-time correlations do not offer a complete picture of the dynamics.

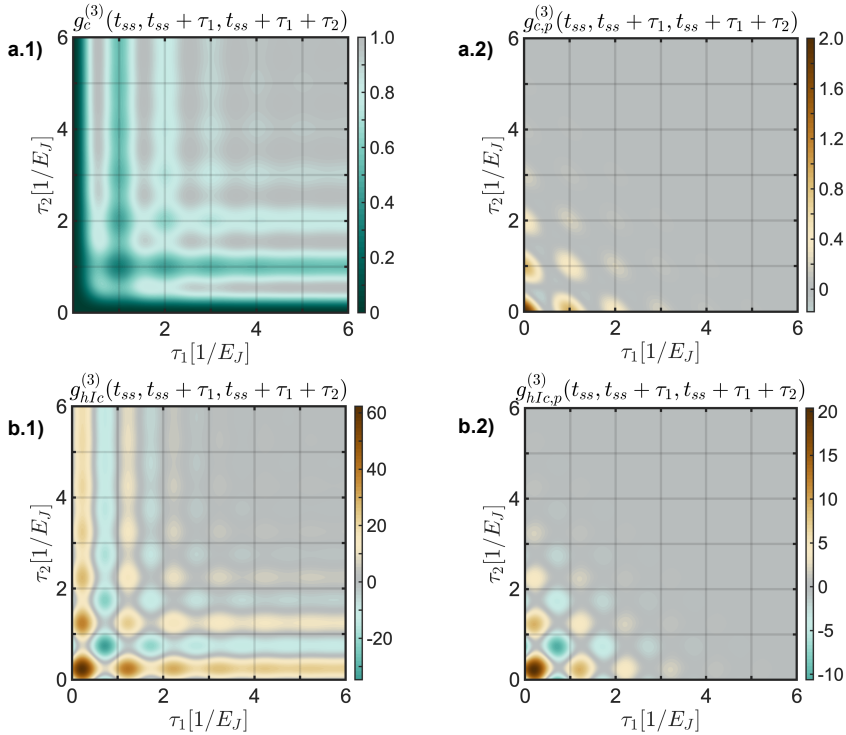


Figure III.A.4.4: Normalized three-time correlations and corresponding pure three-body contributions. **a)** Normalized three-time correlations for the emission into the cold bath $g_c^{(3)}$ (**a.1**) and pure three body contributions to the correlations $g_{c,p}^{(3)}$ (**a.2**); **b)** for the emission from the hot bath followed by the current and emission into the cold bath $g_{hIc}^{(3)}$ (**b.1**) and pure three body contributions $g_{hIc,p}^{(3)}$ (**b.2**). The system is taken in steady state at the starting time t . In grey, the correlations in the long time limit $(\tau_1, \tau_2) \rightarrow +\infty$. The coupling to the baths is taken at $\kappa = 2\pi \times 0.0151\text{GHz}$ and the other operation parameters are set to the values in Table III.A.2.1.

Conclusion

We studied a simple autonomous two-qubit thermoelectric engine powered by heat baths. We derived and calculated its efficiency and power as well as the mean values and fluctuations of work and heat. Using methods from quantum optics and open quantum systems we showed how the fluctuations of work and heat can be defined and evaluated for autonomous systems with a constant steady state. Indeed, while work could be directly derived from the current produced at the Josephson junction, the heat involved a detection-like process by the cold bath. Even though those variables are very different in nature, their mean values and fluctuations were found to be equivalent: for every heat quantum $\hbar\omega_c$ transferred to the cold heat bath a work of $2eV$ was done by the engine. Moreover, we were able to reveal the strokes of the engine by calculating the two-time correlation functions of these quantum processes and predicted a regularity in the timing of quanta arriving into or leaving from the baths and bursts of current around these detection events. Although applied to a specific quantum machine, our analysis protocol can be used for a range of engine designs and may inspire efforts to quantify the interplay between, e.g., maximum power and maximum efficiency of heat engines and thermodynamic uncertainty relations [156–160].



III.B POWERING A QUANTUM THERMOELECTRIC ENGINE BY PROJECTIVE MEASUREMENTS

Introduction

In the previous section, we focused our analysis on a quantum thermoelectric engine powered by two heat baths. We showed that this design allows us to produce positive usable electric work on average. Our analysis also enabled us to look into the dynamics of the engine and reveal the strokes in the energy transfer. The heat exchange with the baths proved to be a complex process that could be described by a detection-like model. This encouraged us to transform the design of our engine and replace one or both baths with a process offering more control. While measurements have been viewed as a source of decoherence—coherences that were recently experimentally measured in [161]—inducing a decrease in quantum engine efficiency [162, 163], this same effect was suggested as a possible source of work [164]. Numerous previous studies have considered quantum engines involving measurements at various operation stages: in lieu of a hot bath [165–167] or a cold bath [168], or acting on a two-qubit-two-bath machine to enhance its operation [169]. Those studies showed that powering a quantum engine using a measurement protocol was indeed possible.

This insight then poses the question of the measurement itself: powering a machine by measuring it seems to violate the fundamental laws of thermodynamics, as it appears to be generating work without a source instead of merely transforming energy. This question is far from being novel [170]. It was first posed by Maxwell who described an experiment in which an intelligent demon would sort out gas particles, thus decreasing the entropy of the system and violating the Second law of thermodynamics [171]. The validity of the Second law was later restored by taking into account the cost of the measurement process—by Szilard [172] and Brillouin [173]—which

lead to the development of Shannon's information theory [174] as well as Landauer's erasure principle [98, 175, 176]. The nature and properties of the measurement in the context of quantum thermodynamics was investigated in, e.g., Refs. [93, 177] where the cost of measurement and memory erasure were derived, and in Ref. [178] which quantified the maximum work that can be extracted by projectively measuring the density matrix. Furthermore, theoretical [179] and experimental [180, 181] implementations of the demon have supported the feasibility of work extraction from system measurement.

In our study, we focus on an engine design based on Fig. **III.A.2.1** where the baths are now replaced by a measurement protocol. Our modified engine allows us to both assess whether a fully quantum system can produce positive work on average as well as quantify the energy cost of projective measurements. By deriving and analyzing the periodic steady state of our machine, we show that for such a design, while unselective projective measurements cannot lead to a net work production on average, an adaptive measurement scheme allows a positive work generation directly related to the heat provided by the measurements.

Chapter III.B.2 describes the new system and its operational protocol (Sec. III.B.2.1). Then, after an introduction to the theory of projective measurements in the density matrix formalism, it provides the relevant operators used in this study (Sec. III.B.2.2) and the transformed master equations (Sec. III.B.2.3). In Chapter III.B.3 we briefly describe the situation where either the hot (Sec. III.B.3.2) or the cold bath (Sec. III.B.3.3) is replaced by a selected measurement scheme. Finally, Chapter III.B.4 presents the case of a thermoelectric engine powered solely by measurements: we derive a periodic steady state for our system in Sec. III.B.4.1. This allows us to assess the work production that can be obtained on average when measurements are powering the engine (Sec. III.B.4.3) and when our measurement protocol is selectively adapted (Sec. III.B.4.4).

We abusively designate frequencies by the period they correspond to as it allows for a more intuitive discussion of the results. The quantities designated by the letters T or τ stand for time periods and can easily be converted into frequencies by taking their inverse.

Procedure overview and relevant Master Equations

Starting from the two-qubit thermoelectric engine previously studied, we modify the design and replace one or both baths by a measurement protocol (see Fig. **III.B.2.1**). We restrict our investigation to projective measurements. In this chapter, the operation schemes of the modified engine are presented first. Then, the chosen measurement operators and relevant master equations are given after a short introduction to the theoretical framework. *In the following sections, $\hat{M}_{h(c)}$ is used as a generic notation for a measurement on the hot (h) or cold (c) side.*

III.B.2.1 System and operation protocol

III.B.2.1.a Measurement powered systems

As depicted in Fig. **III.B.2.1**, the system is practically identical to the thermoelectric engine studied in Part III—a hot (h) and a cold (c) qubit of respective frequencies ω_h and ω_c , coupled to a Josephson junction with respective coupling constants λ_h and λ_c , the only difference being the replacement of one or both heat baths by a measurement device.

In this study we set $\lambda_h = \lambda_c = \lambda = \pi/4$ as it ensures the most efficient energy transfer. The engine parameters are given in Table **III.A.2.1**.

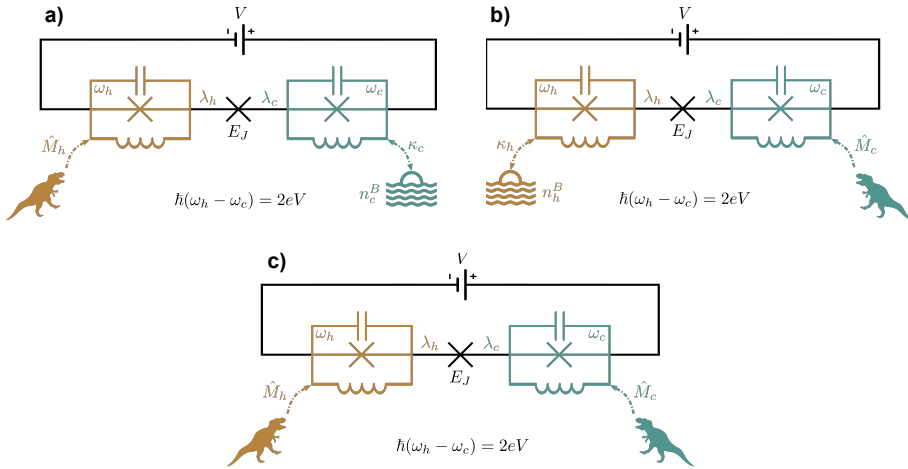


Figure III.B.2.1: Schematic representation of a two-qubit engine powered by measurements and performing work by resonant tunneling of Cooper pairs against a bias voltage V . Excitation transfer between the qubits is mediated by a tunneling current with Josephson oscillations tuned to the difference $2eV = \hbar(\omega_h - \omega_c)$ between the qubit excitation energies. The qubits are coupled to the Josephson junction with constants $\lambda_{h,c}$. **a)** The cold qubit (green) is coupled with rate κ_c to a bosonic heat bath with average excitation numbers n_c^B ; the hot qubit (yellow) is projectively measured by a chosen protocol \hat{M}_h which replaces the hot bath in Fig. III.A.2.1. **b)** The hot qubit is coupled with rate κ_h to a bosonic heat bath with average excitation numbers n_h^B ; the cold qubit is projectively measured by a chosen protocol \hat{M}_c which replaces the cold bath. **c)** Both the cold and the hot baths are replaced by respective measurement protocols \hat{M}_h and \hat{M}_c . The detail of the measurement protocols are given in Secs. III.B.2.1.b and III.B.2.2.b.

III.B.2.1.b Operation protocol

We restrict ourselves to the case where the cold and/or hot side are each measured once at each cycle. Fig. III.B.2.2 shows the schematic procedure for the situation where both baths are replaced; Fig. III.B.2.2 a) shows the case where we start the process by measuring the hot side (HC) and b) shows the situation where the cold side is measured first (CH). The procedure is conducted as follows (described for the specific case HC for

clarity):

1. The system is prepared in a given state ρ_0 (e.g. the ground state with $\rho_{0000} = 1$, a pure state evolved for a chosen time according to Eq. (III.A.2.5) or the two-bath steady state).
2. At $t = t_0$, the system is measured on the hot side by \hat{M}_h (generic notation for a chosen measurement scheme, see Sec. III.B.2.2.b for details). The state of the system is then given by $\rho^h(t)$ following the procedure in Sec. III.B.2.2.a.
3. The system is left free to evolve during a chosen time t_1 according to the relevant master equation defined in Sec. III.B.2.3 (denoted by \mathcal{L} on Fig. III.B.2.2).
4. At $t = t_0 + t_1$, the system is measured on the cold side by \hat{M}_c . The state of the system is then given by $\rho^{hc}(t)$.
5. The system is left free to evolve during a chosen time t_2 according to the relevant master equation.
6. Steps 2 to 5 are repeated for the number of cycles, N_{cycles} permitted in the chosen duration of the simulation $T_{simulation}$ given by $N_{cycles} = \lfloor \frac{T_{simulation}}{T_{cycle}} \rfloor$ where $T_{cycle} = t_1 + t_2$ is the duration of a measurement cycle. If the duration of the simulation is taken longer than a multiple of the cycle length, the system is left free to evolve according to the relevant master equation during the remaining time.

The measurements are instantaneous point measurements, applied at $t_0 + t_1$ and $t_0 + t_1 + t_2$. If the CH procedure is chosen, the cold qubit is measured in step 2 and the hot one in step 4. In the case of a measurement on one side only, the steps 4 and 5 are ignored and the bath interaction on the other side is included in the master equation.

III.B.2.2 Measuring the qubits

As described in the previous section, the operation of the engine relies on two processes: the measurement operation and the evolution of the resulting state according to the relevant master equation. In this section, we describe the former process.

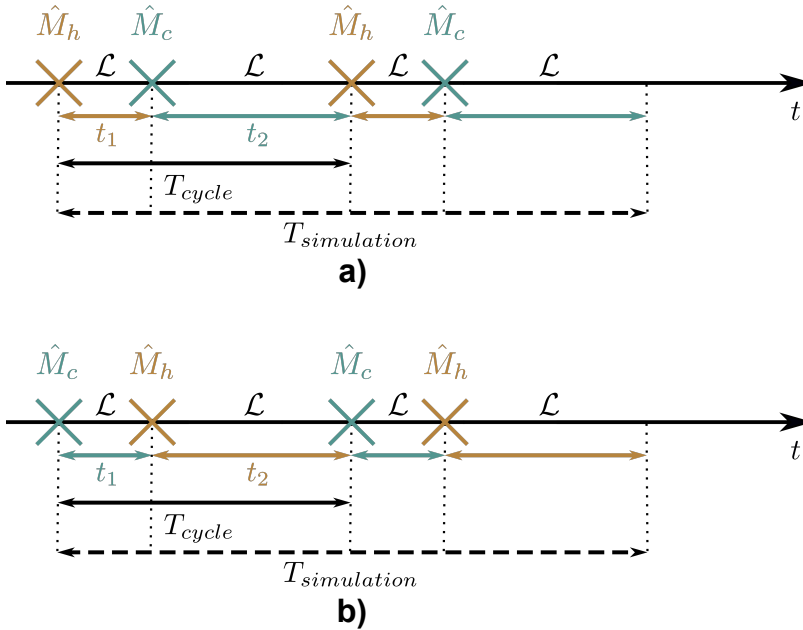


Figure III.B.2.2: Operation protocol of a two-qubit engine powered only by measurements. \hat{M}_h and \hat{M}_c generically represent the relevant measurement schemes given in Sec. III.B.2.2.b. After the measurement, the density matrix is evolved according to the relevant master equation (given in Sec. III.B.2.3) during t_1 after the first measurement and t_2 after the second, denoted by \mathcal{L} . The procedure is repeated over $N_{cycles} = \lfloor T_{simulation}/T_{cycle} \rfloor$. **a)** Hot–Cold (HC) scheme which starts with a measurement on the hot side on the initially prepared density matrix; **b)** Cold–Hot (CH) scheme where the initial density matrix is measured on the cold side first.

III.B.2.2.a Theory of projective measurements on the density matrix

The refinement of the description of measurements in quantum mechanics has been on the way since Heisenberg’s introduction of the collapse of the wavefunction [182], and eventually lead to Von Neumann’s formulation of projective measurements [183–185]. This was extended and derived for weak [186–188] and continuous measurements [189–191], leading to the notion of quantum trajectories [146, 147, 192]. We restrict ourselves to

projective measurements and in this section we briefly outline the main effect that the application of a measurement has on the density matrix of a quantum system based on the detailed derivations in Refs. [193] and [194].

General properties of measurements

One can define a set of measurement operators: $\{\hat{M}_i\}_{i=1}^n$ where the i represent the n possible measurement outcomes. If, prior to the measurements, the system is in a state $|\Psi\rangle$, the measurement process possesses the following notable properties:

1. The probability of obtaining the i th outcome is given by $p_i = p(i) = \langle\Psi|\hat{M}_i^\dagger\hat{M}_i|\Psi\rangle$
2. The total probability over all the measurements has to sum to 1, therefore: $\sum_i \hat{M}_i^\dagger\hat{M}_i = \mathbb{1}$. This is the completeness relation.
3. If the i th outcome is observed, the state becomes:

$$|\Psi\rangle \rightarrow |\tilde{\Psi}\rangle_i = \frac{\hat{M}_i|\Psi\rangle}{\sqrt{\langle\Psi|\hat{M}_i^\dagger\hat{M}_i|\Psi\rangle}}.$$

This is the collapse of the wavefunction, or the measurement back action.

Effect on the density matrix

The transformation of a density matrix ρ upon obtaining an outcome i is given by:

$$\rho \rightarrow \tilde{\rho}|_i = \frac{\hat{M}_i\rho\hat{M}_i^\dagger}{\text{Tr}[\hat{M}_i^\dagger\hat{M}_i\rho]} \quad (\text{III.B.2.1})$$

This form can be motivated by the following derivation in the case of a pure state.

We define $\rho = |\Psi\rangle\langle\Psi|$ with Ψ the wavefunction describing the system. Upon a measurement, $|\Psi\rangle$ transforms into $|\tilde{\Psi}\rangle_i = \frac{\hat{M}_i|\Psi\rangle}{\sqrt{p_i}}$. Then, the new density matrix for the measured state is: $\tilde{\rho} = |\tilde{\Psi}\rangle\langle\tilde{\Psi}|$.

Using the properties of the Hermitian conjugate, we have:

$$\begin{aligned}
 \tilde{\rho}|_i &= |\tilde{\Psi}\rangle \langle \tilde{\Psi}| \\
 &= \frac{\hat{M}_i |\Psi\rangle \langle \Psi| (\hat{M}_i)^\dagger}{\sqrt{p_i} \sqrt{p_i}} \\
 &= \frac{\hat{M}_i \rho \hat{M}_i^\dagger}{p_i} \\
 &= \frac{\hat{M}_i \rho \hat{M}_i^\dagger}{\text{Tr}[\hat{M}_i^\dagger \hat{M}_i \rho]}. \tag{III.B.2.2}
 \end{aligned}$$

This relation also holds for mixed states. If the measurement is performed, but the result ignored, the density matrix transforms into

$$\tilde{\rho} = \sum_i \hat{M}_i \rho \hat{M}_i^\dagger, \tag{III.B.2.3}$$

which represents an average over all possible outcomes. We refer to this as an unselective measurement scheme.

For notational simplicity, one can introduce the effects [195]:

$$E_i = \hat{M}_i^\dagger \hat{M}_i, \tag{III.B.2.4}$$

and, following Kraus [196], the operation:

$$\mathcal{M}[\rho] = \sum_i \hat{M}_i \rho \hat{M}_i^\dagger. \tag{III.B.2.5}$$

The ensemble $\{E_i\}_{i=1}^n$ then represents a Positive Operator Valued Measure (POVM), which does not require for the \hat{M}_i to be orthogonal and allows for the outcomes to be continuous.

In the special case where $\{\hat{M}_i\}_{i=1}^n$ is a set of projection operators $\{\hat{P}_i\}_{i=1}^n$ (*i.e.* linear Hermitian operators satisfying $\hat{P}_i^2 = \hat{P}_i$ [197, 198]) Eq. (III.B.2.1) becomes:

$$\tilde{\rho}|_i = \frac{\hat{P}_i \rho \hat{P}_i}{\text{Tr}[\hat{P}_i \rho]}. \tag{III.B.2.6}$$

III.B.2.2.b Choice of measurement operators

We define the rotated basis $(|+\rangle, |-\rangle)$ with angles α and ϕ for a qubit of eigenstates $\{|0\rangle, |1\rangle\}$ and density matrix defined as in Eq. (A.10):

$$\begin{aligned} |+\rangle &= \cos \alpha |0\rangle + e^{i\phi} \sin \alpha |1\rangle, \\ |-\rangle &= \sin \alpha |0\rangle - e^{i\phi} \cos \alpha |1\rangle, \end{aligned} \quad (\text{III.B.2.7})$$

and the projective measurement operators $\{\hat{P}^+(\alpha, \phi), \hat{P}^-(\alpha, \phi)\}$:

$$\begin{aligned} \hat{P}^+(\alpha, \phi) &= |+\rangle \langle +| \\ \hat{P}^-(\alpha, \phi) &= |-\rangle \langle -|. \end{aligned} \quad (\text{III.B.2.8})$$

They verify:

$$\begin{cases} (\hat{P}^+)^\dagger = \hat{P}^+, & (\hat{P}^+)^2 = \hat{P}^+ \\ (\hat{P}^-)^\dagger = \hat{P}^-, & (\hat{P}^-)^2 = \hat{P}^- \\ \hat{P}^+ + \hat{P}^- = \mathbb{1} \end{cases} \quad (\text{III.B.2.9})$$

where the dependence on (α, ϕ) has been omitted for notational simplicity.

Then, for our two-qubit system, we define the measurement operators for the hot side $\{\hat{P}_h^+, \hat{P}_h^-\}$:

$$\begin{aligned} \hat{P}_h^+ &\equiv \hat{P}^+ \otimes \mathbb{1}_C \\ \hat{P}_h^- &\equiv \hat{P}^- \otimes \mathbb{1}_C, \end{aligned} \quad (\text{III.B.2.10})$$

and for the cold side $\{\hat{P}_c^+, \hat{P}_c^-\}$:

$$\begin{aligned} \hat{P}_c^+ &\equiv \mathbb{1}_H \otimes \hat{P}^+ \\ \hat{P}_c^- &\equiv \mathbb{1}_H \otimes \hat{P}^-, \end{aligned} \quad (\text{III.B.2.11})$$

where $\{\hat{P}_h^+, \hat{P}_h^-\}$ and $\{\hat{P}_c^+, \hat{P}_c^-\}$ satisfy the properties in Eq. (III.B.2.9).

III.B.2.3 Master equation evolution of the system

With the measuring procedure described, we shall now consider the second process involved in the engine's operation and define the master equations for which the solutions govern the evolution of the system between measurements.

As the baths are removed on either one or both sides, the rest of the system remains unchanged. In particular, the system is still described by the Hamiltonian in Eq. (III.A.2.2), and the current operator as defined in Eq. (III.A.2.8) remains an appropriate tool for analyzing the performance of the engine. For a bath-less engine, only the evolution due to the Hamiltonian remains. The master equation for the density operator, $\hat{\rho}^{hc}$, describing the system thus reads:

$$\begin{aligned} \frac{d\hat{\rho}^{hc}(t)}{dt} &= -i[\hat{H}_{RWA}, \hat{\rho}^{hc}(t)] \\ &= -i\frac{E_J}{2} \sin(2\lambda_h) \sin(2\lambda_c) \\ &\quad \times \left(\hat{\sigma}_c^+ \hat{\sigma}_h^- \hat{\rho}^{hc}(t) - \hat{\rho}^{hc}(t) \hat{\sigma}_c^+ \hat{\sigma}_h^- + \hat{\sigma}_h^+ \hat{\sigma}_c^- \hat{\rho}^{hc}(t) - \hat{\rho}^{hc}(t) \hat{\sigma}_h^+ \hat{\sigma}_c^- \right). \end{aligned} \quad (\text{III.B.2.12})$$

In this regime, the time evolution of the expectation value of the current is directly given by the expectation values of the qubit occupation numbers:

$$\frac{d\langle \hat{I}(t) \rangle}{dt} = 2e(E_J \sin(2\lambda_h) \sin(2\lambda_c))^2 (\langle \hat{n}_h(t) \rangle - \langle \hat{n}_c(t) \rangle) \quad (\text{III.B.2.13})$$

The quantity $\langle \hat{n}_h(t) \rangle - \langle \hat{n}_c(t) \rangle$, which governs the current dynamics, represents the amount of excitation available for current generation.

In the case where only one bath is replaced by a measurement device, the master equation is the sum of the Hamiltonian interaction described in Eq. III.B.2.12 and the dissipative term corresponding to the remaining bath given in Eq. (III.A.2.6).

The engine's operation protocol as well as the choice of measurement operators give rise to four parameters that can be tested and optimized:

the delays between measurements, t_1 and t_2 , and the orientation of the projectors given by α and ϕ . We take this aspect into consideration in our investigation of the maximum achievable work production from such engine designs, presented in the following sections.

Measurement on the cold or hot side

We start our investigation of the measurement powered engine by testing whether our engine design allows for a conversion of measurement back action into work. For this purpose, we test its performance by replacing one of the baths by an unselective projective measurement scheme (see Ref. [164], Figure 2.a. for an example of an experimental realization of unselective measurements). We show that, by cleverly selecting the projectors, it is indeed possible to reach a performance that equals and even exceeds that of a two-bath setup.

III.B.3.1 Choice of operation parameters

III.B.3.1.a Initial density matrix

We consider two initial configurations for our systems.

The first, ρ_{ss} , is the previously obtained steady state for the two-baths design. This choice corresponds to operating the engine until it has reached steady state and then removing one or both of the baths at the time of the first measurement t_0 . It allows us to see whether the engine's performance can be maintained by the measurements.

The second initial state, $\rho_{1-0} = |0\rangle\langle 0|_h \otimes |0\rangle\langle 0|_c$, is a pure state with both qubits in their ground state ($\rho_{0000} = 1$ and all remaining coefficients equal to zero). This allows us to see whether the measurement protocol can initiate the work production dynamics.

III.B.3.1.b Measurement frequency

The internal dynamics of the energy transfer was shown to be governed by the Josephson frequency E_J (see Sec. III.A.4.1.c) and Fig. III.A.4.2 seems to indicate that the excitation travels from one side of the engine to the other in a time $\tau_E = T_{E_J}/2$ —with T_{E_J} the period associated with the junction frequency. Therefore, one could assume that this characteristic period τ_E would be the optimal measurement delay as it would allow the system to complete its one-directional operation before it is re-initiated. We test this hypothesis by calculating the electric work produced by the engine for a range of different measurement frequencies.

Another regime of interest is that of high frequency measurement. Indeed, one could expect to observe manifestations of the quantum Zeno effect [199] in the limit of small delays between measurements.

The other engine parameters are the ones used throughout our investigation (see Table III.A.2.1).

III.B.3.2 Measurement on the hot side

Several realizations of a quantum heat engine in contact with a cold reservoir and drawing work from a measuring process have been described [165–167]. Our design for such a system, in contact with a cold bath of vanishing temperature and measured on the hot side, is schematically depicted in Fig. III.B.2.1 a). The measurement back action of an unselective measurement on its state (given by $\hat{\rho}^h(t)$) is described by:

$$\begin{aligned} \hat{M}_h \hat{\rho}^h(t) &\equiv \mathcal{P}_h[\hat{\rho}^h(t)] \\ &= \hat{P}_h^+ \hat{\rho}^h(t) \hat{P}_h^+ + \hat{P}_h^- \hat{\rho}^h(t) \hat{P}_h^-, \end{aligned} \quad (\text{III.B.3.1})$$

and the evolution of the system between two projections is given by the relevant master equation (see Sec. III.B.2.3).

III.B.3.2.a Optimal projectors

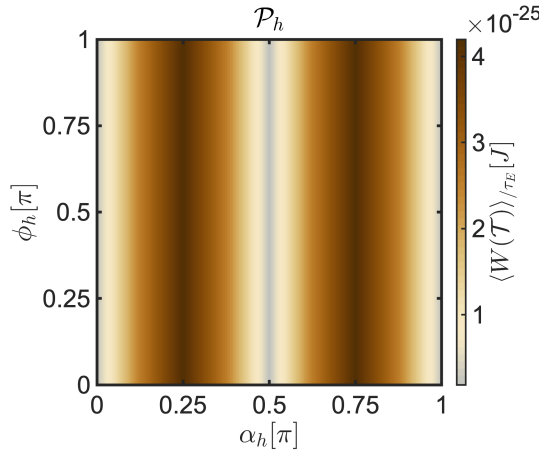


Figure III.B.3.1: Work generated over one period τ_E by the engine measured on the hot side for various projector orientations (α_h, ϕ_h) . It was calculated from the work performed over 10 cycles with a cycle duration $T_{cycle} = \tau_E = T_{EJ}/2$ starting in ρ_{ss} . The maximum achievable work $W_{max,a}^h = 4.2 \times 10^{-25}$ J is reached for $\alpha_h \in \{\pi/4, 3\pi/4\}$. The other engine parameters are given in Table III.A.2.1.

The projectors as defined in Eq. (III.B.2.10) can produce a range of measurement operations as the projection angle α_h and phase ϕ_h can be freely selected. In order to verify whether it is possible to find a set of projectors which will allow us to power the engine, we calculate the output work of the engine measured on the hot side as a function of (α_h, ϕ_h) for the above-mentioned initial states, ρ_{ss} and ρ_{1-0} , and measurement frequency regimes. The angles leading to the maximum work production are the same for these different situations. Figure III.B.3.1 shows the work generated per cycle with $T_{cycle} = \tau_E$ for a system initially taken in ρ_{ss} . The maximum work $W_{max,a}^h = 4.2 \times 10^{-25}$ J—surpassing the work generated by the two-baths setup over the same time interval: $W_{max} = 2.6 \times 10^{-25}$ J—is obtained for an orientation $\alpha_h \in \{\pi/4, 3\pi/4\}$, the phase ϕ_h having no effect on the performance. These angles put the qubit in a mixture of the ground and excited state with equal probability, which ensures that there is always some excitation available for current generation.

III.B.3.2.b Operation regimes

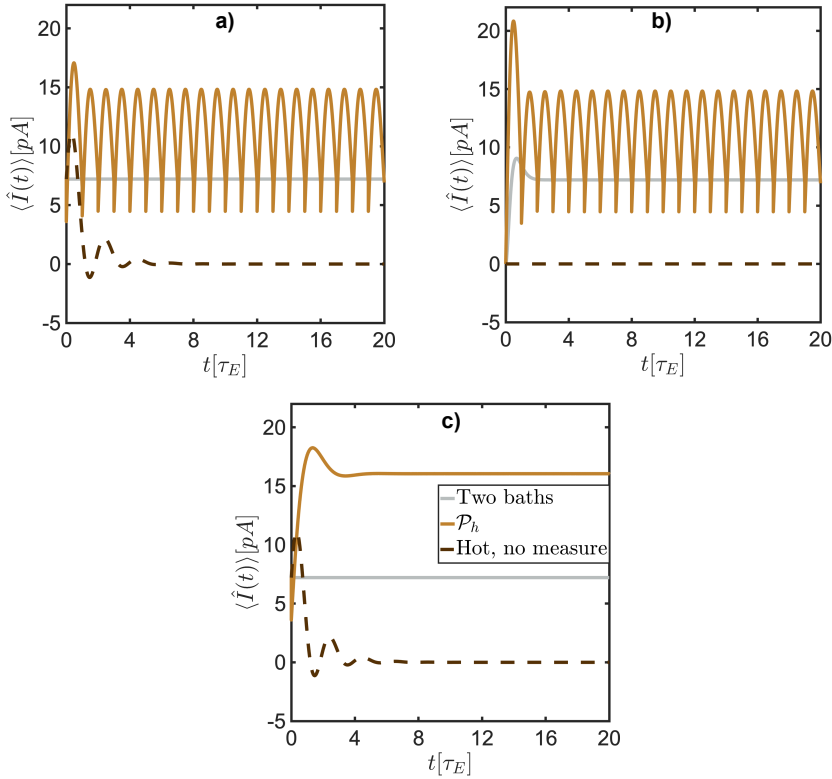


Figure III.B.3.2: Current generated by the engine measured on the hot side for various operation regimes as a function of time (normalized by τ_E). In brown, the unselectively measured system; in dashed dark brown, the current generated by the one bath (cold) engine with no measurement applied to the hot side (*i.e.* where we simulate the dynamics for the entire duration from the one bath master equation); in grey, the current generated by a two-bath engine using the same parameters (see common legend shown in **c**). **a**) Engine operated with a measurement frequency of $T_{cycle} = \tau_E$ and taken initially in the two-baths steady state ρ_{ss} ; **b**) with $T_{cycle} = \tau_E$ and taken initially in ρ_{1-0} ; **c**) with $T_{cycle} = 0.001 \times \tau_E$ and taken initially in ρ_{ss} . The current was calculated with $(\alpha_h, \phi_h) = (\pi/4, 0)$. The other engine parameters are given in Table **III.A.2.1**.

The expectation value of the current generated at the junction $\langle \hat{I}(t) \rangle$ allows us to get a deeper insight into the dynamics of the engine for the different operation regimes. For an engine measured at the engine's characteristic frequency, $T_{cycle} = \tau_E$, each measurement injects excitation into the system, allowing for a positive current to be produced. The resulting current surpasses the two-bath values on average. This allows us to verify that it is both possible to maintain an operational engine after removal of the hot bath (see Fig. **III.B.3.2 a**) and initiate work production dynamics from an initial state with no excitation (see Fig. **III.B.3.2 b**).

When measured with a high frequency, $T_{cycle} = 0.001 \times \tau_E$, both for an engine initially in the two-bath steady state (see Fig. **III.B.3.2 c**) and the pure state ρ_{1-0} , after a few cycles, the density matrix exhibits small oscillations around a constant value which transfer to the engine's current (not discernible on the graphs). This limit current reached after a few τ_E is higher than the two-bath steady state current allowing for a sustained generation of work.

These observations allow us to conclude that it is possible to find a measurement scheme for the hot side which leads to sustained positive work generation that surpasses the work output from a two-bath engine. We can therefore conclude that this measurement protocol efficiently replaces the hot bath.

III.B.3.3 Measurement on the cold side

In Ref. [168] Scully showed that it was possible to operate a quantum heat engine with a hot source only and using a state selective maser as a cooling apparatus. Our setup is shown in Fig. **III.B.2.1 b**). In this case, the back action of the unselective measurements on the system, described by the density matrix $\hat{\rho}^c(t)$, is given by the operation:

$$\begin{aligned} \hat{M}_c \hat{\rho}^c(t) &\equiv \mathcal{P}_c[\hat{\rho}^c(t)] \\ &= \hat{P}_c^+ \hat{\rho}^c(t) \hat{P}_c^+ + \hat{P}_c^- \hat{\rho}^c(t) \hat{P}_c^-, \end{aligned} \quad (\text{III.B.3.2})$$

and the evolution of the system between two projections is given by the relevant master equation (see Sec. III.B.2.3).

III.B.3.3.a Optimal projectors

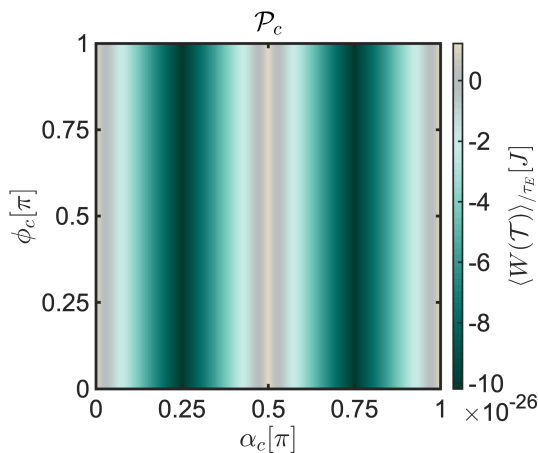


Figure III.B.3.3: Work generated over one period τ_E by the engine measured on the cold side for various projector orientations (α_c, ϕ_c) . It was calculated from the work performed over 100 cycles with a cycle duration $T_{cycle} = 0.1 \times \tau_E$ starting in ρ_{ss} . The maximum achievable work $W_{max,a}^c = 1.2 \times 10^{-26}$ J is reached for $\alpha_c \in \{0, \pi/2, \pi\}$. The other engine parameters are given in Table III.A.2.1.

In order to verify whether removing the cold bath is a viable option, we follow the same investigation procedure as for the hot-side measured engine. The cold bath which leads to the highest work production has no thermal excitations, so the optimal cold-side measurement protocol can be assumed to be the one that replicates this situation. We investigate whether such an engine can sustainably produce positive work by measuring the cold side with periodicity $T_{cycle} = 0.1 \times \tau_E$.

It is possible to find a set of projector orientations (α_c, ϕ_c) , leading to a positive work output when the system is initiated both in ρ_{1-0} and in the two-baths steady state ρ_{ss} . Figure III.B.3.3 shows the work generated per engine period τ_E for a system initially taken in ρ_{ss} . The maximum work $W_{max,a}^c = 1.2 \times 10^{-26}$ J—compared to the two-baths work generated over the same time interval: $W_{max} = 2.6 \times 10^{-25}$ J—is obtained for an orientation $\alpha_c \in \{0, \pi/2, \pi\}$ (the phase ϕ_c , as for the case where the hot side is measured, has no effect on the performance). This operation consists

in flipping the qubit state. However, the very low work output suggests that the positive work output is not sustained over time, which incites us to investigate the evolution of the current produced by the engine subject to measurements on the cold side.

If the engine is measured with a set projectors different from the optimal projectors (*i.e.*, $\alpha_c \notin \{0, \pi/2, \pi\}$), the work it generates is negative. This indicates that the measurement protocol is actually heating the cold side which results in an engine operating in reverse.

III.B.3.3.b Operation regimes

The engine operated with the projector orientations leading to the generation of positive work (where $\alpha_c \in \{0, \pi/2, \pi\}$) exhibits different regimes depending on the measurement frequency. Indeed, for an engine measured at two-bath engine period τ_E , the output current follows very closely the current that one would obtain for the same unmeasured setup. After the first few cycles where we can see bursts, the current rapidly falls to zero (see Fig. III.B.3.4 a)).

When we increase the measurement frequency to $T_{cycle} = 0.1 \times \tau_E$, the current generation phase is more damped: the maximum value of current that can be generated over a cycle is lower than in the previous case but the operation time, over which the engine is operating favorably, is longer. The current eventually falls to zero in this situation as well (see Fig. III.B.3.4 b)). Both of these measurement frequencies lead to an average work per engine period τ_E of $W^c = 1.2 \times 10^{-26}$ J if calculated over 20 two-bath engine cycles.

If we measure the engine with a high frequency on the cold side (Fig. III.B.3.4 c)) shows the engine's current for a measurement performed every $T_{cycle} = 0.01 \times \tau_E$), we observe that the average current drops to a stable value around which it oscillates with small amplitude (the oscillations are not discernible on the graph). However, these oscillations are damped as well and the engine is eventually not generating any current. The average work per engine period obtained for this situation is $W^c = 0.5 \times 10^{-26}$ J and the more frequent the measurements, the lower the work.

These observations reveal the tradeoff between the maximum current, and thus work, we can generate at each cycle and the duration of a favorable operation (*i.e.*, the duration where the engine generates positive work).

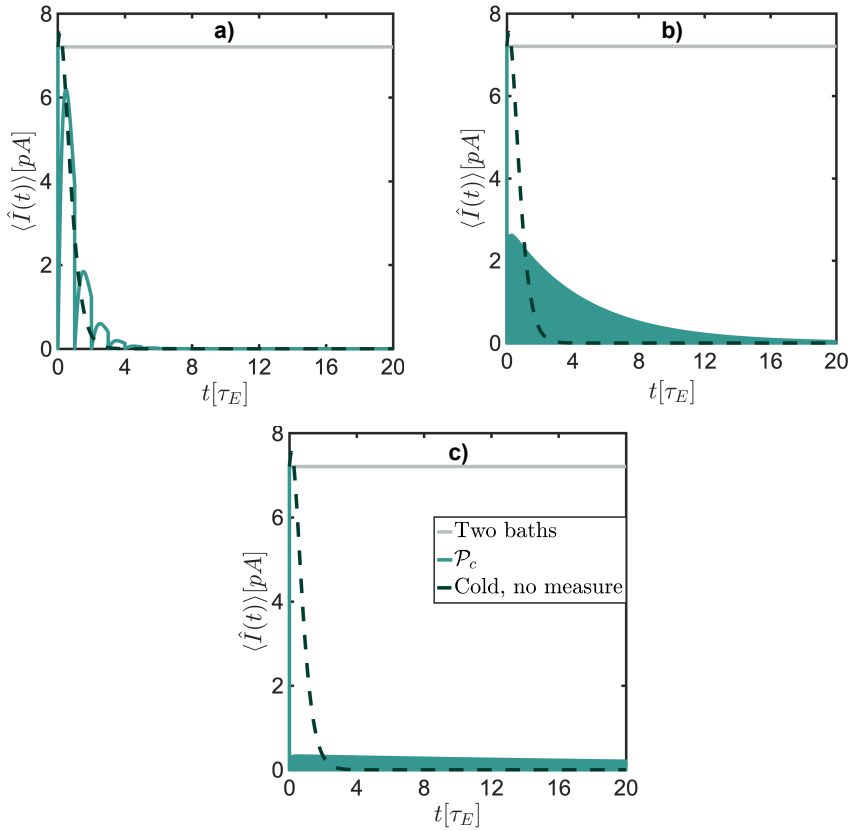


Figure III.B.3.4: Current generated by the engine measured on the cold side for various measurement frequencies as a function of time (normalized by τ_E). In green, the unselectively measured system; in dashed dark green, the current generated by the one bath (hot) engine with no measurement applied to the cold side (*i.e.* where we simulate the dynamics for the entire simulation from the one-bath master equation); in grey, the current generated by a two-bath engine using the same parameters (see common legend shown in **c**). **a**) Engine operated with a measurement periodicity of τ_E ; **b**) with $T_{cycle} = 0.1 \times \tau_E$; **c**) with $T_{cycle} = 0.01 \times \tau_E$. The current was calculated with a system taken initially in ρ_{ss} and with $(\alpha_c, \phi_c) = (\pi/2, 0)$. The other engine parameters are given in Table III.A.2.1.

If the measurement delay is taken large enough to allow for a smoother decay, a shorter delay allows the generation of positive work over longer operation times but with lower maximum amplitude. In all cases, the current eventually drops to zero, which explains the low value of the work output observed in the previous section.

This leads us to conclude that this setup cannot sustainably generate positive work on average. However, if compared to the situation where the cold bath is removed and the system is left free to evolve, adding a measurement device on the cold side allows to access the amplitude/duration tradeoff and to partially maintain the generation of positive work after the removal of the cold bath over longer times.

These investigations confirm that it is indeed possible to find a set of projectors that allow us to power our engine by replacing one of the baths by a measurement device. If the cold bath is replaced, the engine can be powered only for a finite duration, but for an engine measured on the hot side, the generation of average positive work is sustained. The optimal operation parameters depend, however, on the initial state of the system. In particular, the ϕ dependence does not necessarily vanish, and the parameters should be tailored to the chosen system.

Measurement on both sides

In the previous chapter, we showed that it was possible to power a microscopic engine by replacing one of the baths by measurements. The question at this point is: can we produce positive work on average from a machine that does not interact with any baths and is instead measured? We consider the system depicted in Fig. III.B.2.1 c) which is first subjected to an unselective measurement scheme by the operators posed in Sec. III.B.2.2.b. In order to analyze the performance of the engine as a function of the measurement parameters (t_1, t_2, α, ϕ) we derive the periodic steady state of the system and compare our results to selective measurement trajectories. We show that, in the long time limit, there is no net work production on average. However, by adapting the measurement protocol to the state of the system, we are able to durably generate positive work on average.

III.B.4.1 Derivation of the periodic steady state

In this section, we describe the derivation of the periodic steady-state of our system. The convergence of a measurement driven (closed or open) system towards a steady state at infinitely long times was demonstrated in Refs. [200–202]. It was formally derived in a general case by Yudin *et al.* [203] who proved the existence of a periodic steady state for driven quantum systems without using the Floquet formalism for the solutions to linear periodic differential equations [204].

We explicitly derive the periodic steady-state for our measured system.

The details of the derivation outlined in this section can be found in Appendix H.

After one operation cycle, the system has evolved according to:

$$\hat{\rho}_p^{hc}(t + T_{cycle}) = \hat{\mathcal{U}}(\tau_2, \tau_1) \hat{M}_2 \hat{\mathcal{U}}(\tau_1, t) \hat{M}_1 \hat{\rho}_p^{hc}(t) \quad (\text{III.B.4.1})$$

with $T_{cycle} = t_1 + t_2$, the period of our operation cycle, $\tau_1 = t_1 + t$, and $\tau_2 = t_2 + t_1 + t$ for a given time t . The operator \hat{M}_1 denotes the first measurement operation performed on the system, at the time t , and \hat{M}_2 the second one at $t_1 + t$. The couple (\hat{M}_1, \hat{M}_2) is given by (\hat{M}_h, \hat{M}_c) for the HC scheme and (\hat{M}_c, \hat{M}_h) for the CH scheme. The explicit expressions of the measurement operators are given in the following sections. $\hat{\mathcal{U}}(t', t)$ is the time evolution super-operator given by [205]:

$$\hat{\mathcal{U}}(t', t) \hat{\rho}^{hc}(t) = \hat{U}(t', t) \hat{\rho}^{hc}(t) \hat{U}^\dagger(t', t) \quad (\text{III.B.4.2})$$

with $\hat{U}(t', t)$ the evolution operator for our closed system described by the Hamiltonian \hat{H}_{RWA} (Eq. (III.A.2.2)):

$$\hat{U}(t', t) = e^{-i(t'-t)\hat{H}_{RWA}/\hbar} \quad (\text{III.B.4.3})$$

If the system is in steady state at the time t , we require $\hat{\rho}^{hc}(t + T_{cycle}) = \hat{\rho}^{hc}(t)$. By Eq. (III.B.4.1), this means that we should solve the equation:

$$\underbrace{(\mathbb{1} - \hat{\mathcal{U}}(\tau_2, \tau_1) \hat{M}_2 \hat{\mathcal{U}}(\tau_1, t) \hat{M}_1)}_{\hat{\Xi}(\tau_1, \tau_2, t)} \hat{\rho}_p^{hc}(t) = \mathbb{0} \quad (\text{III.B.4.4})$$

In order to solve Eq. (III.B.4.4), we rewrite the master equation given by Eq. (III.B.2.12) in matrix form:

$$\dot{\hat{\rho}}_v^{hc}(t) = L \hat{\rho}_v^{hc}(t) \quad (\text{III.B.4.5})$$

where $\hat{\rho}_v^{hc}$ is the vector form of the density matrix defined in Eq. (III.A.2.4). This first order linear differential equation can be solved analytically and the solution $\hat{\rho}_v^{hc}(t)$ can be rewritten as a decomposition over the eigenvectors of L .

We start our derivation by applying the first measurement operation on the density vector at t . Then, we decompose this new state over the eigensystem of L , which allows us to calculate the evolution of the density matrix until the moment of the second measurement as each eigenvector \mathbf{l}_i associated with the eigenvalue λ_i evolves, from the time t to $t + t_1$ according to $\mathbf{l}_i(t_1) = e^{\lambda_i(t_1)}\mathbf{l}_i(t)$. After applying the second measurement and evolving the density matrix for the remaining time in a similar fashion, we obtain the matrix $\mathbb{1} - \hat{\Xi}(\tau_1, \tau_2, t)$ which we use to find the kernel of $\hat{\Xi}(\tau_1, \tau_2, t)$ and thus solve Eq. (III.B.4.4) and obtain the periodic steady state density matrix $\hat{\rho}_p^{hc}$.

III.B.4.2 Heat provided by the measurements

Equation (III.B.2.13) allows us to see that the quantity $\langle \hat{n}_h(t) \rangle - \langle \hat{n}_c(t) \rangle$ represents the amount of excitation available for current generation. Thus, by calculating the change in the qubit occupation numbers induced by the measurement, we can quantify the additional excitation that it injects into the system and thus the cost of measuring the system.

We define $N_\alpha^M(t)$, the change in occupation number of qubit α (hot or cold) induced by the measurement at time t ,

$$N_\alpha^M(t) = \langle \hat{n}_\alpha(t_+) \rangle - \langle \hat{n}_\alpha(t_-) \rangle, \quad (\text{III.B.4.6})$$

where t_+ refers to the moment right after the measurement is performed, and t_- right before. If $N_h^M(t) - N_c^M(t)$ is positive, a positive current can be generated at t_+ . From these quantities, we can define:

$$Q_\alpha^M(\mathcal{T}) = \hbar\omega_\alpha \int_0^{\mathcal{T}} N_\alpha^M(t) dt \quad (\text{III.B.4.7})$$

The quantity $Q_h^M(\mathcal{T})$ can be seen as the heat provided by the measurement device, in a similar manner as a hot bath, to the system during the operation time \mathcal{T} , and $Q_c^M(\mathcal{T})$, the heat lost by the system due to the process, which can be compared to a heat relaxation into a cold bath. The amount $Q^M(\mathcal{T}) = Q_h^M(\mathcal{T}) - Q_c^M(\mathcal{T})$ represents the net energy made available to the system by the measurement over the operation time \mathcal{T} . If it is positive, a positive work is generated. The energy cost of the measurements performed over \mathcal{T} is given by $Q_h^M(\mathcal{T}) + Q_c^M(\mathcal{T})$.

III.B.4.3 Unselective measurements

We first analyze the performance of our engine by measuring it unselectively. The explicit effect of the measurement operators \hat{M}_h and \hat{M}_c on the density matrix in this case is given by:

$$\mathcal{P}_h[\hat{\rho}^{hc}(t)] = \hat{P}_h^+ \hat{\rho}^{hc}(t) \hat{P}_h^+ + \hat{P}_h^- \hat{\rho}^{hc}(t) \hat{P}_h^-, \quad (\text{III.B.4.8})$$

and

$$\mathcal{P}_c[\hat{\rho}^{hc}(t)] = \hat{P}_c^+ \hat{\rho}^{hc}(t) \hat{P}_c^+ + \hat{P}_c^- \hat{\rho}^{hc}(t) \hat{P}_c^-. \quad (\text{III.B.4.9})$$

III.B.4.3.a Optimal projectors

Similarly to in Secs. III.B.3.2.a and III.B.3.3.a, we search for a set of projectors that allow us to power the engine by measurements alone. Figure **III.B.4.1 a)** shows the work generated per engine period τ_E for different values of (α_h, α_c) with $T_{cycle} = \tau_E = T_{E,J}/2$ and $t_1 = t_2 = \tau_E/2$, for a system initially taken in ρ_{ss} . The maximum work $W_{max,a}^{hc} = 3.9 \times 10^{-26}$ J, compared to work generated by the two-baths engine over the same time interval: $W_{max} = 2.6 \times 10^{-25}$ J, is obtained for the same angles as in the one-side measurement optimization: $\alpha_c \in \{\pi/2, \pi\}$ and $\alpha_h \in \{\pi/4, 3\pi/4\}$. The phases (ϕ_h, ϕ_c) , have no effect on the performance.

As described in Sec. III.B.2.3, $\langle \hat{n}_h(t) \rangle - \langle \hat{n}_c(t) \rangle$ govern the current and thus the work production dynamics. This can be confirmed by comparing the work generated per operation cycle depicted in Fig. **III.B.4.1 a)** to the difference of the integrated qubit occupation numbers per cycle $\mathcal{N}_h(\mathcal{T}) - \mathcal{N}_c(\mathcal{T})$ in Fig. **III.B.4.1 b)**.

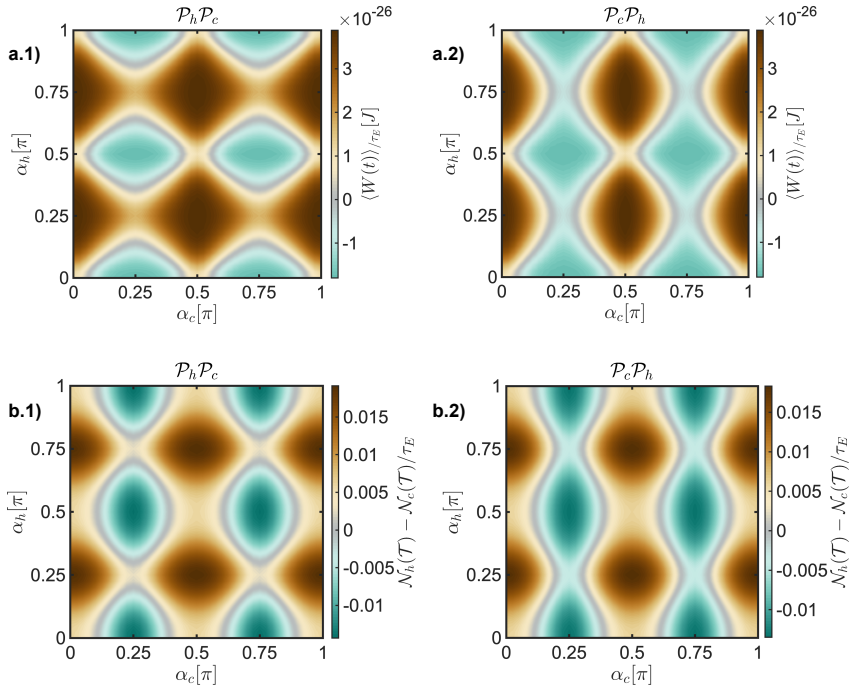


Figure III.B.4.1: **a)** Work generated per engine period τ_E by the engine measured on the hot and cold side for various projector orientations (α_h, α_c). **a.1)** Hot–Cold scheme, according to Fig. III.B.2.2 **a)**; **a.2)** Cold–Hot scheme, according to Fig. III.B.2.2 **b)**. The maximum achievable work $W_{max,a}^{hc} = 3.9 \times 10^{-26}$ J is reached for $\alpha_c \in \{\pi/2, \pi\}$ and $\alpha_h \in \{\pi/4, 3\pi/4\}$ in both the HC and CH schemes. **b)** Integrated qubit occupation number difference per period τ_E : **b.1)** Hot–Cold scheme; **b.2)** Cold–Hot scheme. The calculations were performed over 10 cycles with a cycle duration $T_{cycle} = \tau_E = T_{EJ}/2$, $t_1 = t_2 = \tau_E/2$, and the system initialized in ρ_{ss} . The other engine parameters are given in Table III.A.2.1.

III.B.4.3.b Long-time-limit work

The results presented in the previous section show that it is indeed possible to operate the engine solely by measurements. However, the integrated quantities we considered there do not allow us to see whether the work production is sustained over long operation times. In fact, the low value of maximum obtainable work suggests that it is not.

When we look into the time evolution of the density matrix and the current expectation value for the system measured on both sides, we can see that after the first few cycles, the system converges to a given state. This is the periodic steady state, derived in Sec. III.B.4.1 (see Fig. III.B.4.2 a)). The dynamics of the system with respect to this state depend on the angles of projection and the measurement timing.

III.B.4.3.b.i Measurement at engine characteristic frequency

For measurements performed at $t_1 = t_2 = \tau_E$, resulting in a cycle duration of $T_{cycle} = 2 \times \tau_E$, the HC and CH schemes both produce two density matrices satisfying the periodic condition. These states are reached for any projection angles (α_h, α_c) .

For the HC scheme, the two periodic steady states are: one is $\hat{\rho}_{p,1}^{hc}(t) = (1/2) (|0\rangle\langle 0| + |1\rangle\langle 1|)_h \otimes |0\rangle\langle 0|_c$ (i.e., with $\rho_{0000}^{hc} = \rho_{1100}^{hc} = 1/2$ and all other coefficients equal to zero), it represents a maximal mixing in the hot qubit states while the cold qubit is deexcited; and the other $\hat{\rho}_{p,2}^{hc}(t) = (1/2) (|0\rangle\langle 0| + |1\rangle\langle 1|)_h \otimes |1\rangle\langle 1|_c$ (where $\rho_{0011}^{hc} = \rho_{1111}^{hc} = 1/2$, all other coefficients equal to zero), represents a maximal mixing in the hot qubit states, the cold qubit being excited.

For the CH scheme, the two periodic steady states are similar to the HC states: one given by $\hat{\rho}_{p,1}^{ch}(t) = |0\rangle\langle 0|_h \otimes (1/2) (|0\rangle\langle 0| + |1\rangle\langle 1|)_c$ (i.e., with $\rho_{0000}^{ch} = \rho_{0011}^{ch} = 1/2$ and all other coefficients equal to zero)—representing a maximal mixing in the cold qubit states while the hot qubit is deexcited, and the other $\hat{\rho}_{p,2}^{ch}(t) = |1\rangle\langle 1|_h \otimes (1/2) (|0\rangle\langle 0| + |1\rangle\langle 1|)_c$ (with $\rho_{1100}^{ch} = \rho_{1111}^{ch} = 1/2$, all other coefficients equal to zero) represents a maximal mixing in the cold qubit, the hot qubit being excited.

The system operated in these states is characterized by an excitation going back and forth between the two qubits, leading to a shifting between

positive and equally negative current generation, resulting in zero average work (see Fig. **III.B.4.2 a**). This is exactly similar to the dynamics of the bath-less unmeasured system initiated in the above-mentioned states.

III.B.4.3.b.ii Measurement not at engine frequency

When operated at $T_{cycle} < 2 \times \tau_E$, the periodic steady state for the CH and HC schemes is the same. It is a state of no evolution and no current which is reached for any projection angles and is given by: $\hat{\rho}_p^{hc}(t) = \hat{\rho}_p^{ch}(t) = (1/4) (|0\rangle\langle 0| + |1\rangle\langle 1|)_h \otimes (|0\rangle\langle 0| + |1\rangle\langle 1|)_c$ (*i.e.*, $\rho_{0000} = \rho_{0011} = \rho_{1100} = \rho_{1111} = 1/4$ and all other coefficients equal to zero). It represents a maximal mixing in the two-qubit states.

For $T_{cycle} \ll 2 \times \tau_E$, the engine exhibits a similar behavior to the hot-bath-only engine measured with high frequency. Indeed, after the first measurement, the system remains in a stable state characterized by a low current generation, with oscillations of small amplitude in the density matrix coefficients and current (see Fig. **III.B.4.2 b**). Unlike the engine measured on the cold side, this state does not decay.

III.B.4.3.b.iii Measurement with small angles

We have seen that the angles of the projectors do not affect the periodic steady state. However, they do influence the engine dynamics and how fast it reaches this state. Indeed, smaller angles represent less disruptive projections and result in a slower convergence to the periodic steady state (see Fig. **III.B.4.2 c**).

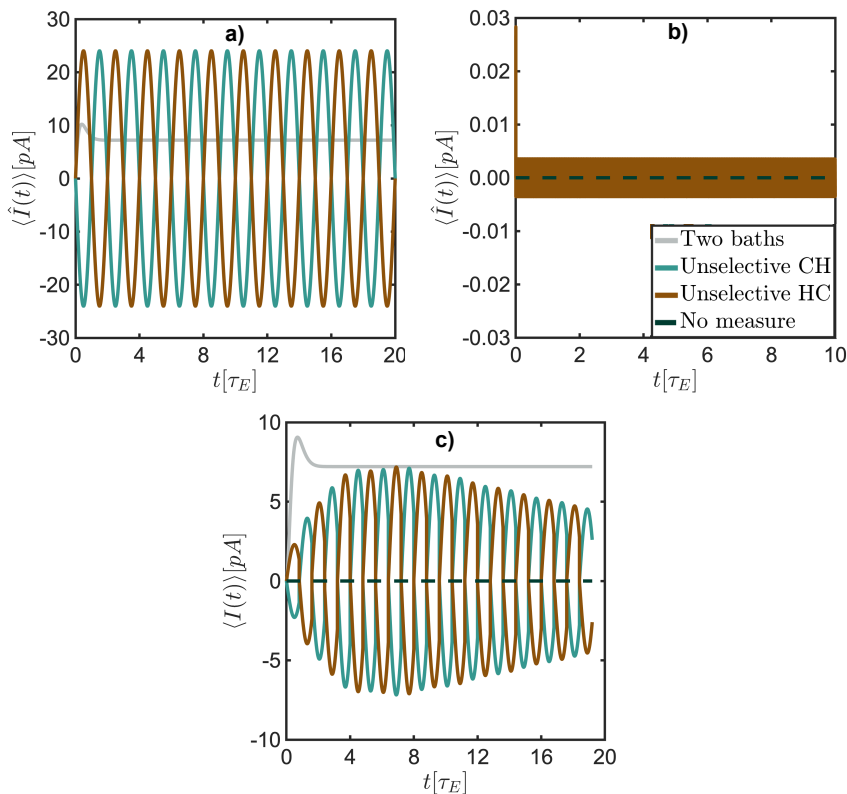


Figure III.B.4.2: Current generated by the engine measured on both sides at various frequencies and angles as a function of time (normalized by τ_E). In green, the current obtained with the CH scheme; in brown, the HC scheme; in dashed dark green, the current obtained for the bath-less unmeasured system (*i.e.* where we simulate the dynamics for the entire duration from the no-bath master equation alone); in grey, the current for the two-bath engine. **a)** The engine is operated with $t_1 = t_2 = \tau_E$, with angles $(\alpha_h, \alpha_c) = (\pi/4, \pi/2)$ and initialized in its periodic steady state. The unmeasured bath-less case follows the HC curve. **b)** High frequency measurement with $t_1 = t_2 = 5 \times 10^{-4} \times \tau_E$, $\alpha_h = \alpha_c = \pi/3$ and the initial state taken as ρ_{1-0} —the CH scheme is not shown but leads to the same current after the first measurement. **c)** Small angle measurement with $t_1 = t_2 = 0.8 \times \tau_E$, $\alpha_h = \alpha_c = \pi/20$ and initial state ρ_{1-0} —the system slowly reaches its steady state of no current generation. The other engine parameters are given in Table III.A.2.1.

III.B.4.3.c Trajectories and work distribution

The work that can be extracted from such a setup is zero on average. Nonetheless, we can look beyond the average properties of the unselective measurements by simulating an ensemble of selective measurement trajectories—where the outcomes are recorded. The physical reality of quantum jumps and trajectories was widely debated [206, 207], being either seen as a mathematical tool [146, 190] or as the experimental record one would obtain in the context of, e.g., photodetection [208–211]. However, a recent work by Mineev *et. al* [212], who managed to predict a quantum jump, suggests the experimental reality of such trajectories. We adopt here the “subjective reality” interpretation, as described in Ref. [207]—*i.e.* the selective measurement trajectories provide the evolution of the system one will experimentally observe if the measurement results are read out.

We simulate the measurement trajectories by initiating the system in the periodic steady state. For each side, at the moment of the measurement t , the system is randomly measured with either \hat{P}_α^+ or \hat{P}_α^- according to their respective probabilities given by $p(\hat{P}_\alpha^\pm)(t) = \text{Tr}[\hat{P}_\alpha^\pm \rho^{hc}(t)]$. The updated density matrix is then given by

$$\widetilde{\hat{\rho}}^{hc}(t_+) = \frac{\hat{P}_\alpha^\pm \rho^{hc}(t_-) \hat{P}_\alpha^\pm}{p(\hat{P}_\alpha^\pm)(t_-)}. \quad (\text{III.B.4.10})$$

According to Borel’s law of large numbers [213], for an infinite number of trajectories, we recover the probability distribution for each time step, and thus the value of the work under the unselective measurement scheme. The number of trajectories considered in our simulations satisfy this property, up to a small deviation.

Figure III.B.4.3 a) shows the work generated for different operation times \mathcal{T} by 10 trajectories. By comparing the trajectories to the record of measurement operators, we notice that \hat{P}_c^+ induces a decrease in the work output (corresponding to a negative current generation) while \hat{P}_c^- does not change the value of the work output, as it projects the system on a state of zero current generation. The processes \hat{P}_h^+ and \hat{P}_h^- have the same effect of work increase (*i.e.* positive current), by half the amplitude of the decrease observed with \hat{P}_c^+ . This is due to our choice of projector angles, $(\alpha_h, \alpha_c) = (\pi/4, \pi/2)$, and measurement delays, $t_1 = t_2 = \tau_E$, and for different parameters, the relation between the projection at each time and its effect on the work output is less distinct (as can be inferred from

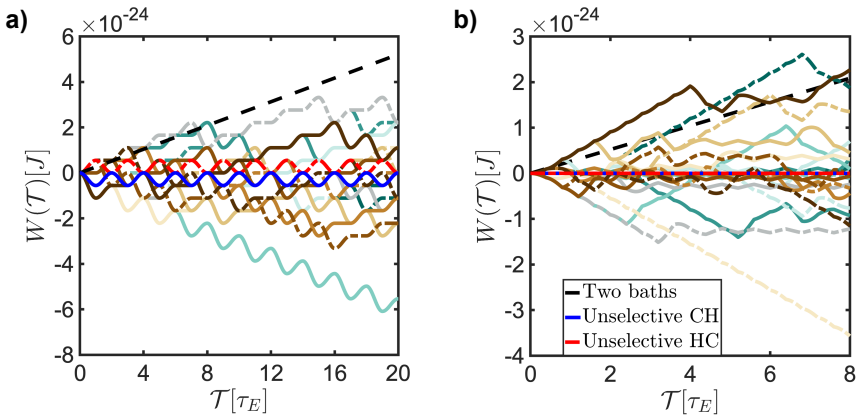


Figure III.B.4.3: Work as a function of operation time \mathcal{T} given in units of engine period τ_E for selective measurement trajectories. Dashed-dotted lines: HC scheme; full lines: CH scheme (the different colors represent different trajectories). In red, the work output for the unselective CH scheme; in blue, the work for the unselective HC scheme. Dashed black line: work as a function of operation time for the two-baths engine initiated in its steady state. **a)** Selective measurement trajectories for the engine operated with $t_1 = t_2 = \tau_E$, $(\alpha_h, \alpha_c) = (\pi/4, \pi/2)$ and initiated in the corresponding periodic steady state; **b)** engine operated with $t_1 = t_2 = 0.4\tau_E$, $\alpha_h = \alpha_c = \pi/3$ and initiated in the corresponding periodic steady state. The simulation was run over 10 trajectories. The other engine parameters are given in Table III.A.2.1.

Fig. III.B.4.3 b)). Based on these considerations, one could wonder if unselectively measuring on the hot side only would not be the best strategy. This, however, does not allow for a durable work output as the system quickly reaches a state of either zero current generation or zero-centered oscillating current, reflecting the fact that the excitation is trapped in the system.

The work distribution obtained from the trajectories (see Fig. III.B.4.4) is discrete due to the properties of the chosen measurement scheme and it follows a gaussian distribution, at both short and longer operation times, suggesting that there is no correlation between measurement occurrences.

The extreme values correspond to an unlikely succession of \hat{P}_c^+ (negative values) or \hat{P}_c^- (positive values) measurements on the cold side. The deviation from the unselective probabilities, which tends to favor the \hat{P}_c^+ projection, is responsible for the shift to negative values in the center of the CH distribution.

These observations offer new possible strategies for powering a quantum thermoelectric engine by measurements. Indeed, the amplitude of work decrease induced by \hat{P}_c^+ being twice the increase allowed by the hot side measurement, they suggest that if a selective measurement operation protocol is considered, a CHH scheme might be more efficient for positive work generation. Based on these considerations, we design a new measurement protocol described in the next section.

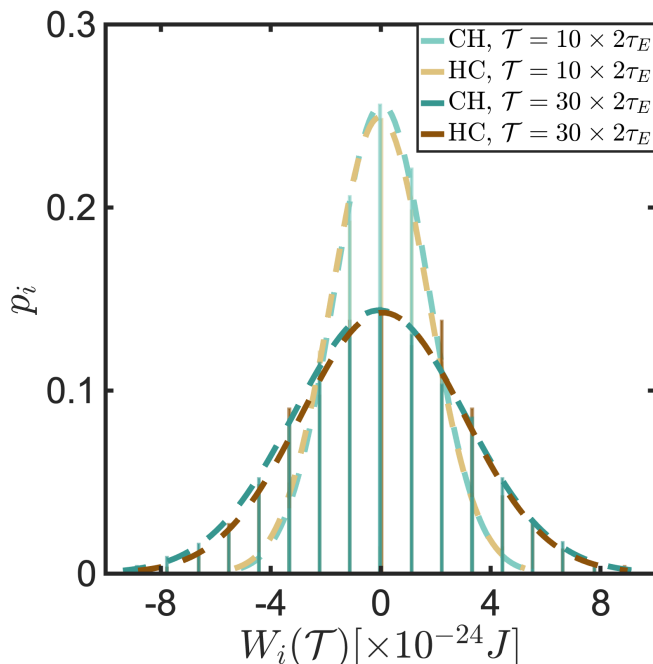


Figure III.B.4.4: Work distribution histograms for selective measurement trajectories compared to the corresponding gaussian distributions (dashed lines). p_i denotes the probability of occurrence of the work value W_i . In light green, the work distribution and gaussian fit obtained for an engine operated with the CH scheme over 10 measurement cycles ($\mathcal{T} = 20 \times \tau_E$)—the mean of the distribution is calculated to be $\mu = 4.3 \times 10^{-26}$ J and the deviation $\sigma = 1.7 \times 10^{-24}$ J; in yellow, with the HC scheme over 10 cycles— $\mu = -3.1 \times 10^{-26}$ J, $\sigma = 1.8 \times 10^{-24}$ J; in dark green, with the CH scheme over 30 cycles ($\mathcal{T} = 60 \times \tau_E$)— $\mu = -5.3 \times 10^{-26}$ J, $\sigma = 3.2 \times 10^{-24}$ J; in brown, with the HC scheme over 30 cycles— $\mu = 7.8 \times 10^{-26}$ J, $\sigma = 3.1 \times 10^{-24}$ J. The engine is operated with $t_1 = t_2 = \tau_E$ and $(\alpha_h, \alpha_c) = (\pi/4, \pi/2)$ and initiated in the corresponding periodic steady state. The simulation was run over 1000 trajectories. The other engine parameters are given in Table III.A.2.1.

III.B.4.4 Adaptive measurements

We showed that the unselectively measured system eventually reaches a state where no work is produced on average. This leads us to consider another measurement strategy where we perform two successive measurements: the first, a selective measurement in the qubit basis of which the outcome determines whether or not the second one, an unselective measurement similar to the one previously described, is applied. As the result of the first measurement is decisive for the rest of the operation, the measurement scheme is adaptive—see Ref. [214] for another example of the implementation of an adaptive measurement scheme in a quantum engine.

In this section, we chose to restrict ourselves to the case $\phi_h = \phi_c = 0$.

III.B.4.4.a Measurement protocol

The adaptive measurement protocol is applied to either one of the qubits, or both. The optimal system state for positive current generation is $(|0\rangle_c, |1\rangle_h)$. We take this into account to construct our new measurement scheme. For the cold side, this is done as follows:

1. The qubit is measured in the $(|0\rangle_c, |1\rangle_c)$ basis.
2. If the measurement outcome is $|1\rangle_c$, then it is unselectively measured in the $(|+\rangle_c, |-\rangle_c)$ basis. If the outcome is $|0\rangle_c$, the state is left unmeasured as this state is optimal for positive current generation.
3. The system is evolved according to the master equation for the chosen time.

If the hot side is adaptively measured, step 2 consists of measuring the qubit in the $(|+\rangle_h, |-\rangle_h)$ basis when the outcome of the first measurement in the qubit basis is $|0\rangle_h$, as this is unfavorable for positive current production. If the outcome of the first measurement is $|1\rangle_h$, the state is left unmeasured.

We define:

$$\begin{aligned}\hat{G}_h &= (|0\rangle\langle 0|)_H \otimes \mathbb{1}_C, & \hat{E}_h &= (|1\rangle\langle 1|)_H \otimes \mathbb{1}_C, \\ \hat{G}_c &= \mathbb{1}_H \otimes (|0\rangle\langle 0|)_C, & \hat{E}_c &= \mathbb{1}_H \otimes (|1\rangle\langle 1|)_C.\end{aligned}\tag{III.B.4.11}$$

The new sets of measurement operators are then given by:

$$\begin{cases} \hat{M}_h^{(1)} = \hat{E}_h \\ \hat{M}_h^{(2)} = \hat{P}_h^+(\alpha)\hat{G}_h \\ \hat{M}_h^{(3)} = \hat{P}_h^-(\alpha)\hat{G}_h \end{cases} \quad (\text{III.B.4.12})$$

and:

$$\begin{cases} \hat{M}_c^{(1)} = \hat{G}_c \\ \hat{M}_c^{(2)} = \hat{P}_c^+(\alpha)\hat{E}_c \\ \hat{M}_c^{(3)} = \hat{P}_c^-(\alpha)\hat{E}_c \end{cases} \quad (\text{III.B.4.13})$$

where $\{\hat{M}_h^1, \hat{M}_h^2, \hat{M}_h^3\}$ and $\{\hat{M}_c^1, \hat{M}_c^2, \hat{M}_c^3\}$ each form a complete set. The effect of such measurements on the density matrix, if the outcome is ignored, reads:

$$\begin{aligned} \mathcal{M}_h[\hat{\rho}^{hc}(t)] &= \hat{E}_h \hat{\rho}^{hc}(t) \hat{E}_h \\ &\quad + \hat{P}_h^+ \hat{G}_h \hat{\rho}^{hc}(t) \hat{G}_h \hat{P}_h^+ + \hat{P}_h^- \hat{G}_h \hat{\rho}^{hc}(t) \hat{G}_h \hat{P}_h^-, \end{aligned} \quad (\text{III.B.4.14})$$

and

$$\begin{aligned} \mathcal{M}_c[\hat{\rho}^{hc}(t)] &= \hat{G}_c \hat{\rho}^{hc}(t) \hat{G}_c + \\ &\quad \hat{P}_c^+ \hat{E}_c \hat{\rho}^{hc}(t) \hat{E}_c \hat{P}_c^+ + \hat{P}_c^- \hat{E}_c \hat{\rho}^{hc}(t) \hat{E}_c \hat{P}_c^-. \end{aligned} \quad (\text{III.B.4.15})$$

If a given side is not adaptively measured, the operations described in Eqs. (III.B.4.14) and (III.B.4.15) are applied.

III.B.4.4.b Maximum obtainable work

The adaptive measurement scheme allows for a sustained positive work production (see Fig. III.B.4.5 a). Indeed, it is possible to find a set of projector angles and measurement delays that engender a periodic steady state of positive current. The angles, α_h and α_c , determine the degree of state mixing and thus the emergence of non-zero coefficients in the

density matrix, while the delays, t_1 and t_2 , determine the amplitude of these coefficients. As we can see in Figure III.B.4.5 b), this measurement scheme deposits an increasingly positive amount of heat, $Q^M(\mathcal{T})$, into the system over the operation time \mathcal{T} to be converted into work by the system. Employing an adaptive measurement protocol on either side is enough to surpass the two-bath engine work output by a comparable amount and when both sides are measured in this way, the work output is doubled.

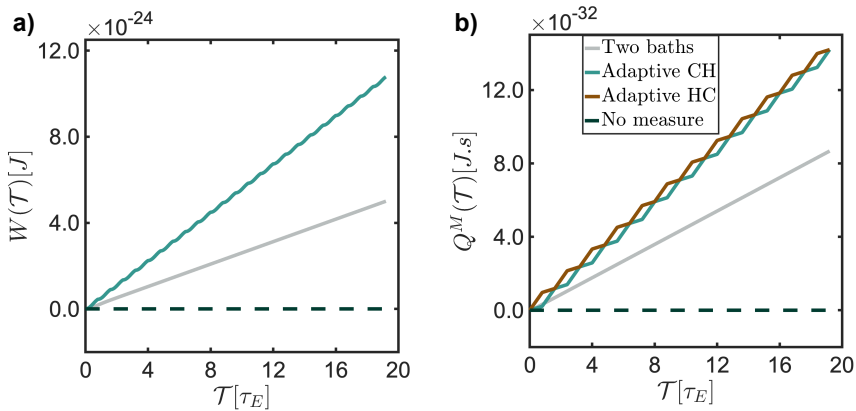


Figure III.B.4.5: Work produced by the engine adaptively measured on both sides and heat provided by the measurements. In green, the CH scheme; in brown, the HC scheme; in dark green, the bath-less unmeasured system (*i.e.* where we simulate the dynamics for the entire operation from the no bath master equation alone); in grey, the current for the two-bath engine. **a)** Work produced by the engine adaptively measured on both sides as a function of the operation time \mathcal{T} —the HC scheme curve is not depicted as it is identical to the CH curve. **b)** Total net excitation $Q^M(\mathcal{T})$ made available to the system over the operation time \mathcal{T} by the measurements as defined in Sec. III.B.4.2. The engine is operated with $t_1 = t_2 = 0.4 \times T_{E,J}$ and $\alpha_h = \alpha_c = \pi/3$, and initialized in the corresponding periodic steady state. The other engine parameters are given in Table III.A.2.1.

Conclusion

We demonstrated that, while operating a two-qubit thermoelectric engine with a measurement device substituting one of the heat baths is possible, an unselectively projected engine on both sides does not lead to a sustained work production. This illustrates Feynman’s considerations on the ratchet and pawl [215]: our measured system eventually reaches a state where it is equally probable for both qubits to be excited—similar to the ratchet and pawl being at the same temperature—and the energy quantum oscillates back and forth between the two sides. However, by adaptively measuring the system, we are able to sustainably generate work, as the periodic steady state of the system in this case allows for positive current production.

Our analysis offers helpful theoretical tools for analyzing the performance of such an engine, which can be used to find an optimal operation protocol using any set of positive operator valued measures (POVMs), for instance.

The quantum thermoelectric engine driven solely by measurements can be an interesting basis for experimental realization, especially in cases where the size of the device does not permit an efficient separation between the heat baths.



PART IV:

SUMMARY AND OUTLOOK

Summary and Outlook

Following in the footsteps of giants, I attempted to grasp the concept of heat and form a definition of its nature by investigating it from different perspectives at the microscopic level.

First, from an ion trapper's perspective, presented in Part II, where I took part in developing a cooling technique for calcium ion Coulomb crystals in a Paul trap. In this perspective heat is assimilated with temperature, and as high temperature is synonymous with a poor state definition, it is an undesirable. The driven micromotion, inherent to this type of traps, when excited by the cooling laser, leads to an increase in the temperature of the trapped ions. By pulsing the laser at the frequency of the micromotion, instead of applying continuous cooling, we were able to form colder crystals. We were thus able to avoid transferring heat to our system.

In Chapter II.1, an introduction to the field of ion trapping is given. Then, the theoretical grounds of ion trapping and Doppler cooling are set (Chapter II.2). In particular we showed that, by design, Paul traps were responsible for an emergence of a driven motion of the ions—the micromotion. Under the effects of the micromotion, the ions were shown to oscillate at the same frequency as the radio-frequency alternating field trapping them in the radial direction, and with an increasing amplitude with increasing distance from their equilibrium position. The modification of the optimal laser detuning for Doppler due to the presence of micromotion was presented. In (Chapter II.3), we described our system and experimental setup. In particular, we motivated the necessity of a new cooling strategy as our setup, where the cooling laser beam forms a 45° angle with the trap axis, which renders the excitation of micromotion unavoidable. The new strategy consisted in pulsing the laser at the RF frequency. The pulsed cooling optimization was presented in Chapter II.4. We showed that by carefully choosing the detuning and intensity of the cooling laser, as well

as the length and timing of the pulse, we were able to obtain Coulomb crystals at half the temperature of continuously cooled crystals. We also showed that this cooling procedure allowed us to form structures that would be unstable if continuously cooled, as they possess a large radial extension: large crystals of thousands of ions and radial discs—pancakes. In Chapter II.5 we presented the Molecular Dynamics simulation tool that allowed us to assess the temperature of our experimental crystals. We used this tool in Chapter II.6 to investigate the phase transition between the three-dimensional Coulomb crystal and the two-dimensional pancake including the effects of micromotion. The presence of micromotion did not seem to influence the ratio of axial to radial frequencies at which the transition occurred. A natural further step would be to test our predictions experimentally. The pulsed cooling scheme that we developed can be used to enhance the cooling efficiency of various systems, if they are subject to periodic driven motion.

Then, in Part III, I took the perspective of a quantum machinist.

Part III.A focuses on a two-qubit thermoelectric engine in which the two qubits are connected by a Josephson junction and each coupled to a heat bath. If operating favorably, the engine generates positive current at the junction by transfer of excitation from the hot qubit to the cold qubit. The bareness of the system allowed us to derive analytical expressions for its operation (Chapter III.A.2). In particular, we were able to describe the mean values and fluctuations of the electric work and heat transferred into the cold bath (Chapter III.A.3). We showed that for long operation times, the mean values and variances of work and heat are proportional: for each heat quantum $\hbar\omega_c$ transferred to the cold bath, work of 2 eV was generated by the engine. The derivation of the heat fluctuations lead us to describe the emission of heat into the cold bath by a photodetection process made by the bath, acting as a detector, on the cold qubit. In addition, we were able to follow the excitation traveling through the engine by calculating a selected set of two- and three-time correlation functions (Chapter III.A.4). We showed that for low values of the coupling to the baths, the excitation stays trapped in the system and travels back and forth between the hot and cold side, thus producing positive and negative current. The analytical tools that we developed, although applied to a specific system, can be used to examine the steady state and dynamical properties of a range of engine designs.

In Part III.B, the design of the engine was modified. Instead of being connected to a bath, one or both qubits were projectively measured. This new operation protocol was described in Chapter III.B.2. We first focused on an engine where the bath is substituted on only one side (Chapter III.B.3). We showed that, for an engine measured on the hot side, it was possible to find a measurement frequency and set of projection operators that allowed us to surpass the work output of the two-bath engine. The measurement on the cold side did not allow us to operate the machine durably, as the current eventually fell down to zero, the measurements heating up the cold qubit. It allowed us, however, to sustain the operation of a two-bath engine in steady state after the removal of the cold bath, offering a tradeoff between the duration of favorable operation and maximum amplitude of the current. We then turned our attention to an engine powered solely by measurements (Chapter III.B.4). In order to assess its performance, we derived the periodic steady state of the system—Sec.III.B.4.1. We showed that, for an unselectively measured engine, this state generated no current on average. However, the projection angles and the frequency of the measurements determined how fast the system would reach the periodic steady state—Sec. III.B.4.3. This incited us to modify our measurement strategy and, based on our observation of selective measurement trajectories, we designed an adaptive measurement scheme—Sec. III.B.4.4. We showed that in this situation, we could double the work output compared with the two-bath engine. The measurements were successfully replicating heat baths.

These investigations allowed me to see several aspects of heat at the microscopic level. If combined, a few common properties of heat arise. First, heat is provided by an external source acting on the system. Second, it induces excitation in the system. Finally, this excitation can have several manifestations—a faster motion, the generation of electric work, ... These properties lead me to form the following definition:

Heat is the additional excitation trapped in a system after the action of an external source.

A few questions then arise. If heat could be defined, what about work? While the separation between work and heat is intuitive macroscopically—work is what the system does, heat is the amount of energy it gains or loses that can allow it to do work—in the microscopic regime it is not as straightforward. Coming back to the example of the two-qubit engine

connected to an ancillary ladder investigated in Ref. [105], the excitation of the ladder is described as the work the system produces. However, this process could also be seen as heat transferred from the qubits to the ladder. Is it then really possible to give a general definition of work or should it remain specific to each situation? One could consider applying the same protocol and, operating the two-qubit engine with different working bodies.

Another question concerns the measuring process in itself. We claimed, in Sec. III.B.4.2, that we could use our setup to quantify the cost of the measurements and thus measuring a system was not free. Which measurement scheme would then be the best in terms of cost *vs.* work production, *i.e.* efficiency? One could also consider replacing the measurements by another process and use the system to assess its cost.

In a broader scope, the measured engine offers a possible alternative for the experimental realization of microscopic engines, where the separability of heat baths could be challenging to achieve.

To conclude this, not quite short, thesis, I would like to thank you, whomever you might be, for reading it, partially or in totality.

May you have any questions, you are welcome to contact me:

katerina.verteletsky@gmail.com.

APPENDIX

Quantum thermoelectric engine —rotating wave Hamiltonian derivation

In this Appendix, we derive the rotating wave Hamiltonian for the two-heat bath powered quantum thermoelectric engine described in Section III.A.2.1.

A.1 Pauli spin matrices

We recall the definitions of the Pauli spin matrices [216, 217]:

$$\sigma_x = \begin{pmatrix} 0 & 1 \\ 1 & 0 \end{pmatrix}, \quad \sigma_y = \begin{pmatrix} 0 & -i \\ i & 0 \end{pmatrix}, \quad \sigma_z = \begin{pmatrix} 1 & 0 \\ 0 & -1 \end{pmatrix} \quad (\text{A.1})$$

And ladder matrices [217] :

$$\sigma^+ = \frac{1}{2}(\sigma_x + i\sigma_y) = \begin{pmatrix} 0 & 1 \\ 0 & 0 \end{pmatrix}, \quad (\text{A.2})$$

$$\sigma^- = \frac{1}{2}(\sigma_x - i\sigma_y) = \begin{pmatrix} 0 & 0 \\ 1 & 0 \end{pmatrix} \quad (\text{A.3})$$

These matrices are defined assuming that the states are posed as:

$$|+\rangle = |1\rangle = \begin{pmatrix} 1 \\ 0 \end{pmatrix}, \quad (\text{A.4})$$

$$(\text{A.5})$$

$$|-\rangle = |0\rangle = \begin{pmatrix} 0 \\ 1 \end{pmatrix}$$

and thus the two-state density matrix would be:

$$\begin{matrix} \langle 1| & \langle 0| \\ |1\rangle & \begin{pmatrix} \rho_{11} & \rho_{10} \\ \rho_{01} & \rho_{00} \end{pmatrix}. \end{matrix} \quad (\text{A.6})$$

From our definition of the density matrix, we can see that our states are defined as:

$$|+\rangle = |1\rangle = \begin{pmatrix} 0 \\ 1 \end{pmatrix}, \quad (\text{A.7})$$

$$(\text{A.8})$$

$$|-\rangle = |0\rangle = \begin{pmatrix} 1 \\ 0 \end{pmatrix}. \quad (\text{A.9})$$

The two-state density matrix would be:

$$\begin{matrix} \langle 0| & \langle 1| \\ |0\rangle & \begin{pmatrix} \rho_{00} & \rho_{01} \\ \rho_{10} & \rho_{11} \end{pmatrix}. \\ |1\rangle & \end{matrix} \quad (\text{A.10})$$

Therefore, we should use the transpose of the σ^\pm matrices defined previously to account for the substitution. We also use the property: $(A \otimes B)^T = A^T \otimes B^T$ (reminder: $(AB)^T = B^T A^T$). The $\sigma_{x,y,z}$ operators in our case would thus be:

$$\sigma_x = [\sigma^+]^T + [\sigma^-]^T = \begin{pmatrix} 0 & 1 \\ 1 & 0 \end{pmatrix}, \quad (\text{A.11})$$

$$\sigma_y = -i([\sigma^+]^T - [\sigma^-]^T) = \begin{pmatrix} 0 & i \\ -i & 0 \end{pmatrix}, \quad (\text{A.12})$$

$$\sigma_z = [\sigma^+]^T[\sigma^-]^T - [\sigma^-]^T[\sigma^+]^T = \begin{pmatrix} -1 & 0 \\ 0 & 1 \end{pmatrix} \neq (\sigma_z^T). \quad (\text{A.13})$$

The last line is due to the product of ladder operators in σ_z giving rise to the non-linearity. The operators defined in this way preserve their properties applied to the vector form of our states.

Throughout our derivations, we make use of some helpful relations:

- $\sigma^+ |+\rangle = 0$; $\sigma^+ |-\rangle = |+\rangle$; $\sigma^- |+\rangle = |-\rangle$; $\sigma^- |-\rangle = 0$
- $(\sigma^+)^2 = 0$; $(\sigma^-)^2 = 0$
- $\sigma^+ + \sigma^- = \sigma_x$; $\sigma^+ - \sigma^- = i\sigma_y$
- $\sigma^+\sigma^- = \frac{1}{2}(\mathbb{1} + \sigma_z)$; $\sigma^-\sigma^+ = \frac{1}{2}(\mathbb{1} - \sigma_z)$
- $[\sigma^-, \sigma^+] = -[\sigma^+, \sigma^-] = -\sigma_z$
- $\{\sigma^+, \sigma^-\} = \{\sigma^-, \sigma^+\} = \mathbb{1}$

A.2 Derivation of the rotating wave hamiltonian

$\hbar = 1$ in the following equations.

Starting from the Hamiltonian in Eq. (III.A.2.2):

$$\begin{aligned} \hat{H} &= \hbar\omega_h \hat{\sigma}_h^+ \hat{\sigma}_h^- + \hbar\omega_c \hat{\sigma}_c^+ \hat{\sigma}_c^- & (\text{A.14}) \\ &\quad - E_J \cos(2eVt + 2\lambda_h(\hat{\sigma}_h^+ + \hat{\sigma}_h^-) + 2\lambda_c(\hat{\sigma}_c^+ + \hat{\sigma}_c^-)) \\ &= \frac{\omega_h}{2}(\mathbb{1} + \sigma_{z,h}) + \frac{\omega_c}{2}(\mathbb{1} + \sigma_{z,c}) - E_J \cos(2eVt + 2\lambda_h\sigma_{x,h} + 2\lambda_c\sigma_{x,c}) \end{aligned}$$

and using the unitary evolution operator:

$$\begin{aligned} U &= e^{i\omega_h\sigma_h^+\sigma_h^- + i\omega_c\sigma_c^+\sigma_c^-} \\ &= e^{i\frac{\omega_h t}{2}(\mathbb{1} + \sigma_{z,h}) + i\frac{\omega_c t}{2}(\mathbb{1} + \sigma_{z,c})} \\ &\equiv e^{i\frac{\omega_h t}{2}\sigma_{z,h} + i\frac{\omega_c t}{2}\sigma_{z,c}} & (\text{A.15}) \end{aligned}$$

where the last line is valid in the context of the rotating frame transformation. One can verify that $UU^\dagger = U^\dagger U = \mathbb{1}$.

The rotating picture Hamiltonian can be derived [36]:

$$\begin{aligned}
 \hat{H}_R &= \hat{U}\hat{H}\hat{U}^\dagger - i\hat{U}\frac{\partial\hat{U}^\dagger}{\partial t} \\
 &= -\frac{E_J}{2} \left(e^{2ieVt} e^{2i\lambda_h(\sigma_h^+ e^{i\omega_h t} + \sigma_h^- e^{-i\omega_h t})} e^{2i\lambda_c(\sigma_c^+ e^{i\omega_c t} + \sigma_c^- e^{-i\omega_c t})} \right. \\
 &\quad \left. + e^{-2ieVt} e^{-2i\lambda_h(\sigma_h^+ e^{i\omega_h t} + \sigma_h^- e^{-i\omega_h t})} e^{-2i\lambda_c(\sigma_c^+ e^{i\omega_c t} + \sigma_c^- e^{-i\omega_c t})} \right).
 \end{aligned} \tag{A.16}$$

Then, using the properties of the Pauli spin matrices as well as the Baker-Campbell-Hausdorff formula¹ [218] the Hamiltonian can be rewritten [219]:

$$\begin{aligned}
 \hat{H}_R &= -\frac{E_J}{2} e^{2ieVt} \left(\sum_{k=0}^{+\infty} \frac{(2i\lambda_h)^{2k}}{(2k)!} \sum_{l=0}^{+\infty} \frac{(2i\lambda_c)^{2l}}{(2l)!} \right. \\
 &\quad + \sum_{k=0}^{+\infty} \frac{(2i\lambda_h)^{2k}}{(2k)!} \sum_{l=0}^{+\infty} \frac{(2i\lambda_c)^{2l+1}}{(2l+1)!} (\sigma_c^+ e^{i\omega_c t} + \sigma_c^- e^{-i\omega_c t}) \\
 &\quad + \sum_{k=0}^{+\infty} \frac{(2i\lambda_h)^{2k+1}}{(2k+1)!} \sum_{l=0}^{+\infty} \frac{(2i\lambda_c)^{2l}}{(2l)!} (\sigma_h^+ e^{i\omega_h t} + \sigma_h^- e^{-i\omega_h t}) \\
 &\quad + \sum_{k=0}^{+\infty} \frac{(2i\lambda_h)^{2k+1}}{(2k+1)!} \sum_{l=0}^{+\infty} \frac{(2i\lambda_c)^{2l+1}}{(2l+1)!} \\
 &\quad \left. \times (\sigma_h^+ e^{i\omega_h t} + \sigma_h^- e^{-i\omega_h t}) (\sigma_c^+ e^{i\omega_c t} + \sigma_c^- e^{-i\omega_c t}) \right) \\
 &\quad + H.c.
 \end{aligned} \tag{A.17}$$

where *H.c.* is the Hermitian conjugate.

Assuming the resonant case: $\omega_h - \omega_c = 2eV$, and keeping only the resonant time-independent term (*i.e.* making the Rotating Wave Approximation), the Hamiltonian can be expressed as:

$$\hat{H}_{RWA} = \frac{E_J}{2} \sin(2\lambda_h) \sin(2\lambda_c) (\sigma_h^- \sigma_c^+ + \sigma_h^+ \sigma_c^-) \tag{A.18}$$

¹Writing $e^X e^Y = (e^X e^Y e^{-X}) e^X$ and using the equality $C e^A C^{-1} = e^{CAC^{-1}}$, one can rewrite: $(e^X e^Y e^{-X}) e^X = e^{e^X Y e^{-X}} e^X$. Then, using the Hadamard's lemma to the BCH formula: $e^X Y e^{-X} = Y + [X, Y] + \frac{1}{2!} [X, [X, Y]] + \frac{1}{3!} [X, [X, [X, Y]]] + \dots$ (that can be proven by Taylor expanding $f(t) = e^{tX} Y e^{-tX}$ around 0 and then setting $t = 1$), the original operator product can be rewritten: $e^X e^Y = e^{Y + [X, Y] + \frac{1}{2!} [X, [X, Y]] + \frac{1}{3!} [X, [X, [X, Y]]] + \dots} e^X$

Quantum thermoelectric engine —derivation of the steady state expectation value of the current

In this Appendix, we derive the steady state expectation value of the current for the two-heat bath powered quantum thermoelectric engine described in Part III.A.

We start from the current definition in Eq. (III.A.2.8):

$$\begin{aligned}\hat{I} &= \frac{2e}{i\hbar}[\hat{\sigma}_c^+\hat{\sigma}_c^-, \hat{H}_{RWA}] \\ &= -ieE_J \sin(2\lambda_h) \sin(2\lambda_c)(\hat{\sigma}_h^-\hat{\sigma}_c^+ - \hat{\sigma}_h^+\hat{\sigma}_c^-).\end{aligned}\tag{B.1}$$

It is an operator in the Heisenberg picture. Its expectation value can be evaluated in the Schrödinger picture by transferring the time dependence to the density matrix given by: $\langle \hat{I}(t) \rangle = \text{Tr}[\hat{\rho}(t)\hat{I}]$ [220]. Using the properties of the trace, it can be explicitly expressed as [221]:

$$\langle \hat{I}(t) \rangle = -ieE_J \sin(2\lambda_h) \sin(2\lambda_c)(\rho_{1001}(t) - \rho_{0110}(t))\tag{B.2}$$

The steady state expectation value of the current satisfies $\frac{d\langle\hat{I}(t)\rangle}{dt} = 0$, which explicitly reads:

$$\begin{aligned} \frac{d\langle\hat{I}(t)\rangle}{dt} &= \frac{d\text{Tr}[\hat{\rho}(t)\hat{I}]}{dt} \\ &= \text{Tr}\left[\frac{d\hat{\rho}(t)}{dt}\hat{I}\right] \\ &= -ieE_J \sin(2\lambda_h) \sin(2\lambda_c) \text{Tr}\left[\frac{d\hat{\rho}(t)}{dt}\hat{\sigma}_h^-\hat{\sigma}_c^+ - \frac{d\hat{\rho}(t)}{dt}\hat{\sigma}_h^+\hat{\sigma}_c^-\right] \\ &= 0. \end{aligned} \quad (\text{B.3})$$

where $\frac{d\hat{\rho}(t)}{dt}$ satisfies the master equation (III.A.2.5).

The time derivative of the current expectation value can be rewritten as a function of the spin number operators of the two qubits ($\hat{n}_h = \hat{\sigma}_h^+\hat{\sigma}_h^-$ and $\hat{n}_c = \hat{\sigma}_c^+\hat{\sigma}_c^-$):

$$\begin{aligned} \frac{d\langle\hat{I}(t)\rangle}{dt} &= -\left(\kappa_h\left(n_h^B + \frac{1}{2}\right) + \kappa_c\left(n_c^B + \frac{1}{2}\right)\right)\langle\hat{I}(t)\rangle \\ &\quad + 2e(E'_J)^2(\langle\hat{n}_h(t)\rangle - \langle\hat{n}_c(t)\rangle) \end{aligned} \quad (\text{B.4})$$

with $E'_J = E_J \sin(2\lambda_h) \sin(2\lambda_c)$.

For the qubit coupled to the bath α , $\langle\hat{n}_\alpha(t)\rangle = \text{Tr}[\hat{\rho}(t)\sigma_\alpha^+\sigma_\alpha^-]$ and its steady state expression can be found using :

$$\frac{d\langle\hat{n}_\alpha(t)\rangle}{dt} = -i\langle[\hat{n}_\alpha, \hat{H}_{RWA}]\rangle + \kappa_\alpha(n_\alpha^B - (2n_\alpha^B + 1)\langle n_\alpha^B \rangle) \quad (\text{B.5})$$

which leads to:

$$\begin{cases} \langle\hat{n}_h\rangle_{ss} = -\frac{\langle\hat{I}\rangle}{2e} \frac{1}{\kappa_h(2n_h^B+1)} + \frac{n_h^B}{2n_h^B+1} \\ \langle\hat{n}_c\rangle_{ss} = \frac{\langle\hat{I}\rangle}{2e} \frac{1}{\kappa_c(2n_c^B+1)} + \frac{n_c^B}{2n_c^B+1} \end{cases} \quad (\text{B.6})$$

Assuming $\kappa_h = \kappa_c = \kappa$, Eq. (B.4) and (B.6) can be combined to give the analytical expression for the steady state expectation value of the current given in Eq. (III.A.2.8):

$$\begin{aligned} \langle\hat{I}\rangle_{ss} &= \frac{e}{(n_h^B + n_c^B + 1)} \\ &\quad \times \frac{n_h^B - n_c^B}{\left[\frac{1}{\kappa} + \frac{\kappa}{(E'_J)^2}(2n_c^B + 1)(2n_h^B + 1)\right]}. \end{aligned} \quad (\text{B.7})$$

Quantum thermoelectric engine —derivation of the work fluctuations

In this Appendix, we derive the variance of the work produced by the engine described Sec. III.A.3.2.a.

We recall Eq. (III.A.3.4):

$$\text{Var}[W(\mathcal{T})] = \langle \hat{W}(\mathcal{T})^2 \rangle - \langle \hat{W}(\mathcal{T}) \rangle^2 \quad (\text{C.1})$$

where $\langle \hat{W}(\mathcal{T})^2 \rangle$ can be calculated from the two-time correlation function

of the current :

$$\begin{aligned}
 \langle \hat{W}(\mathcal{T})^2 \rangle &= V^2 \left\langle \left(\int_0^{\mathcal{T}} \hat{I}(t) dt \right) \left(\int_0^{\mathcal{T}} \hat{I}(t') dt' \right) \right\rangle \\
 &= V^2 \left\langle \int_0^{\mathcal{T}} \int_0^{\mathcal{T}} \hat{I}(t) \hat{I}(t') dt dt' \right\rangle \\
 &= V^2 \int_0^{\mathcal{T}} \int_0^{\mathcal{T}} \langle \hat{I}(t) \hat{I}(t') \rangle dt dt' \\
 &= V^2 \int_0^{\mathcal{T}} \left[\left(\int_0^{\mathcal{T}} \langle \hat{I}(t) \hat{I}(t') \rangle dt' \right)_{t' \geq t} + \left(\int_0^{\mathcal{T}} \langle \hat{I}(t) \hat{I}(t') \rangle dt' \right)_{t' < t} \right] dt \\
 &= V^2 \left(\int_0^{\mathcal{T}} \int_0^{\mathcal{T}} \langle \hat{I}(t) \hat{I}(t') \rangle dt' dt \right)_{t' \geq t} + V^2 \left(\int_0^{\mathcal{T}} \int_0^{\mathcal{T}} \langle \hat{I}(t) \hat{I}(t') \rangle dt' dt \right)_{t' < t} \\
 &= 2V^2 \left(\int_0^{\mathcal{T}} \int_0^{\mathcal{T}} \mathcal{R}e \left(\langle \hat{I}(t) \hat{I}(t') \rangle \right) dt' dt \right)_{t' \geq t} \tag{C.2}
 \end{aligned}$$

where we used the commutability of the expectation value and time integral operations, the time-dependence being held by the operators in the Heisenberg picture. The last line was calculating using, for $t' > t^1$:

$$\langle \hat{I}(t) \hat{I}(t') \rangle = \left(\langle \hat{I}(t') \hat{I}(t) \rangle \right)^* . \tag{C.3}$$

Then, using the substitution $t' = t + \tau, \tau \geq 0$:

$$\begin{aligned}
 \langle \hat{W}(\mathcal{T})^2 \rangle &= 2V^2 \left(\int_0^{\mathcal{T}} \int_0^{\mathcal{T}} \mathcal{R}e \left(\langle \hat{I}(t) \hat{I}(t') \rangle \right) dt' dt \right)_{t' \geq t} \\
 &= 2V^2 \left(\int_0^{\mathcal{T}} \int_0^{\mathcal{T}} \mathcal{R}e \left(\langle \hat{I}(t) \hat{I}(t + \tau) \rangle \right) d\tau dt \right. \\
 &\quad \left. - \int_0^{\mathcal{T}} \int_0^t \mathcal{R}e \left(\langle \hat{I}(t) \hat{I}(\mathcal{T} + \tau) \rangle \right) d\tau dt \right) . \tag{C.4}
 \end{aligned}$$

¹See end of section for a brief explanation

If the integration time \mathcal{T} is large enough, Eq. (C.4) becomes:

$$\begin{aligned}
 \langle \hat{W}(\mathcal{T})^2 \rangle_\infty &= \lim_{\mathcal{T} \rightarrow +\infty} 2V^2 \left(\int_0^\mathcal{T} \int_0^\mathcal{T} \mathcal{R}e \left(\langle \hat{I}(t) \hat{I}(t + \tau) \rangle \right) d\tau dt \right. \\
 &\quad \left. - \int_0^\mathcal{T} \int_0^t \mathcal{R}e \left(\langle \hat{I}(t) \hat{I}(\mathcal{T} + \tau) \rangle \right) d\tau dt \right) \\
 &\approx \lim_{\mathcal{T} \rightarrow +\infty} 2V^2 \left(\int_0^\mathcal{T} \int_0^\mathcal{T} \mathcal{R}e \left(\langle \hat{I}(t_{ss}) \hat{I}(t_{ss} + \tau) \rangle \right) d\tau dt \right. \\
 &\quad \left. - \mathcal{R}e \left(\langle \hat{I} \rangle_{ss} \right) \int_0^\mathcal{T} \int_0^t d\tau dt \right) \\
 &= \lim_{\mathcal{T} \rightarrow +\infty} 2V^2 \left(\int_0^\mathcal{T} \int_0^\mathcal{T} \mathcal{R}e \left(\langle \hat{I}(t_{ss}) \hat{I}(t_{ss} + \tau) \rangle \right) d\tau dt - \langle \hat{I} \rangle_{ss} \int_0^\mathcal{T} t dt \right) \\
 &= \lim_{\mathcal{T} \rightarrow +\infty} 2V^2 \left(\int_0^\mathcal{T} \int_0^\mathcal{T} \mathcal{R}e \left(\langle \hat{I}(t_{ss}) \hat{I}(t_{ss} + \tau) \rangle \right) d\tau dt - \langle \hat{I} \rangle_{ss} \frac{\mathcal{T}^2}{2} \right) \\
 &= \lim_{\mathcal{T} \rightarrow +\infty} 2V^2 \left(\int_0^\mathcal{T} \mathcal{R}e \left(\langle \hat{I}(t_{ss}) \hat{I}(t_{ss} + \tau) \rangle \right) d\tau \left(\int_0^\mathcal{T} dt \right) - \langle \hat{I} \rangle_{ss} \frac{\mathcal{T}^2}{2} \right) \\
 &= \lim_{\mathcal{T} \rightarrow +\infty} 2V^2 \mathcal{T} \left(\int_0^\mathcal{T} \mathcal{R}e \left(\langle \hat{I}(t_{ss}) \hat{I}(t_{ss} + \tau) \rangle \right) d\tau - \langle \hat{I} \rangle_{ss} \frac{\mathcal{T}}{2} \right) \\
 &= \lim_{\mathcal{T} \rightarrow +\infty} 2V^2 \mathcal{T} \left(\int_0^\mathcal{T} \left[\mathcal{R}e \left(\langle \hat{I}(t_{ss}) \hat{I}(t_{ss} + \tau) \rangle \right) - \frac{\langle \hat{I} \rangle_{ss}}{2} \right] d\tau \right) \quad (C.5)
 \end{aligned}$$

The variance at large \mathcal{T} is then given by (where the limits were dropped for notation simplicity):

$$\begin{aligned}
 Var[W(\mathcal{T})]_\infty &= \langle \hat{W}(\mathcal{T})^2 \rangle_\infty - \langle \hat{W}(\mathcal{T}) \rangle_\infty^2 \\
 &= V^2 \left(2\mathcal{T} \int_0^\mathcal{T} \left[\mathcal{R}e \left(\langle \hat{I}(t_{ss}) \hat{I}(t_{ss} + \tau) \rangle \right) - \frac{\langle \hat{I} \rangle_{ss}}{2} \right] d\tau \right) - V^2 \mathcal{T}^2 \langle \hat{I} \rangle_{ss}^2 \\
 &= V^2 \left[\left(2\mathcal{T} \int_0^\mathcal{T} \left[\mathcal{R}e \left(\langle \hat{I}(t_{ss}) \hat{I}(t_{ss} + \tau) \rangle \right) - \frac{\langle \hat{I} \rangle_{ss}}{2} \right] d\tau \right) - \mathcal{T}^2 \langle \hat{I} \rangle_{ss}^2 \right] \\
 &= 2V^2 \mathcal{T} \int_0^\mathcal{T} \left[\mathcal{R}e \left(\langle \hat{I}(t_{ss}) \hat{I}(t_{ss} + \tau) \rangle \right) - \langle \hat{I} \rangle_{ss}^2 \right] d\tau \quad (C.6)
 \end{aligned}$$

Complex conjugate of the current correlations

We recall Eq. (C.3):

$$\langle \hat{I}(t) \hat{I}(t') \rangle = \left(\langle \hat{I}(t') \hat{I}(t) \rangle \right)^*. \quad (C.7)$$

This expression can be proven as follows:

$$\begin{aligned}
 \left(\langle \hat{I}(t')\hat{I}(t) \rangle\right)^* &= \langle [\hat{I}(t')\hat{I}(t)]^\dagger \rangle \\
 &= \langle [\hat{I}(t)]^\dagger [\hat{I}(t')]^\dagger \rangle \\
 &= \langle [-ieE'_J(\hat{\sigma}_h^- \hat{\sigma}_c^+ - \hat{\sigma}_h^+ \hat{\sigma}_c^-)(t)]^\dagger [-ieE'_J(\hat{\sigma}_h^- \hat{\sigma}_c^+ - \hat{\sigma}_h^+ \hat{\sigma}_c^-)(t')]^\dagger \rangle \\
 &= \langle [ieE'_J(\hat{\sigma}_c^- \hat{\sigma}_h^+ - \hat{\sigma}_c^+ \hat{\sigma}_h^-)(t)] [ieE'_J(\hat{\sigma}_c^- \hat{\sigma}_h^+ - \hat{\sigma}_c^+ \hat{\sigma}_h^-)(t')] \rangle \\
 &= \langle [ieE'_J(\hat{\sigma}_c^- \hat{\sigma}_h^+ - \hat{\sigma}_c^+ \hat{\sigma}_h^-)(t)] [ieE'_J(\hat{\sigma}_c^- \hat{\sigma}_h^+ - \hat{\sigma}_c^+ \hat{\sigma}_h^-)(t')] \rangle \\
 &= \langle [ieE'_J(\hat{\sigma}_h^+ \hat{\sigma}_c^- - \hat{\sigma}_h^- \hat{\sigma}_c^+)(t)] [ieE'_J(\hat{\sigma}_h^+ \hat{\sigma}_c^- - \hat{\sigma}_h^- \hat{\sigma}_c^+)(t')] \rangle \\
 &= \langle [-\hat{I}(t)] [-\hat{I}(t')] \rangle \\
 &= \langle \hat{I}(t)\hat{I}(t') \rangle
 \end{aligned} \tag{C.8}$$

with $E'_J = E_J \sin(2\lambda_h) \sin(2\lambda_c)$.

Quantum thermoelectric engine —derivation of the heat fluctuations

In this Appendix, we derive the variance of the heat emitted into the cold bath described Sec. III.A.3.2.b

Following the definition of the integrated number of quanta detected in the cold bath in Eq. (III.A.3.7), its variance is given by:

$$\text{Var}[\mathcal{N}_c(\mathcal{T})] = \langle \mathcal{N}_c(\mathcal{T})^2 \rangle - \langle \mathcal{N}_c(\mathcal{T}) \rangle^2 \quad (\text{D.1})$$

Where $\langle \mathcal{N}_c(\mathcal{T})^2 \rangle$ can be calculated from the two-time correlation function of the cold bath field operator:

$$\begin{aligned} \langle \mathcal{N}_c(\mathcal{T})^2 \rangle &= \left\langle \left(\int_0^{\mathcal{T}} \hat{N}_c(t) dt \right) \left(\int_0^{\mathcal{T}} \hat{N}_c(t') dt' \right) \right\rangle \\ &= \left\langle \int_0^{\mathcal{T}} \int_0^{\mathcal{T}} \hat{N}_c(t) \hat{N}_c(t') dt dt' \right\rangle \\ &= \int_0^{\mathcal{T}} \int_0^{\mathcal{T}} \langle \hat{N}_c(t) \hat{N}_c(t') \rangle dt dt' \\ &= \int_0^{\mathcal{T}} \int_0^{\mathcal{T}} \langle \hat{a}_c^\dagger(t) \hat{a}_c(t) \hat{a}_c^\dagger(t') \hat{a}_c(t') \rangle dt dt' \quad (\text{D.2}) \end{aligned}$$

The two-time correlation function in this equation, $\langle \hat{a}_c^\dagger(t) \hat{a}_c(t) \hat{a}_c^\dagger(t') \hat{a}_c(t') \rangle$, is not normal nor time ordered. However, the cold bath acts as a detector for the cold qubit and the statistics of the total number of quanta entering it should follow Glauber's photo-detection principles (see Refs. [222] and [223] for an example of the derivation of the recorded photon intensity). Indeed, the probabilities of detection and emission, can be related to each other and are expressed as function of the time- and normal- ordered correlation functions (see Eqs. (III.A.3.9) and (III.A.3.10)).

The time ordered $\langle : \hat{a}_c^\dagger(t) \hat{a}_c(t) \hat{a}_c^\dagger(t') \hat{a}_c(t') : \rangle$ can be calculated using (derived from [149, 224])¹:

$$\begin{cases} [\hat{a}(t), \hat{a}^\dagger(t')] = \delta(t - t') \\ [\hat{a}(t), \hat{a}(t')] = [\hat{a}^\dagger(t), \hat{a}^\dagger(t')] = 0 \end{cases} \quad (\text{D.3})$$

If $t' \geq t$, $\langle : \hat{a}_c^\dagger(t) \hat{a}_c(t) \hat{a}_c^\dagger(t') \hat{a}_c(t') : \rangle = \langle \hat{a}_c^\dagger(t) \hat{a}_c^\dagger(t') \hat{a}_c(t') \hat{a}_c(t) \rangle$ and:

$$\langle \hat{a}_c^\dagger(t) \hat{a}_c(t) \hat{a}_c^\dagger(t') \hat{a}_c(t') \rangle = \langle \hat{a}_c^\dagger(t) \hat{a}_c^\dagger(t') \hat{a}_c(t') \hat{a}_c(t) \rangle + \delta(t - t') \langle \hat{a}_c^\dagger(t) \hat{a}_c(t') \rangle. \quad (\text{D.4})$$

If $t' < t$, $\langle : \hat{a}_c^\dagger(t) \hat{a}_c(t) \hat{a}_c^\dagger(t') \hat{a}_c(t') : \rangle = \langle \hat{a}_c^\dagger(t') \hat{a}_c^\dagger(t) \hat{a}_c(t) \hat{a}_c(t') \rangle$ and:

$$\langle \hat{a}_c^\dagger(t) \hat{a}_c(t) \hat{a}_c^\dagger(t') \hat{a}_c(t') \rangle = \langle \hat{a}_c^\dagger(t') \hat{a}_c^\dagger(t) \hat{a}_c(t) \hat{a}_c(t') \rangle + \delta(t - t') \langle \hat{a}_c^\dagger(t) \hat{a}_c(t') \rangle. \quad (\text{D.5})$$

Combining Eq. (D.4) and (D.5):

$$\langle \hat{a}_c^\dagger(t) \hat{a}_c(t) \hat{a}_c^\dagger(t') \hat{a}_c(t') \rangle = \langle : \hat{a}_c^\dagger(t) \hat{a}_c(t) \hat{a}_c^\dagger(t') \hat{a}_c(t') : \rangle + \delta(t - t') \langle \hat{a}_c^\dagger(t) \hat{a}_c(t') \rangle. \quad (\text{D.6})$$

Coming back to Eq. (D.2):

¹See end of section for a brief explanation

$$\begin{aligned}
\langle \mathcal{N}_c(\mathcal{T})^2 \rangle &= \int_0^{\mathcal{T}} \int_0^{\mathcal{T}} \langle \hat{a}_c^\dagger(t) \hat{a}_c(t) \hat{a}_c^\dagger(t') \hat{a}_c(t') \rangle dt dt' \\
&= \int_0^{\mathcal{T}} \int_0^{\mathcal{T}} \langle : \hat{a}_c^\dagger(t) \hat{a}_c(t) \hat{a}_c^\dagger(t') \hat{a}_c(t') : \rangle dt dt' \\
&\quad + \int_0^{\mathcal{T}} \int_0^{\mathcal{T}} \delta(t-t') \langle \hat{a}_c^\dagger(t') \hat{a}_c(t) \rangle dt dt' \\
&= \int_0^{\mathcal{T}} \int_0^{\mathcal{T}} \langle : \hat{a}_c^\dagger(t) \hat{a}_c(t) \hat{a}_c^\dagger(t') \hat{a}_c(t') : \rangle dt dt' \\
&\quad + \int_0^{\mathcal{T}} \langle \hat{a}_c^\dagger(t) \hat{a}_c(t) \rangle dt \\
&= \int_0^{\mathcal{T}} \int_0^{\mathcal{T}} \langle \hat{a}_c^+(t) \hat{a}_c^+(t') \hat{a}_c^-(t') \hat{a}_c^-(t) \rangle dt dt' + \int_0^{\mathcal{T}} \langle \hat{a}_c^+(t) \hat{a}_c^-(t) \rangle dt \\
&= \int_0^{\mathcal{T}} \left[\left(\int_0^{\mathcal{T}} \langle \hat{a}_c^+(t) \hat{a}_c^+(t') \hat{a}_c^-(t') \hat{a}_c^-(t) \rangle dt' \right)_{t' \geq t} \right. \\
&\quad \left. + \left(\int_0^{\mathcal{T}} \langle \hat{a}_c^+(t) \hat{a}_c^+(t') \hat{a}_c^-(t') \hat{a}_c^-(t) \rangle dt' \right)_{t' < t} \right] dt \\
&\quad + \int_0^{\mathcal{T}} \langle \hat{a}_c^+(t) \hat{a}_c^-(t) \rangle dt \\
&= 2 \left(\int_0^{\mathcal{T}} \int_0^{\mathcal{T}} \langle \hat{a}_c^+(t) \hat{a}_c^+(t') \hat{a}_c^-(t') \hat{a}_c^-(t) \rangle dt' dt \right)_{t' \geq t} \\
&\quad + \int_0^{\mathcal{T}} \langle \hat{a}_c^+(t) \hat{a}_c^-(t) \rangle dt \tag{D.7}
\end{aligned}$$

where the last line was derived using Eq. (D.3). Taking into account the fact that the field annihilation operator can be expressed by the emitter lowering operator:

$$\begin{aligned}
\langle \mathcal{N}_c(\mathcal{T})^2 \rangle &= 2\kappa_c^2 \left(\int_0^{\mathcal{T}} \int_0^{\mathcal{T}} \langle \hat{\sigma}_c^+(t) \hat{\sigma}_c^+(t') \hat{\sigma}_c^-(t') \hat{\sigma}_c^-(t) \rangle dt' dt \right)_{t' \geq t} \\
&\quad + \kappa_c \int_0^{\mathcal{T}} \langle \hat{\sigma}_c^+(t) \hat{\sigma}_c^-(t) \rangle dt. \tag{D.8}
\end{aligned}$$

$$\tag{D.9}$$

Substituting $t' = t + \tau$:

$$\begin{aligned}
 \langle \mathcal{N}_c(\mathcal{T})^2 \rangle &= 2\kappa_c^2 \left(\int_0^{\mathcal{T}} \int_0^{\mathcal{T}} \langle \hat{\sigma}_c^+(t) \hat{\sigma}_c^+(t + \tau) \hat{\sigma}_c^-(t + \tau) \hat{\sigma}_c^-(t) \rangle d\tau dt \right. \\
 &\quad \left. - \int_0^{\mathcal{T}} \int_0^t \langle \hat{\sigma}_c^+(t) \hat{\sigma}_c^+(\mathcal{T} + \tau) \hat{\sigma}_c^-(\mathcal{T} + \tau) \hat{\sigma}_c^-(t) \rangle d\tau dt \right) \\
 &\quad + \kappa_c \int_0^{\mathcal{T}} \langle \hat{\sigma}_c^+(t) \hat{\sigma}_c^-(t) \rangle dt \tag{D.10}
 \end{aligned}$$

If the integration time \mathcal{T} is large enough, Eq. (D.10) becomes (following

the derivation of Eq. (C.5)):

$$\begin{aligned}
\langle \mathcal{N}_c(\mathcal{T})^2 \rangle_\infty &= \lim_{\mathcal{T} \rightarrow +\infty} 2\kappa_c^2 \left(\int_0^{\mathcal{T}} \int_0^{\mathcal{T}} \langle \hat{\sigma}_c^+(t) \hat{\sigma}_c^+(t+\tau) \hat{\sigma}_c^-(t+\tau) \hat{\sigma}_c^-(t) \rangle d\tau dt \right. \\
&\quad \left. - \int_0^{\mathcal{T}} \int_0^t \langle \hat{\sigma}_c^+(t) \hat{\sigma}_c^+(\mathcal{T}+\tau) \hat{\sigma}_c^-(\mathcal{T}+\tau) \hat{\sigma}_c^-(t) \rangle d\tau dt \right) \\
&\quad + \kappa_c \int_0^{\mathcal{T}} \langle \hat{\sigma}_c^+(t) \hat{\sigma}_c^-(t) \rangle dt \\
&\approx \lim_{\mathcal{T} \rightarrow +\infty} 2\kappa_c^2 \left(\int_0^{\mathcal{T}} \int_0^{\mathcal{T}} \langle \hat{\sigma}_c^+(t_{ss}) \hat{\sigma}_c^+(t_{ss}+\tau) \hat{\sigma}_c^-(t_{ss}+\tau) \hat{\sigma}_c^-(t_{ss}) \rangle d\tau dt \right. \\
&\quad \left. - \langle \hat{n}_c \rangle_{ss} \frac{\mathcal{T}^2}{2} \right) \\
&\quad + \kappa_c \int_0^{\mathcal{T}} \langle \hat{\sigma}_c^+(t_{ss}) \hat{\sigma}_c^-(t_{ss}) \rangle dt \\
&= \lim_{\mathcal{T} \rightarrow +\infty} 2\kappa_c^2 \left(\int_0^{\mathcal{T}} \langle \hat{\sigma}_c^+(t_{ss}) \hat{\sigma}_c^+(t_{ss}+\tau) \hat{\sigma}_c^-(t_{ss}+\tau) \hat{\sigma}_c^-(t_{ss}) \rangle d\tau \left(\int_0^{\mathcal{T}} dt \right) \right. \\
&\quad \left. - \langle \hat{n}_c \rangle_{ss} \frac{\mathcal{T}^2}{2} \right) \\
&\quad + \kappa_c \langle \hat{\sigma}_c^+(t_{ss}) \hat{\sigma}_c^-(t_{ss}) \rangle \left(\int_0^{\mathcal{T}} dt \right) \\
&= \lim_{\mathcal{T} \rightarrow +\infty} 2\kappa_c^2 \mathcal{T} \left(\int_0^{\mathcal{T}} \langle \hat{\sigma}_c^+(t_{ss}) \hat{\sigma}_c^+(t_{ss}+\tau) \hat{\sigma}_c^-(t_{ss}+\tau) \hat{\sigma}_c^-(t_{ss}) \rangle d\tau \right. \\
&\quad \left. - \langle \hat{n}_c \rangle_{ss} \frac{\mathcal{T}}{2} \right) \\
&\quad + \kappa_c \mathcal{T} \langle \hat{n}_c \rangle_{ss} \\
&= \lim_{\mathcal{T} \rightarrow +\infty} 2\kappa_c^2 \mathcal{T} \left(\int_0^{\mathcal{T}} \left[\langle \hat{\sigma}_c^+(t_{ss}) \hat{\sigma}_c^+(t_{ss}+\tau) \hat{\sigma}_c^-(t_{ss}+\tau) \hat{\sigma}_c^-(t_{ss}) \rangle \right. \right. \\
&\quad \left. \left. - \frac{\langle \hat{n}_c \rangle_{ss}}{2} \right] d\tau \right) \\
&\quad + \kappa_c \mathcal{T} \langle \hat{n}_c \rangle_{ss} \tag{D.11}
\end{aligned}$$

The variance at large \mathcal{T} is then given by (where the limits were dropped

for notation simplicity, see Eq. (6) in Ref. [151] for comparison):

$$\begin{aligned}
 \text{Var}[\mathcal{N}_c(\mathcal{T})]_\infty &= \langle \mathcal{N}_c(\mathcal{T})^2 \rangle_\infty - \langle \mathcal{N}_c(\mathcal{T}) \rangle_\infty^2 \\
 &= 2\kappa_c^2 \mathcal{T} \left(\int_0^{\mathcal{T}} \left[\langle \hat{\sigma}_c^+(t_{ss}) \hat{\sigma}_c^+(t_{ss} + \tau) \hat{\sigma}_c^-(t_{ss} + \tau) \hat{\sigma}_c^-(t_{ss}) \rangle - \frac{\langle \hat{n}_c \rangle_{ss}}{2} \right] d\tau \right) \\
 &\quad + \kappa_c \mathcal{T} \langle \hat{n}_c \rangle_{ss} - \kappa_c^2 \mathcal{T}^2 \langle \hat{n}_c \rangle_{ss}^2 \\
 &= 2\kappa_c^2 \mathcal{T} \left(\left[\langle \hat{\sigma}_c^+(t_{ss}) \hat{\sigma}_c^+(t_{ss} + \tau) \hat{\sigma}_c^-(t_{ss} + \tau) \hat{\sigma}_c^-(t_{ss}) \rangle - \frac{\langle \hat{n}_c \rangle_{ss}}{2} \right] \right. \\
 &\quad \left. - \mathcal{T} \frac{\langle \hat{n}_c \rangle_{ss}^2}{2} \right) \\
 &\quad + \kappa_c \mathcal{T} \langle \hat{n}_c \rangle_{ss} \\
 &= 2\kappa_c^2 \mathcal{T} \left(\int_0^{\mathcal{T}} \left[\langle \hat{\sigma}_c^+(t_{ss}) \hat{\sigma}_c^+(t_{ss} + \tau) \hat{\sigma}_c^-(t_{ss} + \tau) \hat{\sigma}_c^-(t_{ss}) \rangle - \langle \hat{n}_c \rangle_{ss}^2 \right] d\tau \right) \\
 &\quad + \kappa_c \mathcal{T} \langle \hat{n}_c \rangle_{ss} \tag{D.12}
 \end{aligned}$$

Multiplying by the energy carried by each quantum of heat, $\hbar\omega_c$, we recover the variance of the heat dissipated into the cold bath for long time intervals \mathcal{T} :

$$\begin{aligned}
 \text{Var}[Q_c(\mathcal{T})]_\infty &= (\hbar\omega_c)^2 \left(2\kappa_c^2 \mathcal{T} \int_0^{\mathcal{T}} \left[\langle \hat{\sigma}_c^+(t) \hat{\sigma}_c^+(t + \tau) \hat{\sigma}_c^-(t + \tau) \hat{\sigma}_c^-(t) \rangle_{ss} \right. \right. \\
 &\quad \left. \left. - \langle \hat{\sigma}_c^+(t) \hat{\sigma}_c^-(t) \rangle_{ss}^2 \right] d\tau \right. \\
 &\quad \left. + \kappa_c \mathcal{T} \langle \hat{\sigma}_c^+(t) \hat{\sigma}_c^-(t) \rangle_{ss} \right). \tag{D.13}
 \end{aligned}$$

Commutation relations for the field operators

The common field commutation relations used in the derivation of the heat fluctuations are derived in Refs. [150, 224, 225]:

$$\begin{cases} [\hat{a}(t), \hat{a}^\dagger(t')] = \delta(t - t') \\ [\hat{a}(t), \hat{a}(t')] = [\hat{a}^\dagger(t), \hat{a}^\dagger(t')] = 0 \end{cases} \tag{D.14}$$

To summarize the derivation procedure, we shall consider the creation operator of an excitation in the field decomposed over the wave vectors \mathbf{k} :

$$A^-(\mathbf{r}, t) = \sum_{\mathbf{k}, l} K_{\mathbf{k}, l} a_{\mathbf{k}, l}^\dagger e^{-i(\mathbf{k} \cdot \mathbf{r} - \omega_k t)} \quad (\text{D.15})$$

where $K_{\mathbf{k}, l}$ is a proportionality constant, \mathbf{k} is the wave vector associated to the mode of frequency ω_k and l the polarization. \mathbf{r} and t indicate the point in space-time at which the field is evaluated. The term in $e^{\pm(i\omega_k t)}$ arises from the time evolution of the given oscillator mode which reads: $a_{\mathbf{k}, l}^\dagger(t) = a_{\mathbf{k}, l}^\dagger(0)e^{-i\omega_k t}$ and $a_{\mathbf{k}, l}(t) = a_{\mathbf{k}, l}(0)e^{i\omega_k t}$. The commutator of the field operators thus satisfies:

$$\begin{aligned} [A^+(\mathbf{r}, t), A^-(\mathbf{r}', t')] &= \sum_{\mathbf{k}, l} \sum_{\mathbf{k}', l'} K_{\mathbf{k}, l} K_{\mathbf{k}', l'} [a_{\mathbf{k}, l} e^{i(\mathbf{k} \cdot \mathbf{r} - \omega_k t)}, a_{\mathbf{k}', l'}^\dagger e^{-i(\mathbf{k}' \cdot \mathbf{r}' - \omega_{k'} t')}] \\ &= \sum_{\mathbf{k}, l} \sum_{\mathbf{k}', l'} K_{\mathbf{k}, l} K_{\mathbf{k}', l'} [a_{\mathbf{k}, l}, a_{\mathbf{k}', l'}^\dagger] e^{i(\mathbf{k} \cdot \mathbf{r} - \omega_k t)} e^{-i(\mathbf{k}' \cdot \mathbf{r}' - \omega_{k'} t')} \end{aligned} \quad (\text{D.16})$$

where $a_{\mathbf{k}', l'}^\dagger$ and $a_{\mathbf{k}, l}$ are the usual bosonic creation and annihilation operators satisfying $[a_{\mathbf{k}, l}, a_{\mathbf{k}', l'}^\dagger] = \delta(\mathbf{k}, \mathbf{k}')$. Assuming a fine \mathbf{k} grid, the sum may be rewritten as an integral and, for $\mathbf{r} = \mathbf{r}'$, we recognize the Dirac delta function and recover $[\hat{a}(t), \hat{a}^\dagger(t')] = \delta(t - t')$.

The same procedure can be followed to derive the second commutation relation in Eq. (D.14).

Quantum thermoelectric engine —note on Glauber’s photodetection theory

In this Appendix, we provide a quick introduction to Glauber’s photodetection theory [127] introduced in Sec. III.A.3.2.b.i.

The emission to/from one of the photon baths is a detection process. As defined by Glauber [127] and described in Ref. [226], photon detectors mostly rely on a photo-absorption process (a photon is absorbed and an electron, which will be detected, is ejected by photo-electric effect for instance). Therefore, the detection process is a photon annihilation process. This argument is foundation for Glauber’s theory of time and normal ordering of photon creation and annihilation operators in the subsequent detection of two photons at two different times.

If the field can be described by $E(\mathbf{r}, t) = E^+(\mathbf{r}, t) + E^-(\mathbf{r}, t)$ where $E^+(\mathbf{r}, t) = (E^-(\mathbf{r}, t))^\dagger$ and $E^+(\mathbf{r}, t)|0\rangle = 0$ is the photon annihilation operator and the detector is ideal (negligible size, photo-absorption probability independent on the frequency), then the rate at which photons are detected (*i.e.* the probability per time at which a photon of polarization μ is absorbed at a point \mathbf{r} and time t) is proportional to:

$$\begin{aligned}
 \sum_f |\langle f | E_\mu^+(\mathbf{r}, t) | i \rangle|^2 &= \sum_f (\langle f | E_\mu^+(\mathbf{r}, t) | i \rangle)^\dagger \langle f | E_\mu^+(\mathbf{r}, t) | i \rangle \\
 &= \sum_f \langle i | E_\mu^-(\mathbf{r}, t) | f \rangle \langle f | E_\mu^+(\mathbf{r}, t) | i \rangle \\
 &= \langle i | E_\mu^-(\mathbf{r}, t) E_\mu^+(\mathbf{r}, t) | i \rangle
 \end{aligned} \tag{E.1}$$

where $|i\rangle$ is the initial state and $|f\rangle$ a final state where one photon has been absorbed and $\langle f | E_\mu^+(\mathbf{r}, t) | i \rangle$ is the field matrix element for the transition. Therefore, the detector measures $\langle E_\mu^-(\mathbf{r}, t) E_\mu^+(\mathbf{r}, t) \rangle$.

If two detectors situated at \mathbf{r} and \mathbf{r}' record photons at the respective times t and t' ($t' > t$), then the detection rate is proportional to:

$$\sum_f |\langle f | E_\mu^+(\mathbf{r}', t') E_\mu^+(\mathbf{r}, t) | i \rangle|^2 = \langle i | E_\mu^-(\mathbf{r}, t) E_\mu^-(\mathbf{r}', t') E_\mu^+(\mathbf{r}, t) E_\mu^+(\mathbf{r}', t') | i \rangle \tag{E.2}$$

The field can be described as a function of a and a^\dagger operators: $E_\mu^+(\mathbf{r}, t) = (\Gamma a)(\mathbf{r}, t)$ (see Ref. [225] for a proof of the proportionality between the field vector and the ladder operators¹). Thus, the detection rate is measured by $a^\dagger a$ and is proportional to, in the case of two photons being detected at 2 times t' and t by the same detector:

$$\begin{aligned}
 \langle I(\mathbf{r}, t') I(\mathbf{r}, t) \rangle &= \sum_f |\langle f | (\Gamma a)(\mathbf{r}, t') (\Gamma a)(\mathbf{r}, t) | i \rangle|^2 \\
 &= \langle i | (\Gamma^\dagger a^\dagger)(\mathbf{r}, t) (\Gamma^\dagger a^\dagger)(\mathbf{r}, t') (\Gamma a)(\mathbf{r}, t') (\Gamma a)(\mathbf{r}, t) | i \rangle \\
 &= \langle i | (\Gamma^\dagger a^\dagger)(t) (\Gamma^\dagger a^\dagger)(t') (\Gamma a)(t') (\Gamma a)(t) | i \rangle
 \end{aligned} \tag{E.3}$$

where $\hat{I}(\mathbf{r}, t) = (\Gamma a)(\mathbf{r}, t) (\Gamma a)^\dagger(\mathbf{r}, t)$, the field intensity operator. One can define $\hat{n}(V, t) = \int_V \hat{I}(\mathbf{r}, t) d^3r$ —with V a finite volume, the configuration space photon number operator and show that $[\hat{a}_{k,s}^\dagger, \hat{a}_{k',s'}, \hat{n}] = 0$ (with k the wave number and s the polarization) [224].

¹It is shown in Ref. [225] that: $4\pi^2 A_{k,l,t} = c\sqrt{hs_k/\nu_k} \eta_{k,l,t}$ with $A_{k,l,t} = A_{k,l} e^{2\pi i \nu_k t}$ the dynamical component of the vector potential for wave vector k and polarization l ; $\eta_{k,l,t}$ the Heisenberg dynamical variable of the harmonic oscillator and s_k the density of discrete k values.

If the state is described by a density matrix ρ , then Eq. E.3 becomes:

$$\langle I(t')I(t) \rangle = Tr[\rho(\Gamma^\dagger a^\dagger)(t)(\Gamma^\dagger a^\dagger)(t')(\Gamma a)(t')(\Gamma a)(t)]. \quad (\text{E.4})$$

Thus, the ordering of the operators that is relevant to a detection rate is: all creation operators on the left and all annihilation operators on the right with creation operators ordered by increasing time and annihilation operators by decreasing time.

In our case, we consider an ideal detector able to count the excitations and de-excitations from the corresponding qubits—with infinite detection area and adjoined to the qubit (see Refs. [225], [149] and [224] for the derivation of the relation between the field vector and ladder operators).

Quantum thermoelectric engine —derivation of the two-time correlations

In this Appendix, we derive the two-time correlation functions introduced in Sec III.A.4.1

F.1 Hot bath–current correlations

The two-time correlations between the heat extraction from the hot bath and the current through the junction is given by:

$$F_{hI}^{(2)}(t, \tau) = \langle \hat{\sigma}_h^-(t) \hat{I}(t + \tau) \hat{\sigma}_h^+(t) \rangle. \quad (\text{F.1})$$

Assuming that the system has reached steady state at the earliest time

t , it can be expressed as:

$$\begin{aligned}
 F_{hI}^{(2)}(t = t_{ss}, \tau) &= \langle \hat{\sigma}_h^-(t) \hat{I}(t + \tau) \hat{\sigma}_h^+(t) \rangle_{ss} \\
 &= \text{Tr}[\rho_{ss} \hat{\sigma}_h^-(t_{ss}) \hat{I}(t_{ss} + \tau) \hat{\sigma}_h^+(t_{ss})] \\
 &= \text{Tr}[\hat{I}(t_{ss} + \tau) \hat{\sigma}_h^+ \rho_{ss} \hat{\sigma}_h^-] \\
 &= \text{Tr}[\hat{I} \tilde{\rho}^{hI}(t_{ss} + \tau)] \\
 &= -ieE_J \sin(2\lambda_h) \sin(2\lambda_c) \\
 &\quad \times (\tilde{\rho}_{1001}^{hI}(t_{ss} + \tau) - \tilde{\rho}_{0110}^{hI}(t_{ss} + \tau))
 \end{aligned} \tag{F.2}$$

where $\tilde{\rho}^{hI}(t_{ss} + \tau)$ satisfies the master equation Eq. (III.A.2.5) and has the initial condition:

$$\tilde{\rho}^{hI}(t_{ss}) = \hat{\sigma}_h^+ \rho_{ss} \hat{\sigma}_h^-. \tag{F.3}$$

The infinite time limits are given by:

$$\begin{aligned}
 \lim_{\tau \rightarrow \infty} \tilde{\rho}^{hI}(t_{ss} + \tau) &= \langle \hat{\sigma}_h^- \hat{\sigma}_h^+ \rangle_{ss} \rho_{ss} \\
 &= (\rho_{0000,ss} + \rho_{0011,ss}) \rho_{ss}
 \end{aligned} \tag{F.4}$$

and:

$$\begin{aligned}
 \lim_{\tau \rightarrow \infty} F_{hI}^{(2)}(t_{ss}, \tau) &= \langle \hat{I} \rangle_{ss} \langle \hat{\sigma}_h^- \hat{\sigma}_h^+ \rangle_{ss} \\
 &= -ieE_J \sin(2\lambda_h) \sin(2\lambda_c) \\
 &\quad \times (\rho_{1001,ss} - \rho_{0110,ss}) (\rho_{0000,ss} + \rho_{0011,ss}).
 \end{aligned} \tag{F.5}$$

F.2 Current–cold bath correlations

The two-time correlation between the current through the junction and the heat emission into the cold bath is given by:

$$F_{Ic}^{(2)}(t, \tau) = \langle \hat{I}(t) \hat{\sigma}_c^+(t + \tau) \hat{\sigma}_c^-(t + \tau) \rangle. \tag{F.6}$$

Assuming that the system has reached steady state at the earliest time, it can be expressed as:

$$\begin{aligned}
 F_{Ic}^{(2)}(t_{ss}, \tau) &= \langle \hat{I}(t) \hat{\sigma}_c^+(t + \tau) \hat{\sigma}_c^-(t + \tau) \rangle_{ss} \\
 &= \text{Tr}[\rho_{ss} \hat{\sigma}_c^+(t_{ss} + \tau) \hat{\sigma}_c^-(t_{ss} + \tau) \hat{I}(t_{ss})] \\
 &= \text{Tr}[\hat{\sigma}_c^-(t_{ss} + \tau) \hat{I} \rho_{ss} \hat{\sigma}_c^+(t_{ss} + \tau)] \\
 &= \text{Tr}[\hat{\sigma}_c^- \tilde{\rho}^{Ic}(t_{ss} + \tau) \hat{\sigma}_c^+(t_{ss} + \tau)] \\
 &= \tilde{\rho}_{0011}^{Ic}(t_{ss} + \tau) + \tilde{\rho}_{1111}^{Ic}(t_{ss} + \tau)
 \end{aligned} \tag{F.7}$$

where $\tilde{\rho}^{Ic}(t_{ss} + \tau)$ satisfies the master equation Eq. (III.A.2.5) and has the initial condition:

$$\tilde{\rho}^{Ic}(t_{ss}) = \hat{I}\rho_{ss}. \quad (\text{F.8})$$

The infinite time limits are given by:

$$\begin{aligned} \lim_{\tau \rightarrow \infty} \tilde{\rho}^{Ic}(t_{ss} + \tau) &= \langle \hat{I} \rangle_{ss} \rho_{ss} \\ &= -ieE_J \sin(2\lambda_h) \sin(2\lambda_c) (\rho_{1001,ss} - \rho_{0110,ss}) \rho_{ss} \end{aligned} \quad (\text{F.9})$$

and:

$$\begin{aligned} \lim_{\tau \rightarrow \infty} F_{Ic}^{(2)}(t_{ss}, \tau) &= \langle \hat{I} \rangle_{ss} \langle \hat{\sigma}_c^+ \hat{\sigma}_c^- \rangle_{ss} \\ &= -ieE_J \sin(2\lambda_h) \sin(2\lambda_c) \\ &\quad \times (\rho_{1001,ss} - \rho_{0110,ss}) (\rho_{0011,ss} + \rho_{1111,ss}). \end{aligned} \quad (\text{F.10})$$

F.3 Hot bath–cold bath correlations

The two-time correlation between the heat extraction from the hot bath and the heat emission into the cold bath is given by:

$$F_{hc}^{(2)}(t, \tau) = \langle \hat{\sigma}_h^-(t) \hat{\sigma}_c^+(t + \tau) \hat{\sigma}_c^-(t + \tau) \hat{\sigma}_h^+(t) \rangle. \quad (\text{F.11})$$

Assuming that the system has reached steady state at the earliest time, it can be expressed as:

$$\begin{aligned} F_{hc}^{(2)}(t_{ss}, \tau) &= \langle \hat{\sigma}_h^-(t) \hat{\sigma}_c^+(t + \tau) \hat{\sigma}_c^-(t + \tau) \hat{\sigma}_h^+(t) \rangle_{ss} \\ &= \langle \hat{\sigma}_h^-(t_{ss}) \hat{\sigma}_c^+(t_{ss} + \tau) \hat{\sigma}_c^-(t_{ss} + \tau) \hat{\sigma}_h^+(t_{ss}) \rangle \\ &= \text{Tr}[\hat{\sigma}_c^-(t_{ss} + \tau) \hat{\sigma}_h^+ \rho_{ss} \hat{\sigma}_h^- \hat{\sigma}_c^+(t_{ss} + \tau)] \\ &= \text{Tr}[\hat{\sigma}_c^- \tilde{\rho}^{hc}(t_{ss} + \tau) \hat{\sigma}_c^+] \\ &= \tilde{\rho}_{0011}^{hc}(t_{ss} + \tau) + \tilde{\rho}_{1111}^{hc}(t_{ss} + \tau) \end{aligned} \quad (\text{F.12})$$

where $\tilde{\rho}^{hc}(t_{ss} + \tau)$ satisfies the master equation Eq. (III.A.2.5) and has the initial condition:

$$\tilde{\rho}^{hc}(t_{ss}) = \hat{\sigma}_h^+ \rho_{ss} \hat{\sigma}_h^-. \quad (\text{F.13})$$

The infinite time limits are thus given by:

$$\begin{aligned} \lim_{\tau \rightarrow \infty} \tilde{\rho}^{hc}(t_{ss} + \tau) &= \langle \hat{\sigma}_h^- \hat{\sigma}_h^+ \rangle_{ss} \rho_{ss} \\ &= (\rho_{0000,ss} + \rho_{0011,ss}) \rho_{ss} \end{aligned} \quad (\text{F.14})$$

and:

$$\begin{aligned} \lim_{\tau \rightarrow \infty} F_{hc}^{(2)}(t_{ss}, \tau) &= \langle \hat{\sigma}_h^- \hat{\sigma}_h^+ \rangle_{ss} \langle \hat{\sigma}_c^+ \hat{\sigma}_c^- \rangle_{ss} \\ &= (\rho_{0000,ss} + \rho_{0011,ss})(\rho_{0011,ss} + \rho_{1111,ss}). \end{aligned} \quad (\text{F.15})$$

Quantum thermoelectric engine —derivation of the three-time correlations

In this Appendix, we derive the three-time correlation functions described in Sec III.A.4.2

G.1 Hot bath three-time correlations

G.1.a Derivation

The three-time correlation of the emission from the hot bath in the system of 2 qubits can be derived in a similar manner. It is given by:

$$\begin{aligned}
 F_{hhh}^{(3)}(t, \tau_1, \tau_2) &= \langle \hat{\sigma}_h^-(t) \hat{\sigma}_h^-(t + \tau_1) \hat{\sigma}_h^-(t + \tau_1 + \tau_2) \\
 &\quad \times \hat{\sigma}_h^+(t + \tau_1 + \tau_2) \hat{\sigma}_h^+(t + \tau_1) \hat{\sigma}_h^+(t) \rangle
 \end{aligned}
 \tag{G.1}$$

Assuming that the system has reached steady state at the moment of detection and following the method described previously:

$$\begin{aligned}
F_{hhh}^{(3)}(t_{ss}, \tau_1, \tau_2) &= \langle \hat{\sigma}_h^-(t) \hat{\sigma}_h^-(t + \tau_1) \\
&\quad \times \hat{\sigma}_h^-(t + \tau_1 + \tau_2) \hat{\sigma}_h^+(t + \tau_1 + \tau_2) \hat{\sigma}_h^+(t + \tau_1) \hat{\sigma}_h^+(t) \rangle_{ss} \\
&= \text{Tr}[\rho_{ss} \hat{\sigma}_h^-(t_{ss}) \hat{\sigma}_h^-(t_{ss} + \tau_1) \hat{\sigma}_h^-(t_{ss} + \tau_1 + \tau_2) \\
&\quad \times \hat{\sigma}_h^+(t_{ss} + \tau_1 + \tau_2) \hat{\sigma}_h^+(t_{ss} + \tau_1) \hat{\sigma}_h^+(t_{ss})] \\
&= \text{Tr}[\hat{\sigma}_h + (t_{ss} + \tau_1 + \tau_2) \hat{\sigma}_h + (t_{ss} + \tau_1) \hat{\sigma}_h^+ \rho_{ss} \hat{\sigma}_h^- \\
&\quad \times \hat{\sigma}_h^-(t_{ss} + \tau_1) \hat{\sigma}_h^-(t_{ss} + \tau_1 + \tau_2)] \\
&= \text{Tr}[\hat{\sigma}_h + (t_{ss} + \tau_1 + \tau_2) \hat{\sigma}_h + \tilde{\rho}_1^{hhh}(t_{ss} + \tau_1) \hat{\sigma}_h^- \\
&\quad \times \hat{\sigma}_h^-(t_{ss} + \tau_1 + \tau_2)] \\
&= \text{Tr}[\hat{\sigma}_h + \tilde{\rho}_2^{hhh}(t_{ss} + \tau_1 + \tau_2) \hat{\sigma}_h^-] \\
&= \tilde{\rho}_{2,0000}^{hhh}(t_{ss} + \tau_1 + \tau_2) + \tilde{\rho}_{2,0011}^{hhh}(t_{ss} + \tau_1 + \tau_2)
\end{aligned} \tag{G.2}$$

Where $\tilde{\rho}_1^{hhh}(t_{ss} + \tau_1)$ satisfies the master equation Eq. (III.A.2.5) and has the initial condition:

$$\tilde{\rho}_1^{hhh}(t_{ss}) = \hat{\sigma}_h^+ \rho_{ss} \hat{\sigma}_h^- \tag{G.3}$$

Then :

$$\hat{\sigma}_h^+(t_{ss} + \tau_1) \tilde{\rho}_1^{hhh}(t_{ss} + \tau_1) \hat{\sigma}_h^-(t_{ss} + \tau_1) = \hat{\sigma}_h^+ \tilde{\rho}_1^{hhh}(t_{ss} + \tau_1) \hat{\sigma}_h^- \tag{G.4}$$

And $\tilde{\rho}_2^{hhh}(t_{ss} + \tau_1 + \tau_2)$ satisfies the master equation and has for initial condition:

$$\tilde{\rho}_2^{hhh}(t_{ss} + \tau_1) = \hat{\sigma}_h^+ \tilde{\rho}_1^{hhh}(t_{ss} + \tau_1) \hat{\sigma}_h^- \tag{G.5}$$

Then :

$$\begin{aligned}
\hat{\sigma}_h^+(t_{ss} + \tau_1 + \tau_2) \tilde{\rho}_2^{hhh}(t_{ss} + \tau_1 + \tau_2) \hat{\sigma}_h^-(t_{ss} + \tau_1 + \tau_2) \\
= \hat{\sigma}_h^+ \tilde{\rho}_2^{hhh}(t_{ss} + \tau_1 + \tau_2) \hat{\sigma}_h^-
\end{aligned} \tag{G.6}$$

The infinite time limits are thus given by :

$$\begin{aligned} \lim_{\tau_1, \tau_2 \rightarrow \infty} \tilde{\rho}_2^{hhh}(t_{ss} + \tau_1 + \tau_2) &= \langle \hat{\sigma}_h^- \hat{\sigma}_h^+ \rangle_{ss}^2 \rho_{ss} \\ &= (\rho_{0000,ss} + \rho_{0011,ss})^2 \rho_{ss} \end{aligned}$$

And :

$$\begin{aligned} \lim_{\tau_1 \rightarrow \infty} F_{hhh}^{(3)}(t_{ss}, \tau_1, \tau_2) &= \langle \hat{\sigma}_h^-(t) \hat{\sigma}_h^-(t + \tau_2) \hat{\sigma}_h^+(t + \tau_2) \hat{\sigma}_h^+(t) \rangle_{ss} \langle \hat{\sigma}_h^- \hat{\sigma}_h^+ \rangle_{ss} \\ \lim_{\tau_2 \rightarrow \infty} F_{hhh}^{(3)}(t_{ss}, \tau_1, \tau_2) &= \langle \hat{\sigma}_h^-(t) \hat{\sigma}_h^-(t + \tau_1) \hat{\sigma}_h^+(t + \tau_1) \hat{\sigma}_h^+(t) \rangle_{ss} \langle \hat{\sigma}_h^- \hat{\sigma}_h^+ \rangle_{ss} \\ \lim_{\tau_1, \tau_2 \rightarrow \infty} F_{hhh}^{(3)}(t_{ss}, \tau_1, \tau_2) &= \langle \hat{\sigma}_h^- \hat{\sigma}_h^+ \rangle_{ss}^3 \\ &= (\rho_{0000,ss} + \rho_{0011,ss})^3 \end{aligned} \tag{G.7}$$

G.1.b Pure three-body contributions

Similarly to the derivation of $g_{c,p}^{(3)}$, the pure three body contribution, $g_{h,p}^{(3)}$, can be derived for the emission from the hot bath correlations:

$$\begin{aligned} g_{h,p}^{(3)} &= 2 + g_h^{(3)}(t, t + \tau_1, t + \tau_1 + \tau_2) - g_h^{(2)}(t, t + \tau_1) - g_h^{(2)}(t, t + \tau_1 + \tau_2) \\ &\quad - g_h^{(2)}(t + \tau_1, t + \tau_1 + \tau_2) \end{aligned} \tag{G.8}$$

Where, for $t = t_{ss}$:

$$g_h^{(3)}(t_{ss}, t_{ss} + \tau_1, t_{ss} + \tau_1 + \tau_2) = \frac{F_{hhh}^{(3)}(t_{ss}, \tau_1, \tau_2)}{\langle \hat{\sigma}_h^- \hat{\sigma}_h^+ \rangle_{ss}^3} \tag{G.9}$$

And, for $t_i \geq t_{ss}$:

$$g_h^{(2)}(t_i, t_i + \tau_j) = \frac{\langle \hat{\sigma}_h^-(t_i) \hat{\sigma}_h^-(t_i + \tau_j) \hat{\sigma}_h^+ \hat{\sigma}_h^-(t_i + \tau_j) \hat{\sigma}_h^+(t_i) \rangle}{\langle \hat{\sigma}_h^- \hat{\sigma}_h^+ \rangle_{ss}^2} \tag{G.10}$$

G.2 Hot bath–current–cold bath three-time correlations

G.2.a Derivation

The three time correlations of the detection of emission from the hot bath (at $t = t_{ss}$) then current (at $t + \tau_1$) and finally the detection of emission into the cold bath (at $t + \tau_1 + \tau_2$) are given by:

$$\begin{aligned}
 F_{hIc}^{(3)}(t_{ss}, \tau_1, \tau_2) &= \langle \hat{\sigma}_h^-(t) \hat{\sigma}_c^+(t + \tau_1 + \tau_2) \\
 &\quad \times \hat{\sigma}_c^-(t + \tau_1 + \tau_2) \hat{I}(t + \tau_1) \hat{\sigma}_h^+(t) \rangle_{ss} \\
 &= \text{Tr}[\rho_{ss} \hat{\sigma}_h^-(t_{ss}) \hat{\sigma}_c^+(t_{ss} + \tau_1 + \tau_2) \hat{\sigma}_c^-(t_{ss} + \tau_1 + \tau_2) \\
 &\quad \times \hat{I}(t_{ss} + \tau_1) \hat{\sigma}_h^+(t_{ss})] \\
 &= \text{Tr}[\hat{\sigma}_c^-(t_{ss} + \tau_1 + \tau_2) \hat{I}(t_{ss} + \tau_1) \hat{\sigma}_h^+ \rho_{ss} \hat{\sigma}_h^- \\
 &\quad \times \hat{\sigma}_c^+(t_{ss} + \tau_1 + \tau_2)] \\
 &= \text{Tr}[\hat{\sigma}_c^-(t_{ss} + \tau_1 + \tau_2) \hat{I}(t_{ss} + \tau_1) \tilde{\rho}_1^{hIc}(t_{ss} + \tau_1) \\
 &\quad \times \hat{\sigma}_c^+(t_{ss} + \tau_1 + \tau_2)] \\
 &= \text{Tr}[\hat{\sigma}_c^-(t_{ss} + \tau_1 + \tau_2) \tilde{\rho}_2^{hIc}(t_{ss} + \tau_1 + \tau_2) \\
 &\quad \times \hat{\sigma}_c^+(t_{ss} + \tau_1 + \tau_2)] \\
 &= \tilde{\rho}_{2,0011}^{hIc}(t_{ss} + \tau_1 + \tau_2) + \tilde{\rho}_{2,1111}^{hIc}(t_{ss} + \tau_1 + \tau_2)
 \end{aligned} \tag{G.11}$$

Where $\tilde{\rho}_1^{hIc}(t + \tau_1)$ satisfies the master equation Eq. (III.A.2.5) and has the initial condition :

$$\tilde{\rho}_1^{hIc}(t_{ss}) = \hat{\sigma}_h^+ \rho_{ss} \hat{\sigma}_h^- \tag{G.12}$$

Then :

$$\hat{I}(t_{ss} + \tau_1) \tilde{\rho}_1^{hIc}(t_{ss} + \tau_1) = \hat{I} \tilde{\rho}_1^{hIc}(t_{ss} + \tau_1) \tag{G.13}$$

And $\tilde{\rho}_2^{hIc}(t_{ss} + \tau_1 + \tau_2)$ satisfies the master equation Eq. (III.A.2.5) and has the initial condition :

$$\tilde{\rho}_2^{hIc}(t_{ss} + \tau_1) = \hat{I}\tilde{\rho}_1^{hIc}(t_{ss} + \tau_1) \quad (\text{G.14})$$

Then :

$$\begin{aligned} \hat{\sigma}_c^-(t_{ss} + \tau_1 + \tau_2)\tilde{\rho}_2^{hIc}(t_{ss} + \tau_1 + \tau_2)\hat{\sigma}_c^+(t_{ss} + \tau_1 + \tau_2) \\ = \hat{\sigma}_c^-\tilde{\rho}_2^{hIc}(t_{ss} + \tau_1 + \tau_2)\hat{\sigma}_c^+ \end{aligned} \quad (\text{G.15})$$

The infinite time limits are given by :

$$\begin{aligned} \lim_{\tau_1, \tau_2 \rightarrow \infty} \tilde{\rho}_2^{hIc}(t_{ss} + \tau_1 + \tau_2) &= \langle \hat{\sigma}_h^- \hat{\sigma}_h^+ \rangle_{ss} \langle \hat{I} \rangle_{ss} \rho_{ss} \\ &= [\rho_{0000,ss} + \rho_{0011,ss}] [-ieE_J \sin(2\lambda_h) \sin(2\lambda_c) \\ &\quad \times (\rho_{1001,ss} - \rho_{0110,ss})] \rho_{ss} \end{aligned} \quad (\text{G.16})$$

And :

$$\begin{aligned} \lim_{\tau_1 \rightarrow \infty} F_{hIc}^{(3)}(t_{ss}, \tau_1, \tau_2) &= \langle \hat{\sigma}_c^+(t + \tau_2) \hat{\sigma}_c^-(t + \tau_2) \hat{I}(t) \rangle_{ss} \langle \hat{\sigma}_h^- \hat{\sigma}_h^+ \rangle_{ss} \\ \lim_{\tau_2 \rightarrow \infty} F_{hIc}^{(3)}(t_{ss}, \tau_1, \tau_2) &= \langle \hat{\sigma}_h^-(t) \hat{I}(t + \tau_1) \hat{\sigma}_h^+(t) \rangle_{ss} \langle \hat{\sigma}_c^+ \hat{\sigma}_c^- \rangle_{ss} \\ \lim_{\tau_1, \tau_2 \rightarrow \infty} F_{hIc}^{(3)}(t_{ss}, \tau_1, \tau_2) &= \langle \hat{\sigma}_h^- \hat{\sigma}_h^+ \rangle_{ss} \langle \hat{I} \rangle_{ss} \langle \hat{\sigma}_c^+ \hat{\sigma}_c^- \rangle_{ss} \\ &= [\rho_{0000,ss} + \rho_{0011,ss}] \\ &\quad \times [-ieE_J \sin(2\lambda_h) \sin(2\lambda_c) (\rho_{1001,ss} - \rho_{0110,ss})] \\ &\quad \times [\rho_{0011,ss} + \rho_{1111,ss}] \end{aligned} \quad (\text{G.17})$$

G.2.b Pure three-body contributions

Similarly to the derivation of $g_{c,p}^{(3)}$, $g_{hIc,p}^{(3)}$ can be derived for the hot-current-cold correlations:

$$g_{hIc,p}^{(3)} = 2 + g_{hIc}^{(3)}(t, t + \tau_1, t + \tau_1 + \tau_2) - g_{hI}^{(2)}(t, t + \tau_1) - g_{hc}^{(2)}(t, t + \tau_1 + \tau_2) - g_{Ic}^{(2)}(t + \tau_1, t + \tau_1 + \tau_2) \quad (\text{G.18})$$

Where, for $t = t_{ss}$:

$$g_{hIc}^{(3)}(t_{ss}, t_{ss} + \tau_1, t_{ss} + \tau_1 + \tau_2) = \frac{F_{hIc}^{(3)}(t_{ss}, \tau_1, \tau_2)}{\langle \hat{\sigma}_h^- \hat{\sigma}_h^+ \rangle_{ss} \langle \hat{I} \rangle_{ss} \langle \hat{\sigma}_c^+ \hat{\sigma}_c^- \rangle_{ss}} \quad (\text{G.19})$$

And, for $t_i \geq t_{ss}$:

$$g_{hI}^{(2)}(t_i, t_i + \tau_j) = \frac{\langle \hat{\sigma}_h^-(t_i) \hat{I}(t_i + \tau_j) \hat{\sigma}_h^+(t_i) \rangle}{\langle \hat{I} \rangle_{ss} \langle \hat{\sigma}_h^- \hat{\sigma}_h^+ \rangle_{ss}} \quad (\text{G.20})$$

$$g_{hc}^{(2)}(t_i, t_i + \tau_j) = \frac{\langle \hat{\sigma}_h^-(t_i) \hat{\sigma}_c^+(t_i + \tau_j) \hat{\sigma}_c^-(t_i + \tau_j) \hat{\sigma}_h^+(t_i) \rangle}{\langle \hat{\sigma}_c^+ \hat{\sigma}_c^- \rangle_{ss} \langle \hat{\sigma}_h^- \hat{\sigma}_h^+ \rangle_{ss}} \quad (\text{G.21})$$

$$g_{Ic}^{(2)}(t_i, t_i + \tau_j) = \frac{\langle \hat{\sigma}_c^+(t_i + \tau_j) \hat{\sigma}_c^-(t_i + \tau_j) \hat{I}(t_i) \rangle}{\langle \hat{I} \rangle_{ss} \langle \hat{\sigma}_c^+ \hat{\sigma}_c^- \rangle_{ss}} \quad (\text{G.22})$$

Quantum thermoelectric engine —derivation of the time evolution of the measured engine

In this Appendix, we derive the analytical solution to the time evolution of the both-side measured system described in Sec III.B.4.1

H.1 Derivation of the time evolution

We recall the matrix form of the master equation (Eq. (III.B.2.12)) for the bath-free engine, measured both on the cold and hot sides:

$$\dot{\hat{\rho}}_v^{hc}(t) = L\hat{\rho}_v^{hc}(t) \quad (\text{H.1})$$

where $\hat{\rho}_v^{hc}$ is given by:

$$\hat{\rho}_v^{hc} = \begin{pmatrix} \rho_{0000} & \rho_{0001} & \rho_{0100} & \rho_{0101} & \rho_{0010} & \rho_{0011} & \rho_{0110} & \rho_{0111} & \cdots \\ \cdots & \rho_{1000} & \rho_{1001} & \rho_{1100} & \rho_{1101} & \rho_{1010} & \rho_{1011} & \rho_{1110} & \rho_{1111} \end{pmatrix}^T \quad (\text{H.2})$$

$$\hat{\rho}_v^{hc}(t) = e^{Lt} \hat{\rho}_v^{hc}(0). \quad (\text{H.4})$$

Since L is a normal (*i.e.* satisfying $LL^\dagger = L^\dagger L$) 16×16 matrix, it is diagonalizable per application of the spectral theorem [227] and can therefore be written as:

$$L = P\Lambda P^\dagger, \quad (\text{H.5})$$

where P is a unitary matrix with its columns being the orthonormal eigenvectors $\mathbf{l}_i (l_{i,1}, \dots, l_{i,16})$ of L , and Λ the diagonal matrix of corresponding eigenvalues λ_i (with $i \in \llbracket 1, 16 \rrbracket$).

Then, Eq. (H.4) becomes:

$$\hat{\rho}_v^{hc}(t) = e^{P\Lambda P^\dagger t} \hat{\rho}_v^{hc}(0). \quad (\text{H.6})$$

Using the the property $PP^\dagger = P^\dagger P = \mathbb{1}$:

$$\begin{aligned} e^{P\Lambda P^\dagger t} &= \sum_{n=0}^{+\infty} \frac{(P\Lambda P^\dagger t)^n}{n!} \\ &= \sum_{n=0}^{+\infty} \frac{(P\Lambda t P^\dagger)^n}{n!} \\ &= \sum_{n=0}^{+\infty} \frac{P(\Lambda t)^n P^\dagger}{n!} \\ &= P e^{\Lambda t} P^\dagger \end{aligned} \quad (\text{H.7})$$

Using the same explicit expansion of the exponential function, we can recover the property:

$$e^{\Lambda t} = \begin{pmatrix} e^{\lambda_1 t} & 0 & \dots & \dots & 0 \\ 0 & \ddots & 0 & \dots & 0 \\ \vdots & \dots & \ddots & \dots & \vdots \\ \vdots & \dots & \dots & \ddots & 0 \\ 0 & \dots & \dots & 0 & e^{\lambda_{16} t} \end{pmatrix} \quad (\text{H.8})$$

Eq. (H.6) explicitly reads:

$$\hat{\rho}_v^{hc}(t) = \begin{pmatrix} l_{1,1} & \cdots & \cdots & \cdots & l_{16,1} \\ \vdots & \ddots & \cdots & \cdots & \vdots \\ \vdots & \cdots & \ddots & \cdots & \vdots \\ \vdots & \cdots & \cdots & \ddots & \vdots \\ l_{16,1} & \cdots & \cdots & \cdots & l_{16,16} \end{pmatrix} \begin{pmatrix} e^{\lambda_1 t} & 0 & \cdots & \cdots & 0 \\ 0 & \ddots & 0 & \cdots & 0 \\ \vdots & \cdots & \ddots & \cdots & \vdots \\ \vdots & \cdots & \cdots & \ddots & 0 \\ 0 & \cdots & \cdots & 0 & e^{\lambda_{16} t} \end{pmatrix} \\
 \times \begin{pmatrix} l_{1,1}^* & \cdots & \cdots & \cdots & l_{16,1}^* \\ \vdots & \ddots & \cdots & \cdots & \vdots \\ \vdots & \cdots & \ddots & \cdots & \vdots \\ \vdots & \cdots & \cdots & \ddots & \vdots \\ l_{16,1}^* & \cdots & \cdots & \cdots & l_{16,16}^* \end{pmatrix} \begin{pmatrix} \rho_1^{hc}(0) \\ \vdots \\ \vdots \\ \vdots \\ \rho_{16}^{hc}(0) \end{pmatrix}, \tag{H.9}$$

and, after a few matrix multiplications, it simplifies to:

$$\hat{\rho}_v^{hc}(t) = e^{\lambda_1 t} \mathbf{1}_1 \sum_{i=1}^{16} l_{1,i}^* \rho_i^{hc}(0) + \cdots + e^{\lambda_{16} t} \mathbf{1}_{16} \sum_{i=1}^{16} l_{16,i}^* \rho_i^{hc}(0) \tag{H.10}$$

From this we obtain the decomposition:

$$\hat{\rho}_v^{hc}(t) = \sum_{i=1}^{16} r_i e^{\lambda_i t} \mathbf{1}_i \tag{H.11}$$

H.2 Derivation of the periodic steady state

We recall the equation satisfied by the periodic steady state (Eq. III.B.4.4):

$$\begin{aligned} \hat{\rho}_p^{hc}(t + T_{cycle}) &= \hat{\mathcal{U}}(\tau_2, \tau_1) \hat{M}_2 \hat{\mathcal{U}}(\tau_1, t) \hat{M}_1 \hat{\rho}_p^{hc}(t) \\ &= \hat{\rho}_p^{hc}(t) \\ \underbrace{(\mathbb{1} - \hat{\mathcal{U}}(\tau_2, \tau_1) \hat{M}_2 \hat{\mathcal{U}}(\tau_1, t) \hat{M}_1)}_{\hat{\Xi}(\tau_1, \tau_2, t)} \hat{\rho}_p^{hc}(t) &= \mathbb{0} \end{aligned} \tag{H.12}$$

We set $t = 0$ at the moment right before the first measurement. After the measurement is performed, the state of the system is given by $\hat{\rho}_{v,1}^{hc}(0) = \hat{M}_1 \hat{\rho}_v^{hc}(0)$. It is decomposed on the basis of eigenvectors of L in order to evaluate it at the time right before the second measurement:

$$\hat{\rho}_{v,1}^{hc}(t_1) = \sum_{i=1}^{16} r_{i,1} e^{\lambda_i t_1} \mathbf{l}_i \quad (\text{H.13})$$

with:

$$r_{i,1} = \mathbf{l}_i^* \cdot \hat{\rho}_{v,1}^{hc}(0). \quad (\text{H.14})$$

Then, after the application of the second measurement, the density matrix becomes: $\hat{\rho}_{v,2}^{hc}(t_1) = \hat{M}_2 \hat{\rho}_{v,1}^{hc}(t_1)$ and after the evolution time t_2 it is given by:

$$\hat{\rho}_{v,2}^{hc}(t_1 + t_2) = \sum_{i=1}^{16} r_{i,2} e^{\lambda_i t_1} \mathbf{l}_i \quad (\text{H.15})$$

with:

$$r_{i,2} = \mathbf{l}_i^* \cdot \hat{\rho}_{v,2}^{hc}(t_1). \quad (\text{H.16})$$

This succession of operations (Eqs. (H.13) to (H.16)) gives the explicit effect of the periodic operator $\mathbb{1} - \hat{\Xi}(t, \tau_1, \tau_2) = \hat{U}(\tau_2, \tau_1) \hat{M}_2 \hat{U}(\tau_1, t) \hat{M}_1$ from Eq. (H.12).

A periodic solution, satisfying $\hat{\rho}_p^{hc}(t) = \hat{\rho}_{v,2}^{hc}(t_1 + t_2) = \hat{\rho}_v^{hc}(0)$, is then analytically calculated¹ by finding the eigenvectors of $\hat{\Xi}(t, \tau_1, \tau_2)$. As the operations described are not trace preserving, we normalize the solution by its trace. The normalized solution verifies Eq. (H.12) as well.

¹ $\hat{\Xi}$ was calculated with help from the **Mathematica** software and its kernel was calculated using **Matlab**.

H.3 Inverse of a matrix of orthogonal eigenvectors

One can note that if the eigenvectors are orthogonal but not orthonormal, the following relation is satisfied instead of Eq. (H.5):

$$L = P\Lambda P^{-1} \quad (\text{H.17})$$

P^{-1} can be recovered from P^\dagger by dividing the coefficients relative to each eigenvector by their respective norm.

Let us consider a 3×3 matrix K of complex orthogonal vectors $\mathbf{a}(a_1, a_2, a_3)$, $\mathbf{b}(b_1, b_2, b_3)$ and $\mathbf{c}(c_1, c_2, c_3)$:

$$K = \begin{pmatrix} a_1 & b_1 & c_1 \\ a_2 & b_2 & c_2 \\ a_3 & b_3 & c_3 \end{pmatrix} \quad (\text{H.18})$$

We call N_i the norm of the vector $\mathbf{i} \in \{\mathbf{a}, \mathbf{b}, \mathbf{c}\}$. It is given by: $N_i = \sqrt{i_1 i_1^* + i_2 i_2^* + i_3 i_3^*}$. The orthonormal matrix \widetilde{K} then reads:

$$\widetilde{K} = \begin{pmatrix} \frac{a_1}{N_a} & \frac{b_1}{N_b} & \frac{c_1}{N_c} \\ \frac{a_2}{N_a} & \frac{b_2}{N_b} & \frac{c_2}{N_c} \\ \frac{a_3}{N_a} & \frac{b_3}{N_b} & \frac{c_3}{N_c} \end{pmatrix} \quad (\text{H.19})$$

Then, \widetilde{K}^{-1} satisfies $\widetilde{K}^{-1} = \widetilde{K}^\dagger$ and $\widetilde{K}\widetilde{K}^\dagger = \widetilde{K}^\dagger\widetilde{K} = \mathbb{1}$. Explicitly we have:

$$\widetilde{K}K^\dagger = \begin{pmatrix} \frac{a_1}{N_a} & \frac{b_1}{N_b} & \frac{c_1}{N_c} \\ \frac{a_2}{N_a} & \frac{b_2}{N_b} & \frac{c_2}{N_c} \\ \frac{a_3}{N_a} & \frac{b_3}{N_b} & \frac{c_3}{N_c} \end{pmatrix} \begin{pmatrix} \frac{a_1^*}{N_a} & \frac{a_2^*}{N_a} & \frac{a_3^*}{N_a} \\ \frac{b_1^*}{N_b} & \frac{b_2^*}{N_b} & \frac{b_3^*}{N_b} \\ \frac{c_1^*}{N_c} & \frac{c_2^*}{N_c} & \frac{c_3^*}{N_c} \end{pmatrix} \quad (\text{H.20})$$

$$= \begin{pmatrix} \frac{a_1 a_1^*}{N_a^2} + \frac{b_1 b_1^*}{N_b^2} + \frac{c_1 c_1^*}{N_c^2} & \frac{a_1 a_2^*}{N_a^2} + \frac{b_1 b_2^*}{N_b^2} + \frac{c_1 c_2^*}{N_c^2} & \frac{a_1 a_3^*}{N_a^2} + \frac{b_1 b_3^*}{N_b^2} + \frac{c_1 c_3^*}{N_c^2} \\ \frac{a_2 a_1^*}{N_a^2} + \frac{b_2 b_1^*}{N_b^2} + \frac{c_2 c_1^*}{N_c^2} & \frac{a_2 a_2^*}{N_a^2} + \frac{b_2 b_2^*}{N_b^2} + \frac{c_2 c_2^*}{N_c^2} & \frac{a_2 a_3^*}{N_a^2} + \frac{b_2 b_3^*}{N_b^2} + \frac{c_2 c_3^*}{N_c^2} \\ \frac{a_3 a_1^*}{N_a^2} + \frac{b_3 b_1^*}{N_b^2} + \frac{c_3 c_1^*}{N_c^2} & \frac{a_3 a_2^*}{N_a^2} + \frac{b_3 b_2^*}{N_b^2} + \frac{c_3 c_2^*}{N_c^2} & \frac{a_3 a_3^*}{N_a^2} + \frac{b_3 b_3^*}{N_b^2} + \frac{c_3 c_3^*}{N_c^2} \end{pmatrix} \quad (\text{H.21})$$

Which allows us to see that the inverse of K is given by:

$$K^{-1} = \begin{pmatrix} \frac{a_1^*}{N_a^2} & \frac{a_2^*}{N_a^2} & \frac{a_3^*}{N_a^2} \\ \frac{b_1^*}{N_b^2} & \frac{b_2^*}{N_b^2} & \frac{b_3^*}{N_b^2} \\ \frac{c_1^*}{N_c^2} & \frac{c_2^*}{N_c^2} & \frac{c_3^*}{N_c^2} \end{pmatrix} \quad (\text{H.22})$$

Quantum thermoelectric engine

—Measurement matrices for the no-bath system

In this Appendix, we provide the matrix form of the measurement operators for the both-side measured system described in Sec III.B.2.2.b

The measurement operators for the hot side $\{\hat{P}_h^+, \hat{P}_h^-\}$ are given by:

$$\begin{aligned} \hat{P}_h^+ &\equiv \hat{P}^+ \otimes \mathbb{1}_C \\ &= \begin{pmatrix} \cos^2 \alpha & 0 & e^{-i\phi} \cos \alpha \sin \alpha & 0 \\ 0 & \cos^2 \alpha & 0 & e^{-i\phi} \cos \alpha \sin \alpha \\ e^{i\phi} \cos \alpha \sin \alpha & 0 & \sin^2 \alpha & 0 \\ 0 & e^{i\phi} \cos \alpha \sin \alpha & 0 & \sin^2 \alpha \end{pmatrix}, \end{aligned} \quad (\text{I.1})$$

$$\begin{aligned} \hat{P}_h^- &\equiv \hat{P}^- \otimes \mathbb{1}_C \\ &= \begin{pmatrix} \sin^2 \alpha & 0 & -e^{-i\phi} \cos \alpha \sin \alpha & 0 \\ 0 & \sin^2 \alpha & 0 & -e^{-i\phi} \cos \alpha \sin \alpha \\ -e^{i\phi} \cos \alpha \sin \alpha & 0 & \cos^2 \alpha & 0 \\ 0 & -e^{i\phi} \cos \alpha \sin \alpha & 0 & \cos^2 \alpha \end{pmatrix}. \end{aligned} \quad (\text{I.2})$$

And for the cold side $\{\hat{P}_c^+, \hat{P}_c^-\}$ are given by:

$$\begin{aligned}
 \hat{P}_c^+ &\equiv \mathbb{1}_H \otimes \hat{P}^+ \\
 &= \begin{pmatrix} \cos^2 \alpha & e^{-i\phi} \cos \alpha \sin \alpha & 0 & 0 \\ e^{i\phi} \cos \alpha \sin \alpha & \sin^2 \alpha & 0 & 0 \\ 0 & 0 & \cos^2 \alpha & e^{-i\phi} \cos \alpha \sin \alpha \\ 0 & 0 & e^{i\phi} \cos \alpha \sin \alpha & \sin^2 \alpha \end{pmatrix},
 \end{aligned} \tag{I.3}$$

$$\begin{aligned}
 \hat{P}_c^- &\equiv \mathbb{1}_H \otimes \hat{P}^- \\
 &= \begin{pmatrix} \sin^2 \alpha & -e^{-i\phi} \cos \alpha \sin \alpha & 0 & 0 \\ -e^{i\phi} \cos \alpha \sin \alpha & \cos^2 \alpha & 0 & 0 \\ 0 & 0 & \sin^2 \alpha & -e^{-i\phi} \cos \alpha \sin \alpha \\ 0 & 0 & -e^{i\phi} \cos \alpha \sin \alpha & \cos^2 \alpha \end{pmatrix}.
 \end{aligned} \tag{I.4}$$

Bibliography

- [1] K. Verteletsky and K. Mølmer (2019) arXiv:1907.01039 [quant-ph] .
- [2] A. L. Lavoisier, “Traité élémentaire de chimie: présenté dans un ordre nouveau et d’après les découvertes modernes; avec figures,” (Cuchet, 1793) Chap. 1, pp. 4–5.
- [3] S. Carnot, “Réflexions sur la puissance motrice du feu et sur les machines propres à développer cette puissance,” (Bachelier, 1824) Chap. 1, pp. 10–12.
- [4] D. Bernoulli, “Hydrodynamica: sive de viribus et motibus fluidorum commentarii,” (Johannis Reinholdi Dulseckeri, 1738) Chap. 10, pp. 200–244.
- [5] J. C. Maxwell, The London, Edinburgh, and Dublin Philosophical Magazine and Journal of Science **19**, 19 (1860).
- [6] L. Boltzmann, “Weitere studien über das wärmeleichgewicht unter gasmolekülen,” in *Kinetische Theorie II: Irreversible Prozesse Einführung und Originaltexte* (Vieweg+Teubner Verlag, Wiesbaden, 1872) pp. 115–225.
- [7] L. Boltzmann, *Über die Beziehung zwischen dem zweiten Hauptsatze des mechanischen Wärmethorie und der Wahrscheinlichkeitsrechnung, respective den Sätzen über das Wärmegleichgewicht* (Kk Hof- und Staatsdruckerei, 1877).
- [8] R. Clausius, The London, Edinburgh, and Dublin Philosophical Magazine and Journal of Science **2**, 1 (1851).
- [9] E. A. Cornell and C. E. Wieman, Reviews of Modern Physics **74**, 875 (2002).
- [10] S. N. Bose, Zeitschrift für Physik **26**, 178 (1924).
- [11] A. Einstein, S. B. Preuss. Akad. Wiss. phys.-math. Klasse (1924).
- [12] C. Elouard, D. A. Herrera-Martí, M. Clusel, and A. Auffèves, npj Quantum Information **3**, 9 (2017).
- [13] A. E. Allahverdyan and T. M. Nieuwenhuizen, Phys. Rev. E **71**, 066102 (2005).
- [14] V. Balzani, M. Clemente-León, A. Credi, B. Ferrer, M. Venturi, A. H. Flood, and J. F. Stoddart, Proceedings of the National Academy of Sciences **103**, 1178 (2006).
- [15] J. J. J. Roden, D. I. G. Bennett, and K. B. Whaley, The Journal of Chemical Physics **144**, 245101 (2016).
- [16] D. James, Applied Physics B **66**, 181 (1998).
- [17] R. B. Linnet, I. D. Leroux, M. Marcicante, A. Dantan, and M. Drewsen, Phys. Rev. Lett. **109**, 233005 (2012).
- [18] C. Monroe, D. M. Meekhof, B. E. King, S. R. Jefferts, W. M. Itano, D. J. Wineland, and P. Gould, Phys. Rev. Lett. **75**, 4011 (1995).
- [19] D. Gangloff, A. Bylinskii, I. Counts, W. Jhe, and V. Vuletić, Nature Physics **11**, 915 (2015).

- [20] A. Abdelrahman, O. Khosravani, M. Gessner, A. Buchleitner, H.-P. Breuer, D. Gorman, R. Masuda, T. Pruttivarasin, M. Ramm, P. Schindler, *et al.*, *Nature communications* **8**, 15712 (2017).
- [21] T. Lauprêtre, R. B. Linnet, I. D. Leroux, H. Landa, A. Dantan, and M. Drewsen, *Phys. Rev. A* **99**, 031401 (2019).
- [22] D. J. Berkeland, J. D. Miller, J. C. Bergquist, W. M. Itano, and D. J. Wineland, *Journal of Applied Physics* **83**, 5025 (1998).
- [23] M. Drewsen, *Physica B: Condensed Matter* **460**, 105 (2015), special Issue on Electronic Crystals (ECRYS-2014).
- [24] S.-T. Wang, C. Shen, and L.-M. Duan, *Scientific reports* **5**, 8555 (2015).
- [25] W. Paul, H. P. Reinhard, and U. von Zahn, *Zeitschrift für Physik* **152**, 143 (1958).
- [26] J. D. Prestage, G. J. Dick, and L. Maleki, *Journal of Applied Physics* **66**, 1013 (1989).
- [27] D. J. Griffiths, “Introduction to Electrodynamics,” (Pearson Prentice Hall, Upper Saddle River, NJ, 1999) Chap. 3, pp. 110–121, 3rd ed.
- [28] S. Earnshaw, *Trans. Camb. Phil. Soc.* **7**, 97 (1842).
- [29] P. Herskind, *Cavity Quantum Electrodynamics with Ion Coulomb Crystals*, PhD thesis, Aarhus University, Aarhus C, Denmark (2008), supervised by M. Drewsen.
- [30] M. Abramowitz and I. Stegun, *Handbook of Mathematical Functions: With Formulas, Graphs, and Mathematical Tables*, Applied mathematics series (Dover Publications, 1964).
- [31] T. Hänsch and A. Schawlow, *Optics Communications* **13**, 68 (1975).
- [32] D. J. Griffiths, “Introduction to quantum mechanics,” (Pearson Prentice Hall, Upper Saddle River, NJ, 2005) Chap. 9, p. 340, 2nd ed.
- [33] D. J. Wineland and W. M. Itano, *Phys. Rev. A* **20**, 1521 (1979).
- [34] C. J. Foot *et al.*, “Atomic physics,” (Oxford University Press, 2005) Chap. 7, pp. 123–137.
- [35] B. H. Bransden, C. J. Joachain, and T. J. Plivier, “Physics of atoms and molecules,” (Pearson Education India, 2003) Chap. 4, p. 196.
- [36] D. J. Tannor, “Introduction to quantum mechanics: a time-dependent perspective,” (University Science Books, 2007) pp. 186–190.
- [37] H. J. Metcalf and P. van der Straten, “Laser cooling and trapping of neutral atoms,” in *The Optics Encyclopedia* (American Cancer Society, 2007) pp. 977–991.
- [38] D. Leibfried, R. Blatt, C. Monroe, and D. Wineland, *Rev. Mod. Phys.* **75**, 281 (2003).
- [39] P. Staantum, *Quantum Optics with Trapped Calcium Ions*, PhD thesis, Aarhus University, Aarhus C, Denmark (2004), supervised by Drewsen, Michael.
- [40] D. J. Tannor, “Introduction to quantum mechanics: a time-dependent perspective,” (University Science Books, Sausalito, CA, 2007) Chap. 9, pp. 186–190.
- [41] C. Cohen-Tannoudji, *Fundamental systems in quantum optics*, 1 (1990).

- [42] W. D. Phillips, *Rev. Mod. Phys.* **70**, 721 (1998).
- [43] B. H. Bransden, C. J. Joachain, and T. J. Plivier, “Physics of atoms and molecules,” (Pearson Education India, 2003) Chap. 4, pp. 219–220.
- [44] S. Stenholm, *Rev. Mod. Phys.* **58**, 699 (1986).
- [45] R. J. Cook, *Phys. Rev. A* **22**, 1078 (1980).
- [46] R. J. Cook, *Optics Communications* **35**, 347 (1980).
- [47] S. Knünz, M. Herrmann, V. Batteiger, G. Saathoff, T. W. Hänsch, and T. Udem, *Phys. Rev. A* **85**, 023427 (2012).
- [48] J. I. Cirac, L. J. Garay, R. Blatt, A. S. Parkins, and P. Zoller, *Phys. Rev. A* **49**, 421 (1994).
- [49] R. G. DeVoe, J. Hoffnagle, and R. G. Brewer, *Phys. Rev. A* **39**, 4362 (1989).
- [50] E. Wigner, *Phys. Rev.* **46**, 1002 (1934).
- [51] L. Hornekaer, *Single and Multi Species Coulomb Ion Crystals : Structures, Dynamics and Sympathetic Cooling*, PhD thesis, Aarhus University, Aarhus C, Denmark (2000), supervised by M. Drewsen.
- [52] R. W. Hasse and V. V. Avilov, *Phys. Rev. A* **44**, 4506 (1991).
- [53] L. Hornekaer, M. Drewsen, C. Brodersen, J. Schiffer, and J. Hangst, *Hyperfine Interactions* **115**, 37 (1998).
- [54] S. Ichimaru, *Rev. Mod. Phys.* **54**, 1017 (1982).
- [55] J. P. Hansen, *Phys. Rev. A* **8**, 3096 (1973).
- [56] E. L. Pollock and J. P. Hansen, *Phys. Rev. A* **8**, 3110 (1973).
- [57] W. L. Slattery, G. D. Doolen, and H. E. DeWitt, *Phys. Rev. A* **21**, 2087 (1980).
- [58] L. Hornekær, N. Kjærgaard, A. M. Thommesen, and M. Drewsen, *Phys. Rev. Lett.* **86**, 1994 (2001).
- [59] L. Hornekær and M. Drewsen, *Phys. Rev. A* **66**, 013412 (2002).
- [60] L. Turner, *The Physics of Fluids* **30**, 3196 (1987).
- [61] M. Hettrich, T. Ruster, H. Kaufmann, C. F. Roos, C. T. Schmiegelow, F. Schmidt-Kaler, and U. G. Poschinger, *Phys. Rev. Lett.* **115**, 143003 (2015).
- [62] J. Jin and D. A. Church, *Phys. Rev. Lett.* **70**, 3213 (1993).
- [63] A. Kreuter, C. Becher, G. P. T. Lancaster, A. B. Mundt, C. Russo, H. Häffner, C. Roos, W. Hänsel, F. Schmidt-Kaler, R. Blatt, and M. S. Safronova, *Phys. Rev. A* **71**, 032504 (2005).
- [64] R. Gerritsma, G. Kirchmair, F. Zähringer, J. Benhelm, R. Blatt, and C. F. Roos, *The European Physical Journal D* **50**, 13 (2008).
- [65] A. Kramida, Y. Ralchenko, J. Reader, and N. A. Team, “Nist atomic spectra database (ver. 5.6.1),” [Online] (2018), national Institute of Standards and Technology, Gaithersburg, MD.
- [66] H. Harhoff Andersen, *Cooling and manipulating ions in traps with integrated optical cavities*, PhD thesis, Aarhus University, Aarhus C,

- Denmark (2015), supervised by M. Drewsen.
- [67] A. L. Wolf, S. A. van den Berg, C. Gohle, E. J. Salumbides, W. Ubachs, and K. S. E. Eikema, *Phys. Rev. A* **78**, 032511 (2008).
- [68] A. L. Wolf, S. A. van den Berg, W. Ubachs, and K. S. E. Eikema, *Phys. Rev. Lett.* **102**, 223901 (2009).
- [69] I. T. Group, “Measurements of transitions of $^{40}\text{Ca}^+$,” (2015), own measurements performed with HighFinesse WS-U wavemeter.
- [70] H. G. Dehmelt, *Bulletin of the American Physical Society* **20**, 60 (1975).
- [71] H. G. Dehmelt, *Le Journal de Physique Colloques* **42**, C8 (1981).
- [72] W. Nagourney, J. Sandberg, and H. Dehmelt, *Phys. Rev. Lett.* **56**, 2797 (1986).
- [73] J. C. Bergquist, R. G. Hulet, W. M. Itano, and D. J. Wineland, *Phys. Rev. Lett.* **57**, 1699 (1986).
- [74] O. Legrand, *Localization spectroscopy of a single ion in an optical lattice*, PhD thesis, Aarhus University, Aarhus C, Denmark (2015), ch. 12, pp. 111–112, Supervised by M. Drewsen.
- [75] P. Bowe, L. Hornekær, C. Brodersen, M. Drewsen, J. S. Hangst, and J. P. Schiffer, *Phys. Rev. Lett.* **82**, 2071 (1999).
- [76] C. Cohen-Tannoudji, *Physica Scripta* **90**, 088013 (2015).
- [77] E. L. Dereniak and T. D. Dereniak, “Aberrations in optical systems,” in *Geometrical and Trigonometric Optics* (Cambridge University Press, 2008) Chap. 11, pp. 292–327.
- [78] M. Lampton, *Scientific American* **245**, 62 (1981).
- [79] O. Legrand, *Localization spectroscopy of a single ion in an optical lattice*, PhD thesis, Aarhus University, Aarhus C, Denmark (2015), ch. 1, pp. 111–112, Supervised by M. Drewsen.
- [80] N. H. Nielsen, *Measuring the temperature of coulomb crystals*, Master’s thesis, Aarhus University, Aarhus C, Denmark (2011), supervised by M. Drewsen.
- [81] M. Raunbak, *Simulering af temperatureffekter for ion Coulombkrystaller*, Bachelor’s thesis, Aarhus University, Aarhus C, Denmark (2014), supervised by M. Drewsen.
- [82] M. Raunbak, *Manual for Ion Coulomb crystal MD simulator* (2015).
- [83] K. Verteletsky, *Molecular Dynamics (MD) crystal simulation program—Manual* (2017).
- [84] J. I. Cirac and P. Zoller, *Nature* **404**, 579 (2000).
- [85] P. Richerme, *Phys. Rev. A* **94**, 032320 (2016).
- [86] J. W. Britton, B. C. Sawyer, A. C. Keith, C.-C. J. Wang, J. K. Freericks, H. Uys, M. J. Biercuk, and J. J. Bollinger, *Nature* **484**, 489 (2012).
- [87] D. H. E. Dubin, *Phys. Rev. Lett.* **71**, 2753 (1993).
- [88] S. Fishman, G. De Chiara, T. Calarco, and G. Morigi, *Phys. Rev. B* **77**, 064111 (2008).
- [89] B. Liao, A. A. Maznev, K. A. Nelson, and G. Chen, *Nature Communications* **7**, 13174 EP (2016).

- [90] M. Partanen, K. Y. Tan, J. Govenius, R. E. Lake, M. K. Mäkelä, T. Tantt, and M. Möttönen, *Nature Physics* **12**, 460 EP (2016).
- [91] S. Vinjanampathy and J. Anders, *Contemporary Physics* **57**, 545 (2016).
- [92] R. Blattmann and K. Mølmer, *Phys. Rev. A* **96**, 012115 (2017).
- [93] K. Jacobs, *Phys. Rev. E* **86**, 040106(R) (2012).
- [94] M. Perarnau-Llobet, K. V. Hovhannisyan, M. Huber, P. Skrzypczyk, N. Brunner, and A. Acín, *Phys. Rev. X* **5**, 041011 (2015).
- [95] M. Huber, M. Perarnau-Llobet, K. V. Hovhannisyan, P. Skrzypczyk, C. Klöckl, N. Brunner, and A. Acín, *New Journal of Physics* **17**, 065008 (2015).
- [96] C. Jarzynski, *Phys. Rev. Lett.* **78**, 2690 (1997).
- [97] H. Tasaki (2000) arXiv:cond-mat/0009244 [cond-mat.stat-mech] .
- [98] R. Landauer, *IBM Journal of Research and Development* **5**, 183 (1961).
- [99] S. Hilt, S. Shabbir, J. Anders, and E. Lutz, *Phys. Rev. E* **83**, 030102(R) (2011).
- [100] R. Kosloff and A. Levy, *Annual Review of Physical Chemistry* **65**, 365 (2014).
- [101] J. E. Geusic, E. O. Schulz-DuBios, and H. E. D. Scovil, *Phys. Rev.* **156**, 343 (1967).
- [102] A. Levy and R. Kosloff, *Phys. Rev. Lett.* **108**, 070604 (2012).
- [103] A. Ronzani, B. Karimi, J. Senior, Y.-C. Chang, J. T. Peltonen, C. Chen, and J. P. Pekola, *Nature Physics* **14**, 991 (2018).
- [104] M. Youssef, G. Mahler, and A.-S. Obada, *Physica E: Low-dimensional Systems and Nanostructures* **42**, 454 (2010), proceedings of the international conference *Frontiers of Quantum and Mesoscopic Thermodynamics FQMT '08*.
- [105] N. Linden, S. Popescu, and P. Skrzypczyk (2010) arXiv:1010.6029 [quant-ph] .
- [106] G. Maslennikov, S. Ding, R. Hablützel, J. Gan, A. Roulet, S. Nimmrichter, J. Dai, V. Scarani, and D. Matsukevich, *Nature Communications* **10**, 202 (2019).
- [107] J. Roßnagel, S. T. Dawkins, K. N. Tolazzi, O. Abah, E. Lutz, F. Schmidt-Kaler, and K. Singer, *Science* **352**, 325 (2016).
- [108] M. T. Mitchison and P. P. Potts (2018) arXiv:1803.06133 [quant-ph] .
- [109] L. D. Hicks and M. S. Dresselhaus, *Phys. Rev. B* **47**, 12727 (1993).
- [110] T.-H. Liu, J. Zhou, M. Li, Z. Ding, Q. Song, B. Liao, L. Fu, and G. Chen, *Proceedings of the National Academy of Sciences* **115**, 879 (2018).
- [111] P. P. Hofer, J.-R. Souquet, and A. A. Clerk, *Phys. Rev. B* **93**, 041418(R) (2016).
- [112] G. Bochkov and Y. E. Kuzovlev, *Zh. Eksp. Teor. Fiz* **72**, 238 (1977).
- [113] C. Jarzynski, *Phys. Rev. E* **56**, 5018 (1997).
- [114] G. E. Crooks, *Journal of Statistical Physics* **90**, 1481 (1998).

- [115] G. E. Crooks, *Phys. Rev. E* **60**, 2721 (1999).
- [116] G. Hummer and A. Szabo, *Proceedings of the National Academy of Sciences* **98**, 3658 (2001).
- [117] S. Ciliberto, A. Imparato, A. Naert, and M. Tanase, *Journal of Statistical Mechanics: Theory and Experiment* **2013**, P12014 (2013).
- [118] P. Talkner, M. Campisi, and P. Hänggi, *Journal of Statistical Mechanics: Theory and Experiment* **2009**, P02025 (2009).
- [119] M. Campisi, P. Hänggi, and P. Talkner, *Rev. Mod. Phys.* **83**, 771 (2011).
- [120] C. Elouard, N. K. Bernardes, A. R. R. Carvalho, M. F. Santos, and A. Auffèves, *New Journal of Physics* **19**, 103011 (2017).
- [121] S. Suomela, A. Kutvonen, and T. Ala-Nissila, *Phys. Rev. E* **93**, 062106 (2016).
- [122] F. W. J. Hekking and J. P. Pekola, *Phys. Rev. Lett.* **111**, 093602 (2013).
- [123] B. D. Josephson, *Rev. Mod. Phys.* **46**, 251 (1974).
- [124] R. Alicki and R. Kosloff (2018) arXiv:1801.08314 [quant-ph].
- [125] V. Gorini, A. Kossakowski, and E. C. G. Sudarshan, *Journal of Mathematical Physics* **17**, 821 (1976).
- [126] G. Lindblad, *Communications in Mathematical Physics* **48**, 119 (1976).
- [127] R. J. Glauber, *Phys. Rev.* **130**, 2529 (1963).
- [128] B. J. Berne and G. D. Harp, “On the calculation of time correlation functions,” in *Advances in Chemical Physics* (John Wiley & Sons, Ltd, 2007) pp. 63–227.
- [129] M. Lax, *Phys. Rev.* **172**, 350 (1968).
- [130] C. Gardiner and P. Zoller, “Quantum noise: a handbook of markovian and non-markovian quantum stochastic methods with applications to quantum optics,” (Springer Science & Business Media, 2004) pp. 147–148.
- [131] A. D. Armour, M. P. Blencowe, E. Brahim, and A. J. Rimberg, *Phys. Rev. Lett.* **111**, 247001 (2013).
- [132] N. Lörch, C. Bruder, N. Brunner, and P. P. Hofer, *Quantum Science and Technology* **3**, 035014 (2018).
- [133] C. Gardiner and P. Zoller, “Quantum noise: a handbook of markovian and non-markovian quantum stochastic methods with applications to quantum optics,” (Springer Science & Business Media, 2004) pp. 21–23.
- [134] H. Carmichael, “An open systems approach to quantum optics: lectures presented at the université libre de bruxelles, october 28 to november 4, 1991,” (Springer Science & Business Media, 2009) Chap. 1, pp. 5–9.
- [135] S. Haroche and J.-M. Raimond, “Exploring the quantum: atoms, cavities, and photons,” (Oxford university press, 2006) pp. 55, 56, 163–189.
- [136] A. Rivas and S. F. Huelga, “Open quantum systems,” (Springer, 2012) Chap. 4, pp. 33–48.
- [137] R. Loudon, “The quantum theory of light,” (OUP Oxford, 2000) p. 11.
- [138] L. D. Landau and E. M. Lifshitz, “Statistical physics,” (Pergamon Press, 1969) pp. 56–57, 2nd ed.

- [139] L. D. Landau and E. M. Lifshitz, “Statistical physics,” (Pergamon Press, 1969) p. 47, 2nd ed.
- [140] G. Bochkov and Y. E. Kuzovlev, *Soviet Journal of Experimental and Theoretical Physics* **49**, 543 (1979).
- [141] G. Bochkov and Y. Kuzovlev, *Physica A: Statistical Mechanics and its Applications* **106**, 443 (1981).
- [142] G. Bochkov and Y. Kuzovlev, *Physica A: Statistical Mechanics and its Applications* **106**, 480 (1981).
- [143] S. Yukawa, *Journal of the Physical Society of Japan* **69**, 2367 (2000).
- [144] J. Kurchan (2000) arXiv:cond-mat/0007360 [cond-mat.stat-mech] .
- [145] P. Talkner, E. Lutz, and P. Hänggi, *Phys. Rev. E* **75**, 050102 (2007).
- [146] J. Dalibard, Y. Castin, and K. Mølmer, *Phys. Rev. Lett.* **68**, 580 (1992).
- [147] H. Carmichael, “An open systems approach to quantum optics: lectures presented at the université libre de bruxelles, october 28 to november 4, 1991,” (Springer Science & Business Media, 2009).
- [148] J. Eberly and P. Milonni, in *Encyclopedia of Physical Science and Technology (Third Edition)*, edited by R. A. Meyers (Academic Press, New York, 2003) third edition ed., pp. 409 – 439.
- [149] H. J. Kimble and L. Mandel, *Phys. Rev. A* **13**, 2123 (1976).
- [150] L. Mandel and E. Wolf, “Optical coherence and quantum optics,” (Cambridge university press, 1995) Chap. 14.
- [151] A. H. Kiilerich and K. Mølmer, *Phys. Rev. A* **95**, 022110 (2017).
- [152] H. J. Kimble, M. Dagenais, and L. Mandel, *Phys. Rev. Lett.* **39**, 691 (1977).
- [153] Q. Xu, E. Greplova, B. Julsgaard, and K. Mølmer, *Physica Scripta* **90**, 128004 (2015).
- [154] N. Stiesdal, J. Kumlin, K. Kleinbeck, P. Lunt, C. Braun, A. Paris-Mandoki, C. Tresp, H. P. Büchler, and S. Hofferberth, *Phys. Rev. Lett.* **121**, 103601 (2018).
- [155] Q.-Y. Liang, A. V. Venkatramani, S. H. Cantu, T. L. Nicholson, M. J. Gullans, A. V. Gorshkov, J. D. Thompson, C. Chin, M. D. Lukin, and V. Vuletić, *Science* **359**, 783 (2018).
- [156] P. Pietzonka and U. Seifert, *Phys. Rev. Lett.* **120**, 190602 (2018).
- [157] N. Shiraishi, K. Saito, and H. Tasaki, *Phys. Rev. Lett.* **117**, 190601 (2016).
- [158] M. Campisi and R. Fazio, *Nature communications* **7**, 11895 (2016).
- [159] G. Benenti, K. Saito, and G. Casati, *Phys. Rev. Lett.* **106**, 230602 (2011).
- [160] A. M. Timpanaro, G. Guarnieri, J. Goold, and G. T. Landi (2019) arXiv:1904.07574 [quant-ph] .
- [161] J. Klatzow, J. N. Becker, P. M. Ledingham, C. Weinzetl, K. T. Kaczmarek, D. J. Saunders, J. Nunn, I. A. Walmsley, R. Uzdin, and E. Poem, *Phys. Rev. Lett.* **122**, 110601 (2019).
- [162] S. Lloyd, *Phys. Rev. A* **56**, 3374 (1997).
- [163] G. Watanabe, B. P. Venkatesh, P. Talkner, and A. del Campo, *Phys. Rev. Lett.* **118**, 050601 (2017).

- [164] P. Kammerlander and J. Anders, *Scientific reports* **6**, 22174 (2016).
- [165] J. Yi, P. Talkner, and Y. W. Kim, *Phys. Rev. E* **96**, 022108 (2017).
- [166] X. Ding, J. Yi, Y. W. Kim, and P. Talkner, *Phys. Rev. E* **98**, 042122 (2018).
- [167] J. J. Park, K.-H. Kim, T. Sagawa, and S. W. Kim, *Phys. Rev. Lett.* **111**, 230402 (2013).
- [168] M. O. Scully, *Phys. Rev. Lett.* **87**, 220601 (2001).
- [169] L. Buffoni, A. Solfanelli, P. Verrucchi, A. Cuccoli, and M. Campisi, *Phys. Rev. Lett.* **122**, 070603 (2019).
- [170] K. Maruyama, F. Nori, and V. Vedral, *Rev. Mod. Phys.* **81**, 1 (2009).
- [171] C. G. Knott, "Life and scientific work of peter guthrie tait: supplementing the two volumes of scientific papers published in 1898 and 1900," (Cambridge [England]: University Press, 1911) pp. 213–215.
- [172] L. Szilard, *Zeitschrift für Physik* **53**, 840 (1929).
- [173] L. Brillouin, *Journal of Applied Physics* **22**, 334 (1951).
- [174] C. E. Shannon, *Bell System Technical Journal* **27**, 379 (1948).
- [175] C. H. Bennett, *International Journal of Theoretical Physics* **21**, 905 (1982).
- [176] M. B. Plenio and V. Vitelli, *Contemporary Physics* **42**, 25 (2001).
- [177] T. Sagawa and M. Ueda, *Phys. Rev. Lett.* **102**, 250602 (2009).
- [178] A. Solfanelli, L. Buffoni, A. Cuccoli, M. Campisi, A. Solfanelli, L. Buffoni, A. Cuccoli, and M. Campisi (2019) p. arXiv:1905.10262, arXiv:1905.10262 [quant-ph] .
- [179] C. Elouard, D. Herrera-Martí, B. Huard, and A. Auffèves, *Phys. Rev. Lett.* **118**, 260603 (2017).
- [180] N. Cottet, S. Jezouin, L. Bretheau, P. Campagne-Ibarcq, Q. Ficheux, J. Anders, A. Auffèves, R. Azouit, P. Rouchon, and B. Huard, *Proceedings of the National Academy of Sciences* **114**, 7561 (2017).
- [181] P. A. Camati, J. P. S. Peterson, T. B. Batalhão, K. Micadei, A. M. Souza, R. S. Sarthour, I. S. Oliveira, and R. M. Serra, *Phys. Rev. Lett.* **117**, 240502 (2016).
- [182] W. Heisenberg, "The physical principles of the quantum theory," (Dover Publications, 1949) pp. 13–39, translated by C. Eckart and F.C. Hoyt, Department of Physics, University of Chicago.
- [183] P. A. M. Dirac, "The principles of quantum mechanics," (Oxford university press, 1981) pp. 34–48.
- [184] J. von Neumann and R. T. Beyer, *Mathematical Foundations of Quantum Mechanics: New Edition*, new edition ed. (Princeton University Press, 2018).
- [185] G. Lüders, *Annalen der Physik* **15**, 663 (2006), reprint of G. Lüders, *Ann. Phys. (Leipzig)* **8**, 322–328 (1951). Translation and discussion by K. A. Kirkpatrick, New Mexico Highlands University, Las Vegas, New Mexico 87701, USA.
- [186] Y. Aharonov, D. Z. Albert, and L. Vaidman, *Phys. Rev. Lett.* **60**, 1351 (1988).

- [187] Y. Aharonov and L. Vaidman, *Phys. Rev. A* **41**, 11 (1990).
- [188] A. G. Kofman, S. Ashhab, and F. Nori, *Physics Reports* **520**, 43 (2012), nonperturbative theory of weak pre- and post-selected measurements.
- [189] E. B. Davies, *Communications in Mathematical Physics* **15**, 277 (1969).
- [190] M. Srinivas and E. Davies, *Optica Acta: International Journal of Optics* **28**, 981 (1981).
- [191] K. Jacobs and D. A. Steck, *Contemporary Physics* **47**, 279 (2006).
- [192] C. W. Gardiner, A. S. Parkins, and P. Zoller, *Phys. Rev. A* **46**, 4363 (1992).
- [193] C. Gardiner and P. Zoller, “Quantum noise: a handbook of markovian and non-markovian quantum stochastic methods with applications to quantum optics,” (Springer Science & Business Media, 2004) pp. 24–35.
- [194] H. M. Wiseman and G. J. Milburn, “Quantum measurement theory,” in *Quantum Measurement and Control* (Cambridge University Press, 2009) pp. 8–50.
- [195] G. Ludwig, “Ensembles and effects,” in *Foundations of Quantum Mechanics I* (Springer Berlin Heidelberg, Berlin, Heidelberg, 1983) pp. 19, 32–33, 42–43.
- [196] K. Kraus, A. Böhm, J. D. Dollard, and W. H. Wootters, eds., *States, Effects, and Operations Fundamental Notions of Quantum Theory: Lectures in Mathematical Physics at the University of Texas at Austin* (Springer Berlin Heidelberg, Berlin, Heidelberg, 1983).
- [197] J. von Neumann and R. T. Beyer, “Mathematical foundations of quantum mechanics: New edition,” (Princeton University Press, 2018) p. 50, ned - new edition ed.
- [198] C. Cohen-Tannoudji, B. Diu, and F. Laloe, “Quantum mechanics,” (Wiley-VCH, 1977) Chap. *II_B*, pp. 115–116, 121.
- [199] B. Misra and E. C. G. Sudarshan, *Journal of Mathematical Physics* **18**, 756 (1977).
- [200] J. C. Flores, *Phys. Rev. B* **60**, 30 (1999).
- [201] G. Gordon, D. D. B. Rao, and G. Kurizki, *New Journal of Physics* **12**, 053033 (2010).
- [202] J. Yi, P. Talkner, and G.-L. Ingold, *Phys. Rev. A* **84**, 032121 (2011).
- [203] V. I. Yudin, A. V. Taichenachev, and M. Y. Basalaev, *Phys. Rev. A* **93**, 013820 (2016).
- [204] G. Floquet, in *Annales scientifiques de l'École normale supérieure*, Vol. 12 (1883) pp. 47–88.
- [205] A. Rivas and S. F. Huelga, “Open quantum systems,” (Springer, 2012) Chap. 2, pp. 15–17.
- [206] M. B. Plenio and P. L. Knight, *Rev. Mod. Phys.* **70**, 101 (1998).
- [207] H. M. Wiseman, Quantum and Semi-classical Optics: *Journal of the European Optical Society Part B* **8**, 205 (1996).
- [208] H. J. Carmichael, *Phys. Rev. Lett.* **70**, 2273 (1993).
- [209] P. Zoller, M. Marte, and D. F. Walls, *Phys. Rev. A* **35**, 198 (1987).
- [210] H. M. Wiseman and G. J. Milburn, *Phys. Rev. A* **47**, 1652 (1993).

- [211] P. Kochan, H. J. Carmichael, P. R. Morrow, and M. G. Raizen, *Phys. Rev. Lett.* **75**, 45 (1995). (Wiley-VCH, 1977) Chap. *B_{II}*, pp. 166–175.
- [212] Z. Mineev, S. Mundhada, S. Shankar, P. Reinhold, R. Gutiérrez-Jáuregui, R. Schoelkopf, M. Mirrahimi, H. Carmichael, and M. Devoret, *Nature* **570**, 200 (2019).
- [213] M. Émile Borel, *Rendiconti del Circolo Matematico di Palermo* (1884–1940) **27**, 247 (1909).
- [214] C. Elouard and A. N. Jordan, *Phys. Rev. Lett.* **120**, 260601 (2018).
- [215] R. P. Feynman, R. B. Leighton, and M. Sands, “The Feynman lectures on physics, Vol. I: The new millennium edition: mainly mechanics, radiation, and heat,” (Basic books, 2011) Chap. 46.
- [216] C. Cohen-Tannoudji, B. Diu, and F. Laloe, “Quantum mechanics,” (Wiley-VCH, 1977) Chap. *A_{IV}*, pp. 417–419.
- [217] C. Cohen-Tannoudji, B. Diu, and F. Laloe, “Quantum mechanics,” (Wiley-VCH, 1978) Chap. *IX_B*, *A_{IX}*, pp. 972–973, 987.
- [218] B. Hall, C. Brian, *et al.*, “Lie groups, lie algebras, and representations: An elementary introduction,” (Springer Science & Business Media, 2003) pp. 29, 63–89.
- [219] C. Cohen-Tannoudji, B. Diu, and F. Laloe, “Quantum mechanics,” (J. von Neumann and R. T. Beyer, “Mathematical foundations of quantum mechanics: New edition,” (Princeton University Press, 2018) p. 194, ned - new edition ed.
- [220] J. von Neumann and R. T. Beyer, “Mathematical foundations of quantum mechanics: New edition,” (Princeton University Press, 2018) pp. 115–116, ned - new edition ed.
- [221] J. von Neumann and R. T. Beyer, “Mathematical foundations of quantum mechanics: New edition,” (Princeton University Press, 2018) pp. 115–116, ned - new edition ed.
- [222] D. F. Walls and G. J. Milburn, “Quantum optics,” (Springer Science & Business Media, 2007) pp. 46–54, 2nd ed.
- [223] H. J. Carmichael, *J. Opt. Soc. Am. B* **4**, 1588 (1987).
- [224] L. Mandel and E. Wolf, “Optical coherence and quantum optics,” (Cambridge university press, 1995) p. 630.
- [225] P. A. M. Dirac, “The principles of quantum mechanics,” (Oxford university press, 1981) pp. 239–242.
- [226] L. Mandel and E. Wolf, “Optical coherence and quantum optics,” (Cambridge university press, 1995) pp. 573–587.
- [227] H. M. Wiseman and G. J. Milburn, “Quantum measurement theory,” in *Quantum Measurement and Control* (Cambridge University Press, 2009) p. 11.